Master's Degree in Aerospace Engineering - Aerogasdynamics

Active Control of Wall-Bounded Turbulent Flows



Politecnico di Torino

Supervisors:
Prof. Gaetano Maria Di Cicca
Ing. Enrico Saccaggi

Candidate:
Alice Frumusa

Academic Year 2025 / 2026

To my loving family, for the unwavering support and belief in me;
to Riccardo, for his constant encouragement, and love. And to my beloved Pongo,
Robin and Priscilla

Acknowledgements

I would like to express my sincere gratitude to my supervisors, Ing. Enrico Saccaggi and Prof. Gaetano Maria Di Cicca, for their invaluable guidance, support, and encouragement throughout the development of this thesis.

Their expertise and constant support were instrumental in helping me overcome the challenges encountered along the way. Their mentorship has played a fundamental role in both my academic and personal growth, and I am truly grateful for the opportunity to have worked under their supervision.

I am also deeply thankful to my family and my boyfriend for their support, patience, and encouragement throughout this journey. Their presence and understanding have been a continuous source of strength and motivation during my studies.

Abstract

The reduction of aerodynamic drag is a strategic objective to decrease energy consumption and pollutant emissions in modern transportation systems. In high-performance vehicles, such as commercial aircraft, more than half of the total drag is caused by surface skin friction. Studies aimed at characterizing the coherent structures of the turbulent boundary layer [1–3] have demonstrated that the primary contributors to wall shear stress are structures known as sweeps, which are events consisting of high-speed fluid directed toward the wall from the outer region.

To mitigate surface friction, active control techniques focused on reducing the frequency and intensity of these wall-ward sweep events have proven effective. A foundational numerical study by Choi et al. [3] achieved friction reductions of up to 25% through an active control scheme based on wall blowing and suction, applied with velocities equal in magnitude but opposite in direction to those detected at a specific wall-normal plane. This technique, defined as "opposition control", effectively generates a "virtual wall" [4] positioned between the detection point and the physical surface, which ideally blocks the penetration of sweeps. Subsequent experimental wind tunnel tests by Rebbeck and Choi [5, 6] confirmed that a wall-normal synthetic jet, actuated in real-time upon sweep detection, can intercept and attenuate the intensity of such events.

Following Rebbeck and Choi [5, 6] experimental literature, this thesis evaluates the efficacy of active opposition control using a loudspeaker-driven zero-net-mass-flux (ZNMF) synthetic jet on a fully developed turbulent boundary layer. The experimental campaign was conducted in the 8-meter open-circuit wind tunnel at the "Modesto Panetti" Aerodynamics Laboratory of Politecnico di Torino. The control architecture relies on a dual hot-wire anemometry system: an upstream Dantec 55P11 probe detects incoming sweeps via a spatial velocity gradient technique,

while a downstream Dantec 55P15 boundary layer probe conditionally samples the manipulated flow to evaluate structural changes against the uncontrolled baseline.

An important evolution in this research was the transition of the control hardware from a standard analog signal generator to a digital Arduino GIGA microcontroller. This upgrade enabled the creation of customized, asymmetric triangular waveforms, granting control over the blowing and suction phases of the actuator.

Extensive characterization in still-air conditions revealed that mitigating the severity of the suction phase is crucial; rapid suction in crossflow induces a detrimental velocity overshoot, effectively acting as a "synthetic sweep". The optimized asymmetric triangular waveform almost completely eliminated this overshoot, ensuring a strictly counter-advective interaction. A comprehensive parametric study encompassing over 350 measurements demonstrated that optimal phase alignment and momentum injection can yield a maximum localized skin-friction reduction ($\Delta\tau_{wall}$) of approximately 1.95%, and 1.58% respectively for the Arduino GIGA configuration and signal generator configuration. While both setups achieved comparable evaluated skin friction reduction, the Arduino GIGA configuration exhibited superior statistical robustness across a wide array of off-design parameters.

Finally, an energetic saturation limit was identified, proving that excessive actuation amplitude actively disrupts the control objective, overriding the opposition logic and resulting in a net drag penalty.

Contents

List of Figures **xiii**

List of Tables **xxxi**

Nomenclature **xxxiii**

1 Coherent Structures and Control Techniques in Wall-Bounded Turbulence **1**

1.1 Wall-Bounded Turbulence and Coherent Structures 2

1.1.1 The Near-Wall Cycle and Bursting Process and Quasi-Streamwise Vortices 4

1.1.2 Mass Momentum Transfer by Vortical Structures and Skin Friction 8

1.1.3 Outer-Inner Layer Interactions, Horseshoe and Hairpin Vortices and Scaling 11

1.1.4 Investigative Methodologies 16

1.1.5 Coherent Motion Identification and Characterization Techniques 18

1.1.6 Numerical Simulations 19

1.2 Control Strategies for Turbulent Drag Reduction 21

1.2.1 Passive Control and Surface Topology 32

1.2.2 Active Control Techniques: Numerical Investigations 39

1.2.3 Opposition Active Control: Experimental Implementation with Synthetic Jets 44
1.2.4 Physical Interaction: Jet in Crossflow (JICF) 48
1.2.5 Machine Learning and Neural Networks Applied on Turbulent Flow Control 52
1.3 Concluding Remarks 56

2 Experimental Set-Up **57**
2.1 Sensors 57
2.2 Signal Acquisition 62
2.3 Detection Method 63
2.4 Control Procedure 64
2.4.1 First Control Set-up 64
2.4.2 Second Control Set-up 67
2.4.3 Control Actuator Characteristics 70
2.5 Concluding Remarks 70

3 Experimental Campaigns and Data Analysis **73**
3.1 Synthetic Jet Characterization in Still-Air Conditions: 1^{st} Control Set-up 73
3.1.1 Continuous Acquisition and Statistical Characterization . . 74
3.1.2 Plots of All Jet Velocity Profiles with Highlighted Peaks . . 76
3.1.3 Conditionally Averaged Jet Velocity Profiles for All Cases . 81
3.1.4 Effect of Waveform Optimization (Old vs. "new-wave") . . 85
3.1.5 Voltage Amplitude and Divider Influence 90
3.1.6 Parametric Analysis of Frequency and Voltage Amplitude Variation 101
3.1.7 System Time Delay Assessment 103

3.2 Synthetic Jet Characterization in Still-Air Conditions: 2^{nd} Control Set-up 105
3.2.1 Influence of Actuation Amplitude 110
3.2.2 Influence of Wave Asymmetry and Frequency 110
3.3 Experimental Results and Discussion: Wall-Normal Survey 115
3.3.1 Long-Term Time-Averaged Turbulence Statistics 116
3.3.2 Conditionally Averaged Streamwise Velocity Profiles 120
3.3.3 Space-Time Flow Topology Reconstruction 124
3.4 Extensive Parametric Characterization of the Actuation Authority . 127
3.4.1 Data Post-Processing and Analysis Strategy 129
3.4.2 Aggregated Near-Wall Performance and Parametric Analysis 132
3.4.3 Control Parameter Sensitivity and Optimization Maps . . . 143
3.4.4 Comparison of Optimal Control Configurations 145
3.4.5 Statistical Distribution of Control Efficacy 146
3.4.6 Energetic Saturation and Actuation Limits 148
3.5 Concluding Remarks 149

4 Conclusions and Future Work 151
4.1 Summary of the Experimental Work 152
4.2 Key Findings and Physical Insights 152
4.3 Outlook and Recommendations for Future Work 154

Appendix A Hot-Wire Probes Calibration Procedure 155

Appendix B Continuous Acquisition and Data Logging Pseudocode for Jet Characterization 159

Appendix C Multi-Axis Traverse System and Probe Positioning Control Pseudocode 163

Appendix D Data Post-Processing and Conditional Sampling in Still-Air Flow Pseudocode 167

Appendix E Automated Vertical Flow Survey and Profiling Pseudocode 171

Appendix F Data Post-Processing and Statistical Analysis Pseudocode 175

Appendix G Acquisition Algorithms: Repeatability Study of Active Opposition Control 179

Appendix H Near Wall Controlled Flow Data Post-Processing Pseudocode 181

References 185

List of Figures

1.1 Geometry and nomenclature for arch- and hairpin-shaped vortical structures. Image sourced from Robinson [1] 4

1.2 Quadrants from the instantaneous $u'v'$ plane. Image sourced from Robinson [1] 5

1.3 Schematic of a QSV in the buffer region and the inducted bursting process. The rotation of the vortex lifts-up near-wall fluid creating ejections Q_2 (in blue) and blows fluid from the outer region towards the wall, generating sweeps Q_4 (in red). Redrawn and adapted from Robinson [1] 7

1.4 Vorticity lines mapped around a quasi-streamwise vortex, highlighting the characteristic upright and inverted hairpin shapes found in boundary layer flows. Redrawn from Robinson [1] 10

1.5 Idealized hairpin-vortex model proposed by Theodorsen [7], showing a vortical structure rising from a low-speed region with legs near the wall and an inclined head; the labels along the vortex line mark geometric segments of the same structure. Redrawn from Theodorsen [7] 12

1.6 Conceptual schematic of the formation of a hairpin vortex and the associated momentum transport events. From left to right: a localized lift-up of a spanwise vortex filament; the subsequent stretching and tilting driven by the mean shear flow; and the fully developed 3D hairpin structure. The mature vortex induces a characteristic pumping action, generating Q_2 ejections in the central "head" region and Q_4 sweeps on the outer sides, "legs" and "head". 15

1.7 Conceptual decomposition of a symmetric hairpin vortex into its constituent elements. The structure consists of a transverse head and two counter-rotating quasi-streamwise legs. The diagram illustrates how an isolated quasi-streamwise vortex (QSV) can be interpreted as a partial segment of this more complex, idealized configuration. Redrawn and adapted from Robinson [1]. 16

1.8 Vortex generators on a Boeing 737 wing, positioned on its upper surface at the leading edge. Image sourced from Udris [8] 22

1.9 **Left:** Example of $M > 1$ flow over an airfoil without vortex generators, the flow separates and the control surface at the leading edge becomes ineffective, the red lines identify shock waves. **Right:** Example of $M > 1$ flow over an airfoil with vortex generators before the control surface, flow doesn't separate because the vortices induced by the vortex generator energise it by mixing free-stream flow with BL flow. Red lines represent shock waves and dashed lines represent the disrupted shock wave. Image redrawn and adapted from Udris [8] 22

1.10 Flow over a smooth sphere compared to flow over a golf ball, characterized by distributed roughness elements. 24

1.11 Application of the steady blowing technique via film cooling on a turbine blade (CAD rendering). The surface holes allow the injection of high-momentum pre-combustion fluid into the boundary layer. In addition to thermal protection, this active control strategy alters the interaction of near-wall coherent structures, leading to a modification of viscous shear stresses. Image sourced from the website CAESES [9] 26

1.12 Time evolution of a single detection (dot-dash line) and of the ensemble averaged (solid line) u^+ velocity profile during the interaction between the TBL flow and the jet created by the piston. As Rebbeck and Choi highlight [5] the horizontal speed-component presents a *"w-shape"*. Image sourced from Rebbeck and Choi [5] 27

1.13 Flow field generated by the actuation of a DBD. Upon actuation, flow is accelerated away from the electrode by ion collisions, causing entrainment of the surrounding flow above the electrode. After the jet creation, a starting vortex is born, which moves away from the wall enhancing entrainment and generating secondary vorticity along the wall. Image redrawn and adapted from Whalley and Choi [10] . 29

1.14 Microstructure of the AeroSHARK riblet film. Image sourced from Lufthansa Technik [11]. 33

1.15 Characteristic dimensions of riblets with conventional geometries. . 34

1.16 Normalized drag reduction profiles for various riblet topographies, scaled to align along a uniform initial viscous slope. The drag reduction performance is evaluated with respect to two dimensionless geometric parameters: (a) the lateral riblet spacing, s^+, and (b) the square root of the groove's cross-sectional area, ℓ_g^+. Experimental measurements conducted by Bechert et al. [12] are indicated by open triangles, while solid circles represent DNS data obtained by García-Mayoral and Jiménez [13], image sourced from García and Jiménez [14]. 35

1.17 Shark skin ribbed scales. Image sourced form Lufthansa Technik webpage [11] 36

1.18 Characterisation of surfaces with the static contact angle criterion. . 38

1.19 Qualitative schematic of superhydrophobic surfaces mechanisms, with focus on near-wall streamwise velocity gradient. In the diagram, G: gas, L: liquid, S: solid, w: groove width, u_0: streamwise speed. Image sourced from Kouser et al. [15] 38

1.20 Graphic representation of opposition control using the transverse velocity component. Image redrawn and adapted from Choi, Moin and Kim [3] 41

1.21 Mean velocity profiles normalized by $u_{\tau,u}$ (the friction velocity of the uncontrolled flow). —-: no control; - - - -: v-control; .....: w-control; -.-: law of the wall ($u^+ = y^+$ and $u^+ = 2.5\ln y^+ + 5.5$). Image sourced and adapted from Choi, Moin and Kim [3]. 43

1.22 Diagram of the testing set-up. From left to right: a detector with a 1 mm long upstream detecting hot-wire with a 5 μm diameter; after $\Delta x^+ = 72.5$ downstream of the detecting hot-wire sits the control point with the piston-type actuator; a Dantec 55P15 BL hot-wire downstream of the control point. Image sourced from Rebbeck and Choi [5]. 45

1.23 Time history of the wall-normal velocity expressed in wall units v^+, measured from above the control point in still air, upon the actuation of the speaker with a square-wave law. Image sourced from Rebbeck and Choi [6]. 47

1.24 Time history of normalized streamwise velocity. Dashed lines: conditional averages of nine different sweep events; black line: ensemble average of the sweep events. Image sourced from Rebbeck and Choi [6]. 47

1.25 Schematic diagram of the interaction between a circular jet, produced by a jet nozzle mounted flush on a surface, and the incoming crossflow of velocity U_∞. Image sourced from Kelso et al. [16] . . . 49

1.26 Validation of the FNN performance on the validation dataset. Black dashed line: the uncontrolled case; blue solid line: experimentally measured response under control conditions; red solid line: event predicted by the FNN model with the same control parameters of the experimental results. The control action is applied using the actuation parameters $f = 53.10\,\mathrm{Hz}, Vpp = 62.4\,\mathrm{mV_{pp}}, \Delta t = 1.01\,\mathrm{ms}$ in case (a) and $f = 31.54\,\mathrm{Hz}, Vpp = 60.0\,\mathrm{mV_{pp}}, \Delta t = 2.71\,\mathrm{ms}$ in case (b). Image sourced from [17]. 55

2.1 Orange channel ad complete experimental set-up at Politecnico di Torino used for the experimental research on active flow control on wall-bounded turbulent flows through synthetic jets 58

2.2 Dantec 55M10 CTA Standard Bridge anemometer. 59

2.3 Diagram of the testing set-up employed for the online opposition control. The flow direction is from left to right. 59

2.4 Front hot-wire probe, Dantec 55P11. Image sourced form [18] . . . 60

2.5 Front hot-wire probe, Dantec 55P15. Image sourced form [19] . . . 61

2.6 Analog differentiator used during the measurement campaigns to detect sweep events applying the gradient technique on the hot-wire anemometer signal. The BNC input from the hot-wire is on the right, as written on the white tape (HW); while the BNC output to the comparator is positioned on the left. 63

2.7 Comparator used during the measurement campaigns to compare the the gradient technique pre-set threshold on the differentiated hot-wire anemometer signal. White tape identifies the input BNC connector (top left) and the output BNC connector (top right). . . . 64

2.8 Arduino Uno Rev3 board. Image sourced from [20] 65

2.9 Agilent 33120A signal generator. Image sourced from [21] 65

2.10 Diagram of the sinusoidal waves used during measurement campaigns and the respective defining parameters, set manually through the signal generator interface. It is possible to note that for the new wave function the amplitude set through the signal generator represents half of the effective amplitude of the function. 66

2.11 Schematic diagram of the experimental hardware and control logic. The blue-shaded components denote the real-time detection and control loop, while orange blocks represent the client-side architecture and green blocks indicate the flow generation system (motor and inverter). Arrows illustrate the hardware connections and the logical signal flow between instruments. The NI DAQ board is depicted three times to ensure a clear visualization of the signal paths, which end on different channels of the acquisition board. 67

2.12 Arduino GIGA microcontroller. Image sourced from [22]. 67

2.13 General custom triangular wave issued by the controller. 68

2.14 Schematic diagram of the experimental hardware and control logic. The blue-shaded components denote the real-time detection and control loop, while orange blocks represent the client-side architecture and green blocks indicate the flow generation system (motor and inverter). Arrows illustrate the hardware connections and the logical signal flow between instruments. The NI DAQ board is depicted three times to ensure a clear visualization of the signal paths, which end on different channels of the acquisition board. The difference from the first control set-up is that the Arduino Uno Rev 3 microcontroller and the signal generator are replaced by the Arduino GIGA microcontroller. 69

2.15 Actuator 70

3.1 Time-history of the wall-normal velocity signal v'^{+} at a wall distance of $y^{+} = 7$. Red "x" markers indicate the peaks identified by the detection algorithm. The title of each subplot reports the specific actuation parameters in the format [Frequency (Hz), Amplitude (mV), Divider flag (OFF, ON), Actuation law (old or new)]. The reported amplitudes are already halved for cases with the divider circuit turned on. Closer to the wall the maximum wall normal velocity generated by the synthetic jet is higher than further away from the wall. 78

3.2 Time-history of the wall-normal velocity signal v'^{+} at a wall distance of $y^{+} = 18$ for different experimental configurations. Red "x" markers highlight the detected peaks used for the subsequent conditional sampling. The title of each subplot reports the specific actuation parameters in the format [Frequency (Hz), Amplitude (mV), Divider flag (OFF, ON), Actuation law (old or new)]. The reported amplitudes are already halved for cases with the divider circuit turned on. 79

3.3 Time-history of the wall-normal velocity signal v'^{+} at a wall distance of $y^{+} = 27$. Red "x" markers identify the peaks for various actuation cases. The title of each subplot reports the specific actuation parameters in the format [Frequency (Hz), Amplitude (mV), Divider flag (OFF, ON), Actuation law (old or new)]. The reported amplitudes are already halved for cases with the divider circuit turned on. The visualization validates the robustness of the peak-detection algorithm even as the jet signature evolves and attenuates with increasing distance from the orifice. 80

3.4 Ensemble-averaged wall-normal velocity profiles $\overline{v'}^{+}$ at $y^{+} = 7$. Each curve represents the mean of all detected cycles for a specific test case. The title of each subplot reports the specific actuation parameters in the format [Frequency (Hz), Amplitude (mV), Divider flag (OFF, ON), Actuation law (old or new)]. The reported amplitudes are already halved for cases with the divider circuit turned on. At this coordinate, the jet pulses exhibit the highest peak intensity and a well-defined temporal structure. 82

3.5 Ensemble-averaged wall-normal velocity profiles $\overline{v'}^{+}$ at an intermediate wall distance of $y^{+} = 18$. The title of each subplot reports the specific actuation parameters in the format [Frequency (Hz), Amplitude (mV), Divider flag (OFF, ON), Actuation law (old or new)]. The reported amplitudes are already halved for cases with the divider circuit turned on. The plots show the initial stages of jet diffusion and peak attenuation compared to the near-wall measurements (at $y^{+} = 7$). 83

3.6 Ensemble-averaged velocity profiles $\overline{v'}^{+}$ at the furthest measured distance ($y^{+} = 27$). The title of each subplot reports the specific actuation parameters in the format [Frequency (Hz), Amplitude (mV), Divider flag (OFF, ON), Actuation law (old or new)]. The reported amplitudes are already halved for cases with the divider circuit turned on. The profiles appear broader and characterized by lower maximum velocities, reflecting the momentum transfer and the evolution of the synthetic jet structure as it interacts with the surrounding still-air. 84

3.7 Comparison between the electrical signal of the traditional sinusoidal wave ("old-wave") and the half-sine actuation law ("new-wave") implemented via the signal generator. It is possible to note that for the "new-wave" function the amplitude set through the signal generator represents half of the effective amplitude of the function. . 85

3.8 Comparison between the old and new driving waveforms at $y^+ = 7$. The "new-wave" profiles exhibit a higher peak velocity and a significantly reduced negative velocity region (suction effect) immediately before and after the main jet peak velocity, due to the restricted retraction of the speaker membrane.The title of each subplot reports the specific actuation parameters in the format [Frequency (Hz), Amplitude (mV), Divider flag (OFF, ON), Actuation law (old or new)]. The reported amplitudes are already halved for cases with the divider circuit turned on. 86

3.9 Velocity profiles comparing the two waveforms at $y^+ = 18$. The increased temporal duration and the higher maximum intensity of the jet generated by the "new-wave" are visible. The title of each subplot reports the specific actuation parameters in the format [Frequency (Hz), Amplitude (mV), Divider flag (OFF, ON), Actuation law (old or new)]. The reported amplitudes are already halved for cases with the divider circuit turned on. 87

3.10 Waveform comparison at the furthest wall-normal distance $y^+ = 27$. The profiles highlight the reduction in the deceleration slope following the velocity peak for the "new-wave". This trailing-edge elongation is particularly evident for high-voltage amplitude cases and demonstrates the altered temporal evolution of the modified jet. The title of each subplot reports the specific actuation parameters in the format [Frequency (Hz), Amplitude (mV), Divider flag (OFF, ON), Actuation law (old or new)]. The reported amplitudes are already halved for cases with the divider circuit turned on. 87

3.11 Ensemble averaged jet velocity profiles at $y^+ = 18$ and for $\widehat{A} = 100\ mV$. All the profiles are result of the "new-wave" function, from left to right all control parameter remain the same except for the frequency that increases $(30,\ 60,\ 90)\ Hz$. At high voltage amplitudes and lower frequencies, further away from the wall the profile presents the birth of a second peak after the maximum velocity is reached. The effect is more evident with increasing distance from the wall and decreasing frequencies. 89

3.12 Ensemble averaged jet velocity profiles at $y^+ = 27$ and for $\widehat{A} = 100\ mV$. All the profiles are result of the "new-wave" function, from left to right all control parameter remain the same except for the frequency that increases $(30,\ 60,\ 90)\ Hz$. At high voltage amplitudes and lower frequencies, further away from the wall the profile presents the birth of a second peak after the maximum velocity is reached. The effect is more evident with increasing distance from the wall and decreasing frequencies. 89

3.13 Conditioned, ensemble-averaged velocity profiles $\overline{v'^+}$ at $y^+ = 7$, comparing the baseline waveform ("old-wave") without the voltage divider circuit (left) and with the voltage divider circuit activated (right). The comparison highlights the reduction of the suction intensity when the divider is employed. The title of each subplot reports the specific actuation parameters in the format [Frequency (Hz), Amplitude (mV), Divider flag (OFF, ON), Actuation law (old or new)]. The reported amplitudes are already halved for cases with the divider circuit turned on. 92

3.14 Conditioned, ensemble-averaged velocity profiles $\overline{v'^+}$ at $y^+ = 18$, comparing the baseline waveform without (left) and with (right) the voltage divider circuit. This comparison highlights the non-linear scaling between the voltage amplitude supplied to the loudspeaker and the maximum velocity peak achieved by the jet. The title of each subplot reports the specific actuation parameters in the format [Frequency (Hz), Amplitude (mV), Divider flag (OFF, ON), Actuation law (old or new)]. The reported amplitudes are already halved for cases with the divider circuit turned on. 92

3.15 Conditioned, ensemble-averaged velocity profiles $\overline{v'^+}$ at $y^+ = 27$, comparing the baseline waveform without (left) and with (right) the voltage divider circuit. Similar to the previous wall-normal position, the non-linear scaling of the peak velocity with respect to the attenuated input voltage amplitude is evident. The title of each subplot reports the specific actuation parameters in the format [Frequency (Hz), Amplitude (mV), Divider flag (OFF, ON), Actuation law (old or new)]. The reported amplitudes are already halved for cases with the divider circuit turned on. 93

3.16 Conditioned velocity profiles $\overline{v'^+}$ at $y^+ = 7$, tracking the influence of the voltage divider applied to the "new-wave" signal (right), compared to the undivided case (left). he title of each subplot reports the specific actuation parameters in the format [Frequency (Hz), Amplitude (mV), Divider flag (OFF, ON), Actuation law (old or new)]. The reported amplitudes are already halved for cases with the divider circuit turned on. The combined use of the new waveform and the divider yields an overall shape highly consistent with the reference findings by Rebbeck and Choi [6]. 94

3.17 Conditioned velocity profiles $\overline{v'^+}$ at $y^+ = 18$, comparing the "new-wave" signal without (left) and with (right) the voltage divider. The activated divider effectively smooths the deceleration slope. The title of each subplot reports the specific actuation parameters in the format [Frequency (Hz), Amplitude (mV), Divider flag (OFF, ON), Actuation law (old or new)]. The reported amplitudes are already halved for cases with the divider circuit turned on. 95

3.18 Conditioned velocity profiles $\overline{v'^+}$ at $y^+ = 27$, comparing the "new-wave" signal without (left) and with (right) the voltage divider. The title of each subplot reports the specific actuation parameters in the format [Frequency (Hz), Amplitude (mV), Divider flag (OFF, ON), Actuation law (old or new)]. The reported amplitudes are already halved for cases with the divider circuit turned on. 95

3.19 Conditioned, ensemble-averaged velocity profiles $\overline{v'^+}$ at $y^+ = 7$. The plots compare the undivided configuration (left) against the divided configuration with doubled generator voltage (right). The rows correspond to actuation frequencies of 30 Hz (top), 60 Hz (middle), and 110 Hz (bottom). The comparison highlights the non-linear attenuation and the intensity reduction introduced by the ungrounded divider circuit. 98

3.20 Conditioned, ensemble-averaged velocity profiles $\overline{v'^+}$ at $y^+ = 18$, comparing the undivided set-up (left) and the divided set-up with doubled source voltage amplitude (right) across 30, 60, and 110 Hz. The persistent reduction of the maximum velocity peak in the active-divider case is clearly visible. 99

3.21 Conditioned, ensemble-averaged velocity profiles $\overline{v'^+}$ at the furthest measured distance, $y^+ = 27$. The comparative analysis confirms the deviation from the ideal divider scaling behavior, exacerbated by the lack of electrical grounding. 100

3.22 Conditioned, ensemble-averaged velocity profiles $\overline{v'^+}$ at $y^+ = 7$ illustrating the effect of actuation frequency variation using the baseline "old-wave" function without a voltage divider circuit. The subplots from left to right track the severe reduction in jet duration as the frequency increases across 30 Hz, 60 Hz, and 110 Hz. 102

3.23 Conditioned, ensemble-averaged velocity profiles $\overline{v'^+}$ at $y^+ = 7$ tracking the effect of actuation frequency variation using the optimized "new-wave" function with the use of a voltage divider circuit. The sequence from left to right (30, 60, and 110 Hz) highlights the structural robustness of the optimized waveform, which preserves the sharp jet morphology even under high-frequency compression. . 102

3.24 Time history of the phase-conditioned velocity fluctuations $\overline{v'^+}$ at $y^+ \approx 15$ showcasing consecutive synthetic jet cycles. The synchronized timestamps for the electrical trigger generation (orange crosses) and the corresponding aerodynamic response detection (pink crosses) are superimposed to illustrate the periodic stability of the actuation system. 104

3.25 Detailed close-up view of a single synthetic jet actuation cycle showcasing the threshold-crossing detection method. The temporal gap between the signal generator trigger issuance (orange cross) and the physical fluid displacement matching the $\overline{v'^{+}}$ criterion (pink cross) defines the intrinsic electro-mechanical delay ($\Delta t \approx 3.1$ ms, corresponding to $\Delta t^{+} = 5.2$). 104

3.26 Ensemble conditionally averaged wall-normal velocity (v^{+}) profiles over non-dimensional time (t^{+}) for all jet cases studied with fixed asymmetry $x\% = 1\%$. Frequencies range from top to bottom $f = (30, 60, 120, 200)$ Hz and voltage amplitudes from left to right $\widehat{A} = (25, 50, 100)$ mV. The red dashed line in each plot denotes the instant the microcontroller actuated the loudspeaker's amplifier. . . 107

3.27 Ensemble conditionally averaged wall-normal velocity (v^{+}) profiles over non-dimensional time (t^{+}) for all jet cases studied with fixed asymmetry $x\% = 50\%$. Frequencies range from top to bottom $f = (30, 60, 120, 200)$ Hz and voltage amplitudes from left to right $\widehat{A} = (25, 50, 75)$ mV. The maximum voltage amplitude was limited to 75 mV, as the vertical velocities induced at 100 mV significantly exceeded the required jet intensity for opposition control. The red dashed line denotes the actuation trigger. 108

3.28 Ensemble conditionally averaged wall-normal velocity (v^{+}) profiles over non-dimensional time (t^{+}) for all jet cases studied with fixed asymmetry $x\% = 90\%$. Frequencies range from top to bottom $f = (30, 60, 120, 200)$ Hz and voltage amplitudes from left to right $\widehat{A} = (25, 50, 75)$ mV. The red dashed line denotes the actuation trigger. . 109

3.29 Effect of amplitude on the jet velocity profile. Conditional averages of adimentional wall-normal velocity profiles over t^{+}. The vertical red dashed line represents the instant when the Arduino Giga triggered the loudspeaker amplifier with the determined triangular custom wave. Top: Pronounced structural ringing and secondary velocity peaks induced by excessive amplitude ($V_{pp} = \widehat{A} =$ 100 mV).Bottom: A clean expulsion at low amplitude ($V_{pp} = \widehat{A} =$ 25 mV). 111

3.30 Evolution of the jet velocity profile as a function of the wave asymmetry percentage ($x\%$) at a constant frequency of 30 Hz and amplitude of 50 mV. The transition from a highly impulsive ejection ($x\% = 1\%$, top) to a gradual expulsion ($x\% = 90\%$, bottom) is clearly evident, demonstrating strong control authority at low frequencies. 113

3.31 Evolution of the jet velocity profile as a function of the wave asymmetry percentage ($x\%$) at a constant frequency of 200 Hz and amplitude of 50 mV. At this high frequency, the temporal variations between the jet profiles induced by changing $x\%$ become virtually negligible. 114

3.32 Wall-normal profiles of long-term time-averaged turbulence statistics for Test Case 10 ("old-wave") compared against canonical DNS data [23]: (a) Mean velocity profile U^+; (b) Streamwise Reynolds stress $\overline{u'u'}^+$; (c) Streamwise velocity skewness S; (d) Streamwise velocity flatness F. 118

3.33 Wall-normal profiles of long-term time-averaged turbulence statistics for Test Case 13 ("new-wave") compared against canonical DNS data [23]: (a) Mean velocity profile U^+; (b) Streamwise Reynolds stress $\overline{u'u'}^+$; (c) Streamwise velocity skewness S; (d) Streamwise velocity flatness F. 119

3.34 Conditionally-averaged streamwise ensemble averaged velocity fluctuations for Test Case 10 ("old-wave") u'^+ as a function of the non-dimensional time t^+ across discrete wall-normal coordinates (y^+), contrasting the natural uncontrolled coherent event (dashed black line) with the actively controlled response (solid red line). . . 121

3.35 Conditionally-averaged streamwise ensemble averaged velocity fluctuations for Test Case 13 ("new-wave") u'^+ as a function of the non-dimensional time t^+ across discrete wall-normal coordinates (y^+), contrasting the natural uncontrolled coherent event (dashed black line) with the actively controlled response (solid red line). . . 122

3.36 2D space-time reconstruction of the conditionally-averaged streamwise velocity fluctuations u'^{+} in the (t^{+}, y^{+}) plane for Test Case 10 ("old-wave"): (top) Uncontrolled baseline showcasing the natural space-time topology of coherent structures; (bottom) Controlled flow field highlighting the footprint and structural disruption induced by the synthetic jet. After actuation is possible to see a region where the controlled flow shows effectively a streamwise velocity reduction, afterwards there is a *"velocity overshoot bubble"* where speed is recovered and increased greatly compared to the uncontrolled flow. . 125

3.37 2D space-time reconstruction of the conditionally-averaged streamwise velocity fluctuations u'^{+} in the (t^{+}, y^{+}) plane for Test Case 13 ("new-wave"): (top) Uncontrolled baseline showcasing the natural space-time topology of coherent structures; (bottom) Controlled flow field highlighting the aerodynamic footprint and structural disruption induced by the synthetic jet. After actuation is possible to see a region where the controlled flow shows effectively a streamwise velocity reduction, but in comparison with the previous image regarding Test Case 10, the "new-wave" driving function deters the streamwise speed recovery, avoiding the formation of the *"velocity overshoot bubble"*. 126

3.38 Aggregated near-wall velocity profiles ($u^{+} < 5$) for the Arduino Giga set-up (Part 1). The panels depict the ensemble-averaged controlled response (blue solid line) versus the uncontrolled baseline (black dashed line) across low frequency and voltage amplitude variations. 134

3.39 Aggregated near-wall velocity profiles ($u^{+} < 5$) for the Arduino Giga set-up (Part 2). The panels depict the ensemble-averaged controlled response (blue solid line) versus the uncontrolled baseline (black dashed line). This parametric subset focuses on variations of frequency and delay time to evaluate synchronization between the sweep and the control actuation. 135

3.40 Aggregated near-wall velocity profiles ($u^+ < 5$) for the Arduino Giga set-up (Part 3). The panels depict the ensemble-averaged controlled response (blue solid line) versus the uncontrolled baseline (black dashed line). The plots illustrate the controlled streamwise velocity under high-frequency actuation regimes and time delays and varying spatial asymmetry percentages ($x\%$). 136

3.41 Aggregated near-wall velocity profiles ($u^+ < 5$) for the Arduino Giga set-up (Part 4). The panels depict the ensemble-averaged controlled response (blue solid line) versus the uncontrolled baseline (black dashed line). High frequency and higher amplitude voltages are presented in this subset 137

3.42 Aggregated near-wall velocity profiles ($u^+ < 5$) for the Arduino Giga set-up (Part 5). The panels depict the ensemble-averaged controlled response (blue solid line) versus the uncontrolled baseline (black dashed line). This final subset demonstrates the maximum voltage amplitudes studied ($V_{pp} = \widehat{A}$ up to 100 mV). 138

3.43 Aggregated near-wall velocity profiles ($u^+ < 5$) for the analog signal generator benchmark. The panels track the ensemble-averaged controlled response (red solid line) against the uncontrolled flow baseline (black dashed line), serving as the reference case for the active flow control campaign. 139

3.44 Comparison between controlled flows obtained with a set of actuation parameters involving low frequency and low $x\%$ with control settings $\widehat{A} = 30$ mV, $f = 5.0$ Hz, $x\% = 10\%$, $\Delta t = 0.15$ ms (left) and with a set employing high frequency and hig $x\%$ $\widehat{A} = 30$ mV, $f = 5.0$ Hz, $x\% = 90\%$, $\Delta t = 0.15$ ms (right). Dashed black lines: uncontrolled flow, blue line: controlled flow by the triangular custom wave (second control set-up woth Arduino Giga) 141

3.45 Comparison between controlled flows obtained with a set of actuation parameters involving low frequency and high voltage $\widehat{A} = 50$ mV, $f = 20$ Hz, $x\% = 1\%$, $\Delta t = 2$ ms (left) and with a set employing high voltage and high frequency $\widehat{A} = 50$ mV, $f = 200$ Hz, $x\% = 10\%$, $\Delta t = 5$ ms (right). Dashed black lines: uncontrolled flow, blue line: controlled flow by the triangular custom wave (second control set-up with Arduino Giga) 142

3.46 Comparison between controlled flows obtained with a set of actuation parameters involving low amplitude $\widehat{A} = 7$ mV, $f = 30$ Hz, $\Delta t = 2$ ms (left) and with a set employing high voltage $\widehat{A} = 16$ mV, $f = 30$ Hz, $\Delta t = 0.15$ ms (right). Dashed black lines: uncontrolled flow, blue line: controlled flow by the half-sine driving function ("new-wave" first control set-up with signal generator and voltage divider circuit) 143

3.47 Parametric control map for the signal generator configuration. The scatter plot correlates actuation frequency and time delay with the resulting mean skin friction reduction ($\Delta\tau_{wall}$), highlighting discrete optimal operating regions in the parameter space. 144

3.48 Parametric control map for the Arduino Giga set-up utilizing a triangular waveform. The map evaluates control efficacy as a function of the signal's spatial asymmetry ($x\%$) and delay time, revealing the impact of customized wave shapes on wall-bounded turbulence manipulation. 145

3.49 Conditionally-averaged near-wall velocity profiles for the optimal control configurations. Left: signal generator at 30 Hz, 0.1 ms delay, and 13 mV. Right: Arduino Giga at 120 Hz, 8.0 ms delay, 90% asymmetry, and 35 mV. Both cases demonstrate a remarkable attenuation of the u^+ convective peak. 146

3.50 Statistical distribution of the active control efficacy restricted to the near wall region results ($u^+ < 5$) for the signal generator and Arduino Giga configurations. The violin plots illustrate the probability density and interquartile ranges, comparing the variance and robustness of the two hardware setups. 148

3.51 Energetic saturation analysis correlating the actuation amplitude ($V_{pp} = \widehat{A}$) with the resulting skin friction reduction. The negative slope of the regression lines indicates that excessive actuation energy introduces spurious momentum in the wall-bouded turbulence, degrading the control performance and leading to a net increase in drag. 149

List of Tables

1.1 Summary of flow control techniques, their primary goals, and typical applications. 30

3.1 Summary of the experimental test matrix for the synthetic jet characterization in still-air conditions using the sinusoidal ("old-wave") and the half-sine ("new-wave") waveforms. 76

3.2 Summary of the experimental test matrix for the synthetic jet characterization in still-air conditions using the custom triangular waveform. 106

3.3 Wall-distance calibration offsets and viscous scaling parameters for the selected test cases. 116

3.4 Experimental parameter space for the first control set-up. Generator Voltage is the one sent by the signal generator, while the effective voltage amplitude was the voltage effectively fed to the loudspeaker due to the use of a voltage divider circuit with a factor of 1/4. When n.d. is displayed next to the effective voltage amplitude value, it means that the divider was not employed. 129

3.5 Experimental parameter space for the second control set-up, Arduino Giga. 129

3.6 Experimental parameter space bounds for the first control set-up with the signal generator , with restrictions of repeatability and near-wall measurement applied. 147

3.7 Experimental parameter space bounds for the second control set-up Arduino Giga, with restrictions of repeatability and near-wall measurement applied. 147

Nomenclature

Symbols

$\Delta\tau_{wall}$ Variation of skin friction with control actuation

Δt Delay time actuation parameter

δ Boundary layer thickness

$\Delta\tau$ Skin friction variation due to control techniques

δ^* Displacement thickness

$\delta^+ = \frac{\delta u_\tau}{\nu}$ Boundary layer thickness expressed in wall units

$\ell_g + = \sqrt{A_g^+}$ Characteristic riblet length expressed in wall units

η Kolmogorov's micro-scale

μ Dynamic viscosity

ν Kinematic viscosity

$\Omega_x, \Omega_y, \Omega_z$ Mean vorticity in x, y, z directions

ρ Density

τ^+ Time expressed in wall units

τ_0 Skin friction for a smooth wall

τ_w Wall shear stress

θ Momentum thickness

$\widehat{A}$ Actuation voltage amplitude

A_g Riblet groove cross section

A_g^+ Riblet groove cross section expressed in wall units

C_f Skin friction coefficient

f Actuation frequency

f_s Sampling frequency

H Channel half-height

h Riblet depth

h^+ Riblet depth expressed in wall units

k Gradient technique threshold

L Channel length

L Generic system characteristic length

l^+ Viscous units

$q_1, q_2, q_3 \ldots$ Geometric markers identifying vorticity filament portions

$Q_{1,2,3,4}$ Quadrant method coherent structure identification

Re Reynolds number

$Re_\tau = \frac{Hu_\tau}{\nu}$ Friction Reynolds number for channel flows

Re_θ Momentum Reynolds number

s Riblet spacing

s^+ Riblet spacing expressed in wall units

T^+ Gradient technique averaging time

t_s Sampling time

u' Velocity component fluctuation in the streamwise direction

U_0 Centerline channel velocity

$u_\tau = \sqrt{\frac{\tau_w}{\rho}}$ Wall friction velocity

u_j^+ Convection velocity of the low speed velocity region generated by a synthetic jet expressed in wall units

u_s^+ Convection velocity of the high speed velocity region of sweep events

$u_{\tau,u}$ Unmanipulated flow wall friction velocity

v' Velocity component fluctuation in the wall-normal direction

W Channel width

w' Velocity component fluctuation in the spanwise direction

$x\%$ Percentage of the triangular wave with a positive slope

x Streamwise direction

x_{front}^+ Streamwise distance of the front hot-wire from the control orifice

x_{rear}^+ Streamwise distance of the rear hot-wire from the control orifice

y Wall-normal direction

$y^+ = \frac{yu_\tau}{\nu}$ Dimensionless wall distance

y_{front}^+ Wall-normal distance of the front hot-wire from the control orifice

y_{rear}^+ Wall-normal distance of the rear hot-wire from the control orifice

$y_d = \frac{\nu y_d^+}{u_{\tau,u}}$ Detection wall normal distance

y_d^+ Detection wall normal distance expressed in wall units

y_s^+ Viscous sublayer height expressed in wall-units

z Spanwise direction

Acronyms / Abbreviations

BL Boundary layer

CA Static contact angle

CAH Contact angle hysteresis

CNN Convolutional neural network

CTA Constant temperature anemometer

CVP Counterrotating vortex pairs

DBD Dielectric barrier discharge

DNS Direct numerical simulation

DOE Design of experiments

DR Drag reduction

FNN Feed forward neural network

JICF Jet in cross flow

JICF Jet in crossflow

LAN Local area network

LBL Laminar boundary layer

LDA Laser doppler anemometry

LE Leading edge

LHS Latin hypercube sampling

LSMs Large-scale motions

QSV Quasi streamwise vortices

SGS Sub-grid scale

TBL Turbulent boundary layer

TCP Transmission control protocol

TS Tollmien Sclhichting

TTL Transistor-transistor logic

VITA Variable time average method

VLSMs Very large-scale motions

ZNMF Zero-net-mass-flux

Chapter 1

Coherent Structures and Control Techniques in Wall-Bounded Turbulence

The control of wall-bounded turbulent flows represents a field of significant economic and engineering interest, as the ability to reduce skin-friction drag directly translates to substantial reductions in the operational costs of commercial aircraft and marine vehicles [24, 25].
Research in this area has established that near-wall streamwise vortices, correlated with turbulent structures such as sweeps and ejections, and their interactions with the wall are the primary mechanisms responsible for high skin-friction drag [2, 24]. These vortices are part of a larger class of structures defined as coherent motions, which can be considered three-dimensional portions of flow where flow variables (velocity component, density, temperature) show significant correlation over scales larger than the smallest local flow scales [1]. Because these coherent structures are essential contributors to the maintenance, production, and dissipation of turbulence, they have become the primary targets for flow manipulation [26].

The development of effective drag reduction strategies relies on a deep understanding of the near-wall turbulence-production cycle, specifically the "bursting" process characterized by the ejection of low-momentum fluid away from the surface and the sweep of high-momentum fluid toward the wall [1, 27]. Control methodologies are generally categorized into passive and active techniques. While passive

methods, such as riblets or superhydrophobic surfaces, require no external energy, active feedback control utilizes sensors and actuators to disrupt the self-sustaining turbulence cycle in real-time [4]. In recent years, the field has evolved from idealized linear control schemes toward advanced data-driven methodologies, including neural networks and deep learning, to handle the inherent non-linearity and multi-scale nature of turbulent flows [28, 29].

This first chapter will start with a comprehensive overview of the kinematics and dynamics of coherent structures within the turbulent boundary layer on flat-plate in absence of streamwise pressure gradient and for low-Reynolds numbers, following Robinson's review [1]. Subsequently, it will present the various control strategies explored in the literature, ranging from traditional passive modifications to modern active control implementations powered by machine learning.

1.1 Wall-Bounded Turbulence and Coherent Structures

In the turbulent boundary layer, kinetic energy is subtracted from the free-stream and used to generate turbulent fluctuations, then ultimately converted into internal energy by viscosity; this process makes turbulence self-sustaining unless stabilized by external factors [1].
Studying the turbulent boundary layer is crucial in order to comprehend and predict its dynamics and understand the way to manipulate it in engineering applications such as to reduce skin friction in aeronautic applications, maximize mixing in motors' combustion chambers and enhance convection in heat exchangers.

Robinson [1] writes *"the most controversial issues in the field of boundary layer structure can be grouped as follows:*

- *Near-wall streak formation*
- *The bursting process*
- *Mass and momentum transfer from the inner to the outer layers*
- *Mass and momentum transfer from the outer to the inner layers*

- *Reynolds-number effects and appropriate scaling variables for near-wall turbulence-production events*
- *The existence and role of hairpin/horshoe/ring vortices"*

In addition to researching the turbulent boundary layer, the study of outer-flow structures and the phenomenon of entrainment is of interest because of the interaction that inevitably takes place between outer-flow motions and the near-wall region flow. Observations of turbulent boundary layers depend heavily on the measurement methods used, leading to confusion in the characterization of turbulent flow structures. Following the taxonomy proposed by Kline and Robinson [30, 31], coherent motions can be synthesized into eight primary classes, as written by Robinson [1]: "

- *Low-speed streaks in the viscous sublayer*
- *Ejections of low-speed fluid outward from the wall, including lifting low-speed streaks*
- *Sweeps of high-speed fluid inward toward the wall, including inrushes from the outer region*
- *Vortical structures of various forms, Fig. 1.1*
- *Sloping near-wall shear layers, exhibiting local concentrations of spanwise vorticity and* $\frac{\partial u'}{\partial x}$
- *Near-wall "pockets," visible in the laboratory as regions swept clean of marked near-wall fluid*
- *Large (δ-scale) motions capped by three-dimensional bulges in the outer turbulent/potential interface*
- *Shear-layer "backs" of large-scale outer-region motions, consisting of sloping (δ-scale) discontinuities in the streamwise velocity*

"

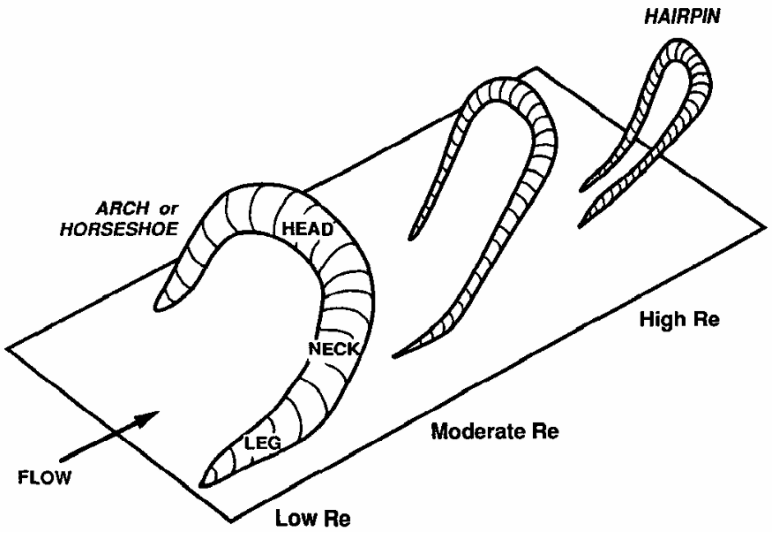


Fig. 1.1 Geometry and nomenclature for arch- and hairpin-shaped vortical structures. Image sourced from Robinson [1]

The physics of wall-bounded turbulent flows is fundamentally rooted in the presence of coherent motions. While no universal definition exists, coherent motions are generally understood as three-dimensional regions of the flow where at least one fundamental variable shows significant correlation with itself or another variable over scales larger than the local flow scales [1].

The following paragraphs will be on the description of the characteristics of the turbulent BL coherent motions and processes and the investigative methods to study them.

1.1.1 The Near-Wall Cycle and Bursting Process and Quasi-Streamwise Vortices

Defining u' and v' as the fluctuating components of velocity, respectively in the streamwise and wall-normal direction, and ρ as the fluid density, it is possible to associate turbulent coherent structures to a quadrant of the instantaneous $u'v'$ plane , represented in Fig. 1.2, according to the sign of their fluctuating components. With this approach, structures that fall into the first quadrant will be defined as **Q1 events** and so on.

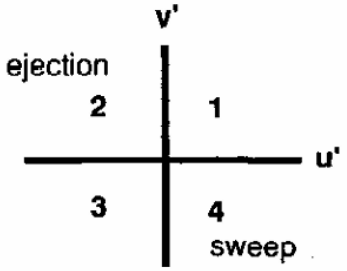


Fig. 1.2 Quadrants from the instantaneous $u'v'$ plane. Image sourced from Robinson [1]

The wall region, is located where

$$y^+ = \frac{y\, u_\tau}{\nu} \leq 100 \tag{1.1}$$

with y as the wall-normal physical distance, ν as the kinematic viscosity of the fluid ($\nu = \frac{\mu}{\rho}$), measured in $[m^2/s]$, u_τ as the friction velocity defined as:

$$u_\tau = \sqrt{\frac{\tau_w}{\rho}} \quad [m/s] \tag{1.2}$$

where τ_w is the wall shear stress and ρ is the fluid density.

The wall region, which contains the viscous sublayer, the buffer region, and part of the logarithmic region, is the primary site where turbulence production takes place. Within this region, the flow is organized into a self-sustaining cycle of low and high-speed streaks, which are elongated regions of fluid that take up approximately 100 viscous units in the spanwise direction.

The quasi-cyclic evolution of these streaks leads to the **bursting** process, which is responsible for the majority of turbulence production in the wall region [1, 27]. The term 'bursting' was originally introduced in the seminal visualization studies of Runstadler [32] and Kline et al. [33] to describe the intermittent process of turbulence production near the wall. In its physical sense, bursting refers to the multi-stage sequence of the lift-up, oscillation, and subsequent violent breakup of low-speed streaks, which results in the ejection of near-wall fluid into the outer regions of the boundary layer. However, as Robinson [1] highlights, the nomenclature has historically suffered from ambiguity.

Throughout the evolution of turbulence research, the term has shifted from a phenomenological description to a detection-based definition. In this second context, 'bursting' identifies specific events captured through conditional sampling techniques, such as the Variable Interval Time Average (VITA) or quadrant-splitting analysis of the Reynolds shear stress ($-u'v'$). Consequently, modern literature often distinguishes between the 'burst' as a physical instability and the 'burst' as a statistical signal corresponding to high-magnitude ejections (Q_2) and sweeps (Q_4).

A fundamental paradigm shift in the understanding of turbulence production occurred when experimental and numerical evidence suggested that the bursting phenomenon is not a localized temporal instability, often described as a sudden 'explosion' of fluid, but rather a process characterized by spatial intermittency and temporal persistence. As Robinson [1] explains, a stationary probe (such as a hot-wire anemometer) records a 'burst' as a sudden, violent velocity excursion. However, DNS data from different papers [34, 35] reveal that this signal is typically the footprint of a long-lived **quasi-streamwise vortex (QSV)**, moving past the measurement station. In this 'alternate scenario', the ejection of low-speed fluid is not an erratic eruption, but a sustained effect caused by vortex induction as the coherent structure is convected downstream [1].

In the conceptual framework proposed by Robinson [1, 35], the buffer region of the turbulent boundary layer is predominantly governed by quasi-streamwise vortices (QSVs). A QSV is defined as a coherent vortical structure aligned primarily along the streamwise axis, though it typically exhibits a characteristic upward tilt as it extends away from the wall.

A defining feature of Robinson's model is the departure from idealized symmetry. While earlier theories often assumed that near-wall vortices existed in perfectly symmetric, counter-rotating pairs, Robinson concluded from numerical simulation data that QSVs frequently occur as single, highly asymmetric entities.

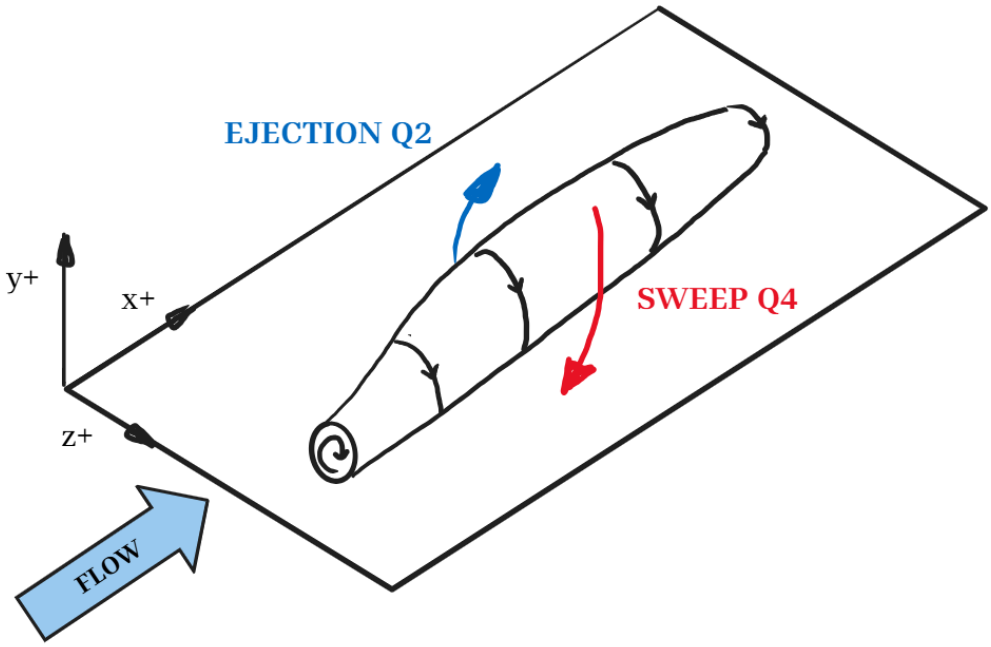


Fig. 1.3 Schematic of a QSV in the buffer region and the inducted bursting process. The rotation of the vortex lifts-up near-wall fluid creating ejections Q_2 (in blue) and blows fluid from the outer region towards the wall, generating sweeps Q_4 (in red). Redrawn and adapted from Robinson [1]

Seeing the bursting phenomenon as the consequence of the passage of a QSV, as explained by Robinson [35], provides the physical rationale for active control strategies, such as opposition control, which aim to negate the inductive effect of these persistent structures.

To summarize, in this QSV-centered framework represented in Fig. 1.3, the bursting process is characterized by:

- **Vortex induction:** The primary mechanism where the rotational motion of a tilted QSV physically displaces fluid. This creates a deterministic relationship between the vortex dynamics and the velocity fluctuations.
- **Ejections (Q_2 events):** they consist of low-speed fluid that is induced to move away from the wall ($u' < 0, v' > 0$). These events are the dominant producers of Reynolds shear stress beyond $y^+ \approx 12$.

- **Sweeps (Q_4 events):** high-speed fluid from the outer layers is rushed toward the wall ($u' > 0, v' < 0$). These dominate the Reynolds stress in the immediate vicinity of the wall ($y^+ < 12$).
- **Spatial intermittency ("*spotty*" [1] nature):** The bursting appears as localized "spots" in the $x-z$ plane because the inductive effects are confined to the narrow region surrounding the vortex core.
- **Temporal persistence:** Unlike a sudden explosion, the bursting process persists for the entire duration of the QSV's passage, reflecting the relatively long lifetime of these coherent structures compared to the duration of the detected "event" by a stationary probe.

The spatial relationship between sweeps and ejections in the buffer layer is fundamentally dictated by the geometry of quasi-streamwise vortices.
Although several structural models suggest a longitudinal arrangement,where a sweep follows an ejection in the streamwise direction, as noted by Moin [36], sweeps and ejections present a predominantly lateral, or "side-by-side", arrangement. The discrepancy between these instantaneous findings and traditional single-point conditional averages likely stems from the inherent limitations of two-dimensional sampling.
Specifically, since QSVs are often lopsided, the vortex-induced bursting process within the $x-z$ plane would be registered by a stationary probe at a definite x coordinate as a sequence where the sweep and the ejection happen separately in time, mistakenly implying a streamwise alignment for what is physically a three-dimensional, laterally-offset structure [1].

1.1.2 Mass Momentum Transfer by Vortical Structures and Skin Friction

In the study of turbulent boundary layers (TBL), vortices are regarded as the fundamental "engines" of momentum exchange. Their significance stems from their ability to persist as coherent entities even when subjected to the chaotic fluctuations of the surrounding flow. Furthermore, their low-pressure cores serve as a primary source for pressure disturbances, influencing the broader flow field. [1].

A defining challenge in this field is the lack of a universal, objective definition for a vortex in viscous, unsteady flows. Robinson et al. [37] proposed a kinematic criterion based on local streamlines:

"A vortex exists when instantaneous streamlines mapped onto a plane normal to the vortex core exhibit a roughly circular or spiral pattern, when viewed from a reference frame moving with the center of the vortex core."

While mathematically convenient, identifying such structures remains difficult. Experimental characterization relies heavily on flow visualization or point-wise vorticity measurements, whereas numerical simulations allow for more sophisticated methods, such as tracking the complex eigenvalues of the velocity gradient tensor or the vorticity lines, identifying regions of significantly reduced pressure representing the vortex-core in the streamwise direction.

The Divergence of Vortex and Vorticity

Being coherent structures, vortices need to persist in time and space, instead vorticity is a local, point-defined property and vorticity lines are curves parallel to the instantaneous-vorticity vector field that, contrary to vortical structures, have to comply with the **Helmholtz** laws of vorticity.

One of the most significant implications for wall-bounded turbulence arises from the second law, which dictates that a vorticity filament cannot terminate within the fluid and in absence of viscous effects it should move with the local fluid particles; unlike idealized vorticity filaments, physical vortices can terminate abruptly within the fluid and often propagate at convection velocities that differ from the local stream speed.
As a consequence of the second Helmholtz law of vorticity, vorticity lines identified near QSV or sreamwise vortices of the near-wall region of turbulent boundary layer must either form closed loops or attach to the solid boundary; this leads to a common misinterpretation when visualizing flow via vorticity lines.
In the vicinity of a quasi-streamwise vortex (QSV), the integration of vorticity lines often produces "upright" or "inverted" **hairpin** shapes depending on which side of the core the integration originates (Fig. 1.4).
It is essential to recognize that these hairpin patterns are frequently topological artifacts of the shear flow rather than evidence of a physical hairpin-shaped vortex

core.
This physical constraint provides a theoretical basis for the 'hairpin' or 'arch' shapes discussed by Robinson [1], where the 'legs' of the vortex are often observed to be inclined and closely associated with the wall.

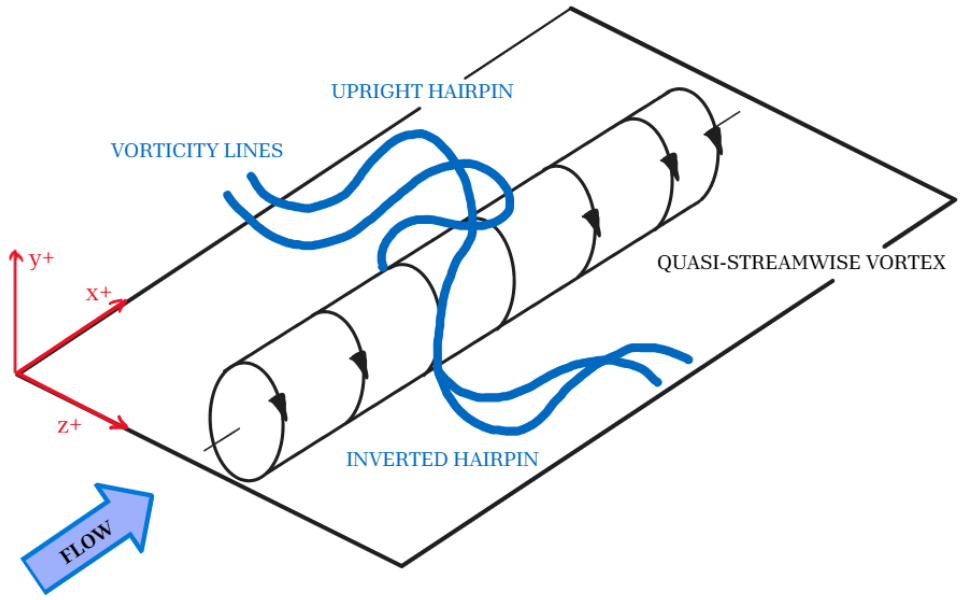


Fig. 1.4 Vorticity lines mapped around a quasi-streamwise vortex, highlighting the characteristic upright and inverted hairpin shapes found in boundary layer flows. Redrawn from Robinson [1]

Dynamic Role of QSVs

At the heart of the near-wall cycle are quasi-streamwise vortices (QSV), vortical structures that unfold predominantly in the streamwise direction that may sometimes be tilted upward from the wall [1].

These vortices are the primary agents of momentum transport; their blowing-suction action creates high-momentum sweeps and lifts low-momentum fluid into ejections. This mechanism is the primary contributor to skin-friction drag; indeed, regions of high shear on the wall are strongly correlated with the specific lateral and downstream positioning of these streamwise-oriented structures, specifically with the downstream streamwise vorticity above the wall. Research indicates that

the maximum correlation occurs when vortices are displaced laterally and located slightly downstream of the high-shear regions.

Because these vortex-induced sweeps and ejections are the dominant sources of Reynolds shear stress, the QSV is recognized as the central structure responsible for the production and maintenance of skin-friction drag [1]. Since QSVs are the main inhabitants of the buffer region, said region is considered to harbour most of turbulence production and dissipation.

1.1.3 Outer-Inner Layer Interactions, Horseshoe and Hairpin Vortices and Scaling

As the friction Reynolds number (Re_τ) increases, the outer layer becomes dominated by **Large-Scale Motions (LSMs)** and **Very-Large-Scale Motions (VLSMs)** [28, 38]. The outer region of the turbulent boundary layer is populated by VLSMs, structures with dimensions of the order of the boundary layer thickness δ.

Large-scale features govern the turbulent-non-turbulent interface, where the entrainment of irrotational free-stream fluid occurs through deeply penetrating 'valleys' of ambient flow while smaller, large-scale eddies LSMs are typically nested beneath them [1].

While the near-wall cycle is largely self-sustaining, these energetic outer structures exert a modulating influence that varies with the Reynolds number on the near-wall events, altering the wall-shear stress and conditioning the production cycle [1, 28].

Hairpin and Horseshoe Vortices

The BL is also home to three-dimensional, inclined vortices with a **hairpin** and **horseshoe** shape and **loop** or **ring** like vortices Fig. 1.1.
If horseshoe/arch vortices are as tall as they are wide, hairpin structures are more stretched with longer legs.

The concept of discrete, inclined vortical loops as the primary mechanism for turbulence variation was first proposed by Theodorsen [7].
Summarized in Fig. 1.5, Theodorsen's classical conceptual model of near-wall

turbulence, suggested the formation of hairpin-like vortical structures that form accross a region of low-speed fluid close to the wall and undergo a growth process, extending into the outer flow as they are convects downstream.

Thedorsen [7] proposed that these structures consist of two elongated legs anchored close to the surface and a head inclined at roughly 45° to the wall, with its spanwise extent increasing proportionally to the distance from the wall [1].

In Fig. 1.5 successive segments of the vortex line are labelled with symbols $q_1, q_2, q_3 \ldots$, which serve only as geometric markers identifying different portions of the same continuous vortical filament rather than physical variables. Through this idealized representation, Figure 1.5 emphasizes how the vortex lifts low-momentum fluid upward, stretches as it rises, and organizes the surrounding flow into a coherent pattern that encapsulates his interpretation of the instantaneous dynamics responsible for turbulence production in the near-wall region.

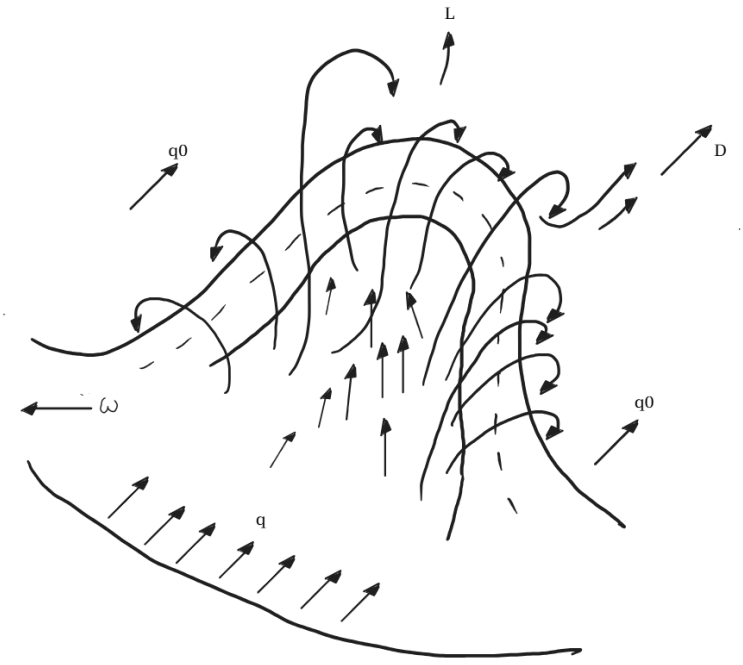


Fig. 1.5 Idealized hairpin-vortex model proposed by Theodorsen [7], showing a vortical structure rising from a low-speed region with legs near the wall and an inclined head; the labels along the vortex line mark geometric segments of the same structure. Redrawn from Theodorsen [7]

Although Theodorsen lacked the high-resolution experimental data we have today, his physical intuition regarding the 45° inclination of these structures has been largely validated by modern DNS and smoke flow visualizations.

Following the initial proposal of discrete vortical loops [7], several decades of research focused on refining the geometry and the regenerative nature of these structures, the conclusions where summarized in Robinson [1].

Rather than isolated events, the consensus evolved toward a model where vorticity lines naturally inclined from the wall, form hairpin-like configurations that serve as a bridge between the near-wall region and the outer flow [39, 40].

The conceptual framework shifted from seeing vortices as static shapes to understanding them as evolving "packets" of structures [41]. In this view, a single horseshoe vortex represents only a moment in a larger process; as these structures convect downstream, they can persist far longer than the lifetime of any individual element. This longevity is attributed to a self-sustaining mechanism where disturbances near the wall continually trigger the birth of new vortical elements, which then follow the preceding ones in a coherent sequence.

A major conceptual breakthrough involved the relationship between the vortex geometry and the "bursting" phenomenon [42]. It was proposed that as a horseshoe-shaped loop is stretched and lifted away from the surface, its trailing "legs" [42] induce a local upward movement of fluid. This action creates a locally unstable shear layer that eventually breaks down, leading to the ejection of low-speed fluid. Simultaneously, the higher "tip" or head of the vortex facilitates the downward transport of high-speed fluid from the outer region toward the wall.
This dual action establishes a feedback loop where the vortex both responds to and creates the instabilities necessary for turbulence production.

A landmark study by Head and Bandyopadhyay on smoke turbulent flow visualizations [43] confirmed Theodorsen's model [7], adding insight about the dependence of three-dimensional coherent structures with the Reynolds number. They observed that while these structures are fewer and appear as squat "horseshoes" or "arches" at lower velocities, they grow in quantity and propagate together and they stretch into elongated, slender hairpins at higher Reynolds numbers, maintaining a characteristic inclination of approximately 45° relative to the wall.

Outer-Inner Layer Interactions

Later visualizations in various wall-bounded flows extended this analysis to include the interaction between the inner and outer regions of the boundary layer [44]. These models suggest that spanwise-oriented vortices in the outer region are not independent entities but are deeply coupled with near-wall turbulence. These larger structures facilitate the entrainment of free-stream fluid on their upstream side while promoting ejections of near-wall fluid on their downstream side. This transition from a two-dimensional view to a fully three-dimensional understanding solidified the idea that the boundary layer is populated by an interconnected web of vortical loops of varying scales.

This evolutionary process from simple 2D elements to complex 3D structures is visually summarized in Fig. 1.6.
The mechanism begins with a localized instability that perturbs a two-dimensional spanwise vortex filament, causing a segment of it to lift away from the wall. As this lifted segment is exposed to the higher-velocity fluid of the mean shear profile, it is convected downstream faster than the sections remaining near the wall. This differential advection stretches and tilts the vortex filament, progressively generating counter-rotating, quasi-streamwise "legs" (Ω_x) alongside the transverse "head" (Ω_z). In its fully developed stage, this three-dimensional hairpin configuration acts as the primary engine for turbulent momentum exchange, inducing the ejection of low-momentum fluid (Q_2) between its legs and drawing down high-momentum sweeps (Q_4) along its outer flanks.

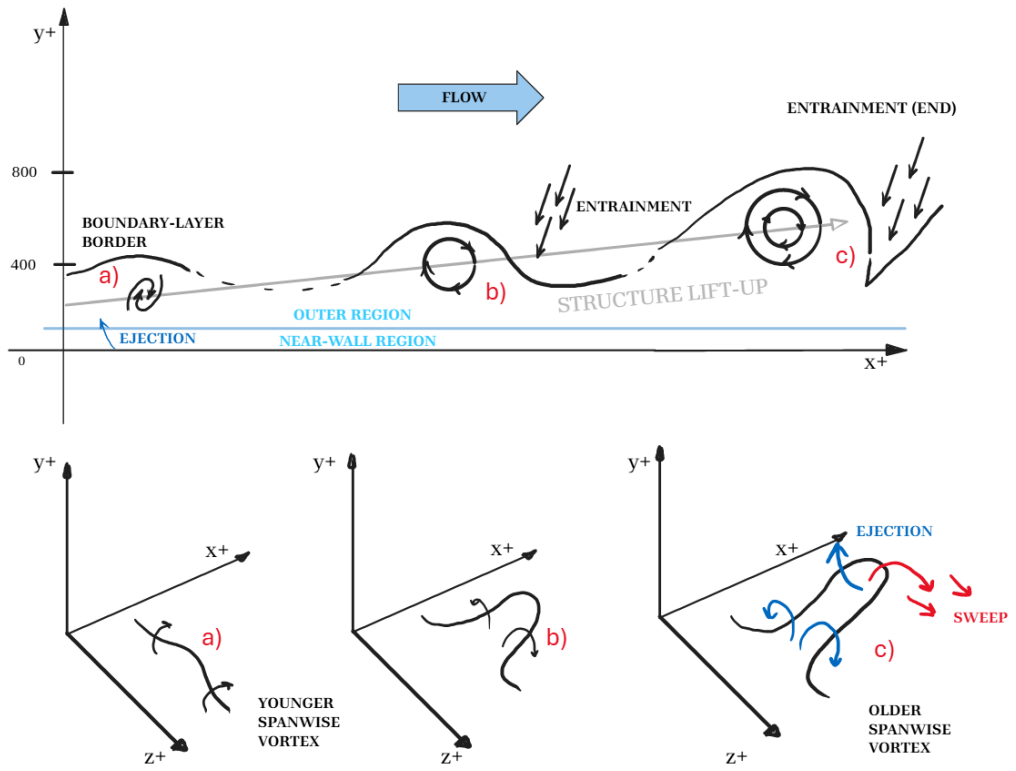


Fig. 1.6 Conceptual schematic of the formation of a hairpin vortex and the associated momentum transport events. From left to right: a localized lift-up of a spanwise vortex filament; the subsequent stretching and tilting driven by the mean shear flow; and the fully developed 3D hairpin structure. The mature vortex induces a characteristic pumping action, generating Q_2 ejections in the central "head" region and Q_4 sweeps on the outer sides, "legs" and "head".

Robinson [1, 35] defined a comprehensive model where the different regions of the BL are populated by distinct, coherent structures.

As said before, in this view the buffer region is the domain of quasi-streamwise vortices. Robinson's [35] synthesis challenged earlier assumptions of symmetry, demonstrating that buffer-layer QSVs predominantly exist as isolated, asymmetric elements rather than the balanced, counter-rotating pairs hypothesized in traditional models.

The outer wake region is characterized by skewed horseshoe structures in low *Re* or hairpin vortices in high *Re* regimes.

The logarithmic and overlap regions serve as zones of intense interaction where these disparate elements merge into complex, multi-scale entities.

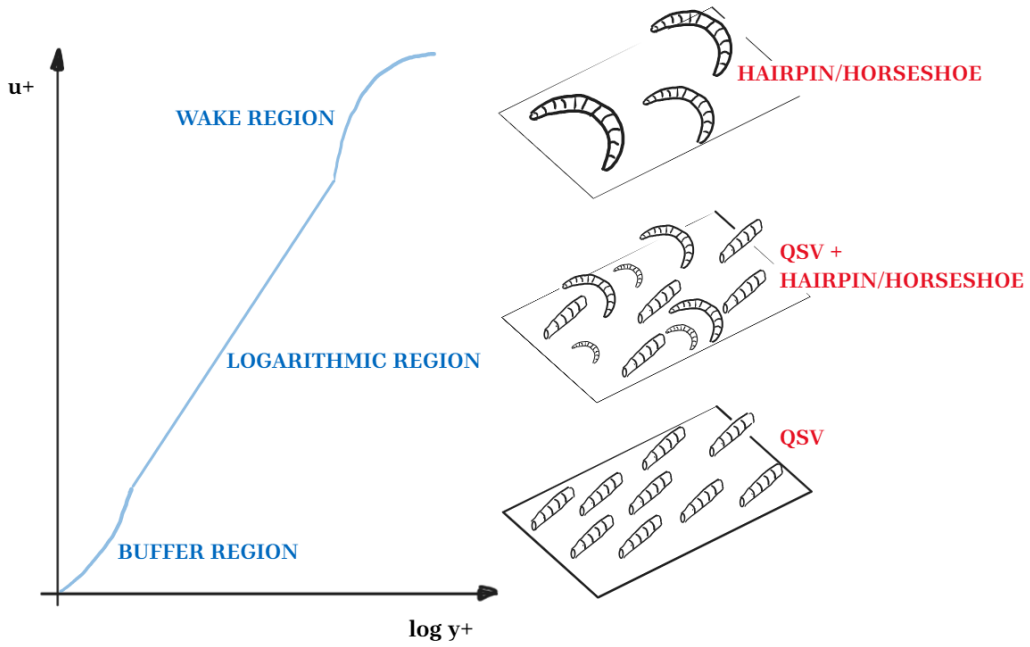


Fig. 1.7 Conceptual decomposition of a symmetric hairpin vortex into its constituent elements. The structure consists of a transverse head and two counter-rotating quasi-streamwise legs. The diagram illustrates how an isolated quasi-streamwise vortex (QSV) can be interpreted as a partial segment of this more complex, idealized configuration. Redrawn and adapted from Robinson [1].

As illustrated in Fig. 1.7, the quasi-streamwise vortex can be viewed as a fundamental constituent of the more complex hairpin structure. While the full hairpin is a common conceptual model, the single QSV is often the most persistent and detectable feature in the near-wall region, directly responsible for the high-shear events targeted by active control strategies.

1.1.4 Investigative Methodologies

Experimental Investigative Methodologies

- **Flow visualization**: historically, flow visualization has served as a cornerstone for the discovery and conceptualization of coherent motions, particularly in facilities operating at low Reynolds numbers, where the increased spatial and temporal scales of the structures facilitate observation.

Techniques utilizing tracers (such as dye, smoke, or hydrogen bubbles) have proven instrumental in elucidating the complex topology of turbulent events. However, as Robinson [1] highlights, visualization remains primarily a qualitative tool. While modern image-processing and particle-tracking methods have introduced a quantitative dimension to these studies, they generally lack the precision of point-probes. Furthermore, these methods are often constrained by their two-dimensional nature; capturing a planar slice of a flow may lead to 'projection' issues, potentially obscuring the inherently three-dimensional and time-evolving character of the turbulent structures.

- **Probes**: the experimental characterization of coherent structures imposes stringent requirements on measurement techniques, primarily necessitating high temporal resolution to resolve the full spectrum of velocity fluctuations. Such high-frequency sampling is essential for the application of advanced conditional signal processing techniques required to extract organized motions from the background turbulence. Consequently, **multi-sensor hot-wire** or **hot-film arrays** are often preferred over other sophisticated single-point techniques, such as **Laser-Doppler Anemometry (LDA)**, when investigating the spatial evolution of the flow. The use of arrays with sensors separated in space allows for the simultaneous sampling of the turbulent field, enabling the identification of correlations across a wide range of spatial scales.
  A critical challenge in the experimental investigation of near-wall coherent structures is the spatial resolution of the sensors. The active part of the probe element is subject to limits, as it must be sufficiently small to resolve compact turbulent motions without significant spatial averaging.
  According to the criteria suggested by Blackwelder and Haritonidis [45], the hot-wire length should not exceed 20 viscous units ($l^+ < 20$) to accurately capture near-wall dynamics. However, this constraint must be balanced with the operational requirement of maintaining a length-to-diameter ratio (l/d) greater than 150 to minimize end-conduction effects. These combined physical limitations have historically restricted high-resolution turbulence studies to low Reynolds numbers ($Re_\theta < 5000$) and subsonic regimes.
  Consequently, as Robinson concludes [1], experimental data for high-Reynolds-number or supersonic flows are predominantly limited to large-scale structures, as the extreme miniaturization required to resolve the inner-layer scales under such conditions remains technologically challenging.

1.1.5 Coherent Motion Identification and Characterization Techniques

Coherent motions can be eventually identified by analysing probe signals statistically and interpreting the results physically. Robinson points out the following methods as the most effective in describing the nature of the streamwise near-wall structures that can be appointed as responsible of the production of Reynolds stress [1].

- **Conditional sampling**: these techniques are designed to extract the "average" footprint of a coherent event by triggering the measurement only when specific physical criteria are met.
  - **VITA (Variable interval time average)**: introduced by Blackwelder and Kaplan [27], this method detects events characterized by high local variance in the streamwise velocity signal. By computing the variance over a short, moving time window, VITA identifies the sharp velocity gradients associated with the passage of internal shear layers and "bursts". However, the results are sensitive to the choice of the averaging time T and the threshold level.
  - **Gradient technique**: this method identifies coherent structures by detecting steep gradients in the velocity signal, typically the streamwise component ($\partial u/\partial t$). It is particularly effective for real-time applications, such as active flow control, because it can be implemented through simple analog circuits or high-speed digital processing. In the context of sweep detection, a trigger is generated whenever the local temporal gradient exceeds a predefined threshold. This technique is often considered a simplified, high-speed alternative to VITA, as it focuses on the leading edge of high-speed structures (sweeps) or the trailing edge of low-speed ones (ejections)[6].
  - **Quadrant analysis ($u'v'$ method)**: proposed by Lu and Willmarth [40], this technique classifies turbulent fluctuations based on their sign in the $u'v'$ plane. A threshold (or "hole") size H is often applied to filter out small-scale background noise, focusing only on high-magnitude events where $|u'v'| > H\overline{u'v'}$. This is the standard tool for quantifying the relative contributions of ejections (Q_2) and sweeps (Q_4) to the total Reynolds shear stress.

  - ***u*-level method**: a simpler threshold-based detection where an event is recorded when the streamwise fluctuation u' exceeds or falls below a certain multiple of the local RMS value. While less sophisticated than VITA, it is effective in identifying the presence of high- or low-speed streaks.

- **Two-point Correlation Tensors and POD**:

  - **Two-point correlations**: by measuring the correlation between velocity fluctuations at two spatially separated points, $R_{ij}(\mathbf{x},\mathbf{r}) = \langle u_i(\mathbf{x})u_j(\mathbf{x}+\mathbf{r})\rangle$, researchers can infer the average spatial extent, inclination, and convection velocity of coherent structures. This method provides a statistical measure of the "average" structure size (e.g., the length of a streak or the diameter of a vortex).
  - **Proper orthogonal decomposition (POD)**: first applied to turbulence by Lumley [46], POD is a mathematical procedure that decomposes the flow field into a set of orthogonal modes. These modes are ranked by their energy content, allowing the most energetic (and thus dynamically significant) coherent structures to be extracted from the chaotic background flow. It is particularly powerful for identifying the "Template" of VLSMs and LSMs in high-Reynolds number flows.

1.1.6 Numerical Simulations

To study wall-bounded turbulent flows two main methods were employed, **large-eddy simulation (LES)** and **direct numerical simulation (DNS)**.

Large Eddy Simulation: LES

Large eddy simulation is based on the modeling of the small turbulent scales and the direct computation of the other scales of the flow through the use of three-dimensional, non-stationary Navier-Stokes equations averaged over the small scales [1].

The rationale behind modeling the the small-scales in LES is theoretically justified by Kolmogorov's similarity hypotheses [47], which suggests that small-scale

structure of turbulence possesses universal character.
Kolmogorov postulated that at sufficiently high Reynolds numbers, the small-scale turbulent motions are statistically isotropic and universal, having lost the 'memory' of the large-scale, geometry-dependent motions that produced them.
This is due to the sequential transfer of kinetic energy through the inertial range; as energy cascades from the large, geometry-dependent eddies down to smaller scales, the directional information of the macro-structures is lost.
In the inertial sub-range, the turbulence becomes statistically independent of the large-scale forcing, here viscous effects are negligible until the Kolmogorov micro-scale (η) is reached. Consequently, while the non-universal large eddies (resolved in LES) are sensitive to boundary conditions and flow geometry, the small eddies (modeled in LES) exhibit a more uniform behaviour that can be effectively captured by generalized sub-grid closures, such as the Smagorinsky model.

Direct Numerical Simulation

DNS represents the most rigorous computational approach, as it solves the Navier-Stokes equations from first principles without the use of any turbulence models. By resolving the full range of spatial and temporal scales, from the large, energy-containing eddies down to the smallest dissipative Kolmogorov microscales (η), DNS provides a high-fidelity numerical method for the quantitative investigation of coherent motions.
As opposed to LES, which relies on sub-grid scale (SGS) closures, DNS captures even the finest near-wall features and the delicate interactions within the viscous sub-layer. However, this uncompromising resolution comes at a massive computational cost; the number of required grid points scales approximately as $Re^{9/4}$ [48], while the total computational effort, including time-stepping, scales as Re^3.
As a result, DNS remains restricted to relatively low-to-moderate Reynolds numbers and computationally intensive for complex aerospace geometries [1].

Direct numerical simulations provide the knowledge of all flow variables, at many spatial coordinates, they allow to study their variation with the change in boundary conditions. DNS proves to be the most powerful approach to study and postulate turbulent flow control techniques [3].

1.2 Control Strategies for Turbulent Drag Reduction

Flow control techniques have several functions, they can be used to enhance turbulence effects, for example to increase the transport of heat in a heat exchanger [49],to mitigate them, for instance to reduce aerodynamic drag and to control laminar-turbulent BL transition. This section will focus on the two latter purposes.

The mitigation of skin-friction drag in wall-bounded turbulent flows is a primary objective in aerodynamic research, as it directly impacts fuel consumption and carbon emissions.

Given that near-wall turbulence is sustained by the self-regenerating cycle of coherent structures, specifically the quasi-streamwise vortices (QSVs) and their induced bursting process described in previous sections, drag reduction can be achieved by disrupting this cycle and altering those organized structures through control strategies.

Control strategies are categorized into passive and active methods:

- **Passive control:**Passive control techniques alter targeted coherent structures without sensing them. Because they require no energy input or feedback loops [3], the control action cannot be dynamically tailored to the instantaneous state of the flow. The most implemented passive control techniques are:

    1. **Large eddy breakup devices LEBUs**: placed in the boundary layer in an attempt to suppress the formation or interaction of organized flow structures.
    2. **Vortex generators**: Aircraft wings are equipped with vortex generators, shown in Fig. 1.8 . Skin friction and adverse pressure gradient on the wing reduce BL energy, causing its separation. Vortex generators become useful because they generate vortices at their tips, that energise the BL flow by mixing it with higher energy free-stream flow. These devices induce laminar-turbulent flow transition as well delaying the flow separation and lowering stall speed, in this way the aircraft is able to fly at high angles of attack at low speeds without stalling [8].

       In transonic and supersonic regimes shock waves form where the wing profile undergoes abrupt changes in curvature, for example at the leading edge, at control surface joints. Shock waves cause flow separation, mak-

ing control surfaces downstream of them ineffective, as a consequence, this highly dangerous effect renders the aircraft uncontrollable. Vortex generators help avoiding flow separation, maintaining control surfaces effectiveness, and sometimes can break up the shock wave itself. Fig. 1.9 summarizes the use of vortex generators to avoid flow separation.



Fig. 1.8 Vortex generators on a Boeing 737 wing, positioned on its upper surface at the leading edge. Image sourced from Udris [8]

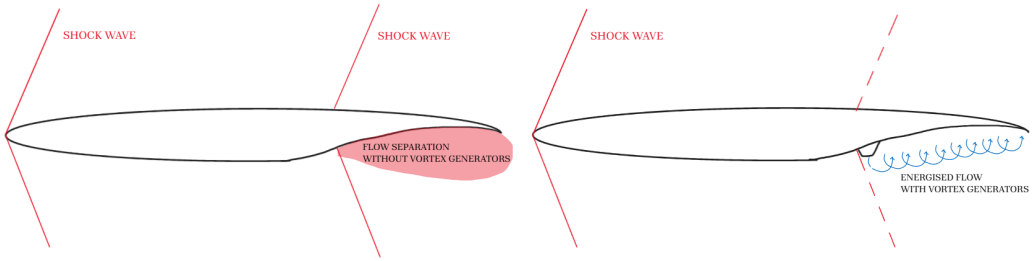


Fig. 1.9 **Left:** Example of $M > 1$ flow over an airfoil without vortex generators, the flow separates and the control surface at the leading edge becomes ineffective, the red lines identify shock waves. **Right:** Example of $M > 1$ flow over an airfoil with vortex generators before the control surface, flow doesn't separate because the vortices induced by the vortex generator energise it by mixing free-stream flow with BL flow. Red lines represent shock waves and dashed lines represent the disrupted shock wave. Image redrawn and adapted from Udris [8]

3. **Two-dimensional boundary layer trips**: wires, steps, gaps ect.. influence the transition enhancing Tollmien-Schlichting waves between the separation and the recovery locations after the element.
   TS waves increase in amplitude and the transition position moves up-

stream, closer to the boundary layer trip. They are usually implemented in wind-tunnels to create controlled and fully developed turbulent flows.

4. **Three-dimensional roughness elements**: isolated or distributed roughness elements (**DREs**), such as **riblets** are used both to reduce drag, by influencing and disrupting turbulent BL coherent structures.
   These devices are also implemented to control the flow transition when turbulent regime is preferred to have a more energized flow.
   A common example of DREs used to develop a turbulent flow over a body is golf balls, the dimples on their surfaces act as tripping devices inducing flow transition, the separation point will move further streamwise and the ball will consequently have a smaller wake implying lower air drag. This design allows the ball to travel further and remain airborne longer by minimizing aerodynamic wake, Fig. 1.10. Three-dimensional distributed roughness elements have higher tripping efficiency than isolated roughness elements and additionally they avoid flow anisotropy of the downstream turbulent flow. In fact, distributed roughness elements are used more as boundary layer trip devices for wind-turbines blades, inlets, airfoils and even sport cars.
5. **Superhydrophobic surfaces SHS**: Superhydrophobic surfaces (SHS) utilize surface topography to sustain a gaseous film, facilitating a state that prevents liquid penetration into the surface micro/nano-ridges.
   This entrapped air layer effectively modifies the fluid-solid interface from a no-slip to a slip boundary condition, where the presence of a non-zero velocity at the wall significantly reduces skin friction drag. The efficacy of this reduction is typically quantified by the slip length b [15].

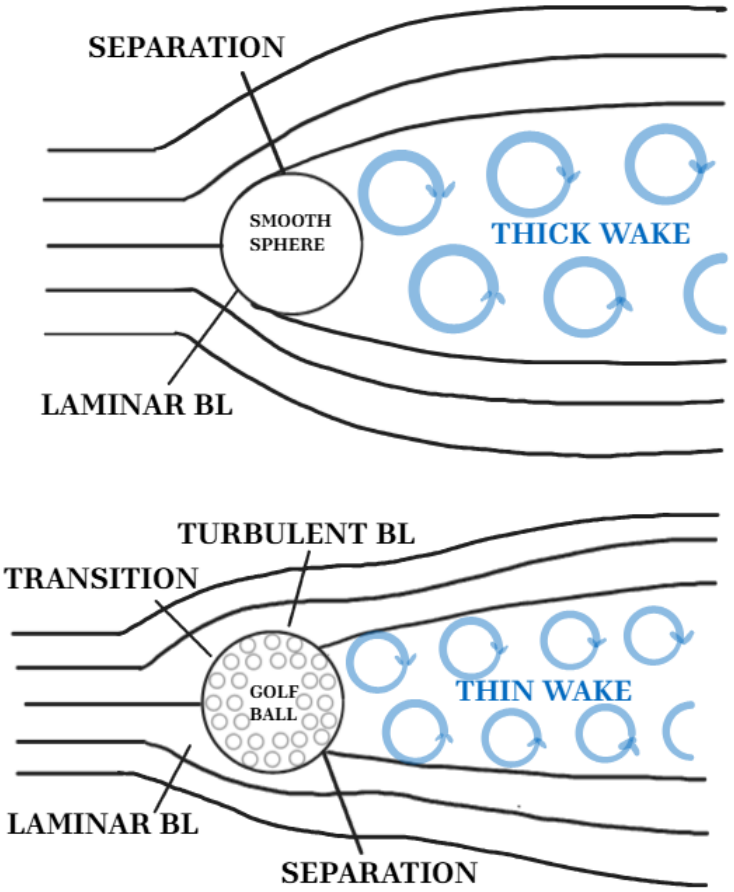


Fig. 1.10 Flow over a smooth sphere compared to flow over a golf ball, characterized by distributed roughness elements.

- **Active control:** techniques that manipulate the targeted coherent structures through the injection of external energy into the system. These methods utilize an actuation mechanism and are further divided based on their logic: *open-loop* strategies apply a predetermined control action regardless of the flow state, whereas *closed-loop (reactive)* strategies utilize sensors and feedback loops to tailor the actuation to the instantaneous dynamics of the flow [49, 3].
  The primary active control techniques used to manipulate boundary layers are:

1. **Mass transfer techniques**: adding or removing fluid at the wall to alter the velocity profile and momentum exchange.
   These techniques can be divided in three categories:

   Steady suction: when low-momentum fluid from near the wall is removed to delay BL separation even under adverse pressure gradients, obtaining a thinner BL, higher skin friction as there is a lower Reynolds number at the wall and stabilizing laminar flow. DNS simulations of uniform TBL suction conducted by Kametani and Fukagata [50] and following experimental proof show that turbulent fluctuations are suppressed and lift enhancement is achieved through this control method.

   Steady blowing: high-momentum fluid is injected into the boundary layer from near wall through pores or slots. DNS [50] and LES simulations conducted on steady blowing active control demonstrated that this technique leads to significant skin friction reduction, with an overall turbulence increase and turbulence lift-up from the wall. Uniform blowing is frequently used to enhance mixing, reduce skin friction or provide film cooling, for example on turbines blades and slotted wings, as represented in Fig. 1.11. Kametani and Fugata [50] present a practical issue that concerns how air mass can be acquired to maintain steady blowing in engineering applications; while on aeroplane wings air could be suctioned at the LE and then conveyed to the blowing control point, on means of transportation like high-speed trains it seems to be less straightforward.
   Synthetic jets (zero-net mass-flux): obtained with actuators that use a diaphragm to alternately blow and suck fluid through an orifice, synthetic jets can be used to selectively nullify the wall-normal high-velocity fluid that travels towards the wall during sweep events. This technique was implemented by Rebbeck and Choi [6], in their experimental study and in the experimental set-up that will be discussed in this thesis. Synthetic jets require no external fluid supply and are excellent for flow control, skin friction reduction as well as enhancing mixing away from the wall.

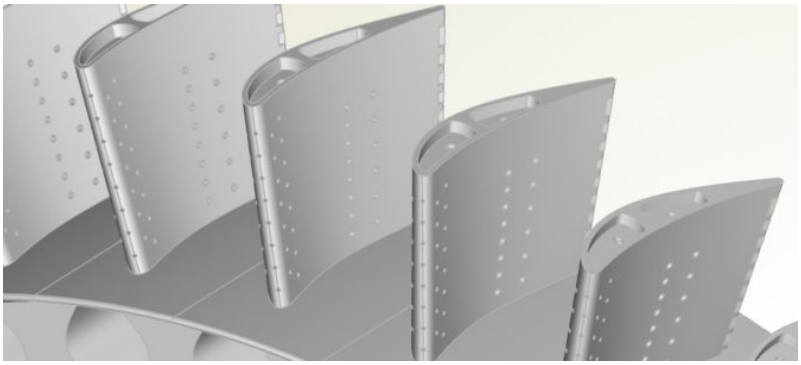


Fig. 1.11 Application of the steady blowing technique via film cooling on a turbine blade (CAD rendering). The surface holes allow the injection of high-momentum pre-combustion fluid into the boundary layer. In addition to thermal protection, this active control strategy alters the interaction of near-wall coherent structures, leading to a modification of viscous shear stresses. Image sourced from the website CAESES [9]

2. **Wall motion and mechanical actuation**: systems that interact physically with the boundary layer through moving pistons/bumps at the wall to disrupt the formation of turbulent structures, such as QSVs. This control method can involve, **spanwise wall oscillations** generated by active surfaces that move perpendicular to the flow, reducing skin friction by breaking up streaks in turbulent BL. Wall motion can be also used to create **travelling waves**, that can reduce drag or pump fluid depending on the wave speed and direction. **Micro-electro-mechanical systems (MEMS)** flaps or "micro-tabs" can be also employed to deploy into the flow to trigger transition or control large-scale vortices.

   Rebbeck and Choi [5] carried out an experimental study of opposition control using a solenoid-driven piston actuator, on near-wall turbulence aiming to disrupt sweeps; the piston was actuated steadily with a frequency of 1 Hz, with a cycle composed of a rising phase that generated a circular jet, a phase during which the piston rested at the risen position and then a withrawal phase. They [5] evaluated the effectiveness of the control by monitoring the reduction or increase of the burst intensity. The burst signature, represented on the $u^+(\tau^+)$ time history in Fig. 1.12, was obtained both for the controlled and uncontrolled case with ensemble averaging of the hot-wire signal, downstream of the control point. Rebbeck and Choi[5] approach in their work represents the starting point of the experimental studies carried out for this master thesis; they concluded

that, by actuating the control system at the correct time it is possible to disrupt the high-speed fluid that travels towards the wall during sweep events.

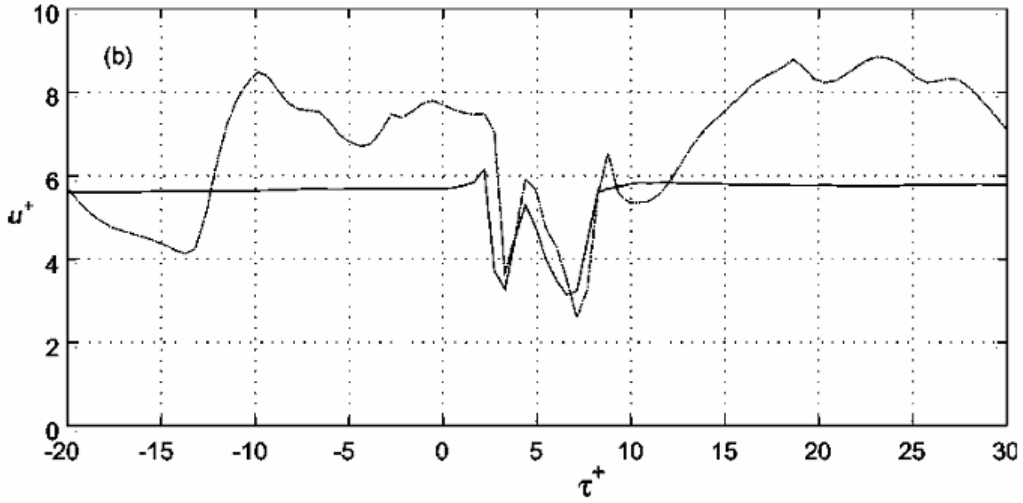


Fig. 1.12 Time evolution of a single detection (dot-dash line) and of the ensemble averaged (solid line) u^+ velocity profile during the interaction between the TBL flow and the jet created by the piston. As Rebbeck and Choi highlight [5] the horizontal speed-component presents a *"w-shape"*. Image sourced from Rebbeck and Choi [5]

3. **Plasma and electromagnetic control**: systems that manipulate the flow through force fields and induce three-dimensional flows away from the wall, completely bypassing the need for mechanical components. Examples include plasma synthetic jet actuators, plasma spark jet actuators, three-dimensional plasma actuators, and plasma vortex generators [51].
   Plasma actuators DBDs (dielectric barrier discharge actuators) stand out in aerodynamic applications because of their fully electrical nature, minimal weight, thin profile, and rapid actuation times. Structurally, a DBD consists of two electrodes separated by a thin dielectric surface: one enclosed within the body and the other exposed to the airflow. The exposed electrode ionizes the surrounding air upon application of a specific alternating current potential difference (order of kV) at a very high frequency (order of kHz) [10].

   The ionization can occur on one or both sides of the electrode, generating plasma layer that imparts an electrohydrodynamic force on the fluid that

mitigates BL separation, energieses and suppresses separated flows and promotes flow mixing. Flow is accelerated and moved away from the electrode through ion collisions [51]. According to Wang et al. [51], DBDs represent extremely promising solutions for removing moving parts on airplanes because of their ability to accelerate flow in the desired direction. DBDs they can be used to generate jets from surfaces on demand; these actuators could replace moving control surfaces for pitch and roll variation, flaps and slats for lift enhancement, and even physical vortex generators.

In fact, experimental investigations employing smoke visualizations and PIV studies of the flow field generated by a DBD, carried out by Whalley and Choi [10], showcased the birth of a starting vortex moving away from the wall in the plasma jet direction, fueled by the entrainment of fluid located above the air-exposed electrode at the moment of actuation. The resulting flow topology, generated by a one-sided plasma actuator, is schematized in Fig. 1.13.

On the other hand, **Electromagnetic flow control (EFC)** targets conductive media, such as seawater, leveraging Lorentz forces produced by electrode-magnet arrays to alter the flow field, dampen turbulent fluctuations, or reduce drag. Specifically, Wang et al. [51] report that Lorentz forcing is capable of generating spanwise travelling waves, which significantly reconfigure near-wall dynamics. This electromagnetic intervention merges low-speed streaks into extended ribbons of low-momentum fluid near the wall boundary. Moreover, the resulting streamwise vortices trigger alternating ejection (Q_2) and sweep (Q_4) events, effectively breaking the turbulence regeneration cycle and achieving substantial reductions in wall friction.

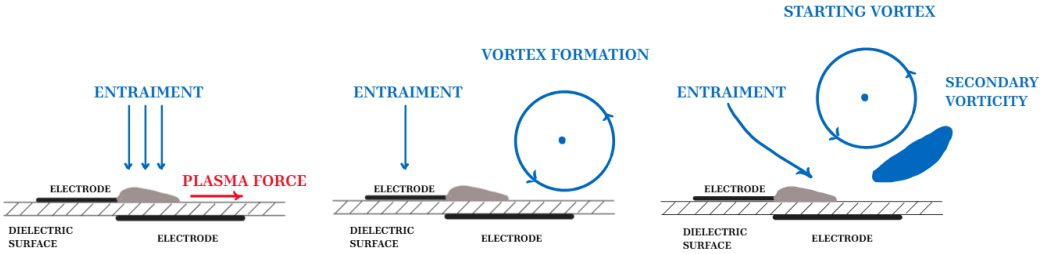


Fig. 1.13 Flow field generated by the actuation of a DBD. Upon actuation, flow is accelerated away from the electrode by ion collisions, causing entrainment of the surrounding flow above the electrode. After the jet creation, a starting vortex is born, which moves away from the wall enhancing entrainment and generating secondary vorticity along the wall. Image redrawn and adapted from Whalley and Choi [10]

4. **Thermal and acoustic actuation**: These techniques manipulate the near-wall flow properties and introduce targeted disturbances to alter the boundary layer dynamics.

   Thermal control relies on localized heating or cooling to modulate the fluid's dynamic viscosity (μ). In liquid environments, heating the wall effectively lowers the local viscosity, which alters the near-wall velocity gradient and yields a reduction in skin-friction drag. Conversely, in gaseous flows, cooling the surface stabilizes the laminar boundary layer by dampening the amplification of Tollmien-Schlichting (T-S) waves, thus delaying the transition to turbulence.

   Acoustic excitation, on the other hand, employs devices such as loudspeakers or piezoelectric transducers to inject specific frequency perturbations into the flow field. This mechanism is primarily utilized to manage flow separation or actively control laminar-to-turbulent transition by promoting early shear-layer roll-up. Flow separation usually causes lift loss, drag increase, stall of moving surfaces and so on... Since turbulent boundary layers have a delayed separation compared to laminar boundary layers, many ways to induce flow transition were studied, finding that periodic perturbations of a laminar boundary layer generated by acoustic actuators are effective in exciting prematurely TS waves [52]. Crucially, acoustic drivers constitute a fundamental actuation mechanism for generating highly responsive zero-net-mass-flux (synthetic) jets in active flow control applications. For instance, in the experimental framework developed by Rebbeck and Choi [6], a loudspeaker was employed

as the primary control actuator. Building upon this methodology, the present thesis adopts an analogous acoustic actuation strategy, utilizing a speaker-driven synthetic jet to actively intercept and mitigate near-wall sweep events. Due to their high-frequency bandwidth and rapid dynamic response, speaker-driven actuators can instantly alternate blowing and suction phases. This makes them exceptionally well-suited for real-time, closed-loop control schemes aimed at intercepting fast-moving coherent structures, such as high-momentum turbulent sweeps [53].

While active control proves to be more effective than passive control solutions, its implementation on an aerodynamic vehicle or body causes the increment of its weight, fuel consumpton, reducing the range and the performance [54] if the drag mitigation effect is not enough to compensate for it. Table 1.1 summarizes flow control techniques analysed.

Table 1.1 Summary of flow control techniques, their primary goals, and typical applications.

Technique	**Primary Goal**	**Typical Applications**
Passive Control		
LEBUs	Suppress the formation or interaction of organized flow structures.	Boundary layer modification
Vortex Generators	Energize the BL via mixing; delay separation, lower stall speed, and disrupt shock waves in high-speed regimes.	Aircraft wings, transonic/supersonic leading edges, control surface joints
2D Boundary Layer Trips	Influence transition by enhancing Tollmien-Schlichting (TS) waves; move transition upstream.	Wind-tunnel testing

Continued on next page...

Table 1.1 – Continued from previous page

Technique	Primary Goal	Typical Applications
3D Roughness Elements	Reduce drag by disrupting coherent structures or induce transition to energize the flow; avoid flow anisotropy.	Golf balls, wind-turbine blades, airfoils, sports cars
Superhydrophobic Surfaces (SHS)	Reduce skin friction drag by creating a slip boundary condition via an entrapped gaseous film.	Fluid-solid interfaces, marine applications
Active Control		
Mass Transfer (Steady Suction)	Remove low-momentum fluid to delay separation, stabilize laminar flow, and suppress turbulent fluctuations.	Lift enhancement, boundary layer stabilization
Mass Transfer (Steady Blowing)	Inject high-momentum fluid to reduce skin friction drag, enhance mixing, or provide thermal protection.	Turbine blade film cooling, slotted wings
Synthetic Jets	Actively nullify wall-normal high-velocity fluid (sweep events) and enhance mixing without external fluid supply.	Real-time flow control, skin friction reduction
Wall Motion / MEMS	Disrupt turbulent streaks/QSVs via spanwise oscillations or travelling waves; trigger transition using micro-tabs.	Turbulent boundary layers, drag reduction

Continued on next page...

Table 1.1 – Continued from previous page

Technique	Primary Goal	Typical Applications
Plasma / Electromagnetic	Reattach separated flows and accelerate fluid via ion collision (DBDs) or Lorentz force (EFC).	Aircraft control surfaces (DBDs), conducting fluids (e.g., seawater)
Thermal Control	Alter near-wall fluid viscosity (reduce drag in liquids, stabilize gas flow) via localized heating/cooling.	Liquid and gas transport pipelines
Acoustic Excitation	Use specific frequencies to trigger/delay transition or manage flow separation.	Flow separation management

1.2.1 Passive Control and Surface Topology

Passive techniques modify the flow through surface geometry, body geometry or material properties without requiring the use of sensors or external energy, they often rely on biomimicry[1] and are optimized based on the statistical properties of the coherent turbulent structures to control (e.g., riblet spacing s^+ is chosen based on the mean diameter of QSVs).

Passive control is usually implemented in situations where drag reduction devices have to be deployed over large surfaces and must require low maintenance costs [15].

Wang et al. [55] noted that while passive methods are robust, their efficiency is strictly tied to a narrow range of Reynolds numbers, often leading to performance degradation under off-design conditions [49].

[1]The practice of learning from and then emulating nature's forms, processes, and ecosystems to create more sustainable and efficient human designs

Riblets

Historically, riblets have emerged as one of the most successful passive flow-control devices. Consisting of microscopic, longitudinal grooves aligned with the free-stream direction, they effectively restrict the spanwise motion of quasi-streamwise vortices (QSVs) and minimize the wall area exposed to high-momentum fluid sweeps [55, 14].

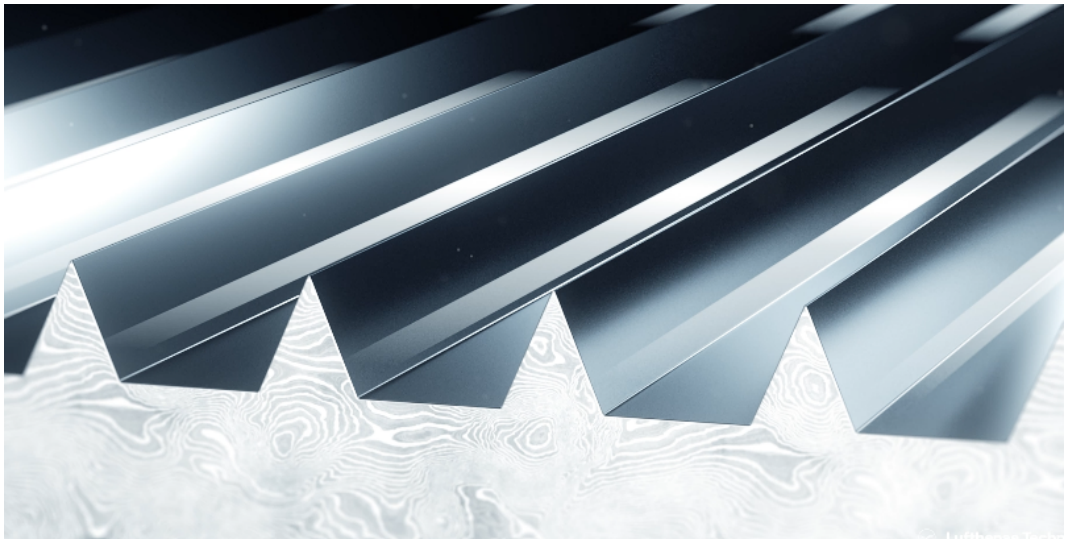


Fig. 1.14 Microstructure of the AeroSHARK riblet film. Image sourced from Lufthansa Technik [11].

By interacting directly with the near-wall turbulent bursting cycle, riblets mitigate the impact of QSVs. This interaction suppresses the sweep events that are primarily responsible for the elevated Reynolds shear stresses.

From a fluid dynamics perspective, the drag reduction mechanism relies on three primary physical effects:

- **Kinematic restriction of cross-flow:** The crests of the riblets act as continuous physical boundaries that impede the spanwise translation of QSVs. By dampening these spanwise velocity fluctuations, the riblets prevent the turbulent structures from scrubbing across the surface, significantly reducing the area affected by localized high shear stress.
- **Displacement of the virtual origin [14]:** According to the theoretical framework established in the literature, riblets induce a differential penetration of the

flow. While the longitudinal flow is able to enter the riblet valleys, the transverse flow associated with the QSVs is blocked by the peaks. Consequently, the turbulent structures perceive an apparent wall (*"the virtual origin"* [14]) that is shifted outward. This vertical displacement distances the core of the vortices from the physical surface, causing the high-velocity sweeps to lose momentum before they can impinge on the valleys.

- **Confinement of high shear stresses:** Although the introduction of a grooved topography inherently increases the total wetted area, the geometry ensures that high-shear interactions are strictly confined to the riblet tips. The fluid residing within the valleys remains relatively stagnant, creating a protective low-speed buffer zone. The skin-friction penalty caused by the increased surface area is therefore substantially outweighed by the drag reduction achieved within the valleys.

As García and Jiménez [14] highlighted, the effect of riblets on drag reduction in proportional to their size and after a certain threshold size, the drag is not reduced but increased.

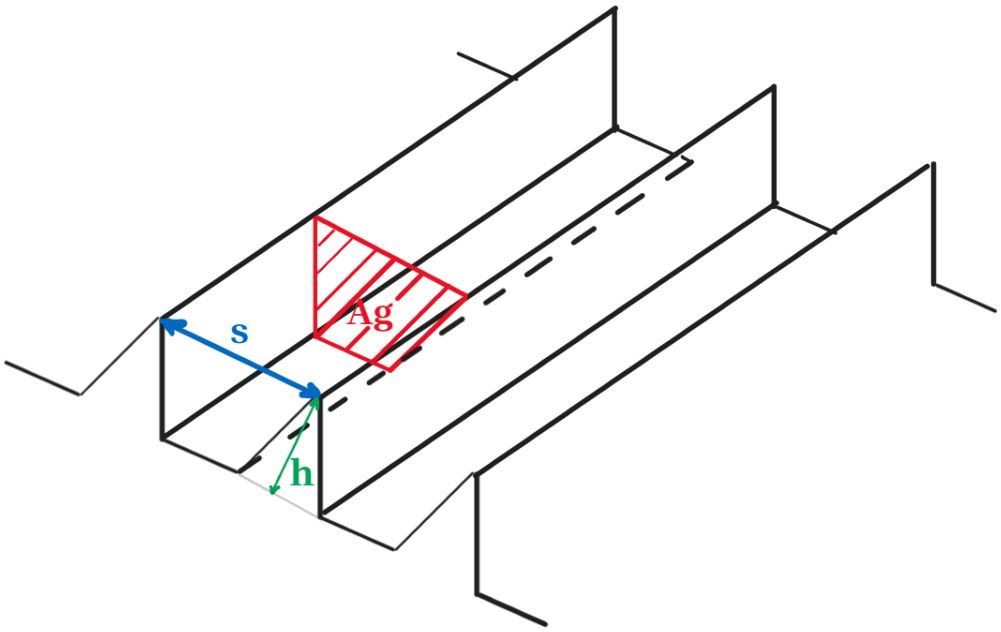


Fig. 1.15 Characteristic dimensions of riblets with conventional geometries.

Riblet effectiveness depends on their size relative to the turbulence scales, measured in non-dimensional "wall units" For conventional riblets geometries one can define the following dimensions, represented in Fig. 1.15, with the respective adimensional quantity expressed in wall units identified with $+$:

- **Riblet spacing s and viscous riblet spacing s^+**: distance between two peaks of the riblets, conventionally used to characterize the effectiveness of riblets in reducing skin friction. In several experimental results, summarized by García and Jiménez [14], with conventional riblets geometries, it is shown that the optimal viscous riblet spacing ranges between $s^+_{opt} = 10 - 20$, as seen in Fig. 1.16, from [14].

- **Riblet depth h and viscous riblet depth h^+**: distance between the tip and the valley of a riblet. If is too small, meaning that the riblets are too small and short, the flow just sees them as a "rough" surface, and drag increases. Whilst, if riblets are too high and large, they actually begin to house the vortices inside the grooves, which significantly increases drag by creating more turbulence.

- **Riblet groove cross section A_g and viscous riblet groove cross section A^+_g:** area of the cross section of the riblet groove, from this quantity one can extrapolate a characteristic length of riblets identified as ℓ^+_g.

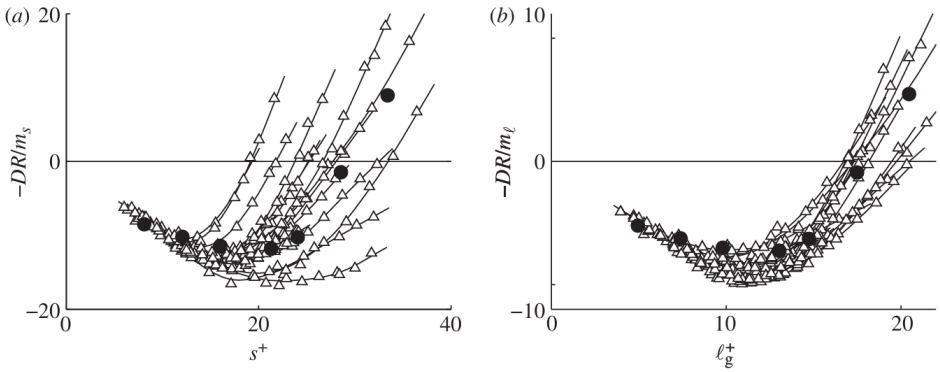


Fig. 1.16 Normalized drag reduction profiles for various riblet topographies, scaled to align along a uniform initial viscous slope. The drag reduction performance is evaluated with respect to two dimensionless geometric parameters: (a) the lateral riblet spacing, s^+, and (b) the square root of the groove's cross-sectional area, ℓ^+_g. Experimental measurements conducted by Bechert et al. [12] are indicated by open triangles, while solid circles represent DNS data obtained by García-Mayoral and Jiménez [13], image sourced from García and Jiménez [14].

It is evident from the graphs in Fig. 1.16 that riblet spacing is not the best variable to collapse and universalize all drag reduction curves from different experiments, corresponding to variable riblet geometries [14].

To quantify riblets effectiveness in reducing skin friction, García and Jiménez [14] found the quantity $l_g^+ = sqrt(A_g^+)$ to be the best candidate, since it reduces scattering across all the experimental results, with the optimal value $\ell_{g,opt}^+ \approx 10.7 \pm 1.0$ as seen in Fig. 1.16.

Drag reduction is measured as $\frac{DR}{mL}$, where L is a generic length, $DR = -\frac{\Delta\tau}{\tau_0}$ with $\Delta\tau$ the variation of skin fricition with riblets and τ_0 as skin friction with a smooth wall, and $m_L = -\frac{\delta(\frac{\Delta\tau}{\tau_0})}{\delta L^+}$ for $L = 0$ is the slope (so that $DR \approx m_L L^+$), [14].

One of the most innovative examples of riblets is the AeroSHARK [11, 56] surface technology which consists of a film made of 50 micrometer prism ribs, represented in Fig. 1.14 that is applied to the aircraft surface in order to significantly reduce frictional drag.

AeroSHARK films are designed by Lufthansa Technik and BASF Coatings [11, 56], studying shark skin. Shark skin is made of ribbed scales, represented in Fig. 1.17, which shift independently according to flow to lower skin friction and reduce energy dissipation.

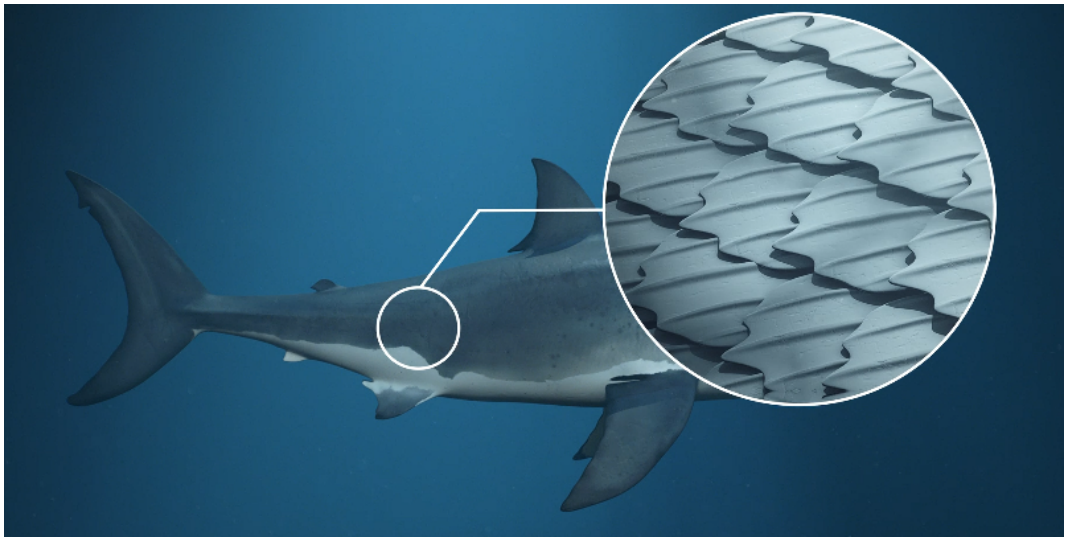


Fig. 1.17 Shark skin ribbed scales. Image sourced form Lufthansa Technik webpage [11]

This technology is currently deployed on long-haul aircraft such as the Boeing 777, resulting in a reduction in skin friction of about 8–10% locally,providing 1 % reduction in fuel consumption and CO_2 emissions [56, 11]. Industrial applications of passive biomimetic surfaces, such as the NovaFlex SharkSkin functional films developed by BASF Coatings, have demonstrated drag reductions of approximately 1 % on commercial aircraft [56].

Superhydrophobic Surfaces SHS

More recent advancements were obtained in the study of liquid environment, finding application in ships or oil pipeline flows to mitigate drag, reduce fuel consumption, increase cruise or transportation velocity. Some of the passive drag reduction technologies in this fields involve superhydrophobic surfaces (SHS), which induce a "slip" condition at the wall, making them fluid repellent, as happens naturally in lotus leaves [15].

Superhydrophobic surfaces (SHSs) reduce drag through the combined effect of surface topography and low surface energy, which facilitates a liquid-repellent state. A surface is formally classified as superhydrophobic when it exhibits:

- A **static contact angle (CA)** greater than 150°, that implies that fluid tends to bead up into nearly perfect spheres on the surface, as shown in Fig. 1.18.
- A **contact angle hysteresis (CAH)** below 5°. The CAH measures how easily a droplet starts sliding accross the surface.

The fundamental mechanism for drag reduction is the maintenance of the Cassie-Baxter state [15], where air is trapped within the surface asperities, that are micro/nano-ridges or posts obtained on the wall. This trapped gas forms a meniscus that acts as a lubricating layer, allowing the fluid to slip over the surface rather than adhering to it. If the fluid penetrates these cavities the superhydrophobic property and the associated drag reduction are lost.

Effective SHSs can produce a slip length of up to 400 μm [15], which reduces the near-wall velocity gradient by having a non-zero velocity of the flow at the surface, as shown in Fig. 1.19 from Kouser et al. [15]. Consequently SHSs lead to a great reduction in skin-friction shear stress.

In turbulent regimes, SHSs further mitigate drag by reducing vortices intensities and physically displacing quasi-streamwise vortices away from the wall, thereby interrupting the high-momentum sweep events that contribute to frictional resistance [15].

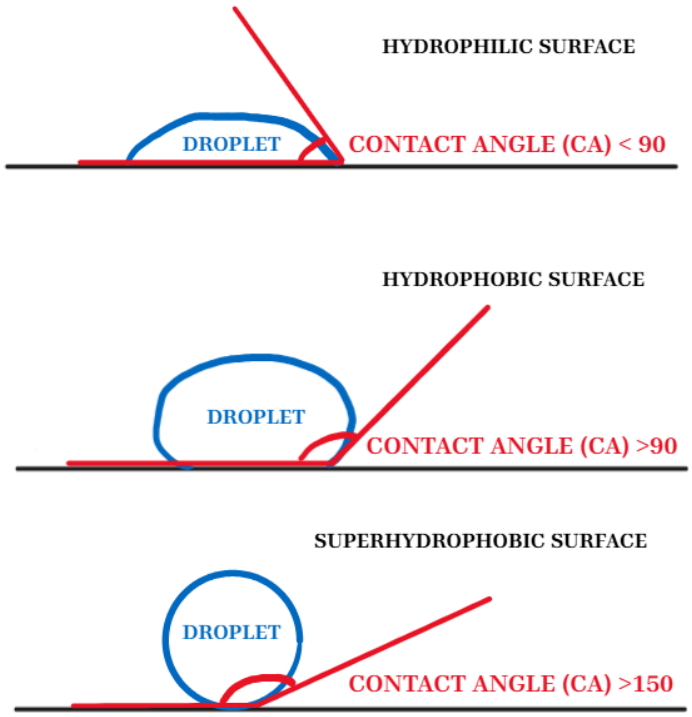


Fig. 1.18 Characterisation of surfaces with the static contact angle criterion.

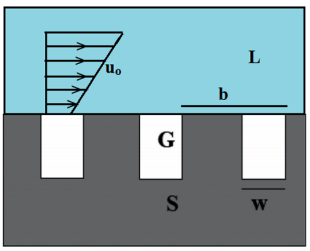


Fig. 1.19 Qualitative schematic of superhydrophobic surfaces mechanisms, with focus on near-wall streamwise velocity gradient. In the diagram, G: gas, L: liquid, S: solid, w: groove width, u_0: streamwise speed. Image sourced from Kouser et al. [15]

1.2.2 Active Control Techniques: Numerical Investigations

Active control introduces external energy into the boundary layer to manipulate its structure and achieve drag reduction. These techniques are generally classified into two categories based on their operational logic:

- **Open-loop (pre-determined) control:** These methods act on the flow field regardless of its instantaneous state. Examples include spanwise wall oscillations or steady blowing and suction.
- **Closed-loop (reactive) control:** These schemes utilize sensors to detect the arrival of specific coherent structures and activate actuators in real-time to counter them. As established by Kravchenko et al. [57], regions of high instantaneous skin friction are strongly correlated with the presence of quasi-streamwise vortices (QSVs). The majority of reactive control techniques aim to target these localized events, potentially offering higher efficiency than global methods.

Early numerical investigations demonstrated that boundary layer transition could be manipulated through local 2D suction or blowing. Specifically, Laurien and Kleiser [58] showed that transition could be postponed when disturbances were introduced out of phase with Tollmien-Schlichting waves.

Opposition Control (OC): Numerical Investigations

Opposition control (OC) is one of the most prominent reactive strategies. Its core principle is to cancel the velocity fluctuations associated with near-wall coherent structures through targeted actuation. Choi, Moin, and Kim [3] conducted a landmark DNS study on fully developed turbulent channel flows to evaluate various OC strategies aimed at suppressing QSVs.

They identified two distinct physical mechanisms driving drag reduction:

1. **Direct mitigation**: Immediately after the control is applied, the high-speed "downwash" (sweep) is deterred, reducing the sweep-induced Reynolds shear stresses near the wall without initially modifying the primary vortices.

2. **Structural alteration**: Subsequently, the control modifies the wall vorticity, preventing the lift-up of structures and disrupting the self-regeneration cycle of turbulence [3].

Choi et al. [3] quantified skin-friction reduction by measuring the pressure gradient required to maintain a constant mass flow rate. The investigated strategies, based on a detection plane located at a distance y_d^+ from the wall, included:

- **Control using the wall normal speed component *"v-control"* [3]:** the fundamental concept is to detect the wall-normal velocity (v) at a sensing plane (y_d^+) and apply an equal and opposite velocity at the wall ($v_w = -v_{detect}$). In this way, when sweeps or ejections were detected blowing and suction were respectively actuated. This study revealed that there seemed to be a *"critical"* detection distance $y_d^+ \approx 10$ that led to a maximum drag reduction of 25%, while further away from that point skin friction increased with the control effect. Similar drag reduction was obtained just by controlling stronger events, implementing a threshold wall normal velocity value over which actuate the blowing or suction, this implied that the majority of skin friction is generated by strong events and to make the control system more efficient it's possible to rule out weaker structures [3].

- **Control using transverse velocity component *"w-control"* [3]:** : detection of the spanwise velocity induced by streamwise vortices at a sensing plane (y_d^+) and inject an equal and opposite velocity at the wall, as in Fig. 1.20. Choi, Moin and Kim obtained 30% drag reduction, again at a critical wall normal distance $y_d^+ \approx 10$, with increased skin friction at values greater than 20.

- **Control using both the wall normal and transverse speed components *"v- and w-control"* [3]:** 30% drag reduction was obtained by applying out of phase blowing and suction at the wall in both y and z directions. Since the simulation was done at low Reynolds number, the control technique led to flow laminarization, although it's highly unlikely that the same thing would happen at high Re.

- **Control using the streamwise velocity component *"u'-control"* [3]:** while the other strategies led to significant drag reductions, the streamwise control

at the wall was the least effective in Choi, Moin and Kim [3] research. Only 10% of drag reduction was achieved with in phase control (and 10% increase for out of phase control), because adding streamwise velocity to the wall flow led to a reduction of the wall speed gradient $\frac{\delta u'}{\delta y}$, related to skin friction.

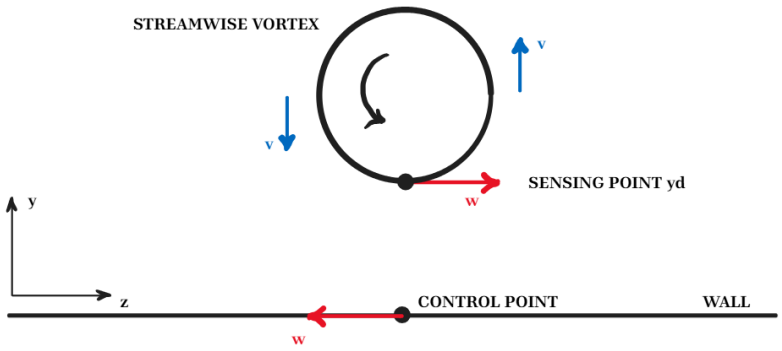


Fig. 1.20 Graphic representation of opposition control using the transverse velocity component. Image redrawn and adapted from Choi, Moin and Kim [3]

Physical Mechanism: The Virtual Wall [4]

Every control approach investigated by Choi, Moin and Kim [3] led to the conclusion that there exists an optimal detection wall distance y_d^+ that leads to maximum drag reduction.

The effectiveness of OC and the explanation of this conclusion was further elucidated by Hammond et al. [4] DNS investigation of v-control applied to a channel fully developed turbulent flow. Obtaining the same results as Choi et al. [3] Hammond et al. [4] introduced the concept of the **"virtual wall"**. By observing isosurfaces of the discriminant of the velocity gradient tensor, they found out that sweep and ejections were almost completely disrupted by the control with $y_d^+ \approx 15$, while at $y_d^+ \approx 25$ QSVs were not nullified.

This mechanism suggests that the opposition actuation effectively creates a plane with zero net vertical momentum transport located approximately in the middle between the physical surface and the detection plane (e.g., at $y^+ \approx 7.5$ for $y_d^+ \approx 15$). This virtual wall [4] suppresses the communication between the flow adjacent to

the wall and the flow in the following layers, thickening the viscous sublayer and pushing the primary vortices further away from the surface. However, if the detection plane is too distant ($y_d^+ > 25$), the control can inadvertently increase drag by drawing high-speed fluid toward the wall [4].

Differences Between Controlled and Uncontrolled Flows

To establish a baseline for evaluating active control methodologies, Choi, Moin, and Kim [3] quantified the differences between manipulated and unmanipulated channel flows using Direct Numerical Simulation (with a detection plane at $y_d^+ \approx 10$ and $Re_c = 3300$). Their findings indicated a consistent trend in the alteration of mean flow properties, largely regardless of the specific control scheme applied. In Chapter 3, these numerical observations will serve as a theoretical benchmark to interpret the experimental results obtained at Politecnico di Torino.

1. **Mean flow properties**

   - **Mean-velocity profiles**: As illustrated in Fig. 1.21, while the controlled flow maintains the standard slope of the universal law of the wall, its logarithmic region exhibits a pronounced upward shift. Specifically, the intersection between the linear viscous sublayer ($u^+ = y^+$) and the log-law region shifts from $y^+ \approx 10$ to $y^+ \approx 15$. This displacement is a primary indicator of a thickened viscous sublayer (which expands from $y_s^+ \approx 5$ to $y_s^+ \approx 10$), a mechanism similarly observed in boundary layers treated with passive drag-reduction devices like riblets.
   - **Mean flow variables**: The application of active control yields a direct reduction in the skin-friction coefficient (C_f). This is accompanied by a corresponding decrease in the boundary layer thickness when expressed in wall units ($\delta^+ = Re_\tau$). Additionally, the flow exhibits a slight reduction in momentum thickness (θ) coupled with an increase in displacement thickness (δ^*) [3].
   - **Turbulence intensities**: The root-mean-square (RMS) profiles of the velocity fluctuations (u, v, w), when normalized by the actual wall-shear velocity u_τ, are globally attenuated under controlled conditions. Furthermore, these profiles demonstrate an outward spatial shift of approx-

imately $\Delta y^+ \approx 5$. Consequently, the peak of turbulence production migrates further from the wall (shifting from $y_s^+ \approx 12$ to $y_s^+ \approx 17$), further corroborating the thickening of the viscous sublayer [3].

- **Reynolds shear stress and vorticity**: The overall Reynolds shear stresses undergo a significant reduction. Quadrant analysis performed by Choi et al. [3] reveals that the control effectively mitigates the intensity of both sweep (Q_4) and ejection (Q_2) events, which are the primary drivers of positive Reynolds shear stress production. Notably, the structural modifications induced by the control dissipate for values of y^+ greater than 20; above this threshold, the flow merely exhibits the aforementioned outward shift. This suggests that the control schemes do not fundamentally alter the outer-region turbulence, but rather displace it away from the wall, thereby starving the near-wall turbulence regeneration cycle. Similarly, RMS vorticity fluctuations are drastically suppressed near the wall, and their local maxima are displaced outward, mirroring the behavior of the velocity fields [3].

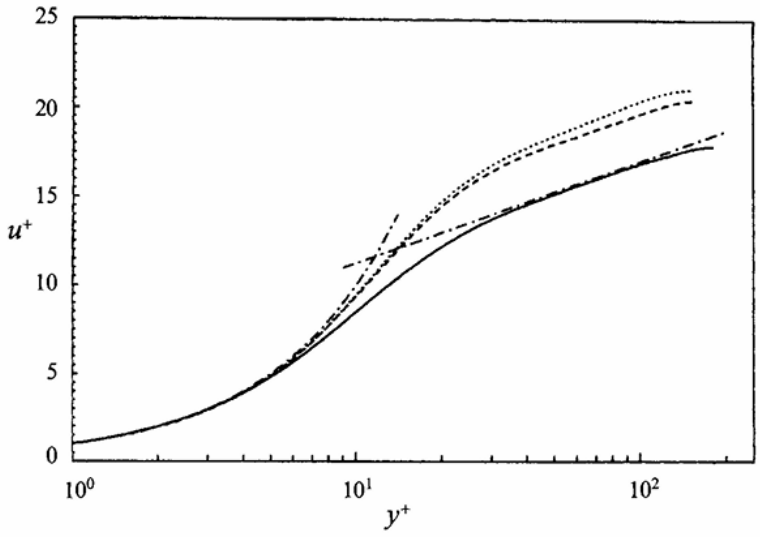


Fig. 1.21 Mean velocity profiles normalized by $u_{\tau,u}$ (the friction velocity of the uncontrolled flow). —-: no control; - - - -: v-control; .....: w-control; -.-: law of the wall ($u^+ = y^+$ and $u^+ = 2.5 \ln y^+ + 5.5$). Image sourced and adapted from Choi, Moin and Kim [3].

1.2.3 Opposition Active Control: Experimental Implementation with Synthetic Jets

Translating the idealized blowing and suction of DNS into physical experiments requires high-frequency actuators capable of generating zero-net-mass-flux (ZNMF) jets, commonly known as synthetic jets.

Evolution of the Experimental Approach

The transition to experimental opposition control was pioneered by Rebbeck and Choi. As introduced in Chapter 1, Section 1.2, in their 2001 study [5] they used a **piston-type actuator** to investigate the impact of wall-normal jets on the "burst signature" of the boundary layer. This was an off-line experiment carried out in a closed-return wind tunnel, where a fully developed turbulent flow was obtained with cylindrical tripping devices.

Their testing set-up, as represented in Fig. 1.22, was composed of: a single hot-wire probe mounted flush with the surface (with only the sensing part and the prongs exposed to the flow to reduce aerodynamic interference); a control point where synthetic jets were generated by a solenoid-driven piston (mounted so that it did not protrude into the flow during the entire actuation cycle); and a Dantec 55P15 BL hot-wire downstream of the control point. The actuator was triggered on the basis of sweep events identified a posteriori using the VITA technique.

As shown in Fig. 1.12, when the jet interacts with the TBL, the streamwise velocity component experiences an initial reduction, followed by an increase. Rebbeck and Choi [5] suggested that this initial velocity reduction is caused by the jet dragging wall-adjacent, slow-speed fluid upward, while the subsequent increase in the u^+ component is due to the generation of a vortex ring by the piston. Upon the withdrawal of the piston, the streamwise component then resettles to its initial value.

They [5] demonstrated that the timing of the actuation is critical, obtaining sweep intensity mitigation for a distance of $x^+ = 90$ after the control point when the actuation timing was correct. Otherwise, incorrect phasing relative to the incoming structure can be detrimental to drag reduction, making open-loop opposition control less effective. They proved that the effectiveness of control relies on real-time event detection and on tailoring the control accordingly. This means that the actuation

must take into account both the latency of the control system and the convection time of the sweep event from the detection point to the control point.



Fig. 1.22 Diagram of the testing set-up. From left to right: a detector with a 1 mm long upstream detecting hot-wire with a 5 μm diameter; after $\Delta x^+ = 72.5$ downstream of the detecting hot-wire sits the control point with the piston-type actuator; a Dantec 55P15 BL hot-wire downstream of the control point. Image sourced from Rebbeck and Choi [5].

The Shift to Real-Time Opposition Control

Building upon the insights gained from their 2001 [5] off-line experiments, Rebbeck and Choi achieved a significant milestone in 2006 by implementing a fully closed-loop, real-time opposition control system in a wind tunnel [6]. The primary objective was to actively suppress the near-wall streamwise vortices by blowing fluid exactly when a high-speed sweep event was detected approaching the actuator.

The experimental set-up was upgraded to support real-time feedback, maintaining the same structure of the previous testing set-up [5], with the only difference being that the piston actuator was replaced by an orifice with a loudspeaker beneath, responsible for the synthetic jet production.

The choice of a loudspeaker for the active control was necessary to make real-time control possible, since the previous piston-type actuator lacked the necessary frequency response.

The new set-up [6] featured: an upstream detection Dantec 55P01 hot-wire (flush-mounted onto the wall) to capture the incoming streamwise velocity component footprint of the coherent structures; the same Dantec 55P15 downstream hot-wire probe, able to move along x, y, z directions to monitor the effectiveness of the actuation; a digital signal processor (DSP) to handle the control algorithm; and a zero-net-mass-flux (ZNMF) synthetic jet actuator situated downstream.

The detection method, this time, was based on the **velocity gradient technique**, with sweep events identified whenever the derivative of the streamwise speed component surpassed a predetermined threshold value. Rebbeck and Choi [6] pointed out that, compared to the VITA technique, the gradient detection method brings along the risk of false detections due to the reduced identification duration. This problem was fixed by imposing a higher threshold ($k = 1$ and $T^+ = 10$) and focusing on high-intensity sweep events.

The core challenge of this real-time implementation was the precise synchronization of the jet actuation with the passing structure. In fact, they [6] had to consider a fixed time delay ($t^+ \approx 3$) that included the loudspeaker latency, the delay due to the convection of the sweep event from the detection point to the control point, and the system delay from detection to actuation. Rebbeck and Choi [6] developed a control logic that calculated a specific time delay based on the convection velocity of the near-wall structures traveling from the detection point to the actuation point. This took into account that the shear layer is inclined at around 8° to the flow, the distance of the detecting probe from the wall, and the distance of the virtual wall [4]. When the sweep was detected, a TTL trigger was sent to a wave generator that would send a square-wave signal to the actuator of the acoustic diaphragm.

Fig. 1.23 shows the v^+ profile detected by Rebbeck and Choi [6] right above the control point, with the wind tunnel turned off. They [6] interpret the jet profile by identifying an initial *blowing* phase, where v^+ increases almost linearly with t^+ until, at the end of the wave input, a peak of $v^+ = 9.1$ is reached. Afterwards, v^+ decreases to zero and then presents a long *suction* phase, caused by the retraction of the acoustic membrane, where the hot-wire identifies an effective negative velocity as positive (due to its incapacity to discern flow sign).

Ensemble averages of the streamwise velocity fluctuations after actuation showed a stretched oval region of low momentum fluid from the control point, sided by two high-speed regions, suggesting the birth of two counter-rotating vortices caused by the crossflow jet-boundary layer interaction [6].

Sweep events were identified and isolated by conditional sampling of the measured streamwise velocity signals, and then the sweep signature was obtained by an ensemble average of sweep events [6]. Rebbeck and Choi [6] pointed out that the sweep signature is defined by an abrupt increase in the streamwise velocity, as is clearly visible in Fig. 1.24.

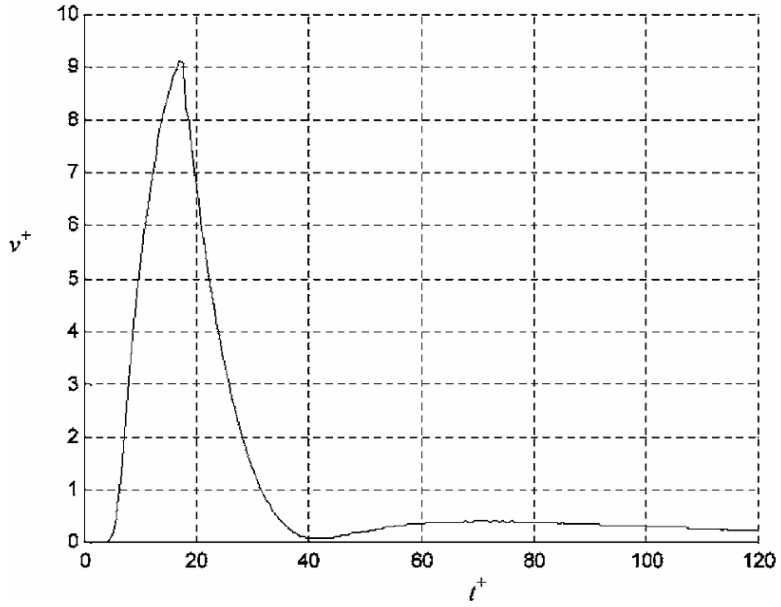


Fig. 1.23 Time history of the wall-normal velocity expressed in wall units v^+, measured from above the control point in still air, upon the actuation of the speaker with a square-wave law. Image sourced from Rebbeck and Choi [6].

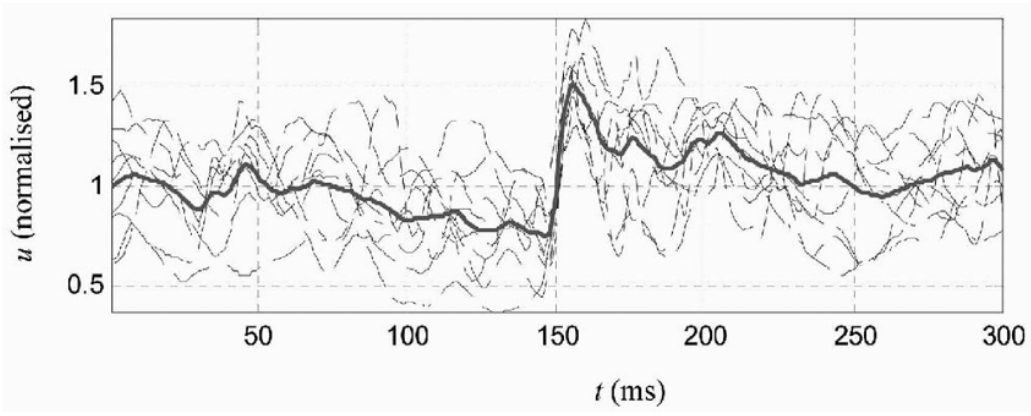


Fig. 1.24 Time history of normalized streamwise velocity. Dashed lines: conditional averages of nine different sweep events; black line: ensemble average of the sweep events. Image sourced from Rebbeck and Choi [6].

The results of the real-time opposition control were highly promising. By applying an equal and opposite wall-normal velocity to the incoming sweep events, the region of low speed created by the jet effectively weakened sweep events. This created a virtual wall [4] that blocked high-speed fluid from reaching the surface

in both the streamwise and spanwise directions, reducing the streamwise velocity fluctuations near the wall for a region downstream of the control point of at least $x^+ \approx 100$.

Rebbeck and Choi [6] suggested that the slow-speed region induced by the synthetic jet convects slower ($u_j^+ \approx 6$) than the high-speed region ($u_s^+ \approx 14$) of fluid that travels towards the wall. This is because the first region comes from near the wall while the second one originates higher up, causing the streamwise speed to re-increase downstream of the control point (approximately at $x^+ \approx 100$). However, the intensity of the streamwise velocity is lower for the controlled case compared to the uncontrolled scenario after the effect of the opposition control comes to an end. They [6] observed that the optimal attenuation occurred when the amplitude of the synthetic jet was carefully matched to the intensity of the incoming event, providing definitive experimental proof that targeted, real-time interference can effectively weaken the turbulence regeneration cycle and reduce local skin-friction drag.

1.2.4 Physical Interaction: Jet in Crossflow (JICF)

The effectiveness of opposition control strategies is strongly related to the complex fluid dynamics generated by the interaction between the control jet and the incoming crossflow. In most practical implementations, the actuator introduces a wall-normal jet into a flow moving parallel to the surface, creating a configuration commonly referred to as **Jet in Crossflow (JICF)**.

Understanding the physics of this interaction is essential because the synthetic jet does not simply inject momentum into the boundary layer, but modifies the near-wall turbulence through the generation and manipulation of three-dimensional vortical structures.

The fundamental characteristics of a jet in crossflow were extensively investigated by Kelso et al. [16] through flow visualization techniques (both with dye in water and with smoke in a wind tunnel) and hot-wire measurements, who demonstrated that even the apparently simple configuration of a round jet exiting from a wall produces a highly complex vortex system.

The interaction between the jet and the external flow causes the deformation of the jet shear layer along with the formation of large-scale coherent structures summarized as follows:

- A **horseshoe vortex** originates upstream and around the jet orifice.
- A **separation region** inside the jet orifice, on the upstream side.
- **Roll-up of the jet shear layer**, due to TS instabilities from the relative motion between the jet and the crossflow, that causes the reorientation of the jet axis towards the streamwise direction.
- As a consequence of the jet shear layer roll-up and deviation from the wall-normal direction, two **counter-rotating vortices** form on the sides of the jet axis and the crossflow's boundary layer separates.
- A **wake** region forms underneath the bent jet, comprised of streamwise vortices at the wall and vertical vortices that are similar to a vortex street downstream of a thick body.

Fig. 1.25 shows a schematic diagram of the coherent structures that originate from the interaction between a jet, produced by a jet nozzle mounted flush on a surface, and the incoming crossflow of velocity U_∞ [16].

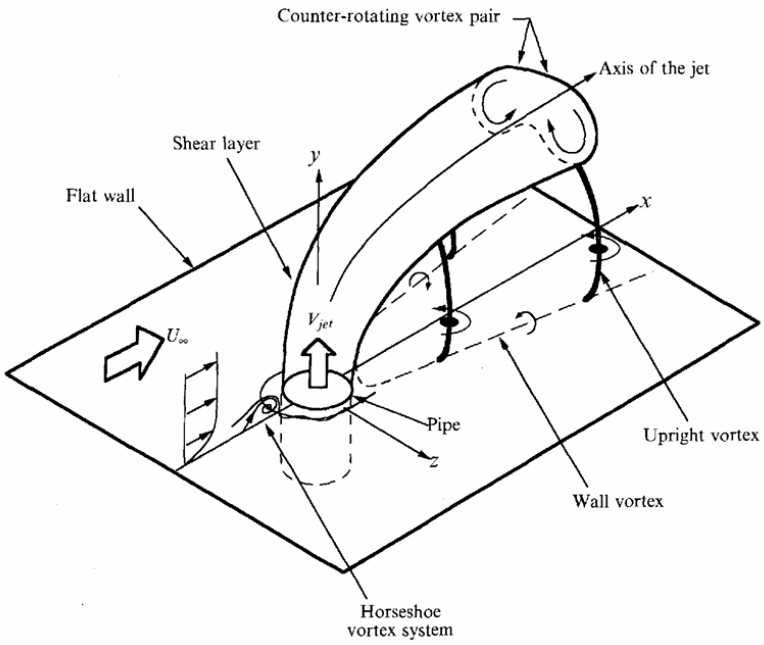


Fig. 1.25 Schematic diagram of the interaction between a circular jet, produced by a jet nozzle mounted flush on a surface, and the incoming crossflow of velocity U_∞. Image sourced from Kelso et al. [16]

One of the dominant features of the flow is the formation of a pair of streamwise vortices with opposite rotation, known as the **Counter-rotating Vortex Pair (CVP)**. These vortices originate from the reorientation of the vorticity contained in the jet shear layer generated by it getting unstable: as the jet bends under the effect of the crossflow, the initially azimuthal vorticity is tilted and stretched, producing a pair of counter-rotating structures that convect downstream. Kelso et al. [16] observed that the vortex rings generated by the jet shear layer progressively deform and contribute to the formation of the CVP through a tilting and folding mechanism of the vorticity field.

The CVP represents one of the main mechanisms responsible for momentum transfer between the jet and the surrounding boundary layer. Due to its rotational motion, the vortex pair induces a strong three-dimensional displacement of the surrounding fluid, promoting mixing and transporting low-momentum fluid away from the wall. Although this effect can be beneficial in some engineering applications such as film cooling or mixing enhancement, in the context of drag reduction the generation of excessive vortical activity must be carefully controlled. An improperly designed jet may increase turbulence production instead of reducing it.

Another important structure associated with the JICF is the **horseshoe vortex system**. When the incoming boundary layer encounters the jet obstacle, the adverse pressure gradient generated upstream of the jet causes the boundary layer to separate and wrap around the jet exit, as would happen to the flow around a solid thick body, forming a horseshoe-shaped vortex. Kelso et al. [16] showed experimentally that this vortex system develops upstream of the jet and remains connected with the downstream vortex structures. The separated wall vorticity can be lifted away from the surface and eventually merge with the CVP, contributing additional circulation to the overall flow field. Therefore, the JICF cannot be considered as the simple superposition of a jet and a boundary layer, but rather as a coupled system of multiple interacting vortex structures.

In opposition control applications, such as the control scheme used by [6] and implemented in this thesis, the synthetic jet exploits these mechanisms to modify the interaction between turbulent structures and the wall. The main objective is to interfere with the incoming sweep events, which are responsible for transporting high-momentum fluid toward the wall and increasing the local skin-friction coefficient. By injecting momentum in the wall-normal direction at the appropriate location

and timing, the jet creates a physical barrier (*virtual wall* [4]) that displaces these high-shear structures away from the surface. As a consequence, the intensity of the near-wall turbulence regeneration cycle can be reduced, producing a decrease in skin-friction drag.

However, the characteristics of the interaction between the jet and the crossflow depend critically on the correct calibration of the jet parameters. The most important nondimensional parameter is the **velocity ratio** or **blowing ratio**, generally defined as the square root of the ratio of the momentum flux from the jet orifice to the momentum flux of the crossflow over equal areas [16]. When both the jet flow and the crossflow have the same densities this ratio is obtained as:

$$R = \frac{V_{jet}}{U_\infty}$$

where V_{jet} is the time averaged volume flux divided by the area of the jet (which can be approximated with the jet velocity) and U_∞ is the local crossflow velocity [16]. This parameter represents the relative strength of the actuator compared with the external flow. For low values of R, the jet momentum may be insufficient to interact effectively with the incoming turbulent structures. In this case, the jet is rapidly bent by the crossflow and remains confined near the wall, producing only limited modification of the boundary layer.

On the other hand, excessively large blowing ratios can generate undesirable effects. A strong jet may penetrate too deeply into the external flow, creating additional vortical structures, increasing mixing, and introducing new sources of turbulence. Kelso et al. [16] observed that increasing the velocity ratio modifies the topology of the JICF's vortex system, with phenomena such as vortex breakdown and more complex wake structures appearing at higher values of the velocity ratio. These effects highlight the existence of an optimal range of jet momentum where the actuator can modify the turbulent structures without introducing excessive disturbances.

The complexity of the JICF also explains why modern control strategies increasingly combine physical understanding with data-driven methods. The nonlinear relationship between jet parameters, vortex formation, and turbulent response makes analytical optimization extremely difficult. Deep Learning approaches, discussed in the following sections, provide a possible solution by learning the relationship between measurable flow quantities and the required actuation strategy.

1.2.5 Machine Learning and Neural Networks Applied on Turbulent Flow Control

Recent developments in opposition control have focused on overcoming the limitations that have prevented its direct application to real engineering systems. Although classical opposition control strategies demonstrated remarkable drag reduction capabilities in numerical simulations [5], their practical implementation remains challenging because they require information about the instantaneous flow field above the wall, high volumes of data to analyse and difficult conditions to emulate due to the high range of spatial and temporal scales that characterize fluid mechanics[29]. As explained in the previous Section 1.2.3, the classical opposition control approach consists in measuring the wall-normal velocity at a detection plane located inside the turbulent boundary layer and actuating the control system to produce a velocity component in the opposite direction [6]. This approach creates a virtual wall [4] that reduces the interaction between near-wall sweep structures and the surface, limiting the generation of high skin-friction regions. However, placing sensors inside the flow is difficult from both a mechanical and operational point of view, especially for aerospace applications where reliability and aerodynamic efficiency are critical and sensor intrusiveness has to be minimized [59].

A major research direction has therefore been the development of control strategies based only on quantities measurable directly at the wall [24]. Wall shear stress and pressure measurements represent attractive alternatives because they can be obtained using non-intrusive or minimally intrusive sensors integrated into the surface. The main difficulty is that the relationship between wall quantities, their response to wall actuations and the turbulent structures responsible for drag production is impossible to be obtained analitically in a closed form due to the complexity of the Navier-Stokes equations [24]. For this reason, data-driven approaches have emerged as promising tools for extracting hidden correlations from large datasets of turbulent flows.

Machine Learning (ML) provides a framework capable of learning complex relationships between input and output variables without requiring an explicit analytical representation of the system [24]. In fluid mechanics, ML techniques have been increasingly employed for reduced-order modelling, flow reconstruction, optimization, and active flow control. As discussed by Brunton et al. [29], modern machine learning approaches are particularly attractive for fluid dynamics problems because

turbulent flows generate large amounts of experimental and numerical data, while traditional analytical approaches often struggle with nonlinear and high-dimensional systems. In fact, Machine learning can increase the domain knowledge and help automate the flow control system and its optimization [29].

The first applications of neural networks to turbulence control appeared before the current Deep Learning era. Lee et al. [24] demonstrated that a neural-network-based off-line controller could learn the relationship between wall shear stresses and the required wall actuation. Their approach used only wall information as input to train the neural network to implement a control scheme of blowing and suction at the wall, achieving significant drag reduction (20%) in turbulent channel flow numerical simulations. With their results, Lee et al.[24] proved that near-wall measurements contain sufficient information to reconstruct the behaviour of larger turbulent structures. The study represented an important step toward practical implementations because it replaced the need for direct measurements inside the flow with a data-driven estimation process.

More recently, the development of Convolutional Neural Networks (CNNs) has further improved the capability of neural controllers. CNNs are particularly suitable for turbulent flows because their architecture is designed to identify spatial patterns and correlations, similarly to image-processing applications. In wall-bounded turbulence, coherent structures such as streaks and vortices exhibit spatial organization, making CNNs effective tools for extracting relevant features from distributed sensor measurements.

Li et al. [60] investigated a simplified version of opposition control, called **blowing-only opposition control**. In Rebbeck and Choi [6] approach, the actuator alternates between suction and blowing depending on the measured wall-normal velocity. Although effective, this mechanism introduces additional mechanical complexity because the system must actively reverse the flow direction. The blowing-only approach eliminates the suction phase and applies actuation only when upward velocity fluctuations associated with harmful turbulent events are detected.

Li et al. [60] demonstrated that the drag reduction performance of blowing-only opposition control is mainly related to correctly identifying the regions where large wall-normal velocity fluctuations occur. Therefore, instead of predicting the complete velocity field, the neural network only needs to determine the direction of the relevant turbulent motions. This simplification significantly reduces the complexity of the

control problem and makes the approach more suitable for real-time implementation. In their study, a CNN model was trained using wall-based measurements, specifically wall shear stresses, to predict the flow information required for the actuation. The results showed that the trained network could successfully reproduce the required control behaviour and maintain good prediction accuracy even when applied to flow conditions with Reynolds numbers higher than those used during training.

The integration between Deep Learning and opposition control represents an important transition from model-based control strategies toward data-driven adaptive systems. Instead of explicitly describing the turbulent dynamics, the controller learns the optimal relationship between measured quantities and actuator commands directly from examples. This approach is particularly valuable for turbulent flows because the governing Navier-Stokes equations contain all the physical information but solving them in real time for control purposes is computationally prohibitive [29].

Recent works have also explored neural networks not only as direct controllers but also as surrogate models capable of predicting the effect of different control parameters. Saccaggi and Di Cicca [17] applied a Feed Forward Neural Network (FNN) to predict the influence of actuation parameters of a synthetic jet generated by a loudspeaker on sweep events in a fully turbulent channel flow. The FNN model was chosen because of its better capability to learn non-linear mappings, compared to traditional regression techniques, between the actuation and its effect on the sweep event.

The turbulent channel flow in question is the same of this thesis; their objective was to create a model able to reproduce the controlled conditionally averaged flow structures from the uncontrolled state and the chosen actuation parameters. The neural network was trained using a dataset of 130 control triplets, i.e. different combinations of actuation frequency, amplitude, and delay time, obtained through Latin Hypercube Sampling (LHS) technique, which enables the creation of a dataset of equidistant measurement points inside of a multidimensional space. In this work [17] the space for the LHS technique was defined by the upper and lower bounds imposed for the three control parameters and each triplet of parameters was associated to the respective measured uncontrolled and controlled flow streamwise velocity signals. Training of the model was done with 80% of the dataset, to recognize the patterns and relationships within the data, tune its parameters for better predictions

and minimize errors,while the remaining 20% was used for validation, which helps the evaluation of the model's performance. Once trained, the model could faithfully predict the expected control outcome compared with the experimental respective result, as represented in Fig. 1.26, and was used to perform an offline optimization of the actuation parameters, reducing the computational cost compared with direct experimental optimization [17].

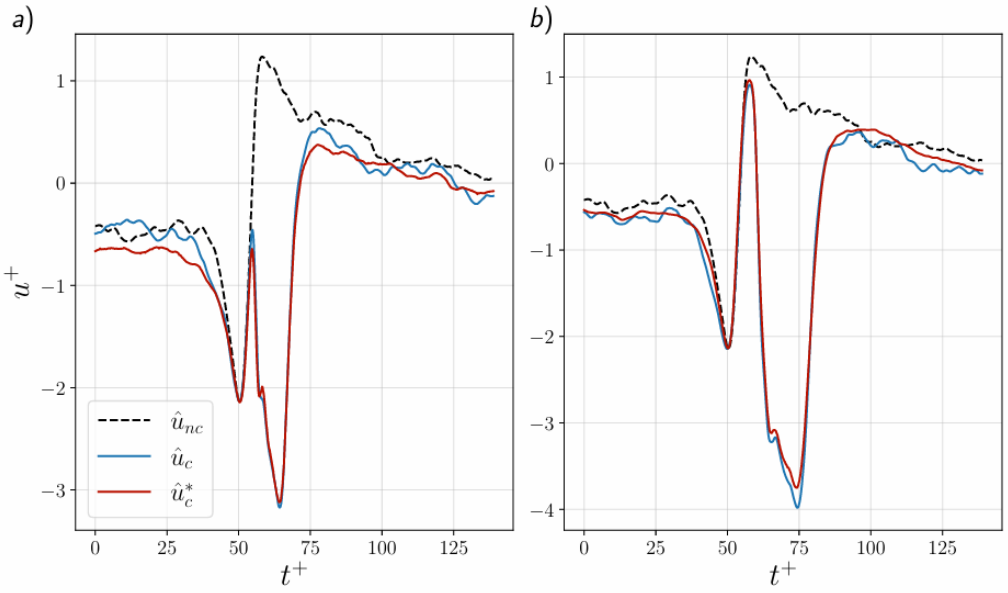


Fig. 1.26 Validation of the FNN performance on the validation dataset. Black dashed line: the uncontrolled case; blue solid line: experimentally measured response under control conditions; red solid line: event predicted by the FNN model with the same control parameters of the experimental results. The control action is applied using the actuation parameters $f = 53.10\,\text{Hz}, Vpp = 62.4\,\text{mV}_{\text{pp}}, \Delta t = 1.01\,\text{ms}$ in case (a) and $f = 31.54\,\text{Hz}, Vpp = 60.0\,\text{mV}_{\text{pp}}, \Delta t = 2.71\,\text{ms}$ in case (b). Image sourced from [17].

This approach highlights another important advantage of Deep Learning methods: once trained, neural networks can act as fast approximations of complex physical systems. Instead of testing every possible control configuration experimentally, the learned model can rapidly explore the parameter space and identify promising solutions. Sensitivity analyses can also be performed to determine which parameters have the greatest influence on drag reduction performance [17].

Despite these advantages, several challenges remain before Deep Learning-based flow control can be fully implemented in industrial applications. Neural networks require large and representative datasets, and their performance depends strongly

on the quality of the training data. Moreover, turbulent flows are characterized by multiple spatial and temporal scales, making generalization outside the training conditions a difficult problem. Overfitting, robustness, and interpretability are therefore key aspects that must be addressed [29].

Nevertheless, the combination of active flow control and Deep Learning represents one of the most promising directions for future drag reduction technologies. By combining physical knowledge of turbulent mechanisms with data-driven prediction capabilities, modern control systems can potentially achieve adaptive and efficient manipulation of complex flows. The transition from ideal numerical demonstrations toward practical aerospace applications will depend on the development of reliable sensor architectures, efficient actuators, and neural controllers capable of operating under real-world conditions [17, 29].

1.3 Concluding Remarks

The study of wall-bounded turbulence has evolved from the identification of coherent structures to the development of sophisticated active control strategies. As discussed, the near-wall region is dominated by quasi-streamwise vortices (QSVs) which, through the induction of sweep and ejection events, are responsible for the majority of skin-friction drag. While passive strategies like riblets provide a robust means of drag reduction by physically restricting these motions, active opposition control offers the potential for higher efficiency by dynamically canceling turbulent fluctuations.

The transition from numerical ideals to experimental reality presents significant challenges, particularly regarding actuator response and real-time detection. The work of Rebbeck and Choi [6] established a fundamental framework for using speaker-driven synthetic jets to intercept high-speed sweeps. Building upon this heritage, the present thesis aims to investigate the interaction between a synthetic jet and a wall-bounded turbulence, with a specific focus on the real-time detection and mitigation of sweep events. The following chapters will detail the experimental set-up, the characterization of the synthetic jet, and the results obtained through the implementation of an active control scheme at Politecnico di Torino.

Chapter 2

Experimental Set-Up

This chapter provides a detailed description of the experimental facility, instrumentation, and control logic employed to investigate active flow control in a turbulent channel flow. The research was conducted in an open-loop wind tunnel, utilizing a hot-wire anemometry system for real-time detection and measurement and a loudspeaker actuator to generate synthetic jets as a the opposition control approach, as done by Rebbeck and Choi [6]. The experimental set-up and the flow parameters are consistent with those previously described and validated by Saccaggi and Di Cicca [17, 61, 62], ensuring the reliability and comparability of the results. Particular attention is given to the evolution of the control hardware, moving from a standard signal generator configuration to a more versatile custom system based on the Arduino GIGA microcontroller, which allows for advanced waveform manipulation and automated parameter tuning.

2.1 Sensors

For this thesis, measurement campaigns were carried out in an open-loop wind tunnel, with rectangular channel with its length equal to $L = 8\ m$, its height of $2H = 70\ mm$ and a width of $W = 30\ cm$. The wind tunnel and the rectangular channel dimensions ($AR = 4.28$) correspond to the facility utilized in the studies by Saccaggi and Di Cicca [17, 61, 62]. Fig. 2.1 shows Politecnico's orange channel where measurements were conducted.



Fig. 2.1 Orange channel ad complete experimental set-up at Politecnico di Torino used for the experimental research on active flow control on wall-bounded turbulent flows through synthetic jets

A tripping strip obtained from sandpaper is placed at the beginning of the channel to induce turbulent flow transition in a controlled way, providing a fully developed wall-bounded turbulent flow at the testing section.

Upstream of the channel, there is a motor whose rotational speed can be varied via an inverter, thereby adjusting the flow velocity. Specifically, during the various experimental campaigns, the rotational speed was set to approximately 345 rpm. However, it was observed that during operation, the motor's rotational speed tends to gradually increase until it settles at 350 rpm. It is hypothesized that this behavior is due to long-term motor oscillations and the stabilization of the circuits within the machine's control system during operation.

The following parameters varied between the different measurement campaigns, that were taken over several months, that will be presented in Chapter 3:

- The imposed centerline velocity U_0 ranged between $(3.2,\ 3.3)\frac{m}{s}$.
- The evaluated friction velocity u_τ ranged between $(1.52,\ 1.61)\frac{m}{s}$.
- The resulting friction Reynolds number $Re_\tau = \frac{u_\tau H}{\nu}$ ranged between $(365,\ 420)$.

To perform the velocity measurements, two hot-wire probes were utilized, equipped with a tungsten sensor wire, featuring a diameter of 5 μm and a length of 1.25 mm. Each sensor is connected to a Dantec 55M10 CTA Standard Bridge anemometer, represented in Fig. 2.2.



Fig. 2.2 Dantec 55M10 CTA Standard Bridge anemometer.

Fig. 2.3 presents the testing section set-up:

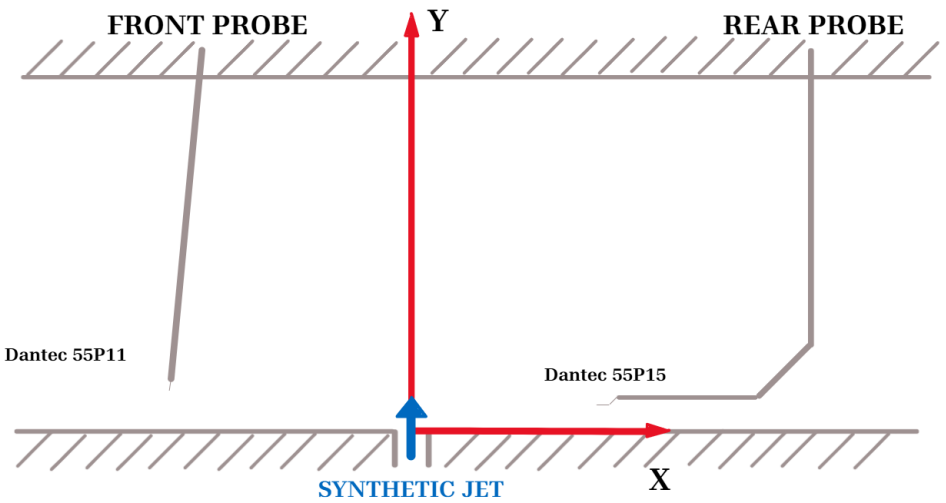


Fig. 2.3 Diagram of the testing set-up employed for the online opposition control. The flow direction is from left to right.

The front probe (Fig. 2.3) relative to the control hole, which is a Dantec 55P11 model (Fig. 2.4), was mounted on a manual protractor stage, which allowed for positioning adjustments along an arc-shaped path. This configuration enabled the probe to be moved simultaneously in the streamwise and wall-normal directions. Furthermore, the front probe was secured to the protractor via a rubber sleeve; this mounting solution provided the flexibility to manually raise or lower the sensor, allowing for precise tuning of the sweep detection point according to the experimental requirements [4]. The front probe is inserted into the channel through a slot machined into its upper Plexiglas wall. During the several measurements, the upstream probe position was changed manually to better understand the effect of the position of the detection point on the opposition control.

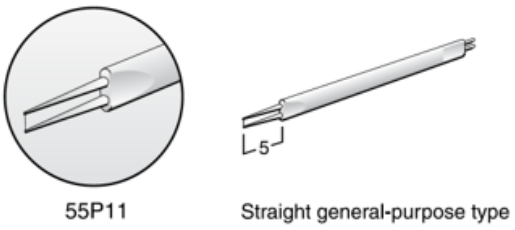


Fig. 2.4 Front hot-wire probe, Dantec 55P11. Image sourced form [18]

The downstream probe, is a Dantec 55P15 model designed for boundary layer studies thanks to its offset prongs (Fig. 2.5). It was mounted via a right-angle probe support, through a slit obtained on the upper Plexiglas surface of the channel, onto a two-axis traverse system. The axis system allowed automatic adjustments both along the streamwise and wall-normal directions, with positioning accuracies of 25 μm and 40 μm, respectively. For the measurement campaigns, the rear probe as well was positioned at different wall-normal distances to survey the evolution of the streamwise velocity with y^+, focusing on positioning it as close as possible to the wall to evaluate u^+ variation and near-wall coherent turbulent structures alteration with the effects of control.

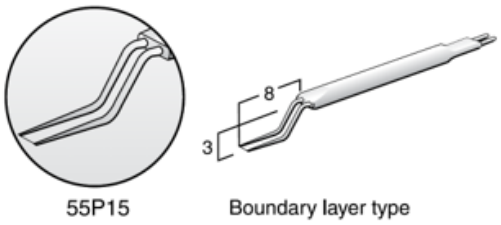


Fig. 2.5 Front hot-wire probe, Dantec 55P15. Image sourced form [19]

Hot-Wire Calibration

Both probes were calibrated before every measurement campaign using the King's Law. The automated calibration procedure was performed using a custom Python script, the full psudocode of which is provided in Appendix A, of the client-serve architecture, as explained later in Chapter 2, Section 2.1.1.

During calibration, it is crucial to position the probes to minimize mutual aerodynamic interference; therefore, the downstream probe was moved as far as possible from the upstream one. Additionally, both sensors were aligned as precisely as possible with the centerline of the channel.

Positioning the Pitot tube at the centerline of the channel, to measure flow streamwise velocity U at that position (where the hot-wires are positioned), calibration starts with the wind tunnel turned off, the anemometers voltage are then recorded as the motor speed is increased in increments of 10 RPM, reaching a value higher than the nominal operating speed used during the measurement campaigns (345 RPM).

The streamwise velocity U, was computed by converting the voltage output of the pressure transducer connected to the Pitot tube into velocity through its calibration constants.

To correlate the measured anemometer voltage with the flow velocity measured with the Pitot tube, King's law was employed:

$$E^2 = A + B \cdot U^n \tag{2.1}$$

where E is the voltage across the anemometer, U is the flow velocity measured by the Pitot tube, and A, B, and n are the calibration constants to be determined.

By performing a non-linear square fit, knowing the anemometer's voltage E and the flow velocity U, the calibration constants are computed.

The anemometer consists of a tungsten wire acting as one arm of a Wheatstone bridge; when the wire is not exposed to any flow, the bridge remains in equilibrium. However, when the sensor is placed in a flow, the bridge balance is disturbed because the wire's resistance depends on its temperature. Convective cooling from the flow reduces the wire's temperature, thus establishing a relationship between flow velocity and the cooling rate of the wire. The sensor is heated by the Joule effect through a current passing through it, resulting in a potential drop, E, across the anemometer.

Once the probes are calibrated, it is possible to relate the flow velocity to the electrical power dissipated by the convective heat exchange between the fluid and the hot-wire, thereby enabling precise measurement of the flow velocity.

2.2 Signal Acquisition

Signal acquisition was managed via a 16-bit National Instruments PCI-MIO-16-XE-10 board installed on a workstation at a 10 Hz sample rate, according to [61, 17].

Data acquisition, signal transmission, and post-processing were managed through a laptop-to-workstation connection over a LAN, utilizing a Python-based client-server architecture communicating via the TCP protocol. Within this framework, the experimental process is driven by the laptop (client), which transmits specific commands to the workstation (server) regarding either signal acquisition, probe calibration, or control parameter updates ect...

This configuration provided a centralized control interface, enabling remote management of the automatic traverse system for the downstream probe directly from the Python shell.

Once an instruction is executed, the client retrieves the feedback or the acquired data buffer, allowing the raw signals to be processed locally on the laptop. Furthermore, the entire acquisition process could be triggered and monitored remotely, ensuring a streamlined experimental workflow where both probe positioning and signal recording were integrated into a single, unified control environment.

2.3 Detection Method

As done by Rebbeck and Choi [6], sweep events were identified in real-time with the streamwise velocity component measured by the front probe by applying the gradient technique to it. The gradient of the streamwise component is computed by an analog differentiator, shown in Fig.2.6, connected to the upstream probe from the anemometer voltage signal; subsequently, a comparator, represented in Fig.2.7, that recognizes sweep events when the gradient exceeds a pre-set threshold. This threshold was determined to obtain a number of sweep events consistent with those produced by the VITA (Variable-Interval Time-Averaging) method as explained in [27] with a threshold of $k = 1.0$ and an averaging time of $T^+ = 10$.



Fig. 2.6 Analog differentiator used during the measurement campaigns to detect sweep events applying the gradient technique on the hot-wire anemometer signal. The BNC input from the hot-wire is on the right, as written on the white tape (HW); while the BNC output to the comparator is positioned on the left.

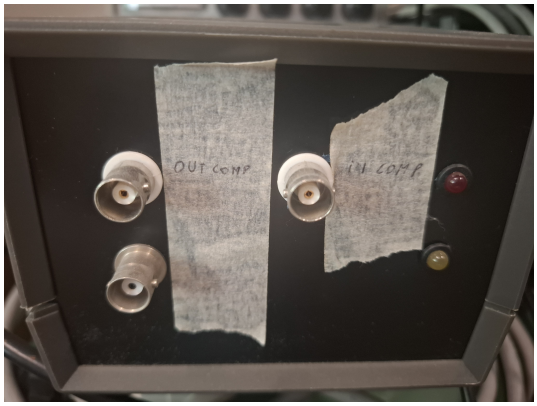


Fig. 2.7 Comparator used during the measurement campaigns to compare the the gradient technique pre-set threshold on the differentiated hot-wire anemometer signal. White tape identifies the input BNC connector (top left) and the output BNC connector (top right).

2.4 Control Procedure

The synthetic jet actuation system and the general layout for opposition control follow the methodology established in [61, 62]. During this thesis research, the experimental set-up was updated, here the changes will be explained with their effects on the control.

2.4.1 First Control Set-up

In the first set-up, upon sweep detection, a square-wave signal (TTL) is sent to an Arduino Uno Rev3 board, which is programmed to take in account the convection time that the detected sweep structure will take from the detection point to the control location and the actuator system latency, by introducing a delay ΔT. The delay can be modified through the workstation thanks to the connection between the two through USB.



Fig. 2.8 Arduino Uno Rev3 board. Image sourced from [20]

After said delay, the microcontroller then sends a TTL to an Agilent 33120A signal generator, shown in Fig. 2.9,connected to the workstation with a R2-232 serial port. The signal generator is triggered and sends a singular-period sine signal characterized by manually pre-set wave parameters, which are:

- Amplitude $\widehat{A}$ in mV.
- Frequency f in Hz.

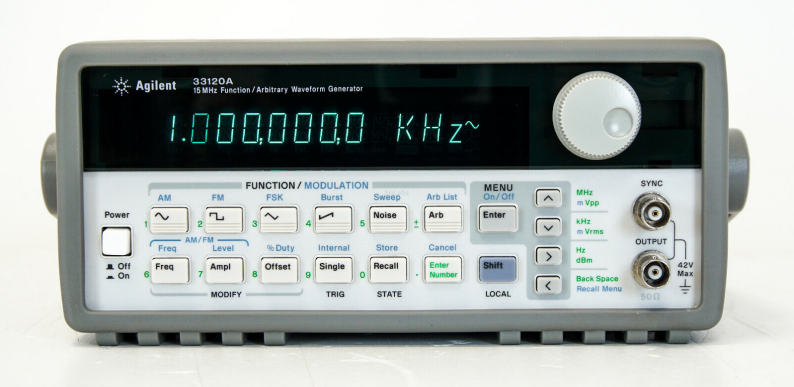


Fig. 2.9 Agilent 33120A signal generator. Image sourced from [21]

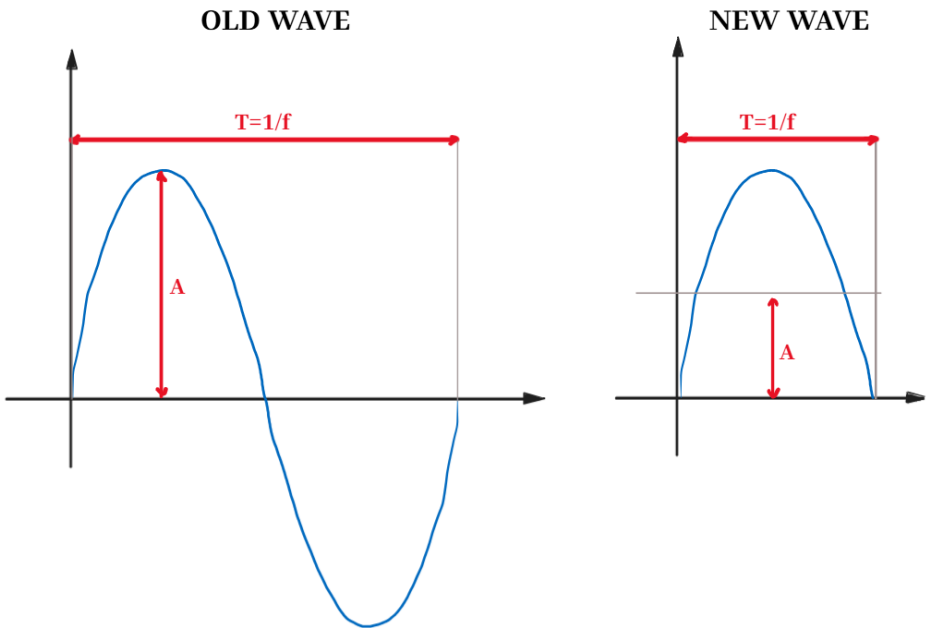


Fig. 2.10 Diagram of the sinusoidal waves used during measurement campaigns and the respective defining parameters, set manually through the signal generator interface. It is possible to note that for the new wave function the amplitude set through the signal generator represents half of the effective amplitude of the function.

During the measurement campaigns, the wave form was changed (as shown in Fig. 2.10), in order to use an actuation law that is alway positive with the objective to have a softer suction phase, and the respective effect was studied (see Chapter 3). The meaning of the wave parameters are represented in figure 2.10. All the parameters were changed in order to study and seek maximum reduction of the sweep intensity (in terms of u^+).

Finally the sine function generated is sent to a Kenwood KAC-5205 amplifier that drives a loudspeaker, which emits a jet according to the sine design through a 1 *mm* diameter orifice, equivalent to 11 viscous units.

As the hot-wire signal is sampled at 10 kHz from the NI DAQ board, the TTL as well is collected in order to have the information of when the sweeps are detected. Sampling the TTL allows easier conditional sampling and ensemble averaging in the post-processing phase. Fig. 2.11 schematizes the complete experimental set-up hardware and logic with the first control set-up implemented.

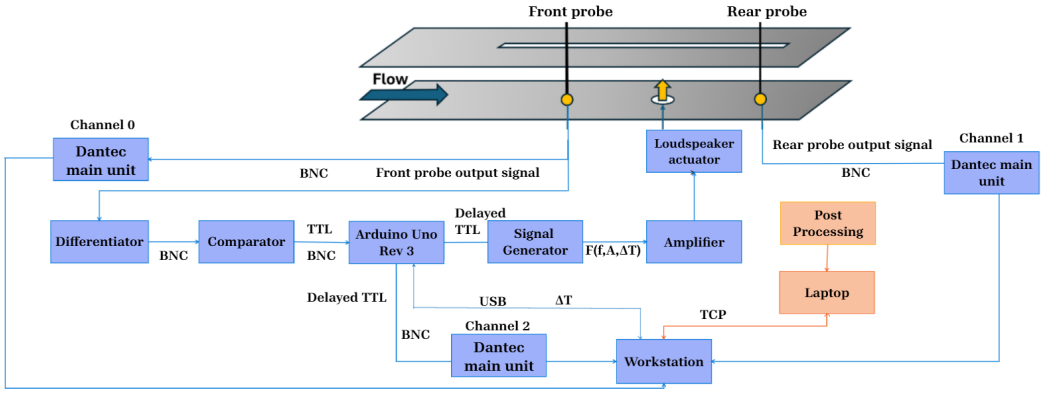


Fig. 2.11 Schematic diagram of the experimental hardware and control logic. The blue-shaded components denote the real-time detection and control loop, while orange blocks represent the client-side architecture and green blocks indicate the flow generation system (motor and inverter). Arrows illustrate the hardware connections and the logical signal flow between instruments. The NI DAQ board is depicted three times to ensure a clear visualization of the signal paths, which end on different channels of the acquisition board.

2.4.2 Second Control Set-up

In the second set-up, upon sweep detection, a square-wave signal (TTL) is sent to an Arduino GIGA controller, in Fig.2.12, connected to the workstation through USB (as in the first control set-up).

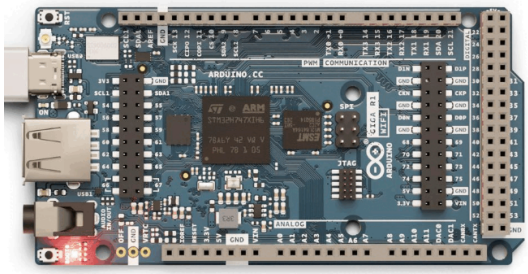


Fig. 2.12 Arduino GIGA microcontroller. Image sourced from [22].

The Arduino GIGA was programmed like the Arduino Uno Rev 3 to introduce a time delay, ΔT, between the detection instant and the control actuation to account for the convection time between the upstream probe and the jet orifice, as well as the actuator response. The delay imposed by the Arduino is a control parameter varied during the measurement campaigns; indeed, the controller is connected to the

workstation via a USB port to automatically adjust the delay time. In addition to delaying the signal, the Arduino GIGA samples the TTL signal and transmits it to the workstation, facilitating the identification of the sweep detection instant during the post-processing phase.

During the several measurement campaigns, the effect of the type of wave issued to the actuator was investigated, to do so the Arduino GIGA controller was also programmed to generate custom triangular waves, defined by:

- T: period/duration of the signal, provided as the inverse of a frequency [s];
- $\widehat{A}$: amplitude provided in [V];
- ΔT: time delay provided in [ms];
- $x\%$: percentage of the triangular wave with a positive slope.

The choice of a triangular actuation law is rooted in the need to investigate the authority that the actuation parameters have on the suction phase of the jet, with the final ojective to make such phase as weak as possible. As will be seen in Chapter 3, a steep and aggressive suction phase causes an excessive amount of fluid to be recalled by the actuator, leading to the creation of a *"synthetic sweep"* that causes a great increase in the streamwise velocity component.

The aforementioned parameters were varied during the measurement campaigns. Fig. 2.13 illustrates the generic triangular wave generated by the controller.

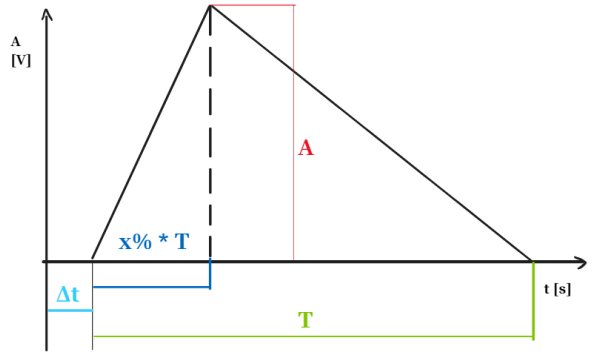


Fig. 2.13 General custom triangular wave issued by the controller.

As for the first control set-up, the generated signal is amplified by a Kenwood KAC-5205 amplifier and sent to a loudspeaker, which emits a jet according to the custom wave design through the control orifice. Fig. 2.14 schematizes the complete experimental set-up hardware and logic with the second control set-up implemented.

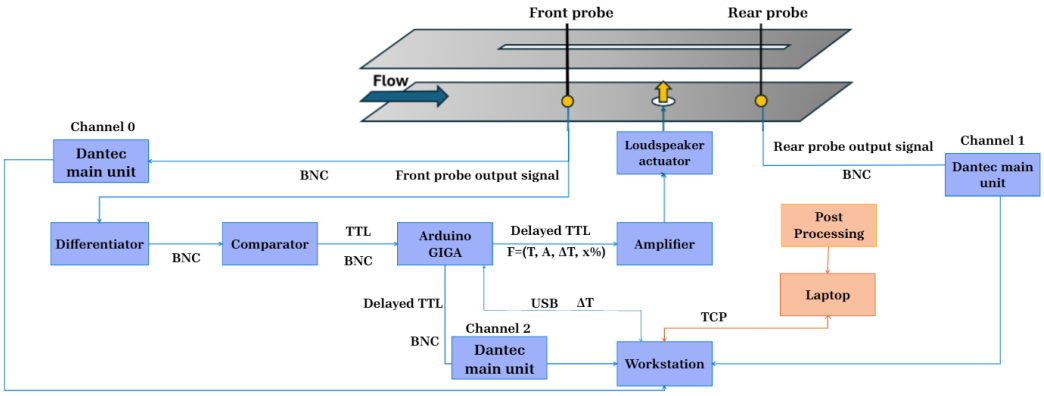


Fig. 2.14 Schematic diagram of the experimental hardware and control logic. The blue-shaded components denote the real-time detection and control loop, while orange blocks represent the client-side architecture and green blocks indicate the flow generation system (motor and inverter). Arrows illustrate the hardware connections and the logical signal flow between instruments. The NI DAQ board is depicted three times to ensure a clear visualization of the signal paths, which end on different channels of the acquisition board. The difference from the first control set-up is that the Arduino Uno Rev 3 microcontroller and the signal generator are replaced by the Arduino GIGA microcontroller.

The program implemented on both the Arduino microcontrollers, for either the first and the second control set-up is created making sure to prevent any loss of detection triggers; incorporating a cyclic buffer[1] of ample capacity, ensuring that every identified event is recorded [61].

For both control setups, the downstream probe measures the controlled flow velocity signal, which is conditionally averaged during post-processing using the TTL information sampled by the Arduino. This allows for optimal centering of the time window for averaging, enabling the visualization of the sweep event. The uncontrolled flow signal is also conditionally averaged to compare the sweep intensity

[1]A circular buffer (or ring buffer) is a fixed-size data structure managed in a cyclic manner, where the end of the buffer wraps around to the beginning.It serves as a temporary storage area that decouples high-speed data acquisition from slower transmission or processing stages, ensuring a continuous data flow without information loss.

between the uncontrolled and controlled cases, thereby evaluating the effectiveness of the implemented control strategy.

2.4.3 Control Actuator Characteristics

For both control setups the jet generated by the speaker is a synthetic jet, following the experimental set-up of Rebbeck and Choi [6], characterized by zero net mass flux into the channel, as explained in Chapter 1, Section 1.2.

The jet cycle consists of a blowing phase, where mass is injected into the channel for a duration corresponding to $T/2$ for the sinusoidal wave (first control set-up) and to $x\% * T$ for the triangular wave, and a suction phase, where air is removed through the orifice for the remainder of the period. Figure 2.15 shows the actuator.

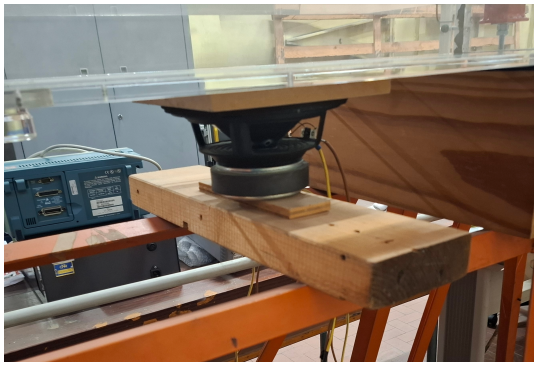


Fig. 2.15 Actuator

2.5 Concluding Remarks

The experimental facility and the methodologies detailed in this chapter establish the robust foundation required for the subsequent active opposition control investigation. By combining a dual hot-wire anemometry system with a real-time gradient detection technique, the set-up achieves the temporal resolution necessary to identify and intercept high-momentum sweep events within the analysed wall-bounded turbulence.

An important improvement of this experimental work lies in the evolution of the control hardware. While the initial configuration, relying on an analog signal

generator and an Arduino Uno Rev3, provided a reliable baseline for conventional sinusoidal actuation, the transition to the Arduino GIGA microcontroller marks a major methodological step forward. This shift to a fully digital control architecture has unlocked the ability to synthesize customized, asymmetric triangular waveforms. As a result, the system gains independent and precise authority over both the duration and intensity of the synthetic jet's blowing and suction phases, a capability that is instrumental in mitigating efficiency losses during the membrane's retraction.

With the physical set-up and the underlying control logic fully established, the next chapter will transition into the core data analysis. It will present the fluid dynamic characterization of the custom synthetic jet under still-air conditions before evaluating its overall effectiveness in modulating u^+ fluctuations and achieving near-wall drag reduction.

Chapter 3

Experimental Campaigns and Data Analysis

This chapter discusses the results obtained during the various experimental campaigns that took place over several months. The analysis starts with the characterization of the actuator performance with no crossflow and proceeds through the preliminary control tests to the final assessment of the opposition control strategy.

3.1 Synthetic Jet Characterization in Still-Air Conditions: 1^{st} Control Set-up

The first phase of the research was dedicated to the characterization of the synthetic jet actuator. A precise understanding of the relationship between the electrical input signal and the resulting velocity field is mandatory to implement an effective real-time opposition control. The ultimate goal of this initial investigation was to find a set of control parameters for the loudspeaker that led to the generation of a jet with a signature comparable to the one obtained by Rebbeck and Choi in their experimental study [6], keeping in mind that their signal issued to the loudspeaker amplifier was a square-wave.

To provide a comprehensive overview of the experimental campaign carried out for the synthetic jet characterization with both the "old-wave" and "new-wave" (see Fig.2.10), a detailed test matrix is presented below. For each of the three investigated

wall-normal positions ($y^+ \approx 7, 18$, and 27), a total of 18 distinct configurations were systematically analyzed. This parameter space covers for both actuation laws, variations in driving frequency (f), nominal input voltage amplitude ($\widehat{A}$), the deployment of a hardware voltage divider circuit. Based on these operating conditions, the driving functions are categorized into the conventional "old-wave" profile and the optimized "new-wave" profile. The complete set of control parameters used for a total of 54 evaluated experimental cases is organized and summarized in Table 3.1.

3.1.1 Continuous Acquisition and Statistical Characterization

To characterize the synthetic jet behavior and ensure the reliability of the turbulent quantities measured within the near-wall turbulent region, a series of continuous acquisition campaigns was conducted.

The rear hot-wire probe was aligned in the streamwise direction with the jet orifice by means of a dedicated Python-based control framework (see Appendix C). With the wind tunnel turned off, the streamwise and spanwise positions were calibrated by manually traversing the probe while the loudspeaker was driven by a constant-rate wave function. During this procedure, the hot-wire signal was monitored in real-time via the National Instruments Measurement and Automation Explorer (NI-MAX). The probe was considered successfully positioned within the potential core of the jet when the signal detected by the probe reached its maximum value.

The experimental procedure, managed through the automated Python framework (see Appendix B), is organized as follows:

1. **Ambient parameters and scaling:** Environmental conditions were monitored at the start of each test (on the 14 of February 2025 $T = 17°$C, $P = 99663$ Pa). These values were used to update the fluid properties and determine the friction velocity $u_\tau = 0.1611$ m/s. All subsequent velocity measurements were normalized in inner wall units ($u^+ = u/u_\tau$) to ensure consistency across different experimental runs.

2. **Actuation control:** The synthetic jet was driven at varying control parameters, ranging as follows:

   (a) **Frequency**: $(30, 60, 110)$ Hz.

(b) **Voltage divider circuit**: to achieve high-precision control over the jet intensity, a voltage divider circuit is employed. Measurements were taken with the divider circuit either activated, resulting in halving of the wave function amplitude, or turned off. Since the voltage divider circuit added significant noise in the signal, due to the fact that it wasn't grounded, soon after this initial campaign it was eliminated.

(c) **Amplitude**: identified as V_{pp} in the script (B) and corresponding to $\widehat{A}$ in Fig. 2.10, it ranged between $(50, 100)$ mV, being halved whenever the voltage divider circuit was activated.

3. **Sampling parameters**: Data acquisition was performed at a sampling frequency of $f_s = 10$ kHz and a sampling time of $t_{sample} = 20$ s.

4. **Wall-normal distance**: three wall normal distances were investigated during this first measurements, $y^+ = (7, 18, 27)$ in order to understand the variation of the jet profile and intensity moving away from the wall.

Post processing of the experimental data was done through a Python script and the following analysis were done:

- **Data initialization and calibration**: loading of the raw voltage signals and conversion into velocity values (u) using the King's law calibration parameters.
- **Scaling**: conversion of the velocity and time scales into inner wall units (v'^+ and t^+) based on the viscous scales (u_τ, l_τ, t_τ) calculated from ambient conditions.
- **Peak detection**: identification of the individual jet actuation events using a peak-finding algorithm, with a prominence threshold set to 15% of the maximum signal intensity to ensure trigger robustness.
- **Conditional sampling**: extraction of temporal windows centered around each detected peak, with a range defined between 30% of the expected period before the peak and 120% after it.
- **Ensemble averaging**: computation of the mean conditioned velocity profile ($\overline{v'}^+$) by averaging all the extracted cycles for each experimental configuration.

- **Parametric data management**: organization of the processed results (mean profiles, coordinates, and actuation parameters) into a structured database (*pandas* [63] DataFrame) for systematic comparison.

Table 3.1 Summary of the experimental test matrix for the synthetic jet characterization in still-air conditions using the sinusoidal ("old-wave") and the half-sine ("new-wave") waveforms.

y^+	**Amplitudes($\widehat{A}$) [mV]**	**Freq. (f) [Hz]**	**Divider**	**Waveforms**
7	25, 50, 100	30, 60, 110	OFF, ON[a]	"old-wave", "new-wave"
18	25, 50, 100	30, 60, 110	OFF, ON[a]	"old-wave", "new-wave"
27	25, 50, 100	30, 60, 110	OFF, ON[a]	"old-wave", "new-wave"

[a] If the voltage divider circuit is turned on the effective voltage amplitude will be $\widehat{A}_{eff} = \widehat{A}/2$

3.1.2 Plots of All Jet Velocity Profiles with Highlighted Peaks

To validate the experimental signal quality and ensure the robustness of the post-processing routine, a preliminary visual inspection of the velocity traces acquired in still-air conditions was conducted. This Section presents the time-history profiles of the wall-normal velocity component, v'^+, measured within the potential core of the synthetic jet across the full range of tested actuation frequencies and generator voltage amplitudes.

The following plots, Figs. 3.1, 3.2, 3.3, illustrate the normalized velocity in inner wall units as a function of the dimensional time t in *ms*, for three different wall-normal distances ($y^+ = [7, 18, 27]$). Each time series includes red *"x"* markers identifying the local maxima detected by the peak-detection algorithm. This visualization serves as a critical verification step, confirming that the algorithm accurately captures every actuation cycle, a fundamental requirement for the subsequent ensemble-averaging and conditional sampling phases.

It can be observed that the jet intensity is higher in the immediate vicinity of the wall and the orifice, where v'^+ reaches its maximum values. As the distance from the surface increases, the wall-normal velocity undergoes an attenuation and exhibits greater variability between individual pulses. For instance, at $y^+ = 27$ (Fig. 3.3), the

peak velocities show more pronounced cycle-to-cycle fluctuations compared to the highly consistent values observed at $y^+ = 7$ (Fig. 3.1).

Furthermore, these temporal traces provide a direct observation of how control parameters, such as actuation frequency and waveform shape, influence the individual jet structure. The clear identification of the peaks demonstrates the stability of the experimental set-up and the absence of significant secondary disturbances or signal noise, providing a reliable foundation for the statistical characterization of the jet behavior.

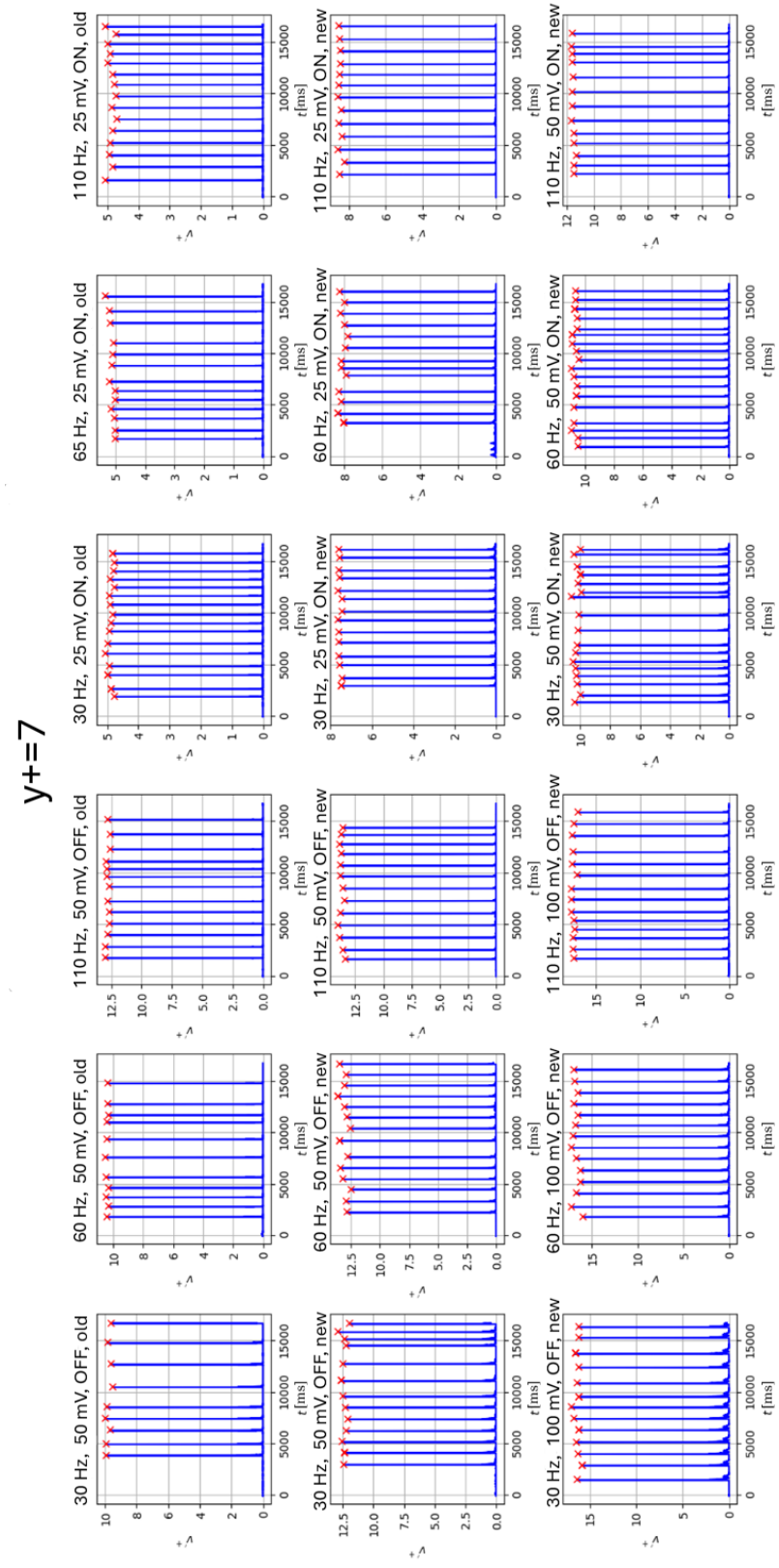


Fig. 3.1 Time-history of the wall-normal velocity signal v'^{+} at a wall distance of $y^{+} = 7$. Red "x" markers indicate the peaks identified by the detection algorithm. The title of each subplot reports the specific actuation parameters in the format [Frequency (Hz), Amplitude (mV), Divider flag (OFF, ON), Actuation law (old or new)]. The reported amplitudes are already halved for cases with the divider circuit turned on. Closer to the wall the maximum wall normal velocity generated by the synthetic jet is higher than further away from the wall.

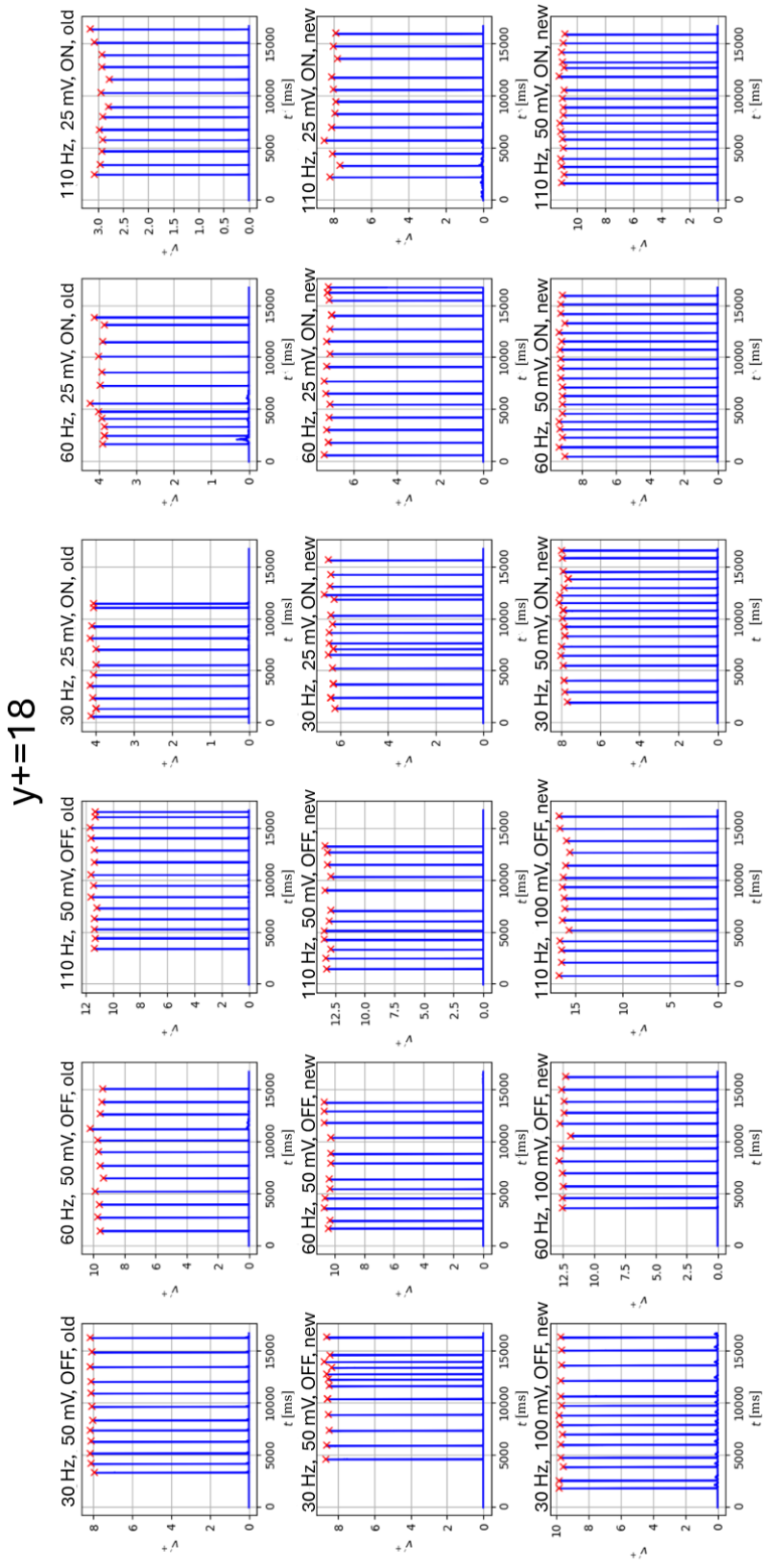


Fig. 3.2 Time-history of the wall-normal velocity signal v'^{+} at a wall distance of $y^{+} = 18$ for different experimental configurations. Red "x" markers highlight the detected peaks used for the subsequent conditional sampling. The title of each subplot reports the specific actuation parameters in the format [Frequency (Hz), Amplitude (mV), Divider flag (OFF, ON), Actuation law (old or new)]. The reported amplitudes are already halved for cases with the divider circuit turned on.

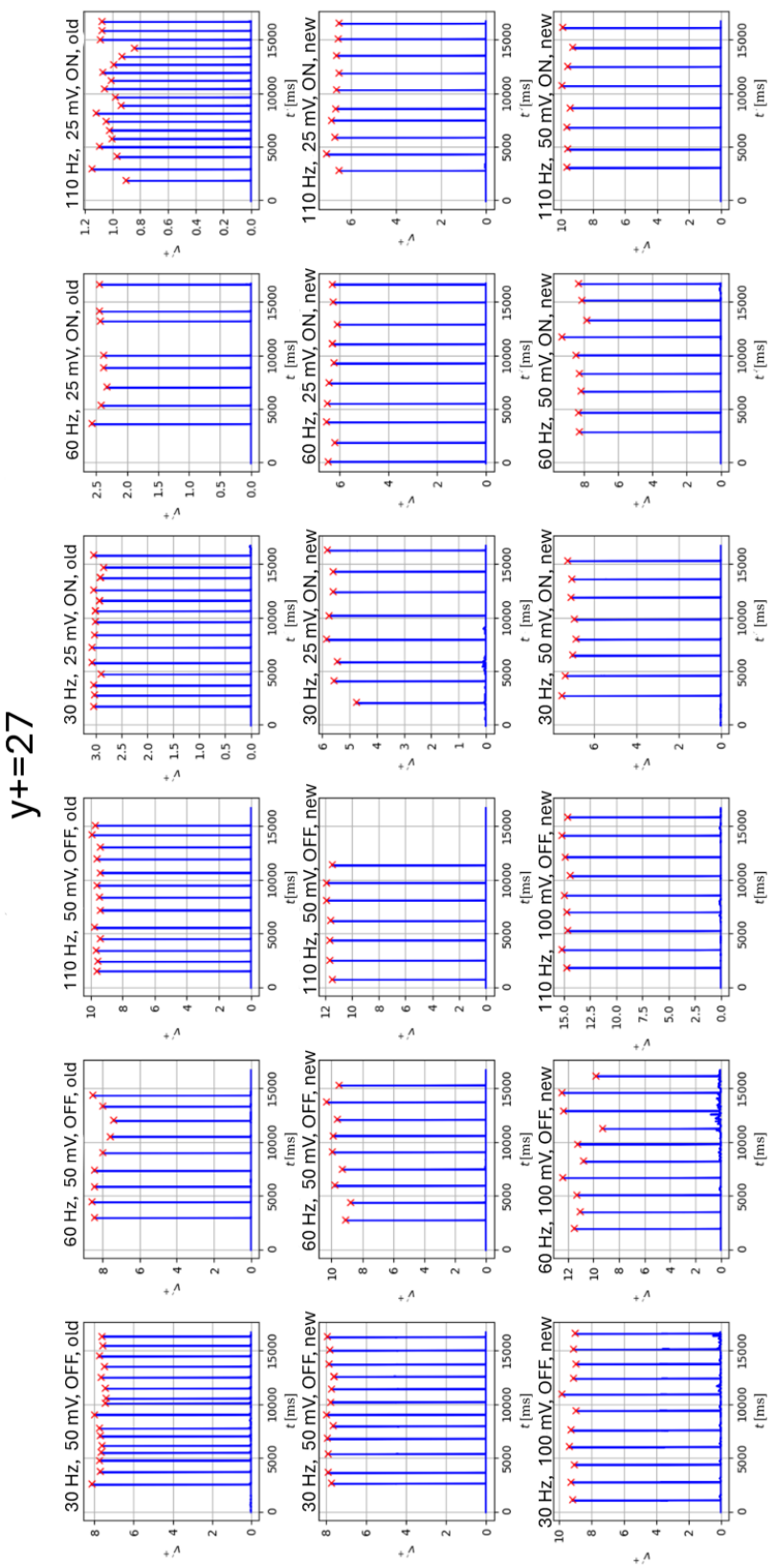


Fig. 3.3 Time-history of the wall-normal velocity signal v'^{+} at a wall distance of $y^{+} = 27$. Red "x" markers identify the peaks for various actuation cases. The title of each subplot reports the specific actuation parameters in the format [Frequency (Hz), Amplitude (mV), Divider flag (OFF, ON), Actuation law (old or new)]. The reported amplitudes are already halved for cases with the divider circuit turned on. The visualization validates the robustness of the peak-detection algorithm even as the jet signature evolves and attenuates with increasing distance from the orifice.

3.1.3 Conditionally Averaged Jet Velocity Profiles for All Cases

Once the individual actuation cycles were identified and validated through the peak-detection algorithm, the ensemble-averaging technique was applied to characterize the mean behavior of the synthetic jet. This procedure involves synchronizing all detected jet velocity profiles with respect to their maximum intensity point and computing the average at each time step. The resulting profiles, denoted as $\overline{v'}^{+}$, filter out stochastic fluctuations and noise, providing a deterministic representation of the jet's temporal evolution for each experimental configuration.

The following figures illustrate the mean conditioned profiles for the three measured wall-normal positions $y^{+} = (7, 18, 27)$. These plots allow for a direct comparison of the influence of actuation parameters such as frequency, voltage amplitude, and waveform, on the jet's morphology.

By observing the profiles across different y^{+} values, it is possible to track the development of the jet as it propagates: while the signal is sharp and intense near the orifice, it undergoes progressive spatial redistribution and attenuation as the distance from the wall increases. It's possible to note that the overall shape obtained of the jet profile for the different parameters is similar to the one obtained by Rebbeck and Choi [5, 6] in their experimental studies (see Fig. 1.23). However, it's important to underline that the wave function employed by Rebbeck ad Choi [6] was not sinusoidal but a square-wave signal.

As their [6] jet profile, the overall jet profiles visible in Figs. 3.4, 3.5, 3.6 present indeed an initial steep quasi-linear blowing phase, ending when the membrane of the loudspeaker reaches the maximum deformation upwards, a following $\overline{v'^{+}}$ reduction as a consequence of membrane relaxation and lastly a blowing phase, more or less intense depending on the voltage amplitude issued to the amplifier. As pointed out by Rebbeck and Choi [6] the suction phase is identified as a positive velocity by the hot-wire, due to its inability to discern flow direction. The maximum wall-normal viscous velocity fluctuation $\overline{v'^{+}}$ attests between 8 and 12, except for when the amplitude set by the loudspeaker (counting the effect of the voltage divider circuit) was of $25mV$, in those cases the maximum reached approximately values ranging between 3 and 6. When the frequency was set to 30 Hz, yielding a duration of approximately 33 ms, the blowing phase presented a duration of around $t^{+} \approx 40$, as in [6].

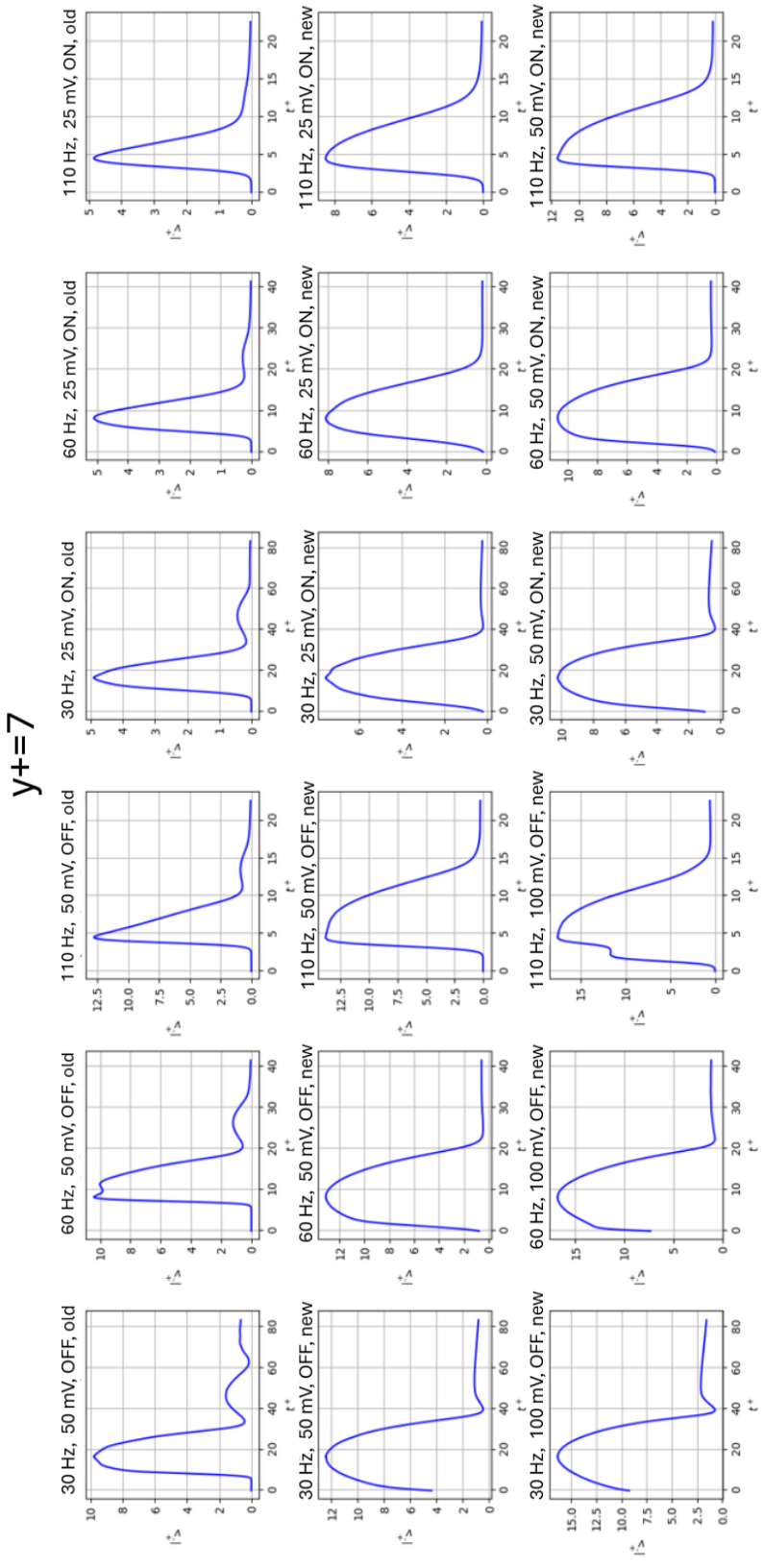


Fig. 3.4 Ensemble-averaged wall-normal velocity profiles $\overline{v}^+$ at $y^+ = 7$. Each curve represents the mean of all detected cycles for a specific test case. The title of each subplot reports the specific actuation parameters in the format [Frequency (Hz), Amplitude (mV), Divider flag (OFF, ON), Actuation law (old or new)]. The reported amplitudes are already halved for cases with the divider circuit turned on. At this coordinate, the jet pulses exhibit the highest peak intensity and a well-defined temporal structure.

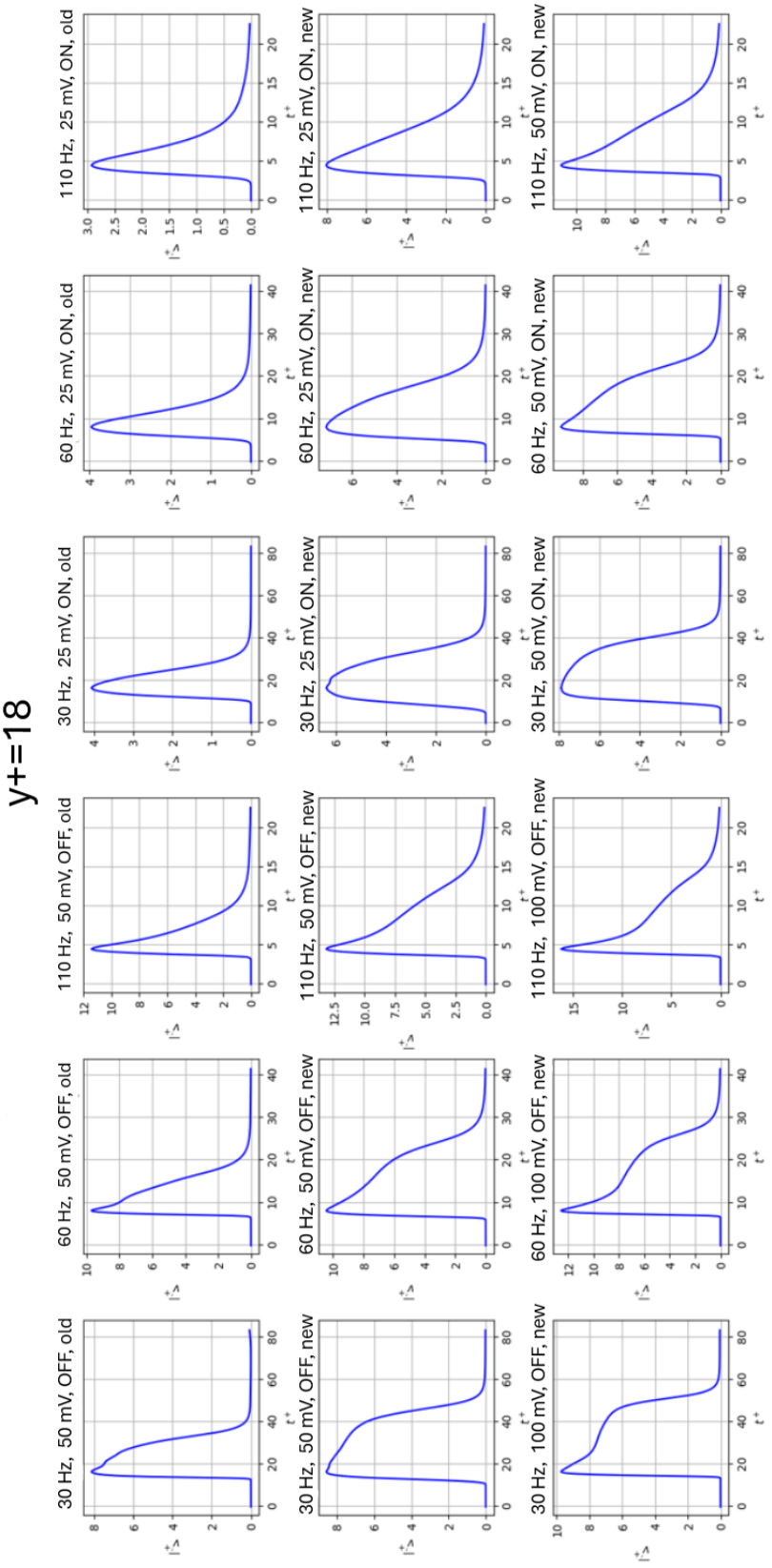


Fig. 3.5 Ensemble-averaged wall-normal velocity profiles $\overline{v'^+}$ at an intermediate wall distance of $y^+ = 18$. The title of each subplot reports the specific actuation parameters in the format [Frequency (Hz), Amplitude (mV), Divider flag (OFF, ON), Actuation law (old or new)]. The reported amplitudes are already halved for cases with the divider circuit turned on. The plots show the initial stages of jet diffusion and peak attenuation compared to the near-wall measurements (at $y^+ = 7$).

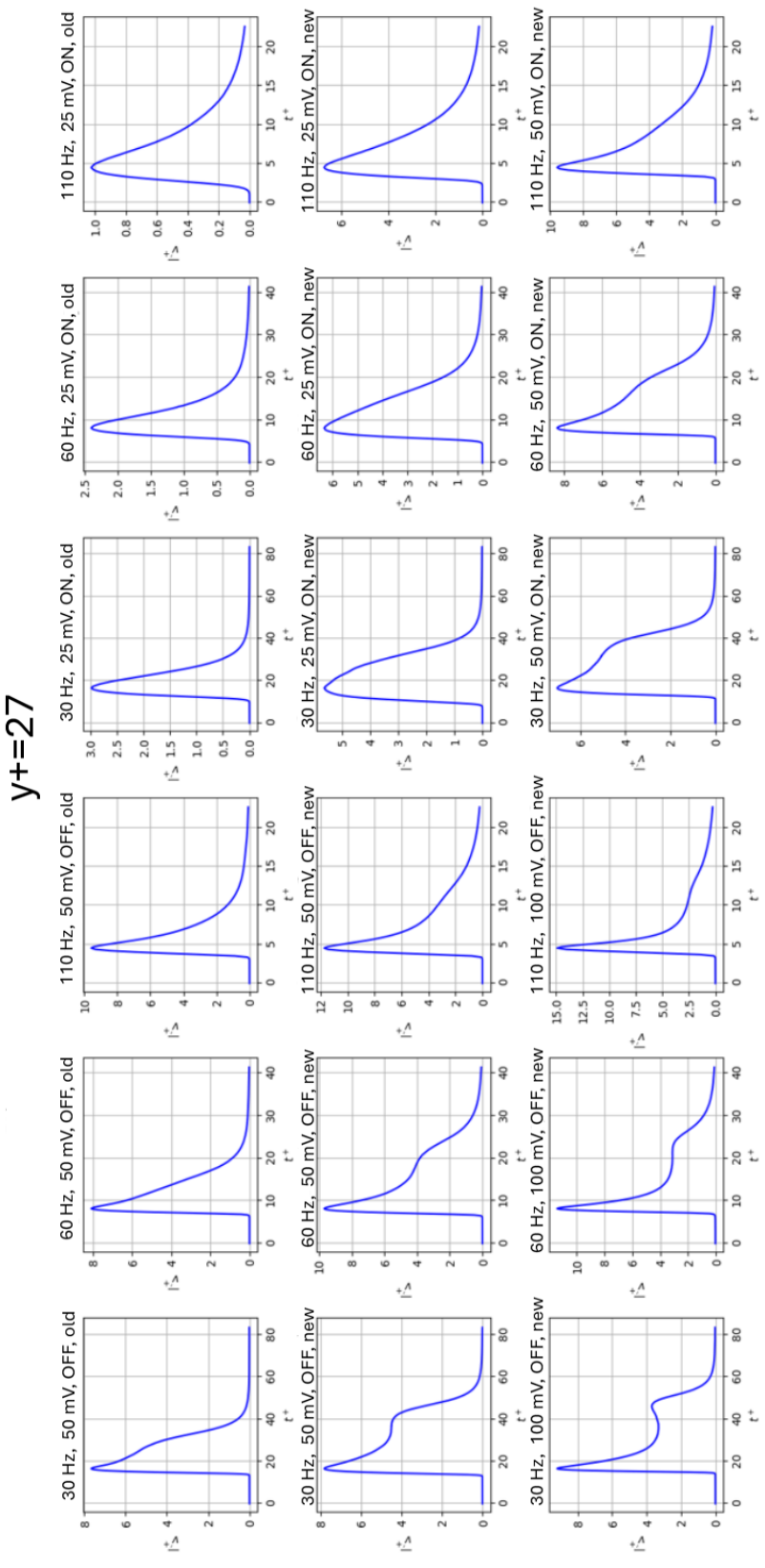


Fig. 3.6 Ensemble-averaged velocity profiles $\overline{v}^+$ at the furthest measured distance ($y^+ = 27$). The title of each subplot reports the specific actuation parameters in the format [Frequency (Hz), Amplitude (mV), Divider flag (OFF, ON), Actuation law (old or new)]. The reported amplitudes are already halved for cases with the divider circuit turned on. The profiles appear broader and characterized by lower maximum velocities, reflecting the momentum transfer and the evolution of the synthetic jet structure as it interacts with the surrounding still-air.

3.1.4 Effect of Waveform Optimization (Old vs. "new-wave")

Initially, the speaker was driven by a standard sinusoidal signal, as explained in 2.4.1, referred to as the *"old-wave"*. However, to better match the typical temporal signature of the detected sweep events, reduce the effect of the suction phase, to maximize the effectiveness of the synthetic jet and optimize the momentum injection into the near-wall turbulent flow, a custom actuation law (*"new-wave"*), consisting of half sinusoidal wave (see Fig. 3.7), was implemented to reduce the duration of the suction phase.

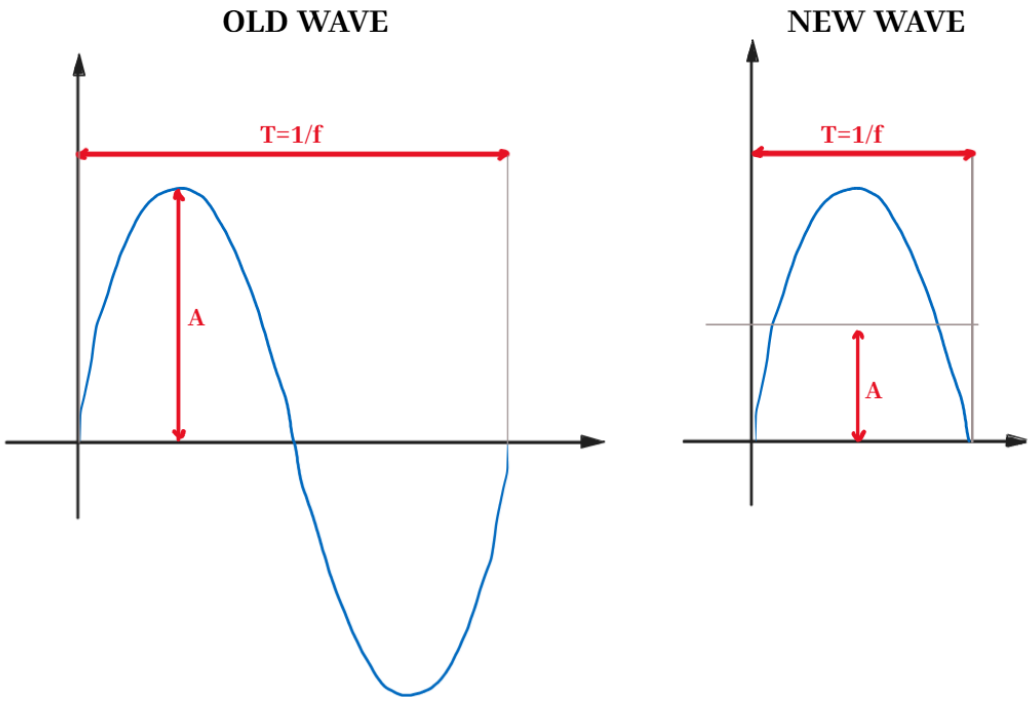


Fig. 3.7 Comparison between the electrical signal of the traditional sinusoidal wave ("old-wave") and the half-sine actuation law ("new-wave") implemented via the signal generator. It is possible to note that for the "new-wave" function the amplitude set through the signal generator represents half of the effective amplitude of the function.

Then with the updated control set-up, 2.4.2, with the firmware uploaded on the Arduino GIGA microcontroller, it was possible to create a custom triangular wave (see Fig.2.13) to have more control on the steepness of the blowing and the suction phases, the jet profile study with this new custom wave will be explained in the following Section 3.2.

Figs. 3.8, 3.9, 3.10 present the comparison , accross the three investigated wall-normal coordinates $y^+ = (7, 18, 27)$ between the ensemble averaged wall-normal velocity $\overline{v'^+}$ profiles created by the jet issued by the new half-sine driving waveform (on the right) and the baseline signal (referred to as the "old-wave" on the left). The comparison was conducted maintaining the same base actuation parameters, $[f = 60\,Hz,\ \widehat{A} = 50\,mV,\ Divider = OFF]$.

The comparative analysis of the conditioned velocity profiles reveals that the implementation of the "new-wave" form significantly alters the jet's profile and temporal characteristics. Most notably, the modified input signal leads to a broader temporal duration of the jet, featuring a prolonged blowing phase and a higher maximum wall-normal velocity ($\overline{v'^+}$).

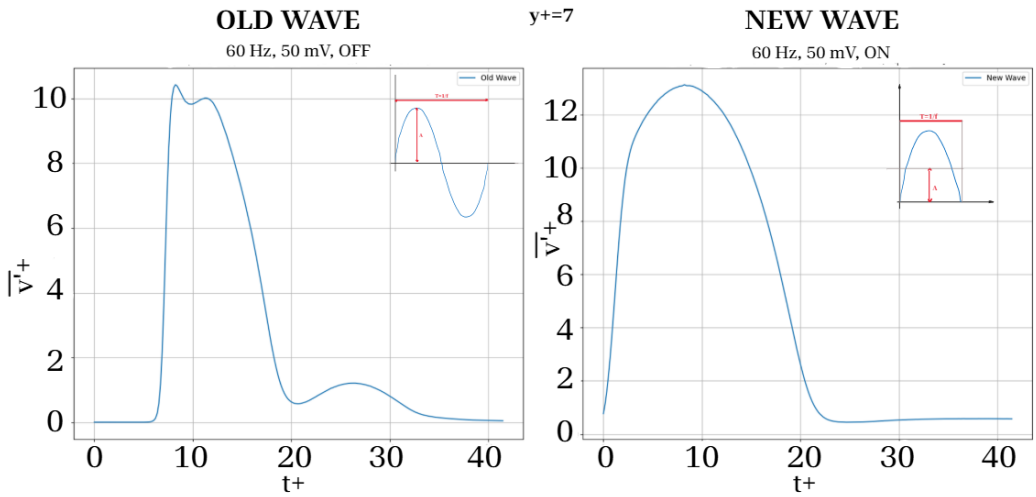


Fig. 3.8 Comparison between the old and new driving waveforms at $y^+ = 7$. The "new-wave" profiles exhibit a higher peak velocity and a significantly reduced negative velocity region (suction effect) immediately before and after the main jet peak velocity, due to the restricted retraction of the speaker membrane.The title of each subplot reports the specific actuation parameters in the format [Frequency (Hz), Amplitude (mV), Divider flag (OFF, ON), Actuation law (old or new)]. The reported amplitudes are already halved for cases with the divider circuit turned on.

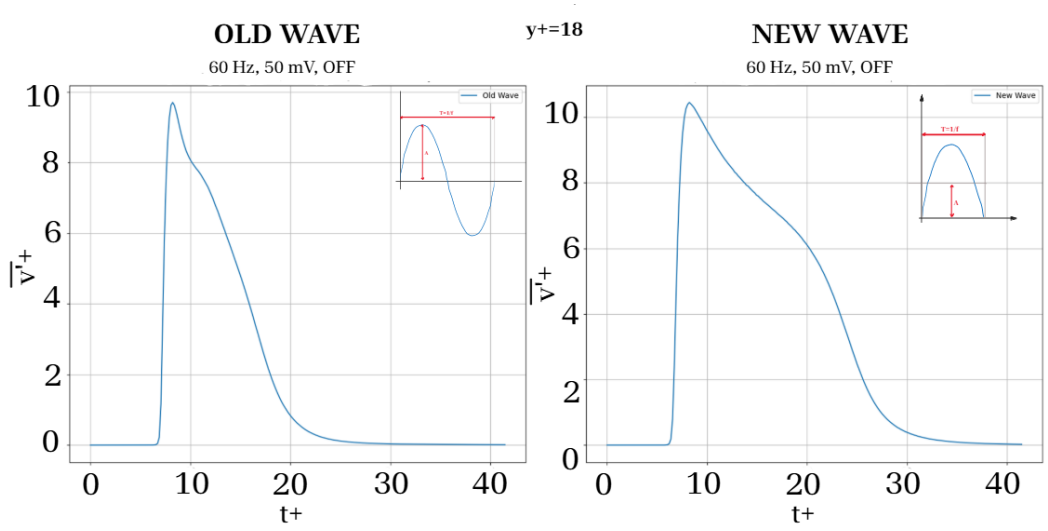


Fig. 3.9 Velocity profiles comparing the two waveforms at $y^+ = 18$. The increased temporal duration and the higher maximum intensity of the jet generated by the "new-wave" are visible. The title of each subplot reports the specific actuation parameters in the format [Frequency (Hz), Amplitude (mV), Divider flag (OFF, ON), Actuation law (old or new)]. The reported amplitudes are already halved for cases with the divider circuit turned on.

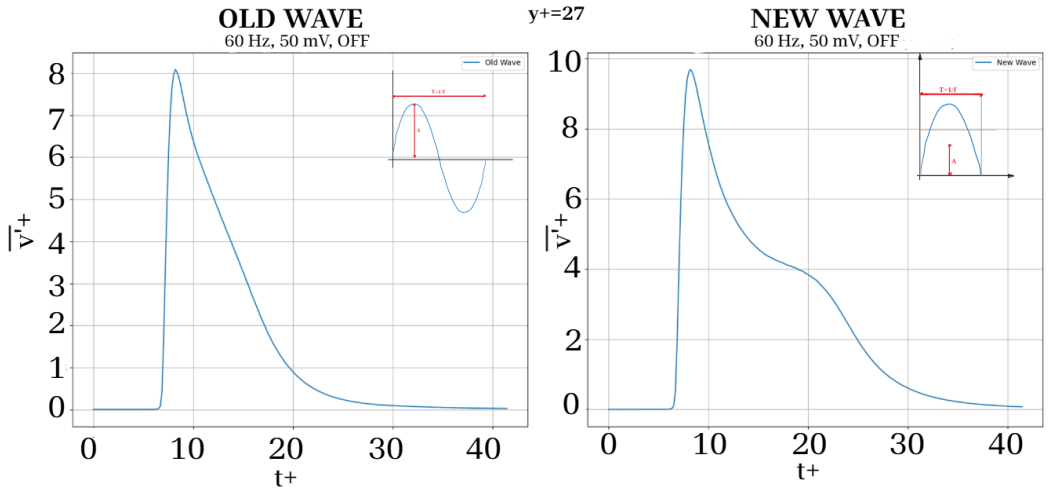


Fig. 3.10 Waveform comparison at the furthest wall-normal distance $y^+ = 27$. The profiles highlight the reduction in the deceleration slope following the velocity peak for the "new-wave". This trailing-edge elongation is particularly evident for high-voltage amplitude cases and demonstrates the altered temporal evolution of the modified jet. The title of each subplot reports the specific actuation parameters in the format [Frequency (Hz), Amplitude (mV), Divider flag (OFF, ON), Actuation law (old or new)]. The reported amplitudes are already halved for cases with the divider circuit turned on.

This amplification can be associated to the electrical properties of the modified signal. Specifically, for the same voltage value set on the signal generator, the new half-sine waveform effectively results in a doubled peak amplitude compared to the baseline case. This increased maximum voltage amplitude supplied to the loudspeaker yields a more vigorous actuation, which in turn generates a higher wall-normal jet velocity. However, the relationship between the input signal and the output velocity is non-linear: a doubled input amplitude does not proportionally translate into a doubled jet intensity.

Furthermore, the near-wall measurements ($y^+ = 7$) (see Figs. 3.8, 3.4) demonstrate a marked reduction in the suction effect across all tested actuation frequencies, as desired. Physically, this improvement is linked to the loudspeaker membrane dynamics: the fact that the new-wave doesn't go into the negatives, prevents the membrane from retracting significantly past its resting position. As a result, the reverse flow of fluid towards the orifice during the suction phase of the synthetic jet cycle is effectively mitigated.

Experimental evidence (documented in the preliminary surveys at Fig. 3.8), demonstrated that near the wall the "new-wave" triggers a jet that maintains a more regular and repeatable shape as the frequency increases. In contrast, the "old-wave" exhibited significant distortions at higher frequencies, particularly when operated without a voltage divider circuit. It's in fact evident in Figs. 3.4, 3.8 that at higher values of $\widehat{A}$ and frequencies, the jet profile shows a irregular behaviour with an oscillation either at its peak or during the negative-slope phase of the profile.

As the distance from the wall increases ($y^+ = 18$ and $y^+ = 27$), a distinct morphological change in the velocity profile becomes apparent. Specifically, the deceleration phase following the velocity peak exhibits a reduced and irregular slope, indicating a more gradual decay of the jet. This trailing elongation becomes more pronounced with increasing distance from the wall and higher generator voltage amplitudes (e.g. at 100 mV), while it tends to diminish at higher actuation frequencies (see Figs. 3.5, 3.6, 3.9, 3.10). This behavior is a direct consequence of the fact that the membrane movement with the "new-wave" function stays always above the resting position, which prolongs the positive actuation phase and alters the interaction of the expelled fluid with the surrounding still-air.

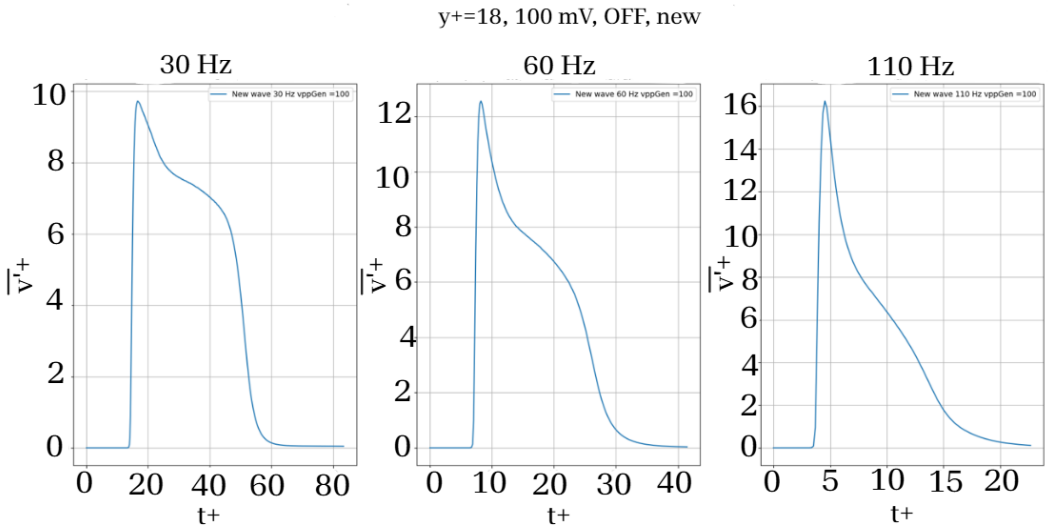


Fig. 3.11 Ensemble averaged jet velocity profiles at $y^+ = 18$ and for $\widehat{A} = 100\ mV$. All the profiles are result of the "new-wave" function, from left to right all control parameter remain the same except for the frequency that increases $(30,\ 60,\ 90)\ Hz$. At high voltage amplitudes and lower frequencies, further away from the wall the profile presents the birth of a second peak after the maximum velocity is reached. The effect is more evident with increasing distance from the wall and decreasing frequencies.

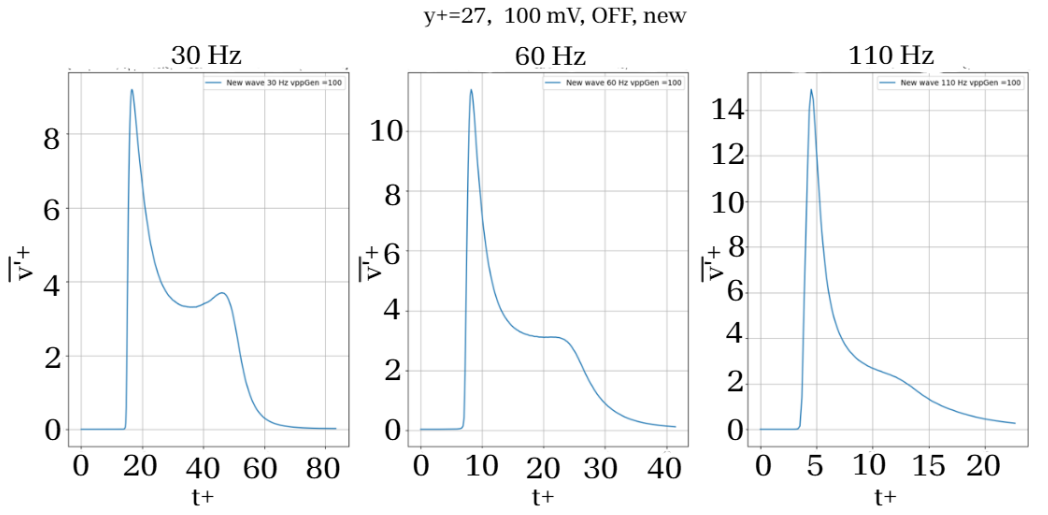


Fig. 3.12 Ensemble averaged jet velocity profiles at $y^+ = 27$ and for $\widehat{A} = 100\ mV$. All the profiles are result of the "new-wave" function, from left to right all control parameter remain the same except for the frequency that increases $(30,\ 60,\ 90)\ Hz$. At high voltage amplitudes and lower frequencies, further away from the wall the profile presents the birth of a second peak after the maximum velocity is reached. The effect is more evident with increasing distance from the wall and decreasing frequencies.

Further away from the wall the velocity profile sees a reduction in slope and even a slope inversion after the peak, that increases with distance from the wall and the signal generator voltage amplitude but decreases with frequency. This effect is visible with the "new-wave" and especially in the case where the $\widehat{A} = 100\ mV$,(see Figs. 3.11, 3.12).

In Figs. 3.11, 3.12 is possible to see that, during the membrane relaxation phase, not only the slope decreases but it increases reaching a new local maximum of $\overline{v'^{+}}$. The increase in slope becomes extreme when the voltage amplitude is $100\ mV$, hence doubled compared to the other cases. As just said, 30 Hz and 60 Hz this effect causes the birth of a second peak in the velocity profile measured at the most distant position from the wall. With the "old-wave" this behavior is way more subtle if not inexistent.

3.1.5 Voltage Amplitude and Divider Influence

Before detailing the influence of the voltage divider circuit, it must be pointed out that the voltage divider circuit was not connected to a common ground during the acquisition of the measurements discussed in this Section.

Voltage Divider Circuit Effects on the Jet Profile With the "Old-Wave" Function

To fully characterize the response of the actuation system, the influence of the input voltage amplitude ($V_{pp} = \widehat{A}$) and the deployment of a voltage divider circuit were investigated. This analysis initially focuses on the baseline actuation condition, utilizing the conventional waveform ("old-wave") across the selected wall-normal positions.

Figs. 3.13, 3.14, and 3.15 present the conditionally sampled, ensemble-averaged jet velocity profiles ($\overline{v'^{+}}$) at wall-normal distances of $y^{+} \approx 7, 18$, and 27, respectively. In each figure, the left plot illustrates the jet velocity profile generated without the voltage divider circuit, while the right plot depicts the profile with the voltage divider circuit activated, maintaining all other control parameters constant. Consequently, when the divider is engaged, the voltage amplitude supplied to the loudspeaker amplifier is halved compared to the baseline actuation.

A primary effect observed when employing the voltage divider circuit is the mitigation of the near-wall suction phase intensity (as seen in Fig. 3.13), although it remains less effective in this regard compared to the implementation of the new waveform. Additionally, the voltage divider circuit induces a more regular jet velocity profile around the peak and during the membrane relaxation phase, effectively eliminating abrupt slope variations (Fig. 3.14).

Furthermore, while the activation of the voltage divider circuit predictably reduces the maximum velocity due to the decreased effective voltage amplitude fed to the speaker, the overall temporal duration of the jet remains consistent with the baseline case. Crucially, halving the input voltage amplitude via the divider does not result in a proportional halving of the maximum $\overline{v'^{+}}$ achieved. This non-linear attenuation is particularly pronounced at greater distances from the wall (Figs. 3.14 and 3.15).

The voltage divider circuit is primarily employed to attenuate the signal and allow finer control over the energy fed to the loudspeaker. However, the experimental results indicate that the relationship between the nominal generator voltage, the attenuated electrical signal, and the resulting wall-normal average jet velocity fluctuation $\overline{v'^{+}}$ is far from strictly linear.

Physically, this discrepancy stems from the mechanical response of the loudspeaker mechanism when driven by the baseline sine wave and the noise induced by the divider. The impedance of the speaker circuit, combined with the mechanical response of the membrane, introduces a damping effect that alters the expected scaling factor of the voltage divider circuit. Consequently, a specific voltage amplitude reduction does not result in a perfectly proportional reduction of the peak jet intensity. This systematic divergence underscores the necessity of a rigorous calibration framework, as the input-output efficiency of the synthetic jet generator is strongly dependent on the operational regime and the specific hardware attenuation path selected.

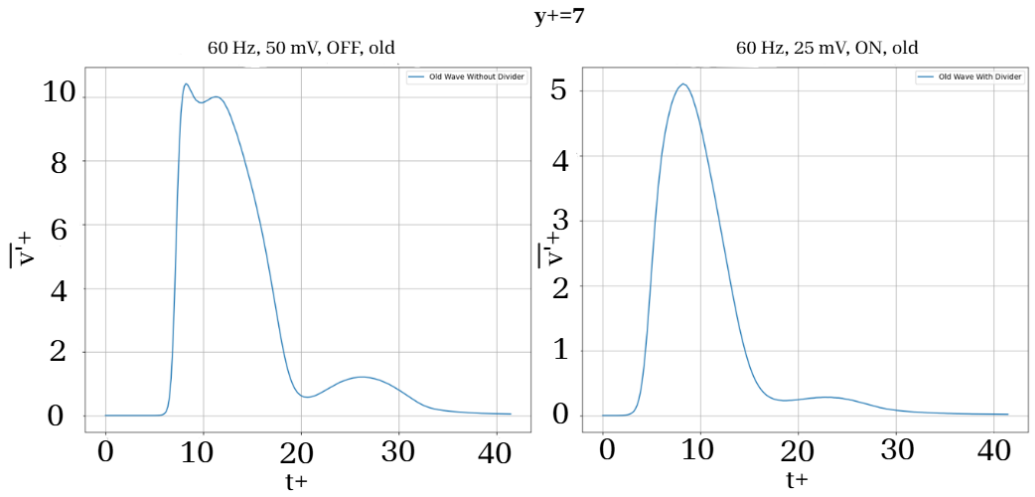


Fig. 3.13 Conditioned, ensemble-averaged velocity profiles $\overline{v'^+}$ at $y^+ = 7$, comparing the baseline waveform ("old-wave") without the voltage divider circuit (left) and with the voltage divider circuit activated (right). The comparison highlights the reduction of the suction intensity when the divider is employed. The title of each subplot reports the specific actuation parameters in the format [Frequency (Hz), Amplitude (mV), Divider flag (OFF, ON), Actuation law (old or new)]. The reported amplitudes are already halved for cases with the divider circuit turned on.

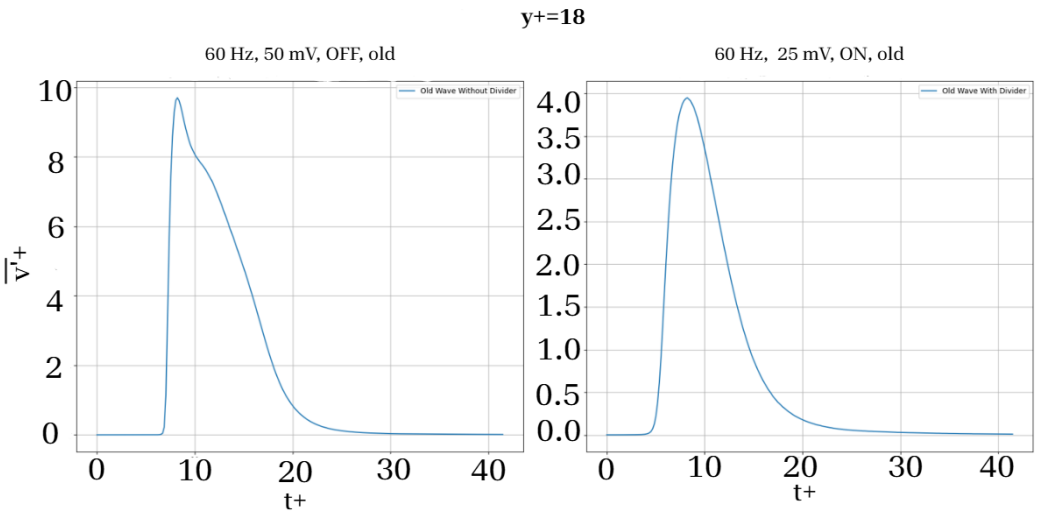


Fig. 3.14 Conditioned, ensemble-averaged velocity profiles $\overline{v'^+}$ at $y^+ = 18$, comparing the baseline waveform without (left) and with (right) the voltage divider circuit. This comparison highlights the non-linear scaling between the voltage amplitude supplied to the loudspeaker and the maximum velocity peak achieved by the jet. The title of each subplot reports the specific actuation parameters in the format [Frequency (Hz), Amplitude (mV), Divider flag (OFF, ON), Actuation law (old or new)]. The reported amplitudes are already halved for cases with the divider circuit turned on.

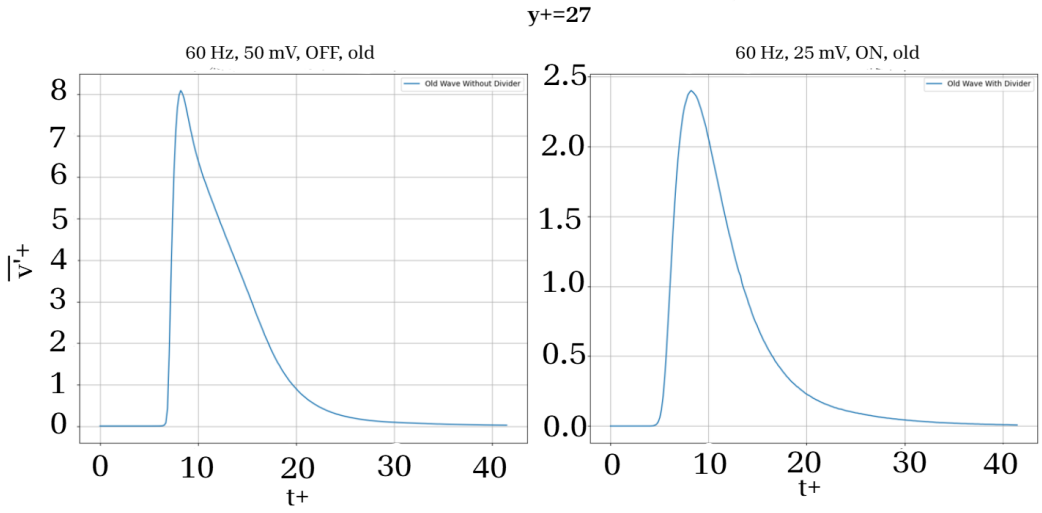


Fig. 3.15 Conditioned, ensemble-averaged velocity profiles $\overline{v'^+}$ at $y^+ = 27$, comparing the baseline waveform without (left) and with (right) the voltage divider circuit. Similar to the previous wall-normal position, the non-linear scaling of the peak velocity with respect to the attenuated input voltage amplitude is evident. The title of each subplot reports the specific actuation parameters in the format [Frequency (Hz), Amplitude (mV), Divider flag (OFF, ON), Actuation law (old or new)]. The reported amplitudes are already halved for cases with the divider circuit turned on.

Voltage Divider Circuit Effects on the Jet Profile with the "New-Wave" Function

Subsequently, the combined effects of the voltage divider circuit and the modified "new-wave" function were investigated. Figs. 3.16, 3.17, and 3.18 contrast the ensemble-averaged velocity profiles generated by the new signal without the divider (left plots) against those obtained with the divider activated (right plots), with all other parameters held constant. Similar to the baseline configuration, the effective amplitude fed to the loudspeaker is halved when the divider is active, despite an identical voltage output from the signal generator.

The introduction of the voltage divider circuit to the new waveform yields several notable differences. First, the velocity profile exhibits a smoother, more regular slope during the deceleration phase. The localized slope increase (or secondary peak) occasionally observed after the primary velocity maximum in the undivided new-wave cases is completely suppressed. Second, while the maximum velocity is inherently reduced by the divider, this reduction is proportionally less severe than the attenuation observed when the divider was applied to the "old-wave" function.

Overall, the combination of the "new-wave" function and the voltage divider circuit generates a more desirable velocity profile. This specific set-up minimizes near-wall suction, eliminates abrupt slope variations, and produces a well-defined jet shape that closely resembles the optimal synthetic jet profiles documented in the literature, such as those obtained by Rebbeck and Choi [6].

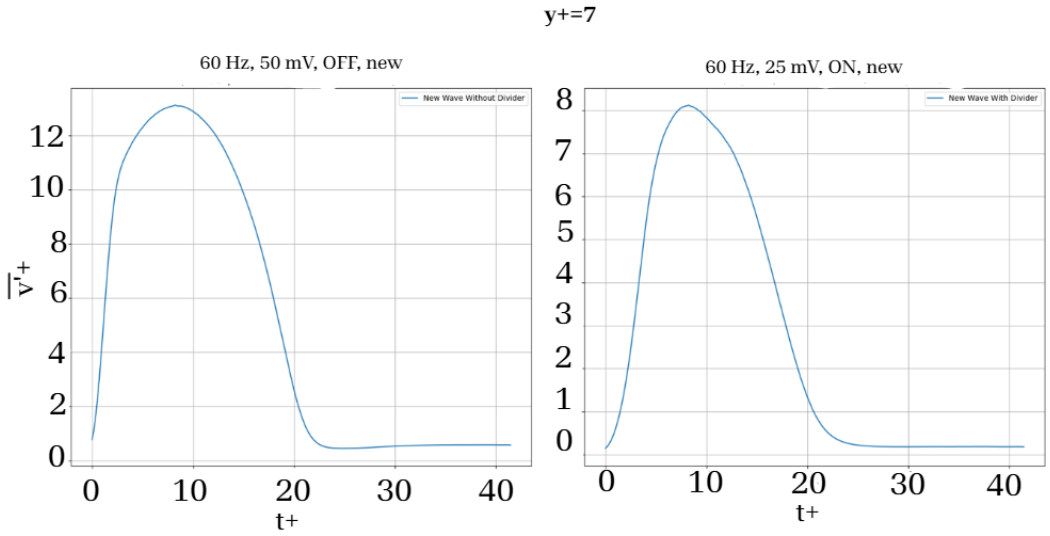


Fig. 3.16 Conditioned velocity profiles $\overline{v'^+}$ at $y^+ = 7$, tracking the influence of the voltage divider applied to the "new-wave" signal (right), compared to the undivided case (left). he title of each subplot reports the specific actuation parameters in the format [Frequency (Hz), Amplitude (mV), Divider flag (OFF, ON), Actuation law (old or new)]. The reported amplitudes are already halved for cases with the divider circuit turned on. The combined use of the new waveform and the divider yields an overall shape highly consistent with the reference findings by Rebbeck and Choi [6].

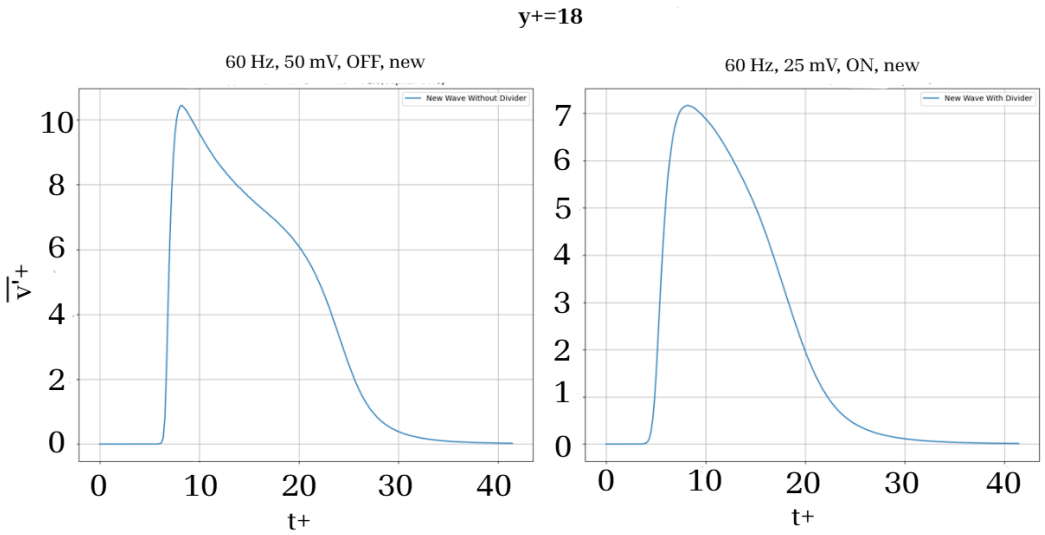


Fig. 3.17 Conditioned velocity profiles $\overline{v'^+}$ at $y^+ = 18$, comparing the "new-wave" signal without (left) and with (right) the voltage divider. The activated divider effectively smooths the deceleration slope. The title of each subplot reports the specific actuation parameters in the format [Frequency (Hz), Amplitude (mV), Divider flag (OFF, ON), Actuation law (old or new)]. The reported amplitudes are already halved for cases with the divider circuit turned on.

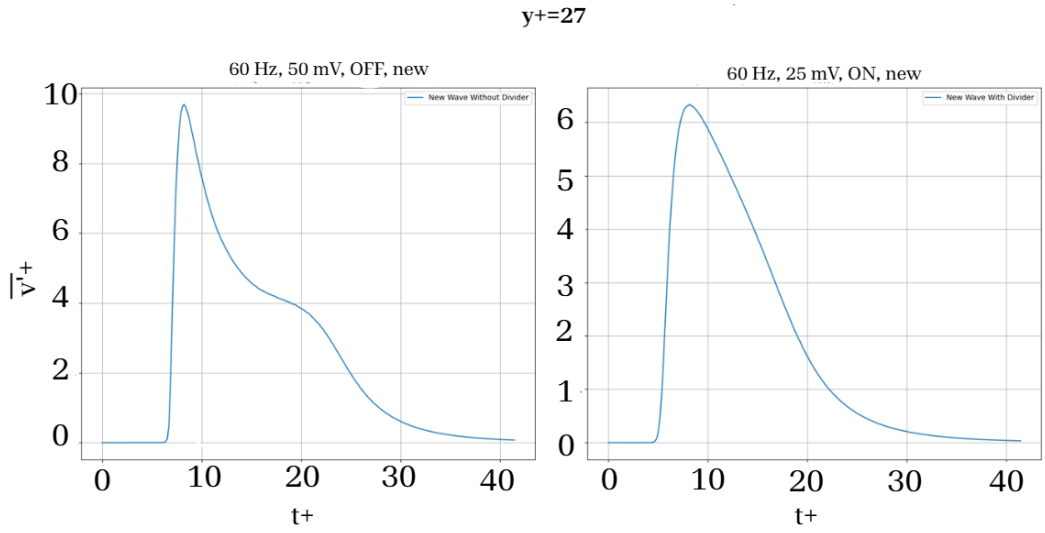


Fig. 3.18 Conditioned velocity profiles $\overline{v'^+}$ at $y^+ = 27$, comparing the "new-wave" signal without (left) and with (right) the voltage divider. The title of each subplot reports the specific actuation parameters in the format [Frequency (Hz), Amplitude (mV), Divider flag (OFF, ON), Actuation law (old or new)]. The reported amplitudes are already halved for cases with the divider circuit turned on.

Analysis of Divider Non-Linearity and Grounding Effects

To verify the linearity of the actuation system's response and assess the accuracy of the hardware signal conditioning, a systematic comparison was conducted using the optimized waveform ("new-wave") as the baseline case. Specifically, two operational scenarios are compared: the baseline configuration without the voltage divider (displayed on the left side of the respective figures) and a configuration where the divider is active but the nominal voltage amplitude set on the signal generator is doubled (displayed on the right side).

Under ideal conditions, the signal halving introduced by the divider, combined with the doubled source voltage amplitude, should supply an equivalent voltage amplitude to the amplifier, thereby generating perfectly identical jet velocity profiles. However, the experimental evidence reveals a clear and systematic divergence between the two cases.

Figs. 3.19, 3.20, and 3.21 illustrate the temporal evolution of the conditionally sampled, ensemble-averaged velocity profiles ($\overline{v'^{+}}$) at wall-normal distances of $y^{+} = (7, 18, 27)$, respectively. Within each figure, the subplots are arranged in rows depicting the increasing actuation frequency from top to bottom, corresponding to 30 Hz, 60 Hz, and 110 Hz.

Furthermore, it should be noted that due to the multi-row layout of Figs. 3.19, 3.20, and 3.21, where three distinct frequencies are vertically stacked, the velocity profiles may visually appear distorted or significantly flattened. This effect is purely a consequence of the vertical graphical compression required by the subplots' layout, whereas the underlying physical scaling and trend consistency remain fully preserved across all configurations

Although the waveform morphology and the temporal development of the jet remain consistent between the two configurations across all investigated heights and frequencies, the undivided configuration consistently exhibits significantly higher peak velocity values compared to the divided, doubled-voltage case. This behavior quantitatively confirms the non-linear and poorly predictable influence of the voltage divider on the electro-acoustic transduction chain.

From a physical and instrumental perspective, this discrepancy can be primarily attributed to the impedance variations introduced by the attenuation circuit. Furthermore, a critical factor lies in the fact that at the time of these measurements, the

voltage divider circuit was not connected to the common ground of the acquisition system. The absence of a stable ground reference fostered the onset of common-mode electrical noise and parasitic capacitive couplings. This ungrounded state altered the effective potential applied to the loudspeaker membrane, ultimately reducing the overall jet blowing intensity compared to the ideal theoretical configuration.

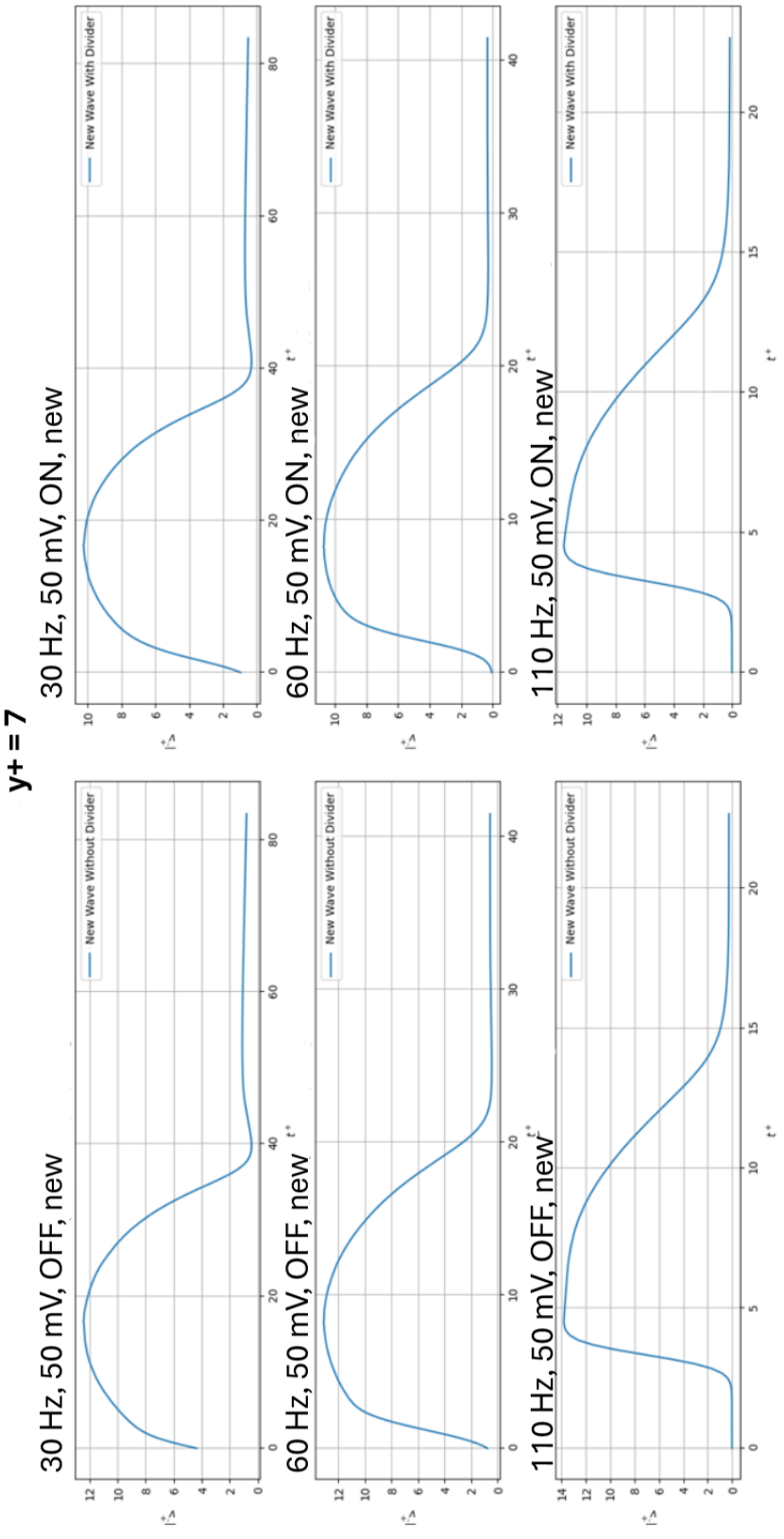


Fig. 3.19 Conditioned, ensemble-averaged velocity profiles $\overline{v'^+}$ at $y^+ = 7$. The plots compare the undivided configuration (left) against the divided configuration with doubled generator voltage (right). The rows correspond to actuation frequencies of 30 Hz (top), 60 Hz (middle), and 110 Hz (bottom). The comparison highlights the non-linear attenuation and the intensity reduction introduced by the ungrounded divider circuit.

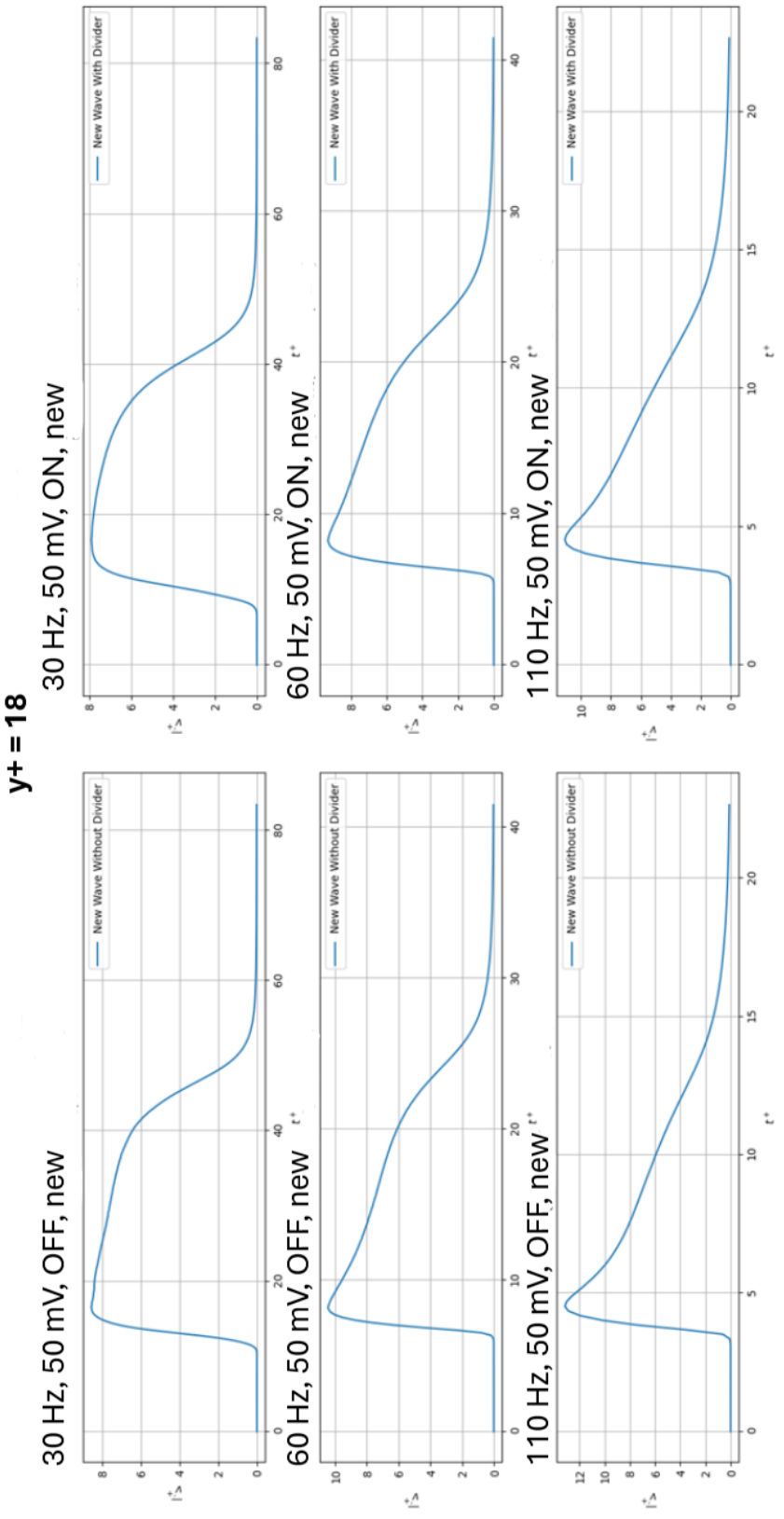


Fig. 3.20 Conditioned, ensemble-averaged velocity profiles $\overline{v'^{+}}$ at $y^{+} = 18$, comparing the undivided set-up (left) and the divided set-up with doubled source voltage amplitude (right) across 30, 60, and 110 Hz. The persistent reduction of the maximum velocity peak in the active-divider case is clearly visible.

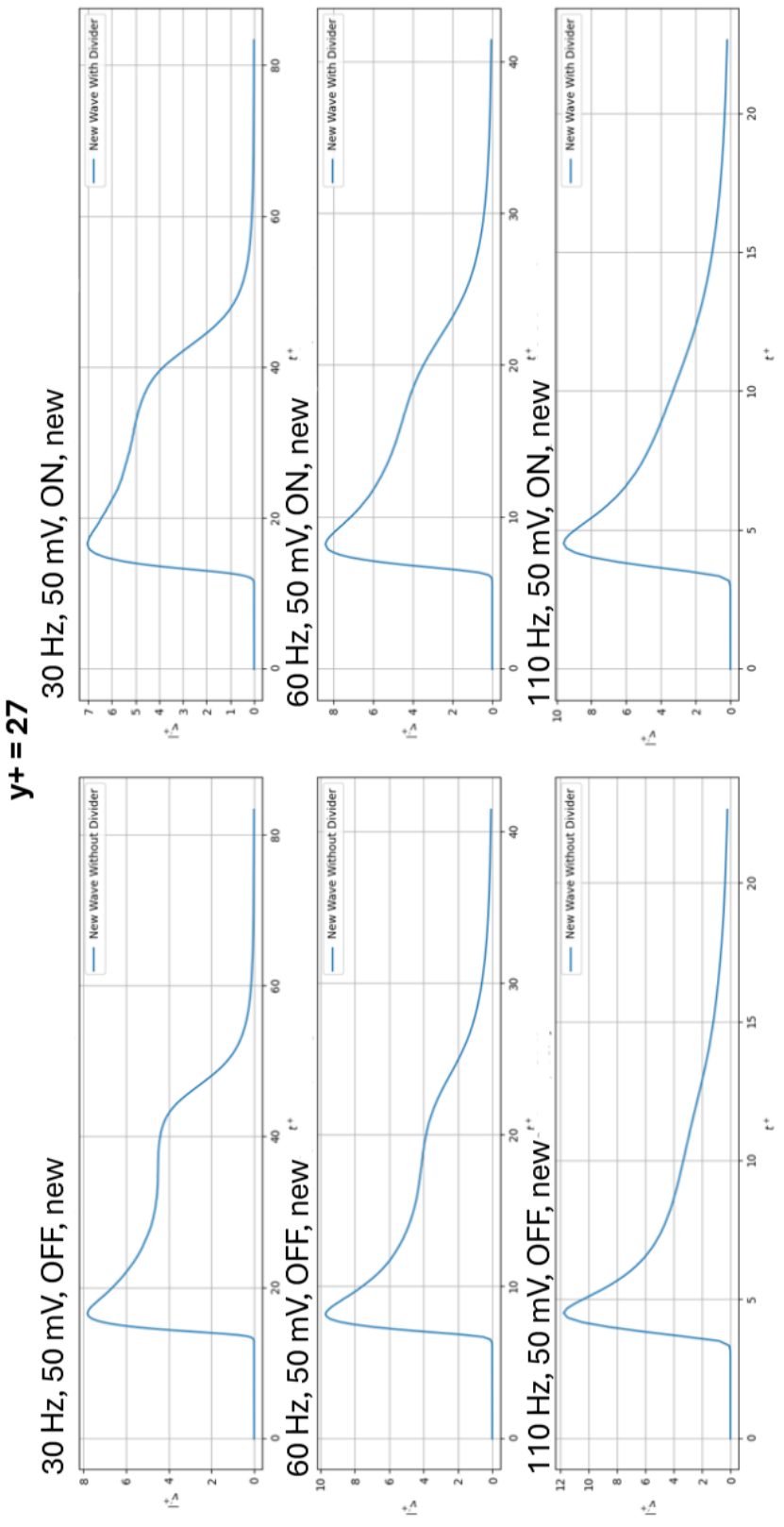


Fig. 3.21 Conditioned, ensemble-averaged velocity profiles $\overline{v'^{+}}$ at the furthest measured distance, $y^{+} = 27$. The comparative analysis confirms the deviation from the ideal divider scaling behavior, exacerbated by the lack of electrical grounding.

3.1.6 Parametric Analysis of Frequency and Voltage Amplitude Variation

The coupled influence of the input voltage amplitude ($V_{pp} = \widehat{A}$) and the driving actuation frequency (f_{gen}) was systematically evaluated by characterizing the jet velocity profiles at a fixed wall-normal coordinate, as in Fig. 3.4. The key findings are structured and discussed below:

- **Voltage amplitude response:** The maximum conditionally averaged wall-normal jet velocity $\overline{v'_{max}}$ scales linearly with the nominal input voltage amplitude ($V_{pp} = \widehat{A}$). Crucially, the implementation of a hardware voltage divider was found to be an unsuitable approach for fine-tuning the signal amplitude fed to the loudspeaker due to its highly non-linear attenuation behavior. In practice, the primary dampening and shaping effects targeted by the divider can be more effectively achieved through the deployment of the optimized "new-wave" profile.

  Overall, an increase in the driving voltage amplitude directly corresponds to a higher peak jet velocity, alongside a simultaneous increase in the near-wall suction phase intensity. This behavior aligns with the underlying electro-mechanical principles of the actuator: a higher voltage amplitude enhances the electrical signal amplitude delivered to the loudspeaker, forcing a larger physical displacement of the internal membrane. This augmented stroke volume inherently drives both a more vigorous fluid expulsion (blowing phase) and a more intense fluid ingestion (suction phase).

- **Frequency effects:** The experimental tests performed across an actuation range from 30 Hz to 110 Hz demonstrate that increasing the frequency leads to a significant compression of the jet time-duration paired with a higher maximum velocity peak. In this framework, the custom "new-wave" driving law proved to be substantially more robust than the baseline "old-wave" configuration, preserving the intended jet shape even at the upper operational limit of the tested frequency range.

  Figs. 3.22 and 3.23 illustrate these frequency-dependent modifications at a near-wall coordinate of $y^+ = 7$. Moving from the left to the right subplots within each figure, the progressive reduction in the temporal duration of the

jet profile is clearly visible as the frequency increments from 30 Hz (left), to 60 Hz (middle), and finally to 110 Hz (right).

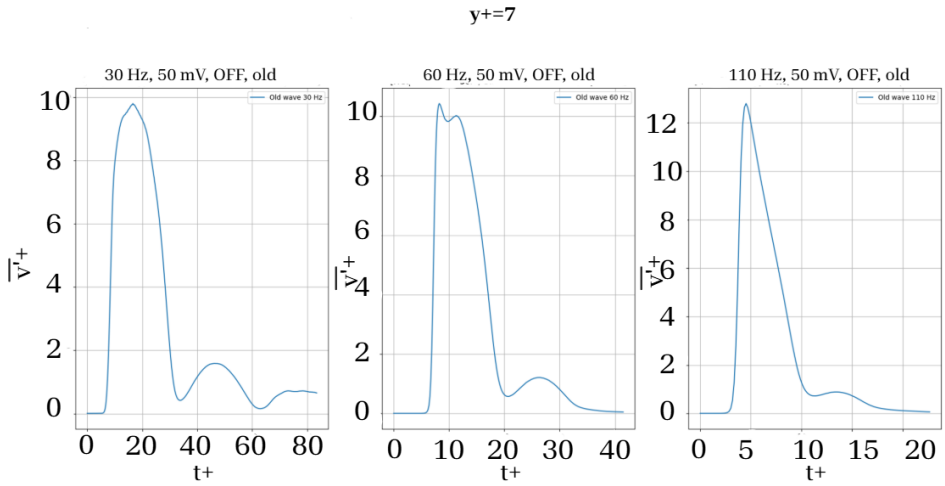


Fig. 3.22 Conditioned, ensemble-averaged velocity profiles $\overline{v'^+}$ at $y^+ = 7$ illustrating the effect of actuation frequency variation using the baseline "old-wave" function without a voltage divider circuit. The subplots from left to right track the severe reduction in jet duration as the frequency increases across 30 Hz, 60 Hz, and 110 Hz.

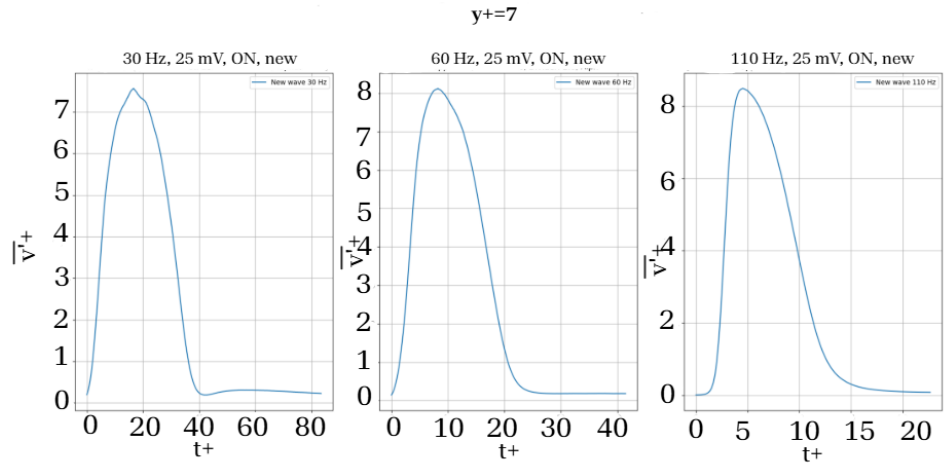


Fig. 3.23 Conditioned, ensemble-averaged velocity profiles $\overline{v'^+}$ at $y^+ = 7$ tracking the effect of actuation frequency variation using the optimized "new-wave" function with the use of a voltage divider circuit. The sequence from left to right (30, 60, and 110 Hz) highlights the structural robustness of the optimized waveform, which preserves the sharp jet morphology even under high-frequency compression.

3.1.7 System Time Delay Assessment

To implement a real-time control logic, a precise quantification of the system's intrinsic response latency is mandatory. This time delay, defined as the total temporal lag between the generation of the electrical trigger command and the physical emission of the fluid jet from the orifice, accounts for both the downstream electronic processing latency and the electro-mechanical inertia of the loudspeaker membrane.

The calibration was performed using a baseline operational configuration characterized by the conventional "old-wave" profile driven at an actuation frequency of $f = 60$ Hz, with a nominal voltage amplitude of $\widehat{A} = 60$ mV and the hardware voltage divider circuit inactive. The velocity fluctuations of the jet were acquired using a Dantec 55P15 hot-wire probe positioned directly over the centerline of the actuator orifice at a fixed wall-normal coordinate of $y^+ \approx 15$. The raw data were recorded with a sampling frequency of $f_s = 10000$ Hz over a total sampling duration of $t_s = 10$ s.

The characteristic system delay Δt was evaluated by computing the time elapsed between the trigger issuance from the signal generator and the physical onset of the jet. Experimentally, the exact arrival time of the jet front at the measurement location was identified using a threshold-crossing method, defined as the precise instant at which the local non-dimensional velocity fluctuation exceeded unity ($v'^+ > 1$).

Figs. 3.24 and 3.25 present the time history of the jet velocity profile captured during this calibration procedure. Specifically, Fig. 3.24 shows the continuous periodic sequence of the generated jets, while Fig. 3.25 provides a focused close-up on a single actuation cycle to highlight the detection mechanism. In both plots, the orange cross designates the exact timestamp of the trigger signal transmission, whereas the pink cross marks the instant of physical jet detection by the hot-wire sensor.

The resulting absolute and wall-bounded non-dimensional time delays are expressed as follows ($u_\tau = 0.161\ m/s$):

$$\Delta t = 0.00310 \text{ s} \approx 3.1 \text{ ms} \tag{3.1}$$

$$\Delta t^+ = \frac{\Delta t\ u_\tau^2}{\nu} = 5.2 \tag{3.2}$$

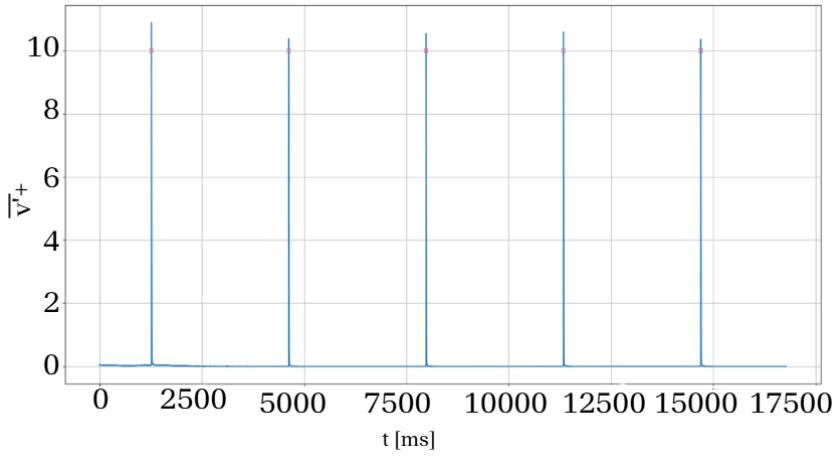


Fig. 3.24 Time history of the phase-conditioned velocity fluctuations $\overline{v'^+}$ at $y^+ \approx 15$ showcasing consecutive synthetic jet cycles. The synchronized timestamps for the electrical trigger generation (orange crosses) and the corresponding aerodynamic response detection (pink crosses) are superimposed to illustrate the periodic stability of the actuation system.

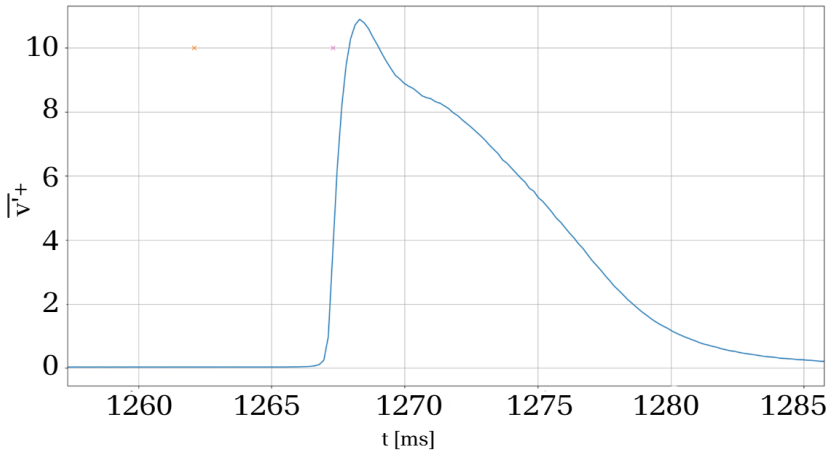


Fig. 3.25 Detailed close-up view of a single synthetic jet actuation cycle showcasing the threshold-crossing detection method. The temporal gap between the signal generator trigger issuance (orange cross) and the physical fluid displacement matching the $\overline{v'^+}$ criterion (pink cross) defines the intrinsic electro-mechanical delay ($\Delta t \approx 3.1$ ms, corresponding to $\Delta t^+ = 5.2$).

3.2 Synthetic Jet Characterization in Still-Air Conditions: 2^{nd} Control Set-up

This section presents an extensive review of the jet velocity profile generated in still-air conditions (no crossflow) by the loudspeaker actuator. In this set-up, the actuator is driven by a custom triangular wave (detailed in Chapter 2, Fig. 2.13) synthesized via an Arduino Giga microcontroller.

The primary objective of this experimental survey was to finely tune the jet duration to effectively counteract the velocity-increase phase of a typical boundary layer sweep event, building upon the observations made during the characterization of the sinusoidal driving function (detailed in Section 3.1).

By measuring the time interval between the detection of the minimum streamwise velocity, immediately preceding the sweep structure, and the subsequent maximum velocity peak, the average "rise time" of an unforced sweep was estimated. This temporal gradient corresponds to an equivalent frequency of approximately 370 Hz, equating to a physical duration of roughly 2.7 ms. Leveraging this information, the control parameters were systematically varied to effectively cancel the sweep signature, aiming to synchronize the peak synthetic jet ejection exactly with the passage of the coherent structure over the orifice.

Furthermore, this measurement campaign aimed to verify the degree of authority over the loudspeaker membrane's retraction phase. The goal was to mitigate the severe suction phase and the consequent *"synthetic sweep"* observed in previous tests, by comparing the actual jet duration against the imposed electrical frequency and wave asymmetry.

The customized triangular driving function is governed by three independent control parameters:

- **Frequency (f [Hz]):** The reciprocal of the total wave period, determining the overall duration of a single actuation cycle.
- **Amplitude ($\widehat{A}$ [mV]):** The peak voltage amplitude supplied to the loudspeaker, governing the displacement of the membrane and the magnitude of the jet ejection velocity.

- **Asymmetry Percentage ($x\%$):** The fraction of the total wave period characterized by a positive slope. This dictates the duration (calculated as $x\%/f$) and the impulsiveness of the blowing phase relative to the suction phase.

To systematically evaluate the influence of these parameters, hot-wire measurements were acquired by positioning the probe at a wall-normal distance of $y^+_{\text{rear}} \approx 6$. The results are depicted in Figs. 3.26, 3.27, and 3.28, which represent all tested control parameter combinations organized by fixed asymmetry percentages of $x\% = (1\%, 50\%, 90\%)$, respectively. The complete experimental matrix outlining the investigated configurations is summarized in Table 3.2.

Table 3.2 Summary of the experimental test matrix for the synthetic jet characterization in still-air conditions using the custom triangular waveform.

Asymmetry ($x\%$)	**Frequencies (f) [Hz]**	**Amplitudes ($\widehat{A}$) [mV]**
1%	30, 60, 120, 150, 200	25, 50, 100
50%	30, 60, 120, 200	25, 50, 75*
90%	30, 60, 120, 200	25, 50, 75*

* Testing at 100 mV was discontinued for $x\% \geq 50\%$ due to excessively high induced wall-normal velocities.

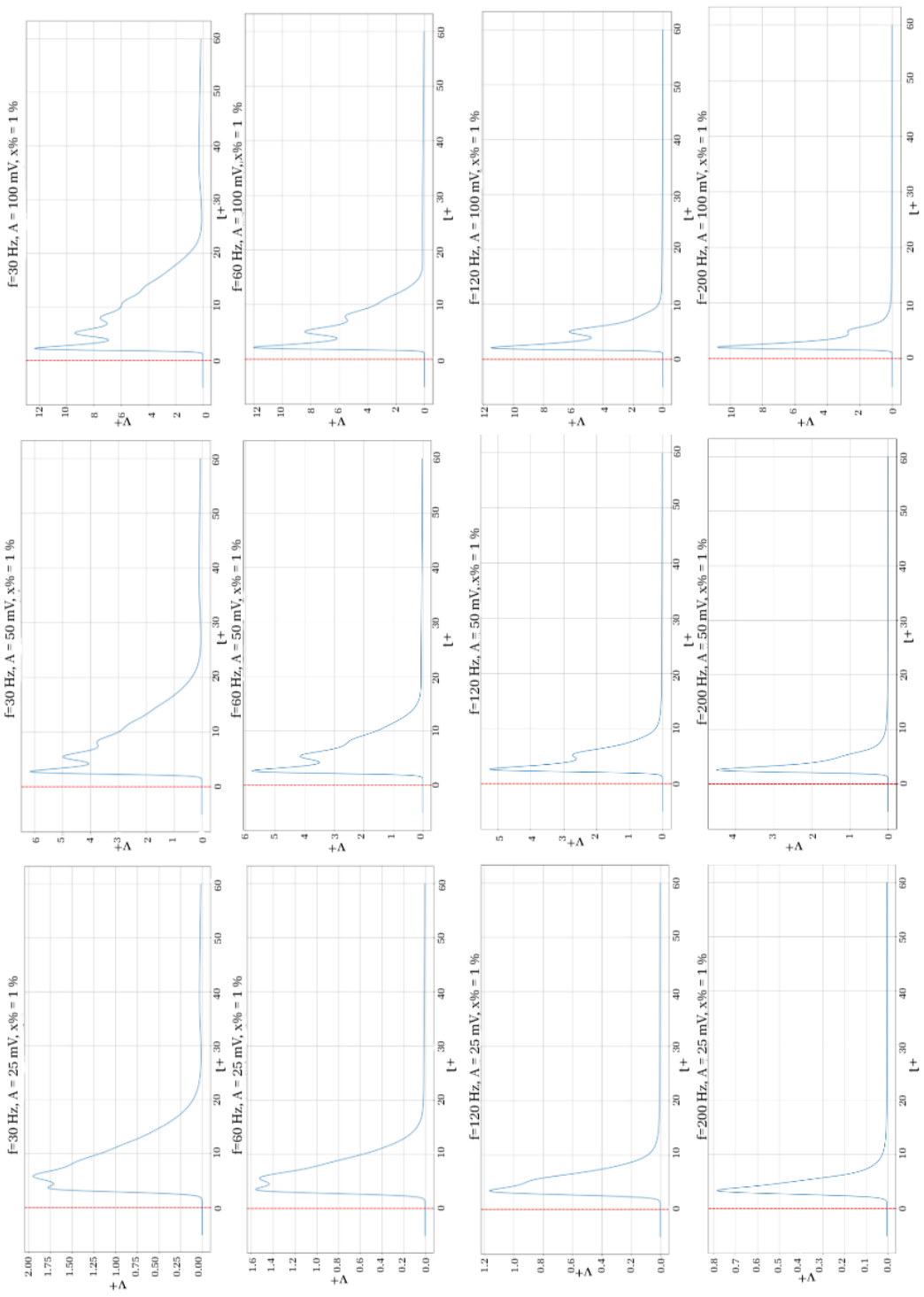


Fig. 3.26 Ensemble conditionally averaged wall-normal velocity (v^+) profiles over non-dimensional time (t^+) for all jet cases studied with fixed asymmetry $x\% = 1\%$. Frequencies range from top to bottom $f = (30, 60, 120, 200)$ Hz and voltage amplitudes from left to right $\widehat{A} = (25, 50, 100)$ mV. The red dashed line in each plot denotes the instant the microcontroller actuated the loudspeaker's amplifier.

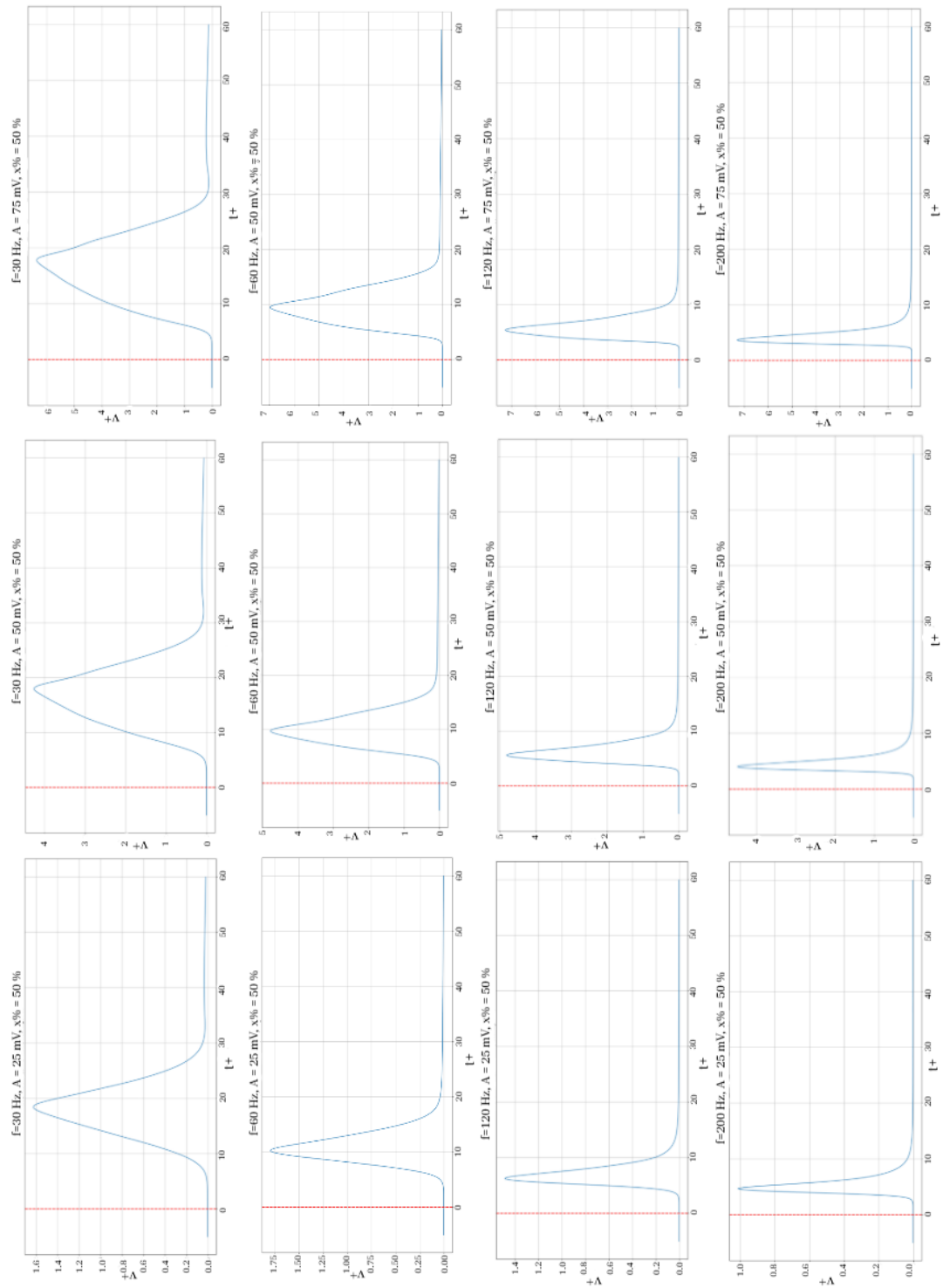


Fig. 3.27 Ensemble conditionally averaged wall-normal velocity (v^+) profiles over non-dimensional time (t^+) for all jet cases studied with fixed asymmetry $x\% = 50\%$. Frequencies range from top to bottom $f = (30, 60, 120, 200)$ Hz and voltage amplitudes from left to right $\widehat{A} = (25, 50, 75)$ mV. The maximum voltage amplitude was limited to 75 mV, as the vertical velocities induced at 100 mV significantly exceeded the required jet intensity for opposition control. The red dashed line denotes the actuation trigger.

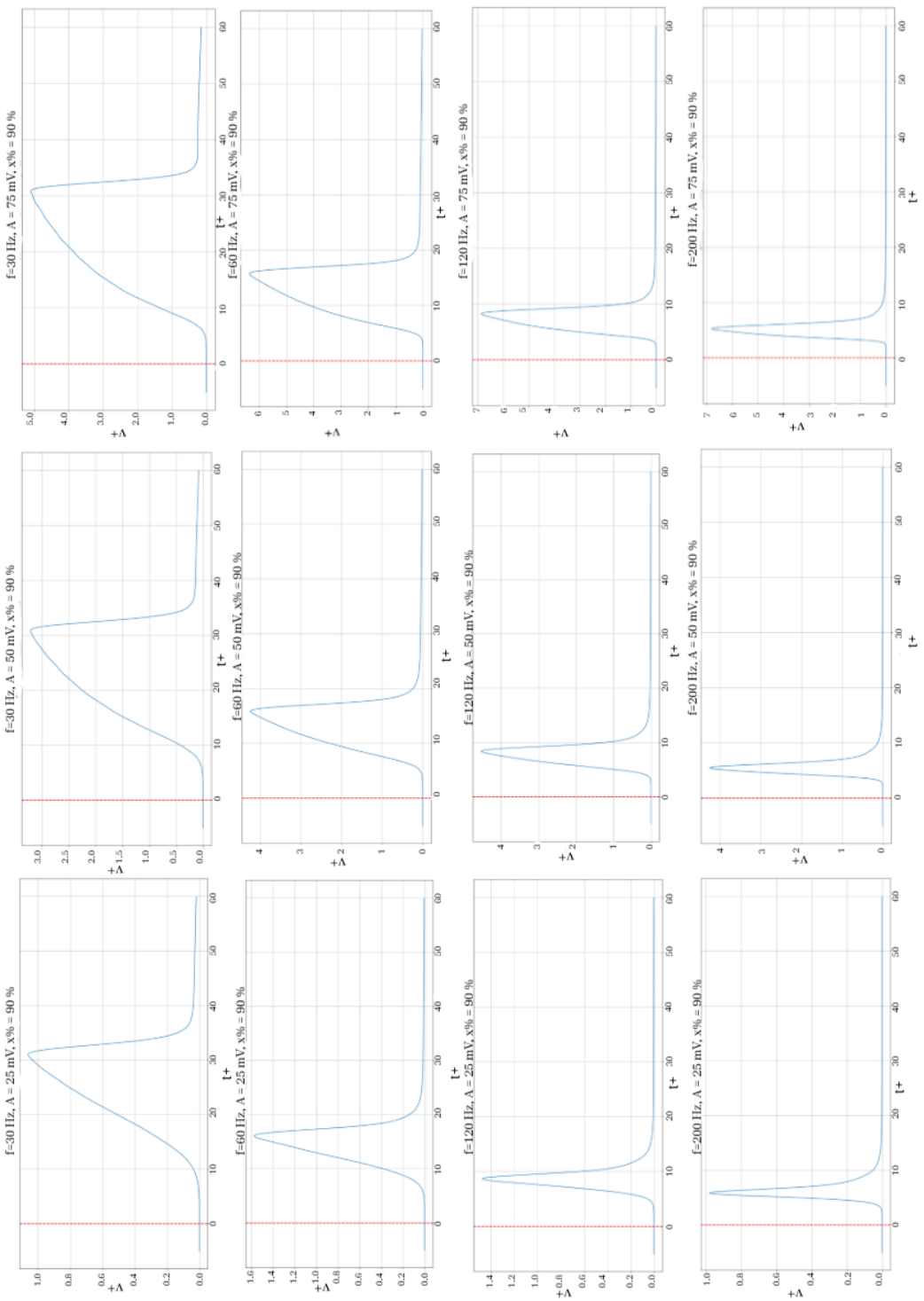


Fig. 3.28 Ensemble conditionally averaged wall-normal velocity (v^+) profiles over non-dimensional time (t^+) for all jet cases studied with fixed asymmetry $x\% = 90\%$. Frequencies range from top to bottom $f = (30, 60, 120, 200)$ Hz and voltage amplitudes from left to right $\widehat{A} = (25, 50, 75)$ mV. The red dashed line denotes the actuation trigger.

3.2.1 Influence of Actuation Amplitude

The amplitude of the driving signal ($\widehat{A}$) directly dictates the peak velocity of the expelled fluid. However, the experimental survey revealed critical non-linearities at the highest tested voltage amplitudes. As observable in the configurations driven at 100 mV with severe asymmetry ($x\% = 1\%$) across all tested frequencies, the velocity profile exhibits prominent secondary peaks immediately following the primary ejection.

It's possible that this phenomenon is physically attributed to the structural "ringing" of the loudspeaker membrane. When subjected to an extremely rapid, highly energetic step-like electrical impulse, the membrane might behave as an underdamped harmonic oscillator, vibrating elastically before settling to its equilibrium position. These hypothesized residual vibrations can translate into a sequence of unwanted, secondary wall-normal velocity fluctuations seen in Fig. 3.29. Fig. 3.29 clearly illustrates this oscillation encountered with parameters $f = 30$ Hz, $\widehat{A} = 100$ mV, $x\% = 1\%$ (Fig. 3.29, top), contrasting it against a clean, single-jet expulsion obtained with a gentler actuation of $f = 120$ Hz, $\widehat{A} = 25$ mV, $x\% = 1\%$ (Fig. 3.29, bottom).

The grid of plots in Fig. 3.26 portrays very clearly the progressive amplification of the irregularities in the wall-normal velocity profiles, as the applied voltage amplitude increases (from left to right). Following the initial measurements at $x\% = 1\%$, the maximum operational amplitude was conservatively capped at 75 mV for the remainder of the test matrix. The 100 mV amplitude was discarded not only to prevent structural fatigue and potential damage to the loudspeaker membrane, but fundamentally because the induced wall-normal velocities (reaching up to $v^+ \approx 12$) were excessively high. As demonstrated in the studies by Rebbeck and Choi [6], blowing amplitudes of such magnitude shift the control mechanism from subtle opposition control to an intrusive fluidic obstacle, which can inadvertently increase drag.

3.2.2 Influence of Wave Asymmetry and Frequency

The most profound aerodynamic variations were achieved by actively modulating the waveform asymmetry percentage ($x\%$) in conjunction with the actuation frequency (f).

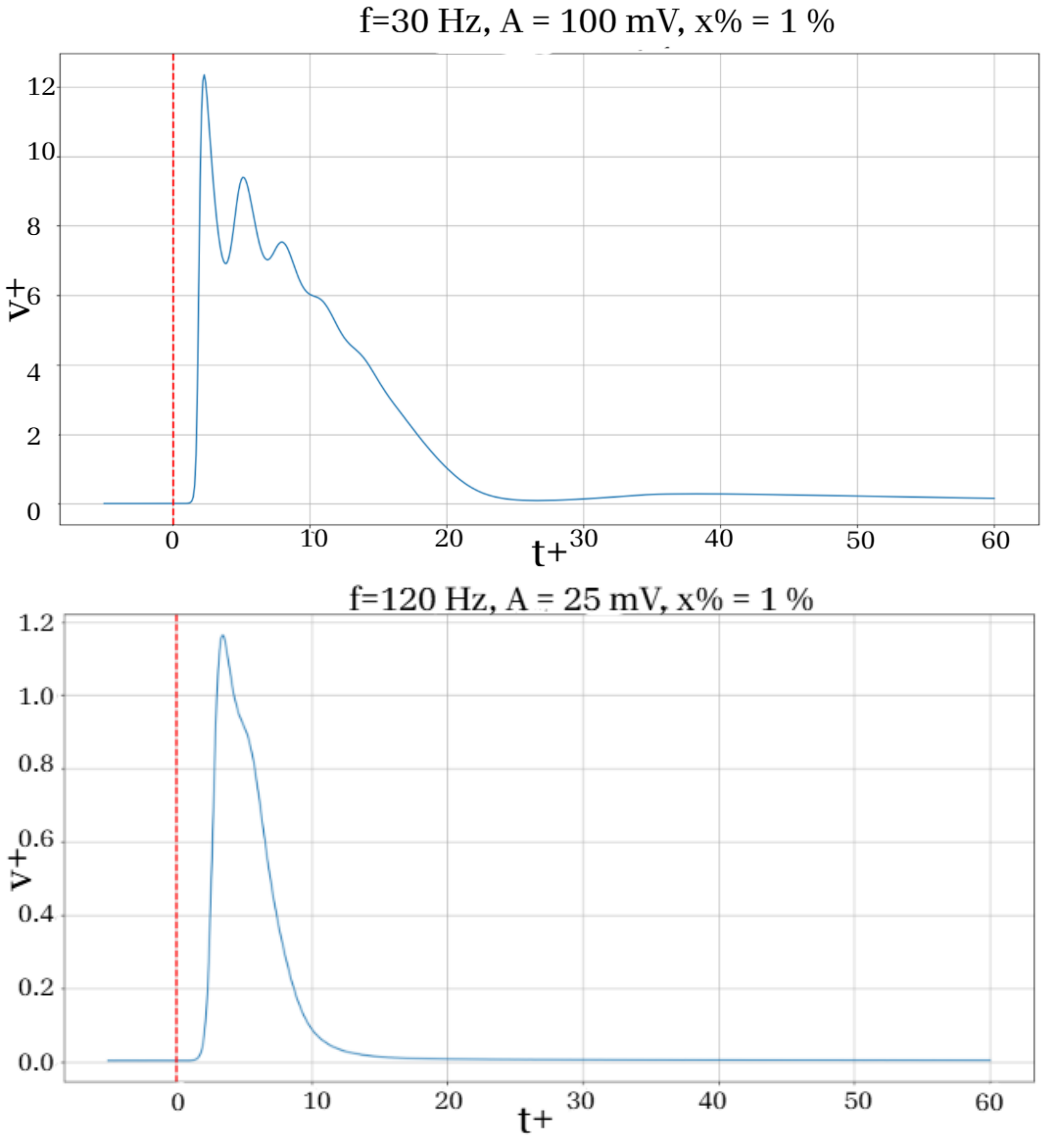


Fig. 3.29 Effect of amplitude on the jet velocity profile. Conditional averages of adimentional wall-normal velocity profiles over t^+. The vertical red dashed line represents the instant when the Arduino Giga triggered the loudspeaker amplifier with the determined triangular custom wave. Top: Pronounced structural ringing and secondary velocity peaks induced by excessive amplitude ($V_{pp} = \widehat{A} = 100$ mV).Bottom: A clean expulsion at low amplitude ($V_{pp} = \widehat{A} = 25$ mV).

When $x\% = 1\%$ (see Fig. 3.26), the blowing phase is highly impulsive. The membrane is driven outward almost instantaneously, generating a steep, velocity gradient that reaches the peak wall-normal velocity (v^+) in a fraction of a millisecond. Consequently, the following retraction phase, which occupies the remaining 99% of the actuation cycle, is significantly more gradual. This smooth suction phase is highly desirable, provided that the amplitude $\widehat{A}$ remains within the operational limits; as previously discussed, excessive amplitudes induce structural ringing that renders the jet profile unpredictable and aerodynamically counterproductive.

Conversely, when $x\% = 90\%$ (see Fig. 3.28), the ejection phase is deliberately prolonged and gradual. This results in a broad, delayed velocity profile that fails to provide the rapid counter-momentum required for effective sweep mitigation. However, it is worth noting that at elevated frequencies, such as $f = (120, 200)$ Hz, the absolute period of the wave becomes so brief that the asymmetry parameter ($x\%$) loses its defining influence over the temporal shape of the jet.

Counter-intuitively, the nominally symmetric electrical configuration ($x\% = 50\%$, see Fig. 3.27) does not yield a perfectly symmetric aerodynamic profile. Instead, the resulting jet exhibits a noticeably steeper gradient during the membrane's retraction phase. This behavior highlights a fundamental electro-mechanical asymmetry: while the amplifier exercises strong temporal authority during the outward ejection (pushing the membrane), the retraction dynamics are heavily dominated by the inherent structural stiffness and the natural elastic recoil of the membrane material, leading to a harsher, less controllable suction phase.

Overall, an inverse relationship exists between the actuation frequency and the control authority of the asymmetry parameter. A direct comparison between Figs. 3.30 and 3.31 unequivocally illustrates this trend. At a low frequency of $f = 30$ Hz, the kinematic signature of the jet changes drastically as $x\%$ is varied. In stark contrast, at $f = 200$ Hz, the dynamic response of the system approaches its mechanical limits, rendering the differences between the jet profiles almost negligible.

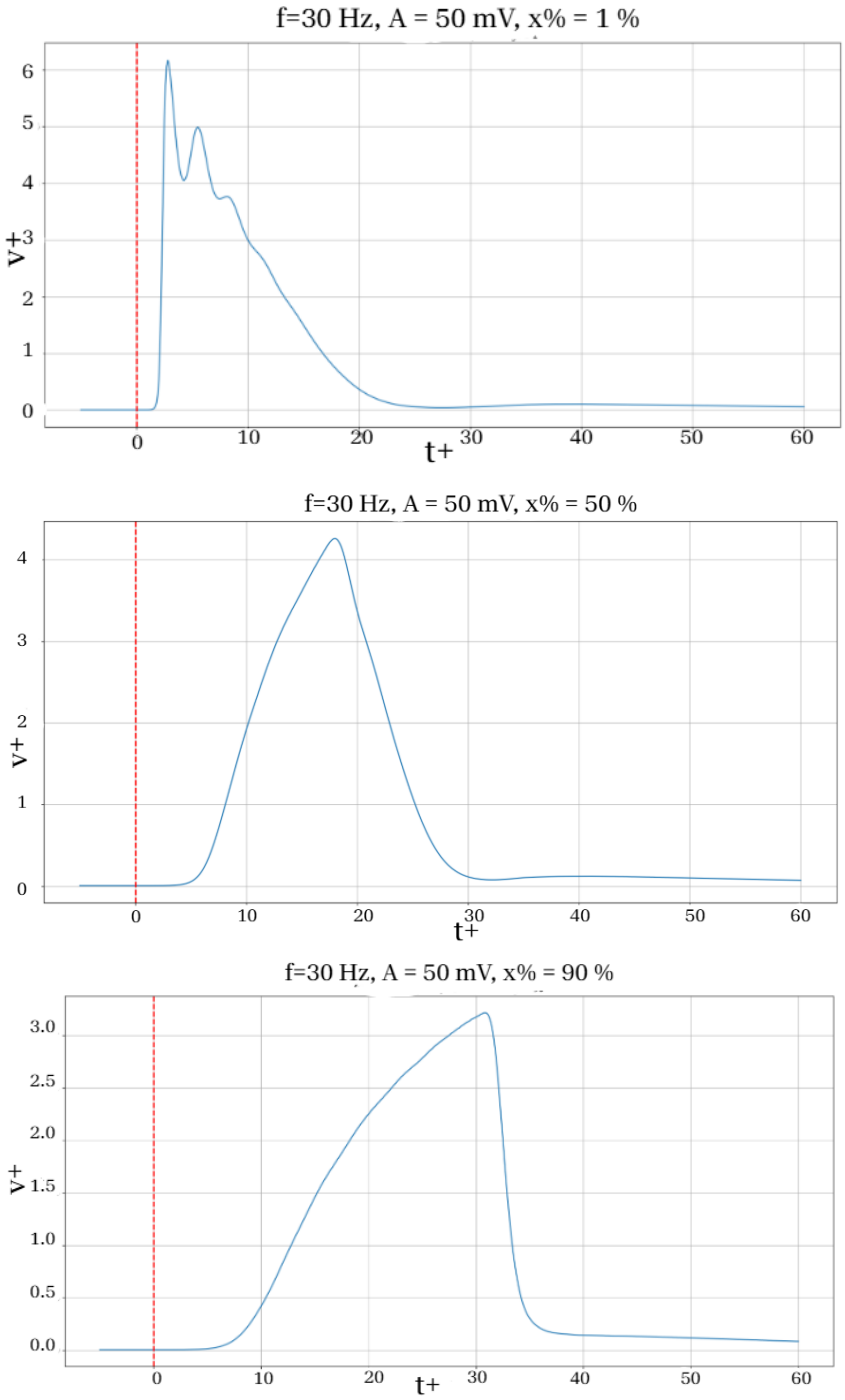


Fig. 3.30 Evolution of the jet velocity profile as a function of the wave asymmetry percentage ($x\%$) at a constant frequency of 30 Hz and amplitude of 50 mV. The transition from a highly impulsive ejection ($x\% = 1\%$, top) to a gradual expulsion ($x\% = 90\%$, bottom) is clearly evident, demonstrating strong control authority at low frequencies.

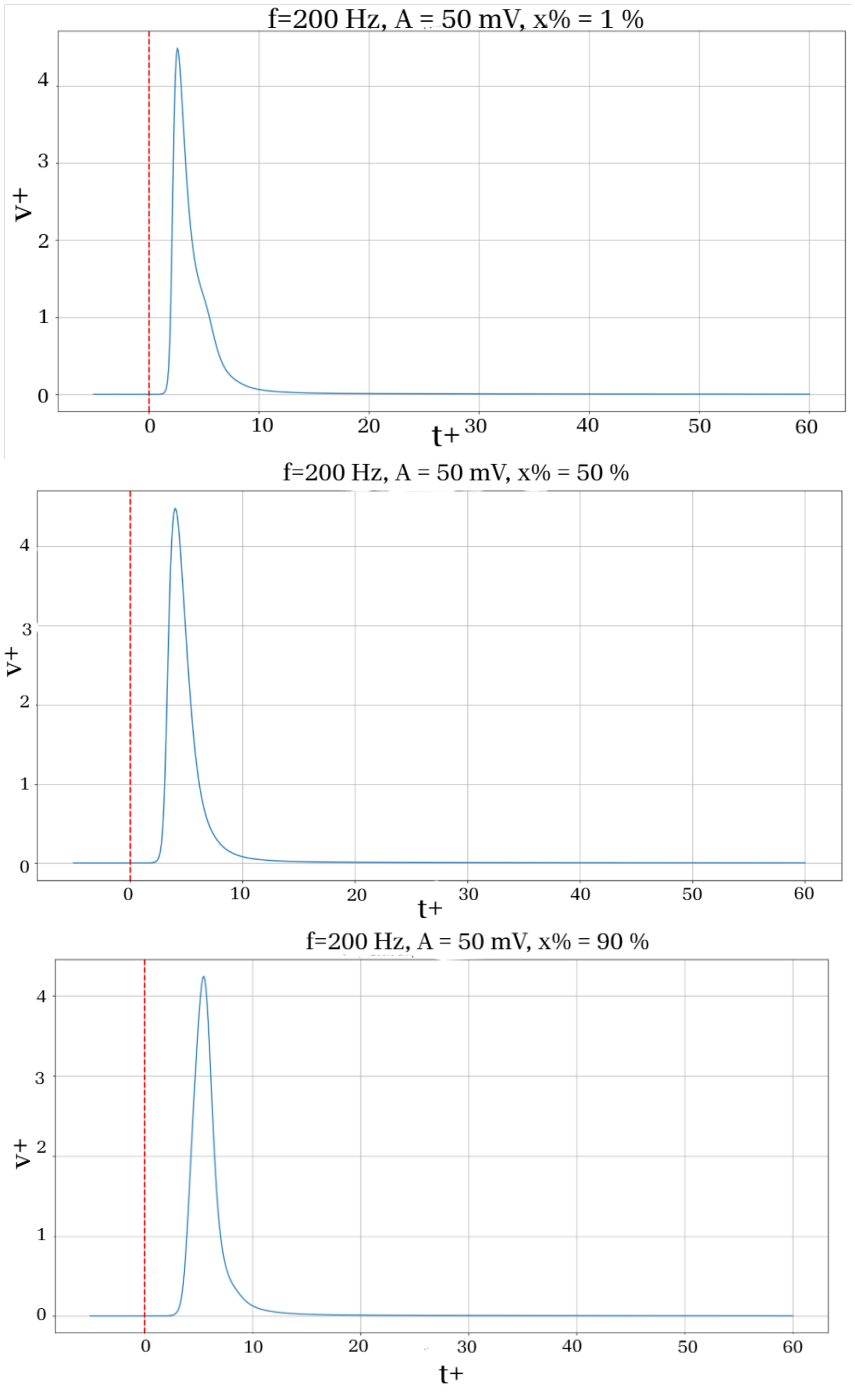


Fig. 3.31 Evolution of the jet velocity profile as a function of the wave asymmetry percentage ($x\%$) at a constant frequency of 200 Hz and amplitude of 50 mV. At this high frequency, the temporal variations between the jet profiles induced by changing $x\%$ become virtually negligible.

Finally, increasing the actuation frequency effectively compresses the entire jet duration. To interact with the ≈ 2.7 ms rise time of the turbulent sweep, the optimal tuning requires a combination of high frequency (e.g., 200 Hz) and severe asymmetry (e.g., $x\% \leq 10\%$). This specific parametric combination guarantees a rapid, concentrated injection of fluid capable of promptly intercepting the advecting coherent structure, while dedicating the vast majority of the cycle period to a slow, non-intrusive membrane retraction that prevents the detrimental "synthetic sweep" effect.

3.3 Experimental Results and Discussion: Wall-Normal Survey

This Section delivers a comprehensive analysis of the experimental results obtained from the wall-normal (y) spatial survey executed through the Python script in Appendix E. The data obtained were then systematically processed using the automated post-processing routines detailed in Appendix F. The focus is centered on two Test Cases:

- Test Case 10, which operating conditions correspond to the baseline "old-wave" Fig.2.10 actuation profile driven at $f = 60$ Hz with an input amplitude of $\widehat{A} = 60$ mV and a delay time of $\Delta_t = 2.207$ ms.
- Test Case 13 which involved the use of the "new-wave", with actuation parameters $f = 30$ Hz with an input amplitude of $\widehat{A} = 12.5$ mV and a delay time of $\Delta_t = 0.15$ ms.

To compensate for the finite physical dimensions of the single boundary-layer hot-wire probe and ensure sub-viscous wall distance accuracy, a wall-distance calibration offset of $\Delta y_0 = 0.162$ mm for Test Case 10 and $\Delta y_0 = 0.284$ mm was determined (see Appendix F). The viscous scaling parameters were: a friction velocity of $u_\tau = 0.165$ m/s for Test Case 10 and $u_\tau = 0.1525$ m/s and a friction Reynolds number $Re_\tau \approx 365$ for Test Case 10 and $Re_\tau \approx 336$ for Test Case 13. The viscous parameters are summarized in Table 3.3.

For both Test Cases 10 and 13, during the measurement campaigns, the front hot-wire probe was positioned at a streamwise distance upstream of the control orifice

Table 3.3 Wall-distance calibration offsets and viscous scaling parameters for the selected test cases.

Parameter	**Symbol [Unit]**	**Test Case 10**	**Test Case 13**
Wall-distance calibration offset	Δy_0 [mm]	0.162	0.284
Friction velocity	u_τ [m/s]	0.165	0.1525
Friction Reynolds number	Re_τ [–]	≈ 365	≈ 336

of $x^+_{front} = -65$ and a wall normal distance of $y^+_{front} \approx 15$; while the rear-probe was positioned at a streamwise distance from the jet orifice of $x^+_{rear} = 76$ and a varying wall-normal distance y^+_{rear} from the closest position possible to the surface to 350, with smaller increments near the wall to have more resolution on the change of flow velocity and structures in the region adjacent to the surface due to the applied control.

The evaluation is conducted by comparing the unactuated flow field (*Uncontrolled*) with the actively modulated flow field (*Controlled*), and DNS data from [23] acting as an unperturbed canonical reference.

The uncontrolled flow streamwise velocity was obtained by measuring the flow with the loudspeaker turned off with the rear-probe at each wall-normal distance, while the controlled flow was measured with the same criterion but with the loudspeaker activated.

3.3.1 Long-Term Time-Averaged Turbulence Statistics

To evaluate the macroscopic, long-term impact of the active opposition control strategy on the wall-bounded turbulence, the first four statistical moments of the streamwise velocity fluctuations were computed over an extended sampling window of $t_s = 240$ s to guarantee strict statistical convergence.

Figs. 3.32 and 3.33 show, respectively for Test Case 10 and Test Case 13, the wall-normal profiles of the non-dimensional mean velocity (U^+), the streamwise Reynolds normal stress ($\overline{u'u'}^+$), the Skewness (S), and the Flatness (F, evaluating the absolute Kurtosis via Pearson's definition) plotted against the viscous wall-normal coordinate y^+.

An analysis of the computed turbulence statistics reveals a noticeable divergence between the theoretical DNS benchmarks [23] and the gathered experimental data, starting at a wall-normal distance of approximately $y^+ \approx 30$. This discrepancy is primarily attributed to the intrusive effect of the upstream (front) hot-wire probe on the signal sampled by the downstream (rear) sensor. Nevertheless, since the primary objective of the active control strategy relies entirely on manipulating the flow within the immediate viscous sublayer and buffer region, the data remains highly reliable and effective within the near-wall zone of interest ($y^+ < 30$).

For both Test Cases, the mean velocity profile U^+ (Fig. 3.32a and 3.33a) demonstrates good agreement between the experimental uncontrolled baseline and the DNS data [23] across the viscous sublayer and the buffer layer.

Upon the activation of the synthetic jet opposition control (*Controlled* curves), an almost complete overlap with the *Uncontrolled* baseline is observed across all four statistical moments. Rather than a system failure, this outcome is intrinsically linked to the physics of the targeted coherent structures and the nature of time-averaged metrics.

The opposition control is designed to manipulate specific, intermittent, and highly localized turbulent events (such as the near-wall sweeps and ejections associated with quasi-streamwise vortices). Because these target structures are transient, the energy injected or subtracted by the localized actuation is inevitably diluted into the broad-band stochastic background turbulence when integrated over a long sampling window (240 s).

Consequently, while classical global statistics confirm that the actuation does not induce unwanted macroscopic effects, they are inherently "blind" to the local near-wall dynamic interaction between the actuator and the flow. To properly isolate and evaluate the control's effectiveness in attenuating the velocity fluctuations during these specific coherent events, it is strictly necessary to transition from time-averaged statistics to conditional averages of the obtained data.

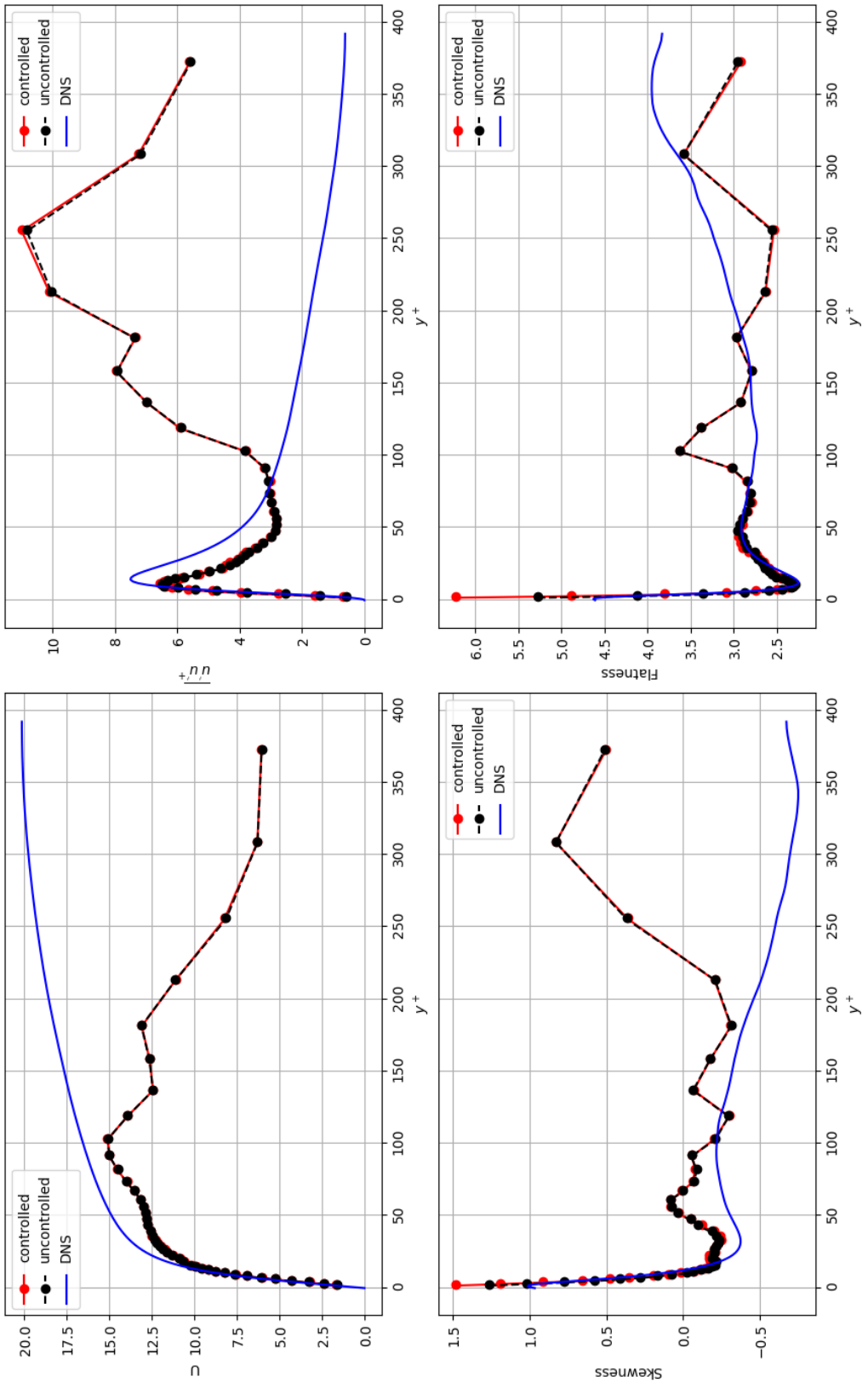


Fig. 3.32 Wall-normal profiles of long-term time-averaged turbulence statistics for Test Case 10 ("old-wave") compared against canonical DNS data [23]: (a) Mean velocity profile U^+; (b) Streamwise Reynolds stress $\overline{u'u'}^+$; (c) Streamwise velocity skewness S; (d) Streamwise velocity flatness F.

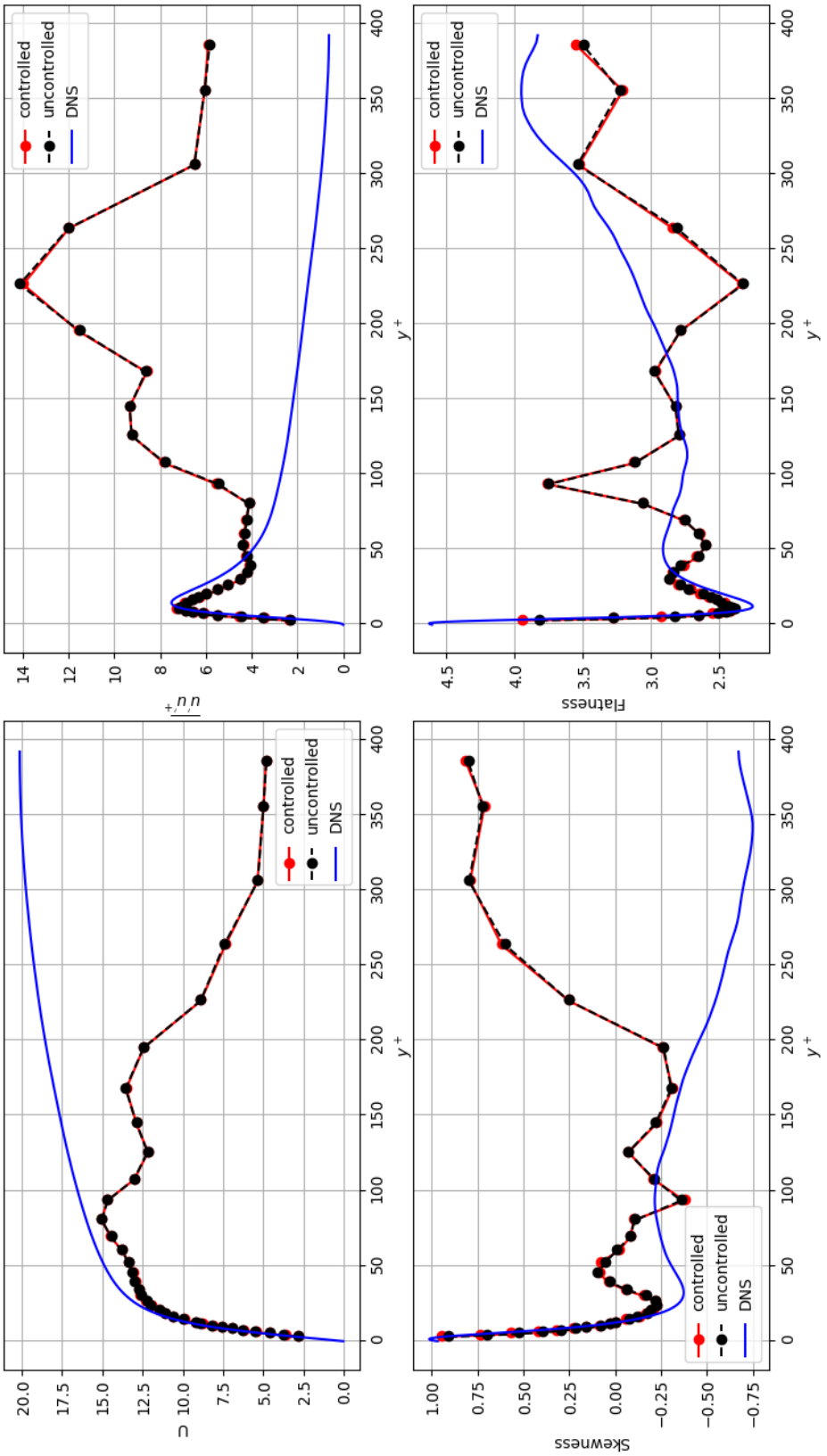


Fig. 3.33 Wall-normal profiles of long-term time-averaged turbulence statistics for Test Case 13 ("new-wave") compared against canonical DNS data [23]: (a) Mean velocity profile U^+; (b) Streamwise Reynolds stress $\overline{u'u'}^+$; (c) Streamwise velocity skewness S; (d) Streamwise velocity flatness F.

3.3.2 Conditionally Averaged Streamwise Velocity Profiles

To discriminate the deterministic footprint of the active control from background stochastic turbulence, conditional averaging was applied to the u'^+ velocity traces based on the synchronized generator trigger signal. Figs. 3.34 and 3.35 present the temporal evolution of the conditionally-averaged non-dimensional velocity fluctuations u'^+ across a selection of discrete wall-normal positions, focusing on the inner region of the turbulent boundary layer (y^+ ranging from $y^+ = 11$ to $y^+ = 22$). In each plot, the non-dimensional time t^+ is centered at the instant of sweep detection, where $t^+ = 0$; note that negative values of t^+ just represent instances before the sweep identification. The controlled curves incorporate an explicit convective time shift allowing for direct alignment with the physical arrival of the synthetic jet.

In both Figs. 3.34 and 3.35, the uncontrolled traces (dashed black lines) represent the conditional average of the unperturbed coherent structures, specifically sweep structures, mapping the natural passage of turbulent events. As noted by Rebbeck and Choi[6], when the sweep event is detected by the hot wire, a sudden streamwise velocity reduction occurs, followed by a steep increase (see dashed black line in 3.34, 3.35). When active control is initiated (solid red lines), the velocity signal is significantly restructured.

As illustrated in the conditional sampling maps for Test Case 10 (Fig. 3.34), the jet actuation initially induces a clear reduction in the streamwise velocity compared to the uncontrolled baseline. However, this attenuation is rapidly followed by a complete velocity recovery. Particularly in the near-wall region, this recovery greatly surpasses the maximum positive fluctuation (u'^+) observed in the unforced flow. This velocity overshoot becomes less evident, yet still present, moving away from the wall, showing that the control effect is mostly localized close to the jet orifice.

This phenomenon can be directly attributed to the intense suction phase identified during the jet profile characterization in Section 3.1.4. Specifically, the wall-normal velocity profile generated by the "old-wave" driving signal features a prolonged and stronger suction phase (see Figs. 3.8–3.10). From a kinematic perspective, this occurs because the old waveform forces the loudspeaker membrane to retract beyond its neutral resting position before the actuation cycle concludes, thereby drawing in fluid more aggressively.

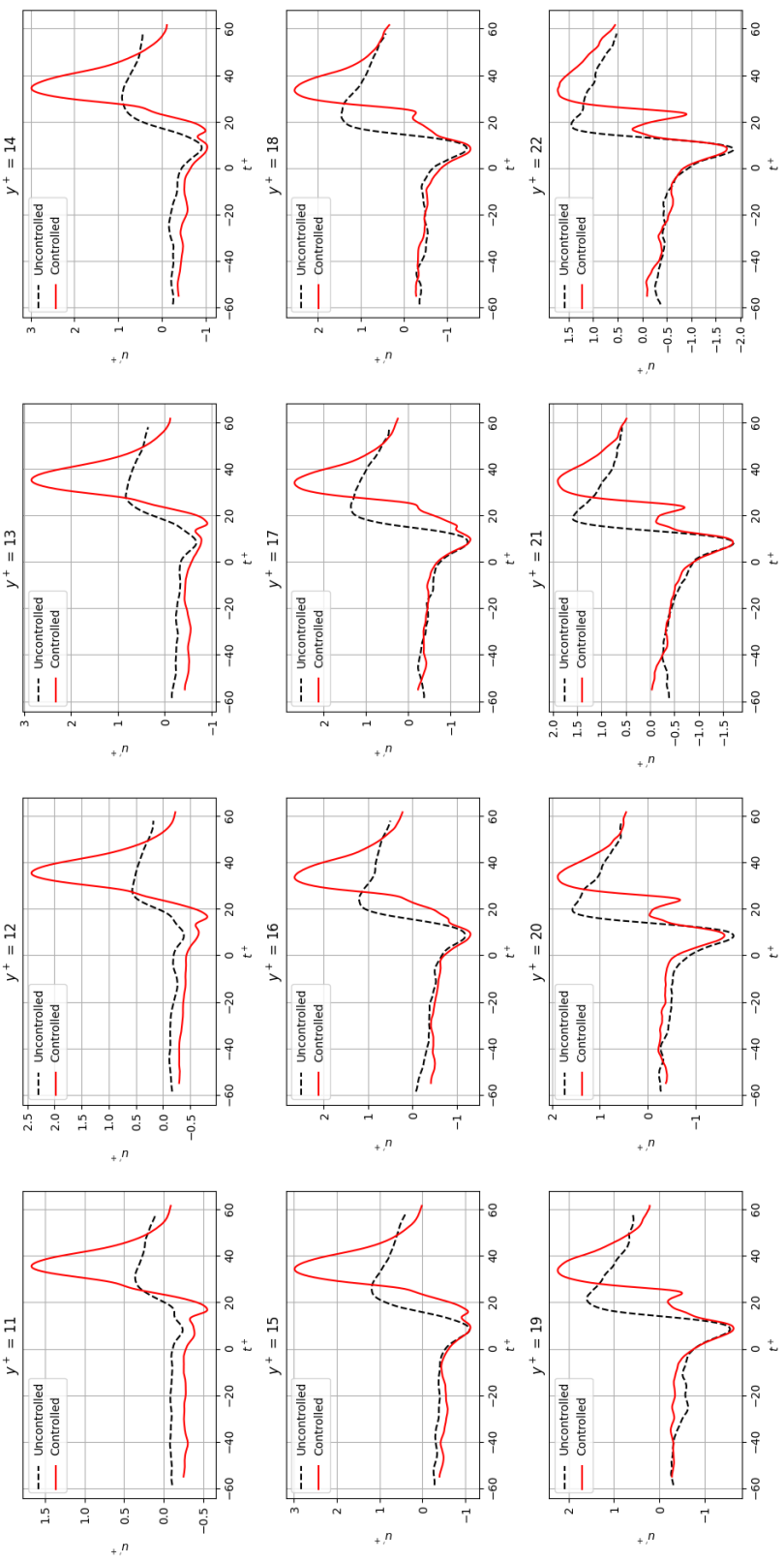


Fig. 3.34 Conditionally-averaged streamwise ensemble averaged velocity fluctuations for Test Case 10 ("old-wave") u'^+ as a function of the non-dimensional time t^+ across discrete wall-normal coordinates (y^+), contrasting the natural uncontrolled coherent event (dashed black line) with the actively controlled response (solid red line).

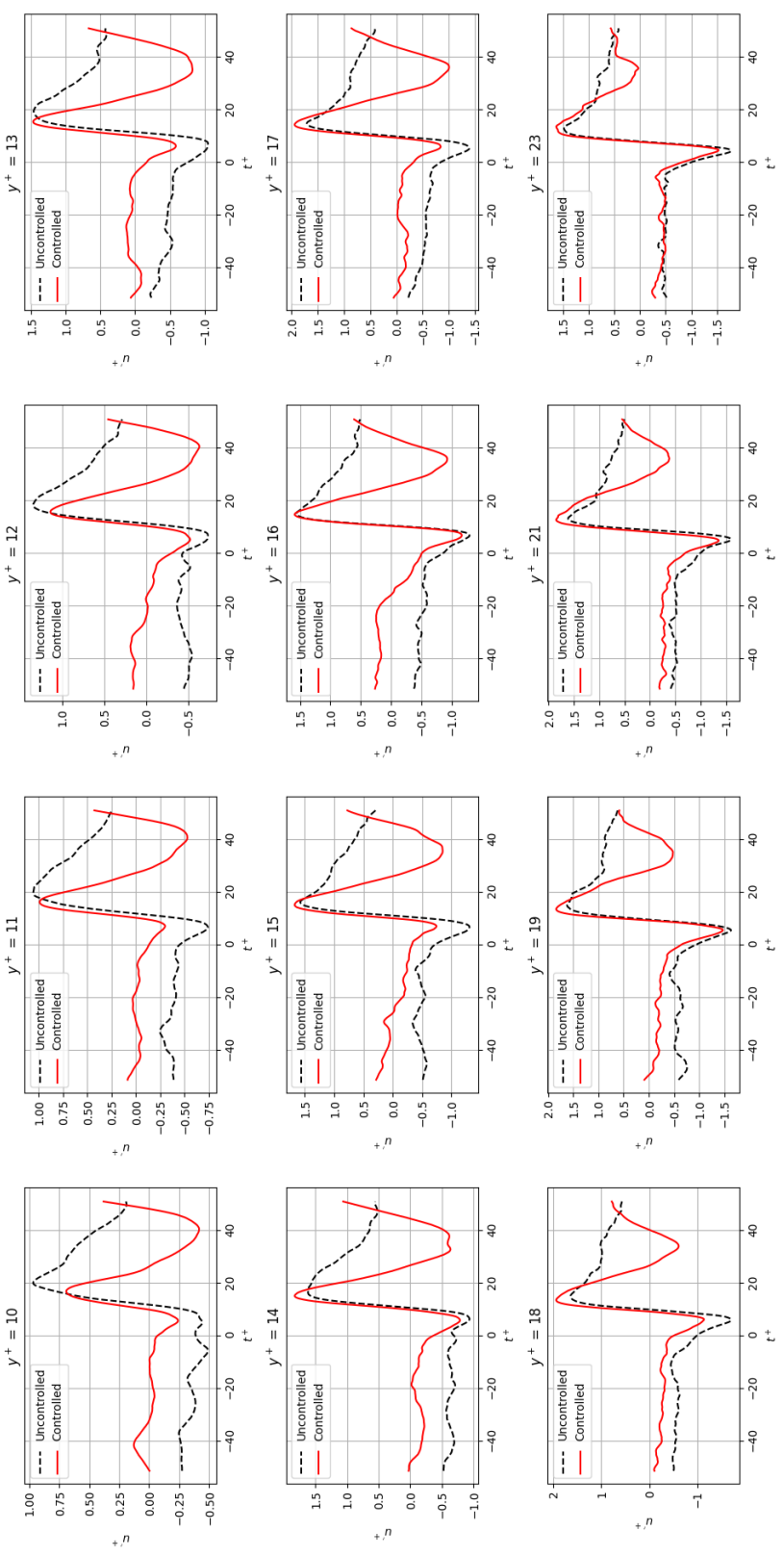


Fig. 3.35 Conditionally-averaged streamwise ensemble averaged velocity fluctuations for Test Case 13 ("new-wave") u'^+ as a function of the non-dimensional time t^+ across discrete wall-normal coordinates (y^+), contrasting the natural uncontrolled coherent event (dashed black line) with the actively controlled response (solid red line).

From an aerodynamic standpoint, this intense suction phase acts as a localized body force that modifies the near-wall momentum balance. Instead of purely opposing the incoming high-momentum fluid associated with a natural sweep event, the strong suction inadvertently reinforces the downward transport of momentum. By entraining fluid towards the wall with increased intensity, the actuator effectively amplifies the downwash of the targeted sweep, leading to the observed velocity overshoot. As will be further detailed in Section 3.3.3, this dynamic interaction becomes even more pronounced, generating a localized region of excess momentum, a *"velocity overshoot bubble"*, close to the wall, which highlights the crucial importance of optimizing the suction phase in opposition control strategies.

A direct comparison between the "old-wave" baseline (Fig. 3.34) and the conditional averages obtained using the "new-wave" driving function (Fig. 3.35) reveals the complete suppression of the previously discussed velocity overshoot. This outcome shows that a mitigated, softer suction phase is crucial for ensuring a more persistent and effective control strategy, as it strictly prevents the near-wall entrainment of high-momentum fluid.

However, the temporal evolution in Test Case 13 indicates a phase shift in the actuator's response. The loudspeaker actuation, and the ensuing streamwise velocity attenuation, occur noticeably later than in Test Case 10. Across all investigated wall-normal distances, the onset of the velocity reduction is observed at a non-dimensional time delay of $\Delta t^+ \approx 20$ relative to the peak velocity of the uncontrolled sweep event and around $t^+ \approx 30$ the control impact becomes more evident.

Unlike the "old-wave" configuration, where the attenuation phase initiates in close proximity to $t^+ = 10$, the delayed response observed in Fig. 3.35 suggests a sub-optimal temporal synchronization. This phase lag implies that the experimentally imposed delay time (Δt) may be excessively large, in addition to the phase shift $\Delta\alpha = -90\,\text{deg}$ characterizing the "new-wave", causing the synthetic jet ejection to trigger too late relative to the advection of the target sweep structure over the control orifice.

Nevertheless, the fact that the "new-wave" driving function prevents the velocity overshoot, ensuring that the local momentum never exceeds the peak of the unforced sweep event, shows that mitigating the abruptness of the suction phase is a sound baseline for subsequent control strategies.

Conversely, the delayed onset of the velocity reduction indicates that the ejection (blowing) must be executed more rapidly. To effectively intercept the advecting sweep structure, it is critical to achieve maximum synthetic jet intensity with minimal temporal delay following the trigger actuation. These combined fluid dynamic observations directly motivated the experimental set-up upgrades detailed in Chapter 2, specifically the integration of a microcontroller to synthesize a custom triangular driving waveform (Fig. 2.13). This tailored approach grants precise, independent control over the temporal gradients of the actuation cycle: it allows for a sharp, rapid blowing phase to immediately impact the flow, while simultaneously maintaining a prolonged, low-intensity suction phase to avoid detrimental near-wall entrainment.

A comprehensive evaluation of these hardware modifications will be discussed in Section 3.4, which presents a detailed comparative analysis of the estimated wall shear stress variations ($\Delta\tau_w$) induced by the "new-wave" (half-sine, Fig. 2.10) and the fully customized triangular driving function (Fig. 2.13).

3.3.3 Space-Time Flow Topology Reconstruction

To gain a comprehensive, continuous visualization of the flow modulation, the discrete conditionally-averaged velocity vectors were compiled into a two-dimensional domain and interpolated onto a refined mesh using a cubic spline scheme. Figs. 3.36 and 3.37 depicts , respectively for Test Case 10 and Test Case 13, the resulting space-time colormaps of the velocity fluctuations u'^{+} in the (t^+, y^+) plane, contrasting the uncontrolled baseline with the actively controlled configuration.

The uncontrolled colormap for both Test Cases (Fig. 3.36 and 3.37, top) illustrate the typical topology of near-wall coherent structures, a low-speed ejection region (dark blue) is then followed by a slanted high-momentum flow region that supposedly represents the sweep event that travels wall-ward.

The activation of the active control loop (Fig. 3.36 and 3.37, bottom) introduces two different velocity field modifications for the different test cases. The continuous, elongated structures observed in the baseline are fragmented and broken down by the localized, high-intensity fluid injection stemming from the wall orifice ($y^+ \to 0$).

Before comparing the topological features of Test Case 10 and Test Case 13, it must be noted that the two configurations operated under slightly different global mean velocity conditions. Consequently, the absolute color scales representing the

streamwise velocity fluctuations (u'^{+}) in the respective space-time colormaps do not correspond to the exact same physical values. Nevertheless, since the overall differences in the unforced fluctuation intensities are negligible compared to the dominant macroscopic effects induced by the actuation, a rigorous qualitative comparison of the flow control footprints remains completely valid.

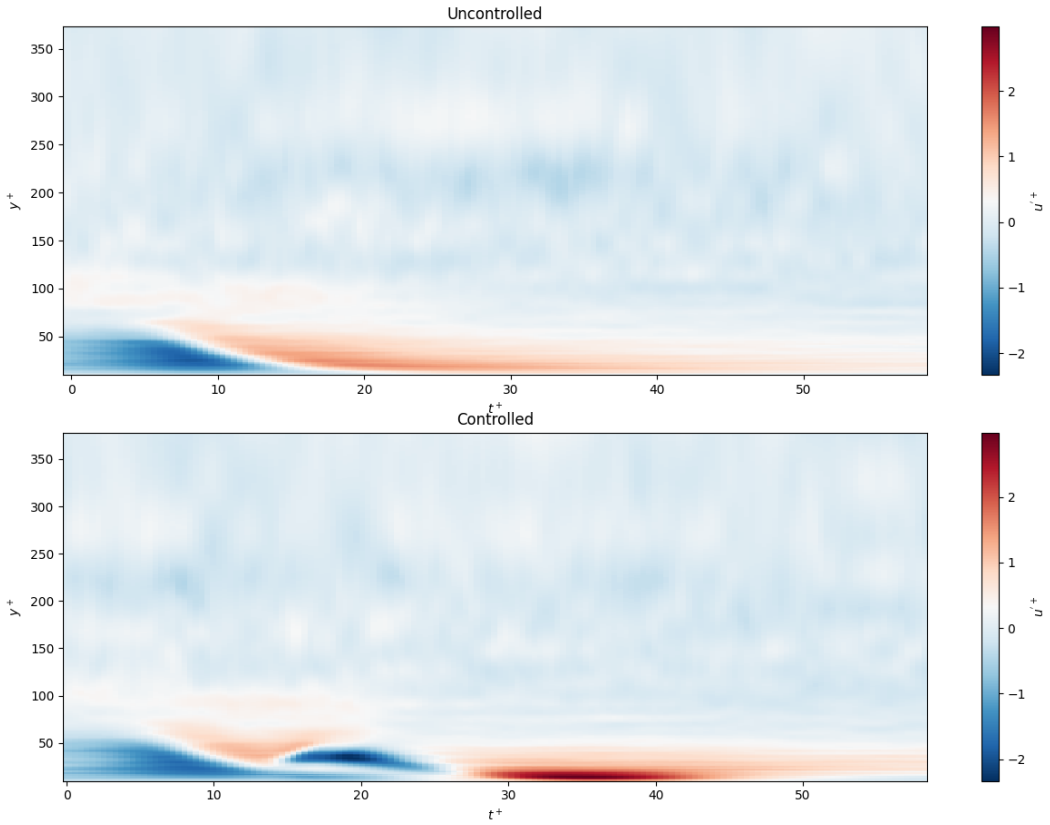


Fig. 3.36 2D space-time reconstruction of the conditionally-averaged streamwise velocity fluctuations u'^{+} in the (t^{+}, y^{+}) plane for Test Case 10 ("old-wave"): (top) Uncontrolled baseline showcasing the natural space-time topology of coherent structures; (bottom) Controlled flow field highlighting the footprint and structural disruption induced by the synthetic jet. After actuation is possible to see a region where the controlled flow shows effectively a streamwise velocity reduction, afterwards there is a *"velocity overshoot bubble"* where speed is recovered and increased greatly compared to the uncontrolled flow.

For Test Case 10 ("old-wave", see Figs. 2.10 and 3.36, bottom), the actuation exhibits a remarkably rapid onset following the detection of the sweep event (which is centered at $t^{+} = 0$). As depicted in Fig. 3.36 (bottom), at approximately $t^{+} \approx 10$, the incoming high-momentum fluid (indicated by the light red region) is effectively intercepted and displaced by a low-momentum region induced by the synthetic jet

blowing phase. This topological signature can be hypothesized to be a partial generation of the *virtual wall* mechanism theorized by Hammond et al. [4], which partially avoids the downward inrush of high momentum velocity toward the wall. However, despite this temporal synchronization, the beneficial effects of the initial streamwise velocity attenuation are compromised by the subsequent *velocity overshoot* region discussed in Section 3.3.2.

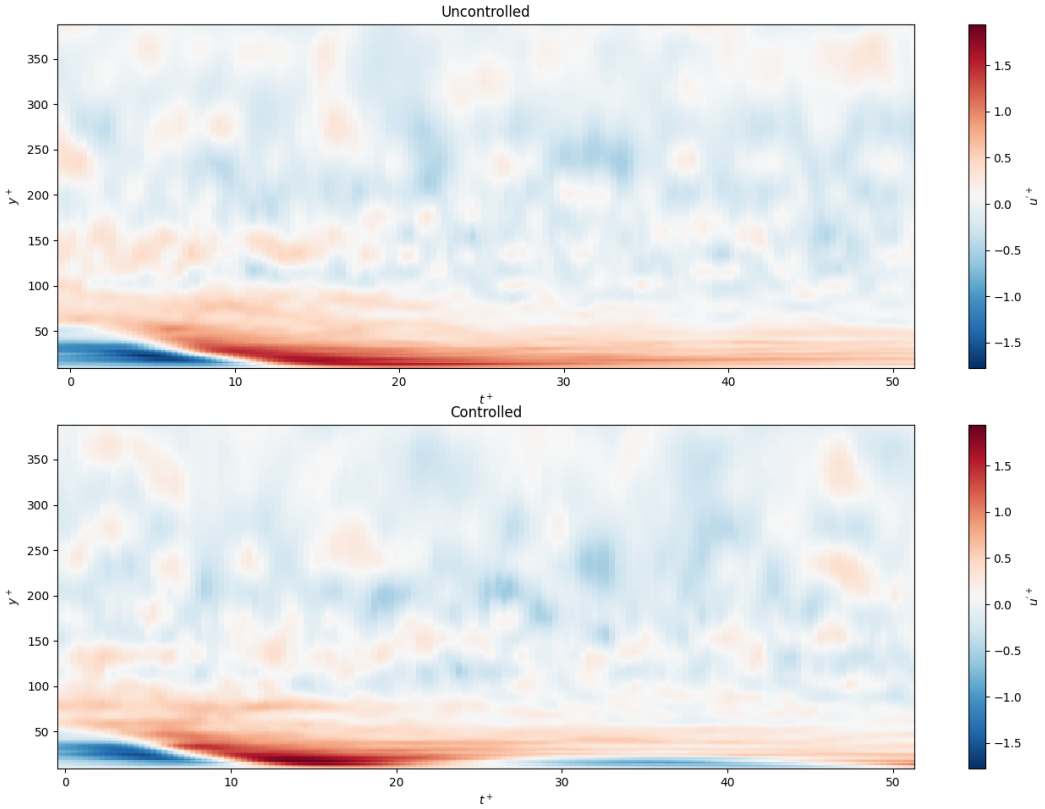


Fig. 3.37 2D space-time reconstruction of the conditionally-averaged streamwise velocity fluctuations u'^+ in the (t^+, y^+) plane for Test Case 13 ("new-wave"): (top) Uncontrolled baseline showcasing the natural space-time topology of coherent structures; (bottom) Controlled flow field highlighting the aerodynamic footprint and structural disruption induced by the synthetic jet. After actuation is possible to see a region where the controlled flow shows effectively a streamwise velocity reduction, but in comparison with the previous image regarding Test Case 10, the "new-wave" driving function deters the streamwise speed recovery, avoiding the formation of the *"velocity overshoot bubble"*.

Specifically, an expansive near-wall zone emerges where the streamwise velocity fluctuations intensely rebound, even exceeding the maximum u'^+ peak of the unforced sweep. As previously established, this is the direct aerodynamic consequence

of the excessively harsh suction phase, which actively entrains high-momentum fluid toward the wall, thereby generating a detrimental *synthetic sweep*.

Conversely, the space-time colormap for Test Case 13 (Fig. 3.37) validates the observations made in Section 3.3.2. The implementation of the "new-wave" driving function prevents the near-wall velocity rebound. By imposing a more gradual and prolonged suction phase, the actuator entrains fluid much less aggressively, thereby avoiding the artificial acceleration of the flow beyond the natural sweep velocities. However, unlike Test Case 10, the "new-wave", with the specific actuation parameters used in this measurements, doesn't oppose the sweep event as well. Because the blowing phase lacks the necessary initial impulsiveness, the high-momentum core of the natural sweep event is allowed to impinge directly upon the wall. The mitigating footprint of the jet actuation (visible as a light blue, low-speed region) only becomes topologically appreciable at a delayed dimensionless time of $t^+ \approx 30$.

In conclusion, this comparison highlights a fundamental physical trade-off between the two baseline waveforms. The "old-wave" in Test Case 10 was capable of partially shielding the surface from the initial sweep impact, but its overly aggressive suction phase triggered an unwanted velocity overshoot (the *synthetic sweep*) likely to penalize the overall skin friction reduction. On the other hand, the "new-wave" in Test Case 13 successfully eliminated the extreme near-wall fluctuations, but exhibited a milder, delayed control authority that failed to intercept the sweep structure in time. This topological evidence strongly underlines the necessity for a more refined calibration of the convective time delay (Δt), the phase shift and ultimately the waveform shape itself, in order to optimally combine the rapid-response interception of the former with the clean, non-disruptive suction phase of the latter.

3.4 Extensive Parametric Characterization of the Actuation Authority

To comprehensively map the efficacy of the active flow control system and optimize the synthetic jet parameters, an extensive parametric study was conducted. Moving beyond the detailed analysis of individual canonical test cases (such as Test Case 10 and Test Case 13), this Section evaluates a wide experimental matrix comprising 357 distinct measurement points, often repeated to test the repeatability of the control

impact at fixed actuation parameters, acquire with the workflow Detailed in Appendix G.

During this survey measurements of the controlled flow were collected, varying actuation parameters manually, along the implementation of the two different control set-ups described in Chapter 2. The objective is to quantify the global impact of varying the actuation driving functions, specifically focusing on the temporal delay, amplitude, and the fundamental shift from symmetric to asymmetric (sinusoidal vs. custom triangular 2.13) waveforms, on the near-wall turbulence dynamics, ultimately evaluating roughly wall skin friction reduction $\Delta\tau_{wall}$. Particularly, the control parameters were varied as explained for the two control setups:

- **First control set-up:** involving a signal generator and, for initial measurements, a voltage divider circuit that reduced the initial signal voltage amplitude by a factor of 4, making the effective voltage amplitude sent to the loudspeaker equal to $Vpp_{eff} = Vpp_{gen}/4$. During the measurement campaign the voltage divider circuit was then eliminated due to the fact that it introduced noise, as also detailed in Section 3.1.5. The driving loudspeaker function was the half-sine represented in Fig.2.10 (right). The actuation parameters implemented are detailed in Table 3.4, keep in mind that the analyzed cases involved several combinations of the actuation parameters.

- **Second control set-up:** the parameters implemented controlled the shape of a triangular custom wave generated by a routine implemented on a microcontroller, as detailed in Chapter 2, Fig. 2.10. The actuation parameters varied as listed in Table 3.5.

During all the measurements, the rear hot-wire probe was positioned at a streamwise position of $x^+ = 65$ downstream the control orifice and a wall-normal position of approximately $y^+ \approx 4$, with sporadic evaluations of the controlled flow further away from the surface. The set sampling frequency was of $f_s = 10000\ Hz$, with sampling time $t_s = 240\ s$ in order to detect a sufficient number of sweep events at each measurement.

Table 3.4 Experimental parameter space for the first control set-up. Generator Voltage is the one sent by the signal generator, while the effective voltage amplitude was the voltage effectively fed to the loudspeaker due to the use of a voltage divider circuit with a factor of 1/4. When n.d. is displayed next to the effective voltage amplitude value, it means that the divider was not employed.

Parameter	**Symbol**	**Unit**	**Values / Range**
Generator voltage amplitude	$V_{pp,gen}$	[mV]	20, 30, 50, 65, 80, 100
Effective voltage amplitude	$V_{pp,eff}$	[mV]	5.0, 7.5, 12.5, 16.25, 20, 25
Effective voltage amplitude(n.d.)	$V_{pp,eff}$	[mV]	30, 35, 40, 50, 100
Time delay	Δt	[ms]	0.1, 0.15, 0.5, 1, 1.2, 2, 3, 5
Frequency	f	[Hz]	10, 30, 40, 45, 50, 60

Table 3.5 Experimental parameter space for the second control set-up, Arduino Giga.

Parameter	**Symbol**	**Unit**	**Values**
Voltage amplitude	V_{pp}	[mV]	20, 25, 30, 35, 40, 50, 60, 75, 100
Time delay	Δt	[ms]	0.0, 0.1, 0.15, 0.5, 1.0, 2.0, 3.0, 4.0, 6.0, 8.0
Frequency	f	[Hz]	5.0, 10, 20, 30, 35, 40, 50, 60, 70, 80, 100, 120, 140, 160, 200
x %	x	[%]	1, 10, 50, 90

3.4.1 Data Post-Processing and Analysis Strategy

To ensure the reliability and statistical significance of the experimental findings, the raw data acquired during the testing campaigns were subjected to a post-processing Python routine through the script detailed in Appendix H. The analysis strategy is designed to transform high-frequency temporal signals into coherent physical metrics, enabling a structured evaluation of the opposition control effectiveness.

The analytical workflow, of the post-processing of the controlled flow data starts with an automated exclusion procedure, to isolate measurements in the near-wall region, selecting only data points characterized by a non-dimensional wall velocity $u^+ < 5$. This spatial constraint ensures that the discussion focuses on the viscous sublayer, where the interaction between the control signal and the fluid structures is most prominent and where there is the region of interest to evaluate the effectiveness of the control actuation. In fact, only measurements of the controlled flow where the rear-probe rested at $y^+ < 5$ were considered, this control was effectuated taking advantage of the viscous sublayer law $u^+ = y^+$ and eliminating all measurements where the average of the streamwise adimensional velocity signal was higher than 5.

Subsequently, to account for variations in sampling and temporal coordination across different test runs with same actuation parameters, the time-series data were normalized and interpolated onto a common temporal grid. This synchronization is critical for accurately calculating the mean profiles and assessing the reproducibility of the system under identical control configurations.

Finally, the processed data are aggregated to synthesize the system's performance, ranging from individual trial repeatability to global energetic evaluations. The findings derived from this methodology are presented and discussed in the following subsections:

- **Aggregated performance:** Evaluations of the controlled flow that were repeated more than once, are averaged together obtaining aggregated averages. The mean controlled and uncontrolled profiles are analyzed to quantify the impact of the control strategy on the skin friction reduction.
- **Control parameter sensitivity:** This section explores the influence of frequency, amplitude, and time delay on the control efficacy, identifying the optimal operational regimes for both control setups, the one were the driving function was produced by a signal generator and the one where an Arduino Giga created a custom triangular wave.
- **Energetic saturation and performance comparison:** Finally, the performance of the different hardware implementations (Signal generator vs. Arduino Giga) is compared, with a particular focus on the saturation limits of the achieved drag reduction.

The performance of the active flow control strategy was evaluated by quantifying the subsequent reduction in wall shear stress (see Appendix H). Given that all analyzed measurements were acquired within the viscous sublayer at a nominal wall distance of $y^+ \approx 4$, the local flow conditions can be characterized with the viscous sublayer law $u^+ = y^+$ and utilizing the known ambient fluid properties and friction velocity scales: $u_\tau = 0.161\,\mathrm{m/s}$, $\nu = 1.51 \times 10^{-5}\,\mathrm{m^2/s}$, and $\mu = 1.82 \times 10^{-5}\,\mathrm{Pa \cdot s}$.

It's important to clarify that the following evaluation of the wall skin friction was obtained using the viscous flow variables, u^+ and y^+, since they were the readily available output of the measurement campaigns. In fact, the Python script used for acquisitions obtained automatically the streamwise viscous velocity component from the hot-wire signal and the viscous distance from the wall.

By definition, the non-dimensional wall distance y^+, the friction velocity u_τ, and the non-dimensional streamwise velocity u^+ are expressed as follows:

$$y^+ = \frac{y u_\tau}{\nu} \tag{3.3}$$

$$u_\tau = \sqrt{\frac{\tau_{wall}}{\rho}} \tag{3.4}$$

$$u^+ = \frac{u}{u_\tau} \tag{3.5}$$

Substituting these definitions into the fundamental Newtonian shear stress formula allows for the simplification of the wall shear stress calculation. By virtue of the linear law valid within the viscous sublayer ($u^+ = y^+$), and exploiting the fact that both velocity and wall-distance values are sufficiently small in the immediate vicinity of the wall, the partial derivative can be closely approximated via finite differences:

$$\tau_{wall} = \mu \frac{\partial u}{\partial y} = \mu \frac{\partial u^+}{\partial y^+} \frac{u_\tau^2}{\nu} \approx \frac{\mu \Delta u^+ u_\tau^2}{\Delta y^+ \nu} \tag{3.6}$$

Where $\Delta y^+ = 4$ corresponds to the fixed dimensionless coordinate of the hot-wire probe at the time of measurement, and Δu^+ is represented by the ensemble-averaged, conditionally-sampled streamwise velocity fluctuation ($\overline{u'^+}$). By substituting the respective velocity fluctuations for the unmanipulated (uncontrolled) and manipulated (controlled) configurations, an estimate of the wall shear stress is obtained for both

states:

$$\tau_{wall,uncon} \approx \frac{\mu \overline{u'^{+}}_{uncon} u_{\tau}^{2}}{4\nu} \tag{3.7}$$

$$\tau_{wall,con} \approx \frac{\mu \overline{u'^{+}}_{con} u_{\tau}^{2}}{4\nu} \tag{3.8}$$

Consequently, the absolute net variation in wall shear stress brought about by the actuation system is determined as:

$$\Delta\tau_{wall}\% = \frac{\tau_{wall,uncon} - \tau_{wall,con}}{\tau_{wall,uncon}} \tag{3.9}$$

In the subsequent sections, only experimental datasets featuring multiple independent repetitions at fixed actuation control parameters are considered, thereby ensuring the statistical repeatability and convergence of the analyzed data.

3.4.2 Aggregated Near-Wall Performance and Parametric Analysis

To evaluate the global impact of the opposition control strategies and verify the statistical reproducibility of the experimental campaign, an analysis of the aggregated mean profiles was performed. Individual experimental runs sharing identical control parameters, voltage amplitude ($V_{pp} = \widehat{A}$), actuation frequency (f), time delay (Δt) for the first control set-up with the signal generator (see Fig. 2.11); voltage amplitude ($V_{pp} = \widehat{A}$), actuation frequency (f), time delay (Δt), and spatial asymmetry factor ($x\%$) for the Arduino Giga set-up (see Fig. 2.14), were grouped and ensemble-averaged.

Crucially, as explained in the previous Subsection 3.4.1, a geometric and physical constraint was applied by removing out all data points outside the viscous sublayer, specifically targeting the region where $y^{+} \approx u^{+} < 5$. Isolating the flow field in such close proximity to the wall is essential: it ensures that the recorded velocity fluctuations are directly linked to the small-scale coherent structures responsible for the generation of wall-shear stress.

Figs. 3.38 through 3.42 present a panoramic of the aggregated averages of the controlled flow with common actuation parameters tested using the Arduino Giga

set-up, while Fig. 3.43 displays the corresponding dataset for the standard signal generator configuration.

In these subplots, the uncontrolled non-dimensional streamwise velocity u^+ of the baseline flow (black dashed line) is systematically compared against the controlled streamwise velocity, represented with solid blue (Figs. 3.38 through 3.42) or red lines (Fig. 3.43). Comparing the Arduino Giga control set-up results (Figs. 3.38 through 3.42) with the signal generator plots (Fig. 3.43), one can notice that the voltage amplitudes of the signal generator are significantly lower; this is because during the survey of the controlled flow with the signal generator control set-up only measurements with the voltage divider circuit were repeated more than once and also they were taken at a distance from the wall that met the geometrical and physical constraint of $u^+ = y^+ < 5$ (viscous sublayer). Despite this, the lack of high voltage amplitudes cases in Fig. 3.43 can be an opportunity to analyze the effect of really low voltage amplitudes showing that skin friction reduction can be obtained even employing low energy jets, reducing the power needed to apply the opposition control schemes in potential engineering applications.

All subplots for Figs. 3.38 through 3.42 have the time origin $t^+ = 0$ centered at the instant of sweep detection, when the comparator sends a TTL to the Arduino Giga or the signal generator.

For both experimental setups the uncontrolled flow (dashed black line) exhibits the characteristic sudden reduction and then abrupt increase in streamwise velocity, denoting the passage of a sweep structure. When the opposition control is active, a clear modification of this convective peak is observed across several parameter combinations. Successful control configurations manifest either as a significant attenuation of the peak magnitude or a visible downward shift in the post-event velocity trace ($t > 0\,\mathrm{s}$). This reduction in u^+ within the viscous sublayer provides direct, quantitative evidence of a localized mitigation of skin friction.

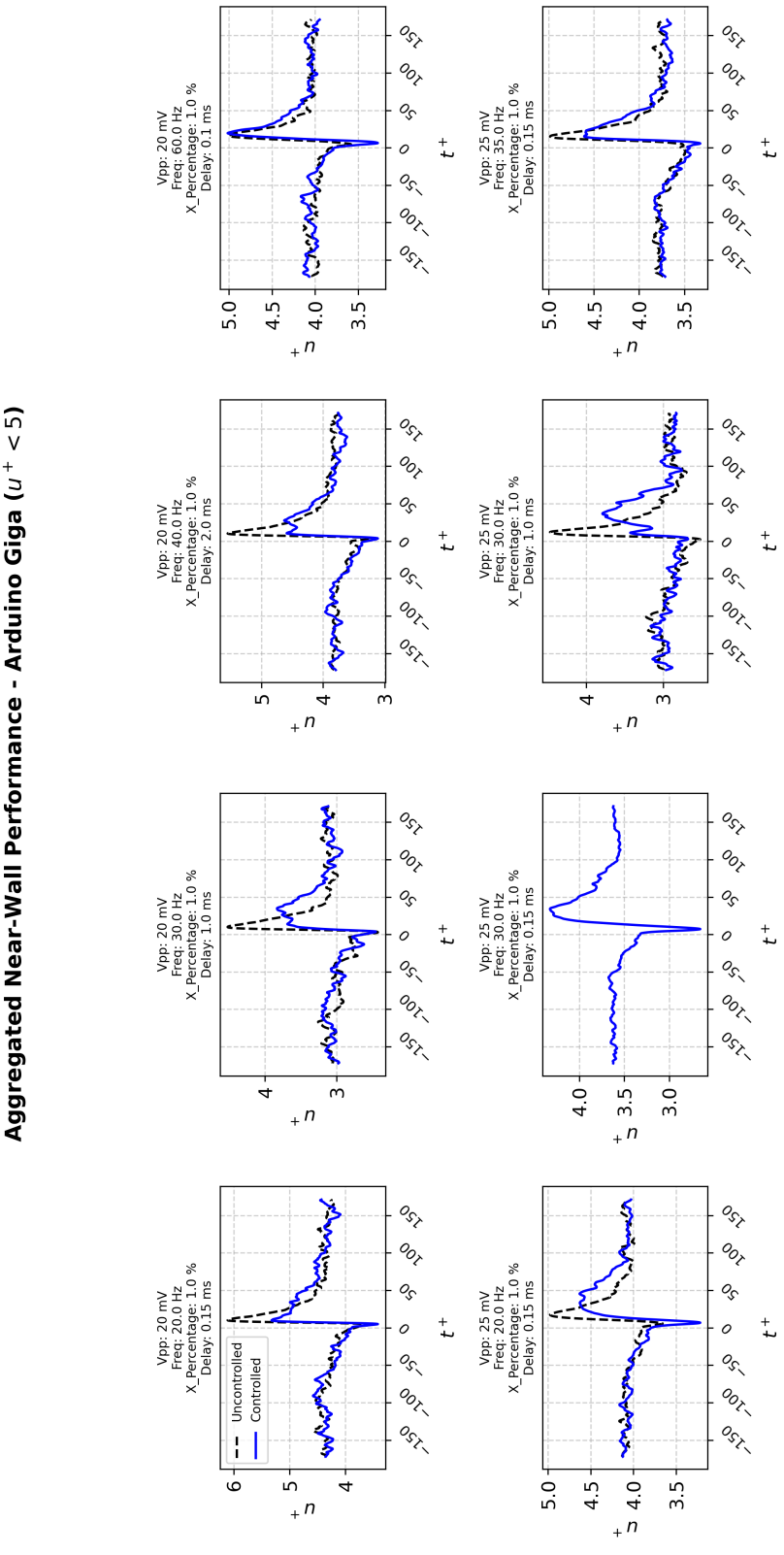


Fig. 3.38 Aggregated near-wall velocity profiles ($u^+ < 5$) for the Arduino Giga set-up (Part 1). The panels depict the ensemble-averaged controlled response (blue solid line) versus the uncontrolled baseline (black dashed line) across low frequency and voltage amplitude variations.

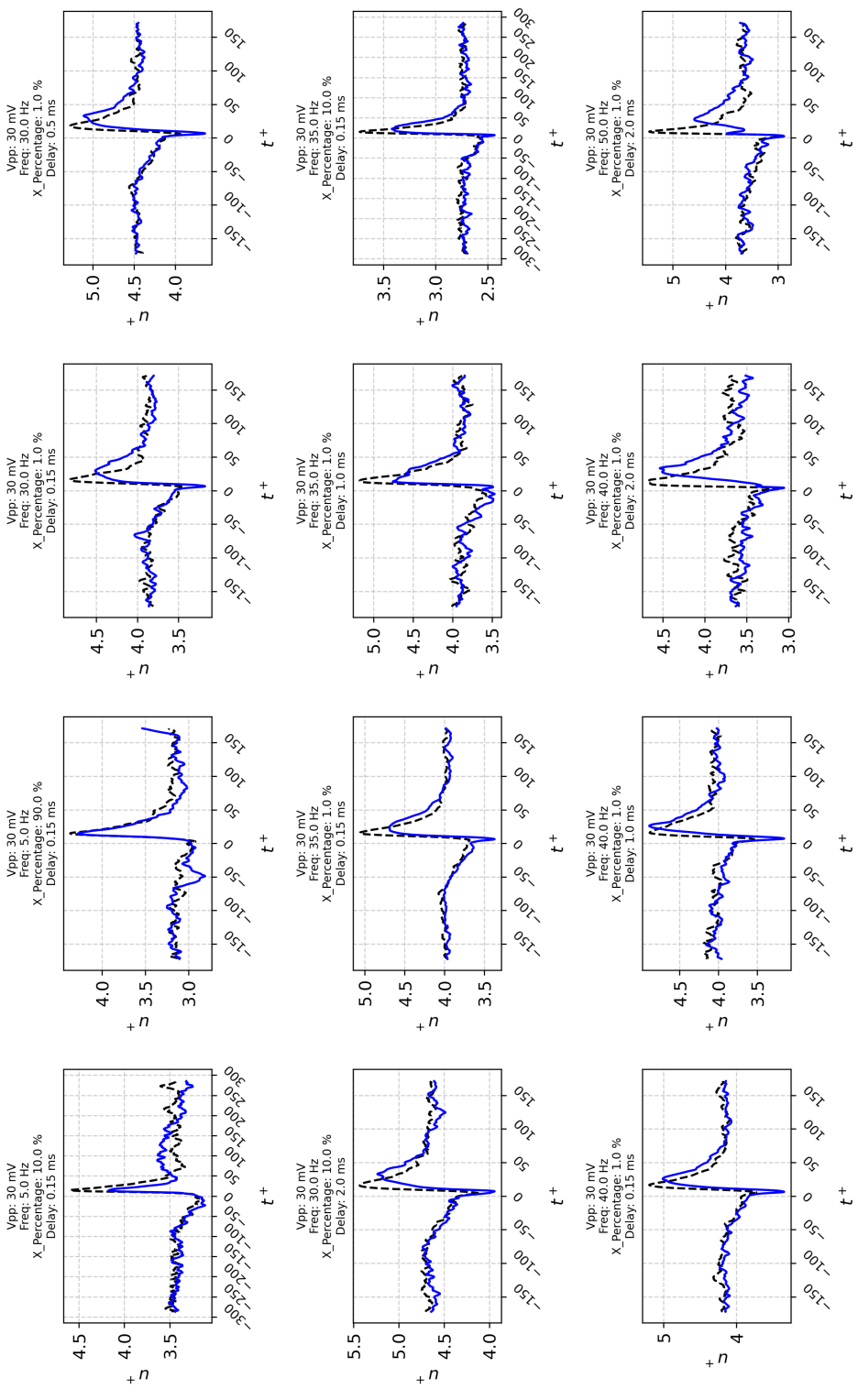


Fig. 3.39 Aggregated near-wall velocity profiles ($u^+ < 5$) for the Arduino Giga set-up (Part 2). The panels depict the ensemble-averaged controlled response (blue solid line) versus the uncontrolled baseline (black dashed line). This parametric subset focuses on variations of frequency and delay time to evaluate synchronization between the sweep and the control actuation.

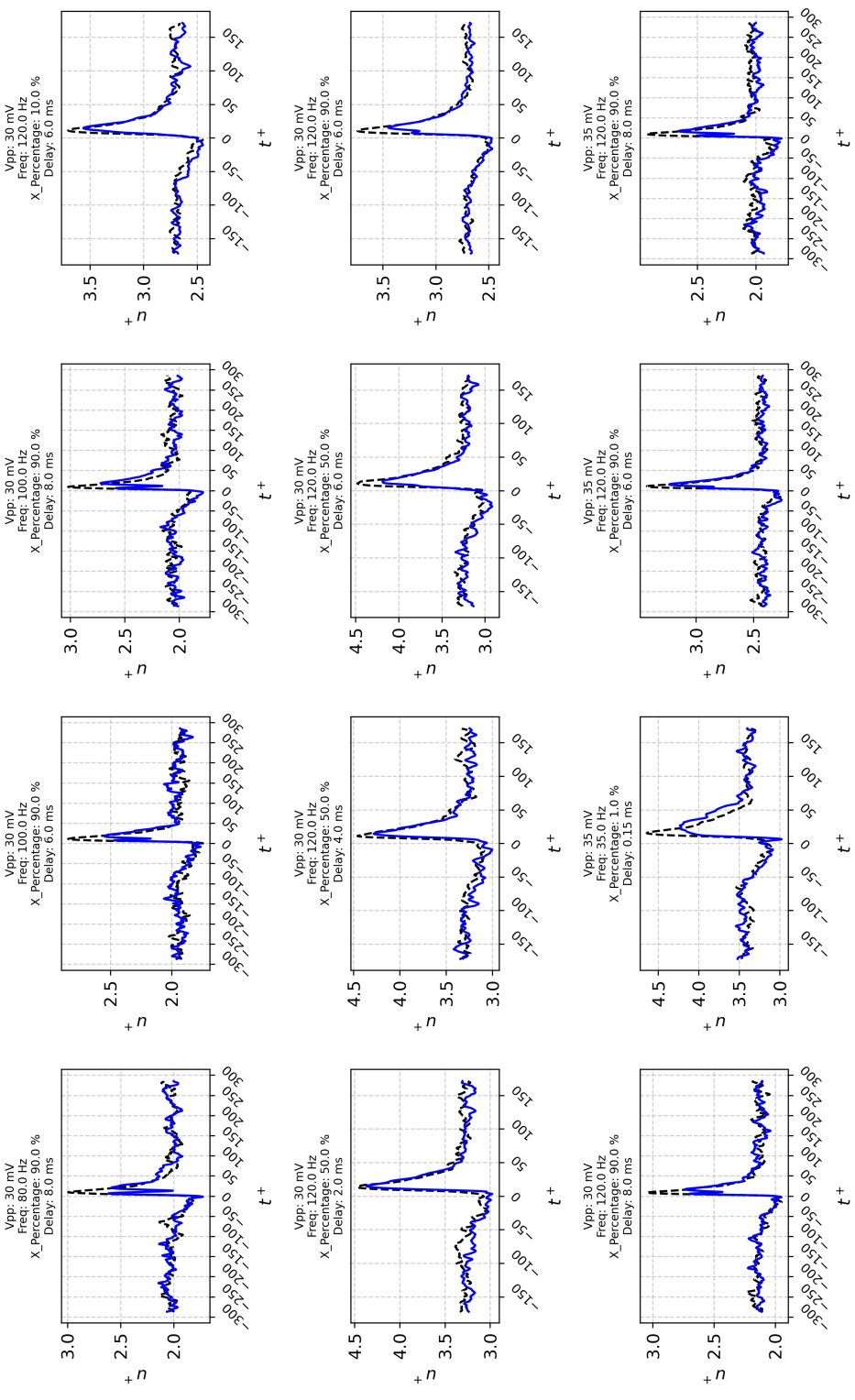


Fig. 3.40 Aggregated near-wall velocity profiles ($u^+ < 5$) for the Arduino Giga set-up (Part 3). The panels depict the ensemble-averaged controlled response (blue solid line) versus the uncontrolled baseline (black dashed line). The plots illustrate the controlled streamwise velocity under high-frequency actuation regimes and time delays and varying spatial asymmetry percentages ($x\%$).

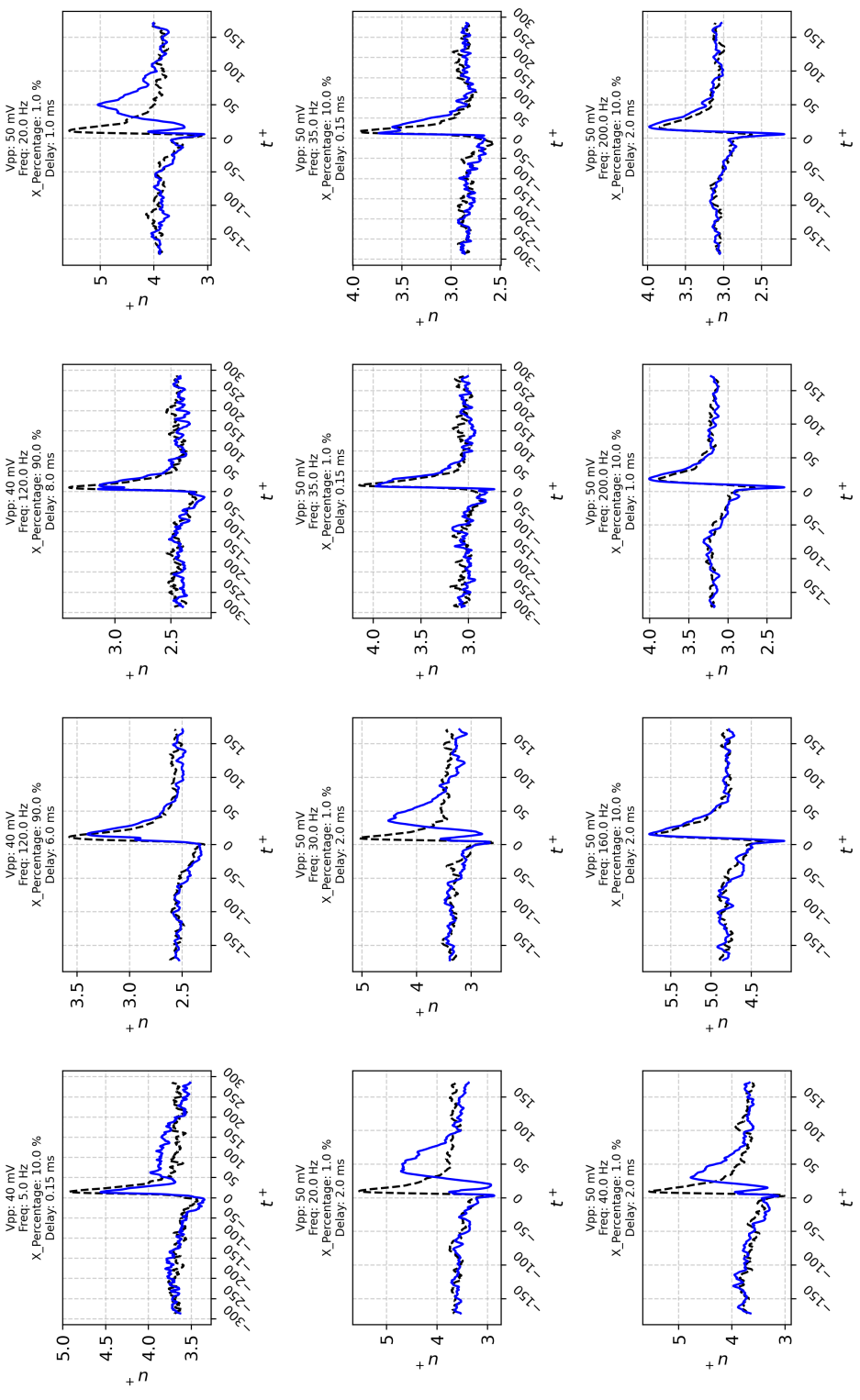


Fig. 3.41 Aggregated near-wall velocity profiles ($u^+ < 5$) for the Arduino Giga set-up (Part 4). The panels depict the ensemble-averaged controlled response (blue solid line) versus the uncontrolled baseline (black dashed line). High frequency and higher amplitude voltages are presented in this subset

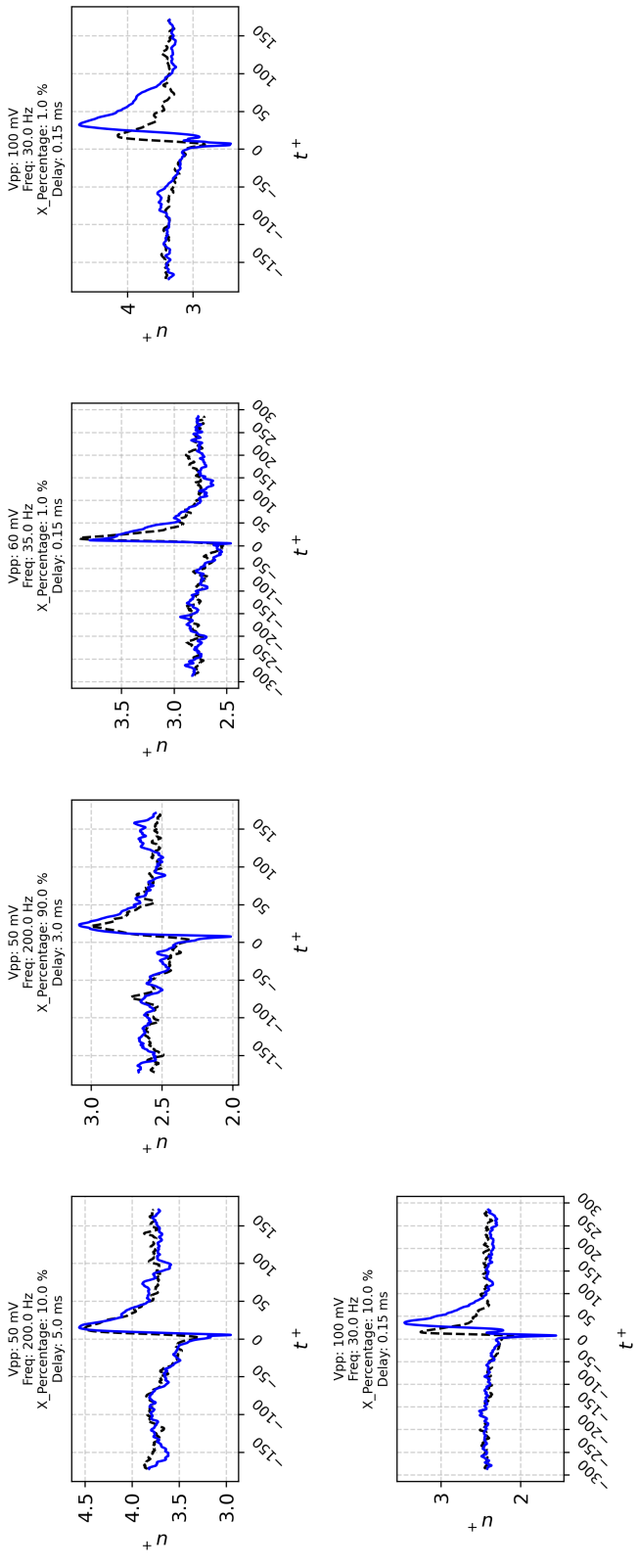


Fig. 3.42 Aggregated near-wall velocity profiles ($u^+ < 5$) for the Arduino Giga set-up (Part 5). The panels depict the ensemble-averaged controlled response (blue solid line) versus the uncontrolled baseline (black dashed line). This final subset demonstrates the maximum voltage amplitudes studied ($V_{pp} = \widehat{A}$ up to 100 mV).

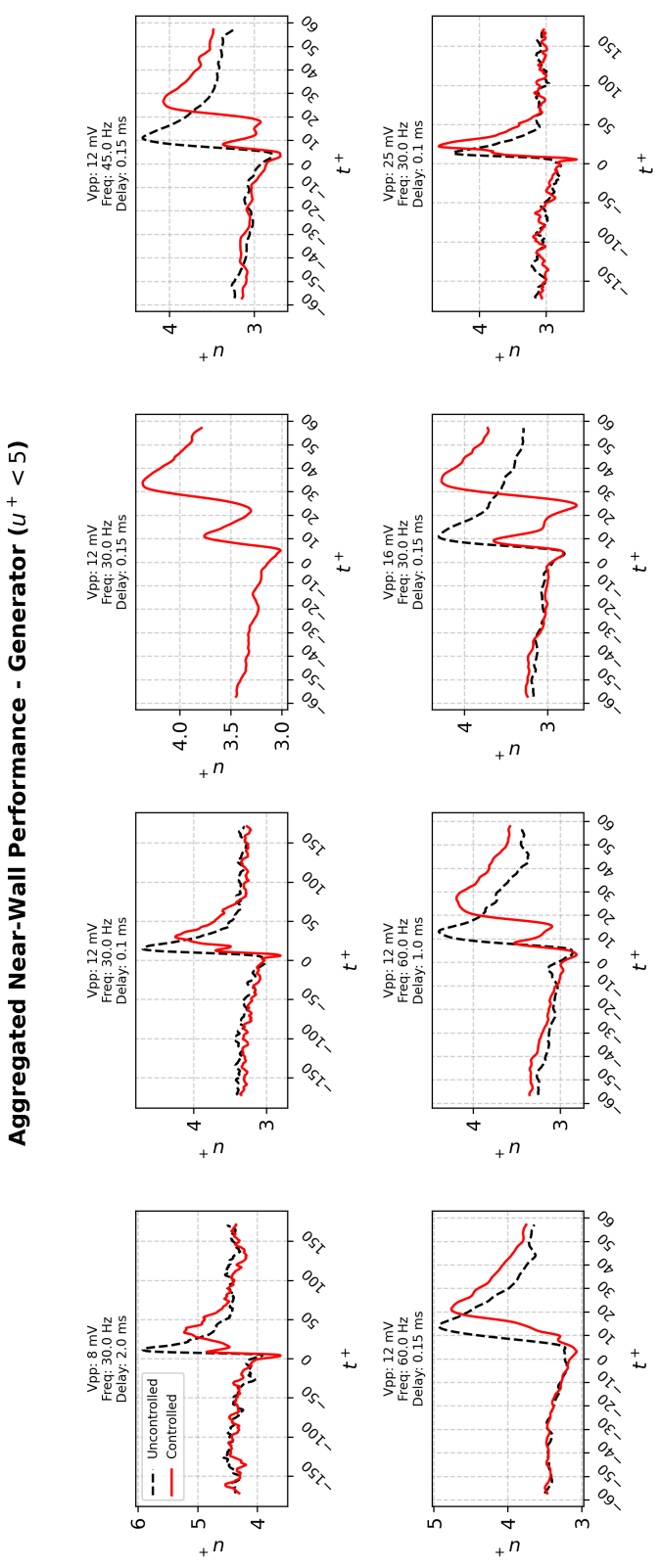


Fig. 3.43 Aggregated near-wall velocity profiles ($u^+ < 5$) for the analog signal generator benchmark. The panels track the ensemble-averaged controlled response (red solid line) against the uncontrolled flow baseline (black dashed line), serving as the reference case for the active flow control campaign.

The main observations that came out of this parametric survey of the controlled flow are gonna be presented in the following paragraphs.

Observed Parametric Impact

- **Frequency vs.** $x\%$ **and time delay** Δt **:** for both the two experimental set ups it's possible to conclude that low frequencies allow the jet to be more prolonged in time, if the frequency is too low, as $f = 5$ Hz the membrane of the loudspeaker might not be impulsive enough to "catch" the sweep event in time as it passes the jet orifice, unless the blowing phase is tuned with other time-related parameters. For example, in Fig. 3.44, are represented two cases of the controlled flow by the custom triangular wave (Arduino Giga), on the left the control settings are $\widehat{A} = 30$ mV, $f = 5.0$ Hz, $x\% = 10\%$, $\Delta t = 0.15$ ms and on the right $\widehat{A} = 30$ mV, $f = 5.0$ Hz, $x\% = 90\%$, $\Delta t = 0.15$ ms. While on the right, the low frequency is balanced by a relatively low value of $x\% = 10$, which represents the percentage of the duration of the actuation cycle characterized by the blowing phase, that allows such phase to be fast enough to counter the sweep event "on time", effectively reducing u^+. In the right case the high value of $x\% = 90$ causes the blowing phase to be too soft, slowing down even more the already tardy jet (due to the low frequency), leading to a ineffective control.

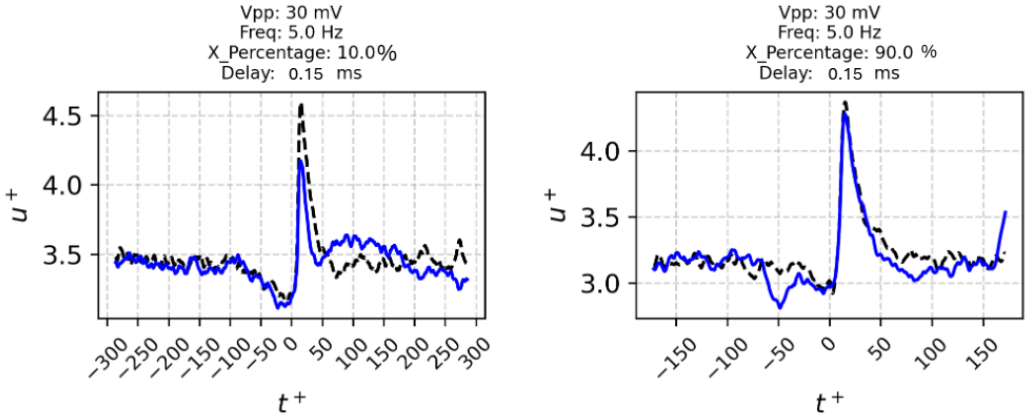


Fig. 3.44 Comparison between controlled flows obtained with a set of actuation parameters involving low frequency and low $x\%$ with control settings $\widehat{A} = 30$ mV, $f = 5.0$ Hz, $x\% = 10\%, \Delta t = 0.15$ ms (left) and with a set employing high frequency and hig $x\%$ $\widehat{A} = 30$ mV, $f = 5.0$ Hz, $x\% = 90\%, \Delta t = 0.15$ ms (right). Dashed black lines: uncontrolled flow, blue line: controlled flow by the triangular custom wave (second control set-up woth Arduino Giga)

- **High values of frequency analyzed vs. high values of voltage amplitude:** high frequency values combined with high voltage amplitudes attenuated the creation of the *"synthetic sweep"* detailed in Section 3.2 the velocity overshoot after the initial u^+ reduction due to the control effect. High voltage amplitudes fed the loudspeaker imply stronger jets, stringer blowing phase and consequently stronger suction phases, that ad seen in the precious sections caused the recovery of streamwise speed after the control was actuated; setting high frequency causes the jet to be almost impulsive, localizing its effect at the actuation instant and avoiding draining the jet as the sweep event ends. However, if the frequency is too high, the jet duration becomes too short to effectively counter the sweep, ending too early and failing to reduce the streamwise velocity of the controlled case compared to the uncontrolled flow. This phenomenon can be clearly observed by comparing the following cases of controlled flow using the second control set-up (triangular custom wave).

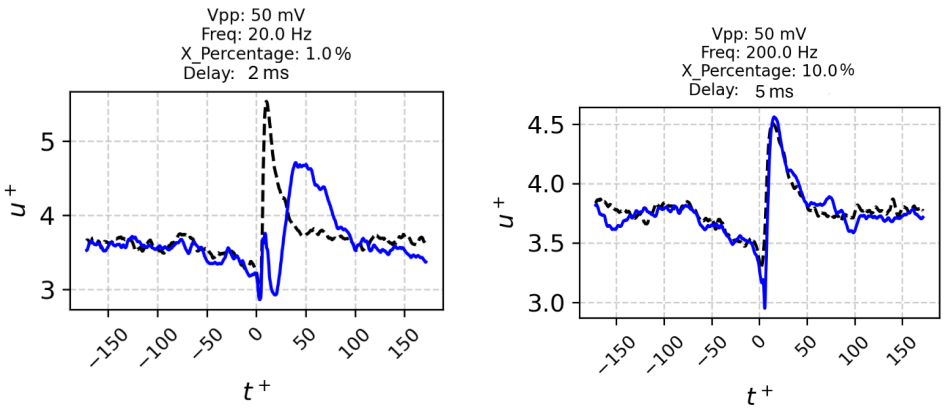


Fig. 3.45 Comparison between controlled flows obtained with a set of actuation parameters involving low frequency and high voltage $\widehat{A} = 50$ mV, $f = 20$ Hz, $x\% = 1\%, \Delta t = 2$ ms (left) and with a set employing high voltage and high frequency $\widehat{A} = 50$ mV, $f = 200$ Hz, $x\% = 10\%, \Delta t = 5$ ms (right). Dashed black lines: uncontrolled flow, blue line: controlled flow by the triangular custom wave (second control set-up with Arduino Giga)

In Fig. 3.45 (left) the actuation parameters are $\widehat{A} = 50$ mV, $f = 20$ Hz, $x\% = 1\%, \Delta t = 2$ ms (high voltage and low frequency) and it's evident that the high voltage effectively reduces the streamwise velocity upon sweep detection, but the harsh suction phase caused by the great amplitude of the driving function creates an overshoot of velocity after the sweep ends, caused by the fluid being recalled aggressively by the loudspeaker membrane. While in Fig.3.45 (right) the actuation parameters are $\widehat{A} = 50$ mV, $f = 200$ Hz, $x\% = 10\%, \Delta t = 5$ ms (high voltage and high frequency) and, even though the delay and percentage change from the left case, the fact that the jet has too much of a short duration is tangible because, after an initial reduction of u^+ of the controlled flow further than the uncontrolled flow, the velocity then recovers completely letting the sweep structure take over, as a matter of fact the peaks of both the black dashed line (unmanipulated flow) and the blue line (manipulated flow) coincide perfectly.

- **High Voltages vs. Low Voltages:** as already detailed in the previous sections, exceedingly high voltages generate a recover in velocity caused by a strong suction phase, after its initial reduction from the jet effect. Even if high voltages can actually be beneficial in countering effectively the sweep structure, if too high and not tuned with other parameters (such as combining high voltages and high frequencies), they can cause the overshoot

that is visible in Fig. 3.46 (right). In Fig. 3.46 a low voltage measurement ($\widehat{A} = 7$ mV, $f = 30$ Hz, $\Delta t = 2$ ms) is compared to a high voltage one ($\widehat{A} = 16$ mV, $f = 30$ Hz, $\Delta t = 0.15$ ms). Note that being cases obtained with the first control set-up, which employed a voltage divider circuit (with division factor of 4) the overall voltages are significantly smaller than the ones implemented on the second control set-up.

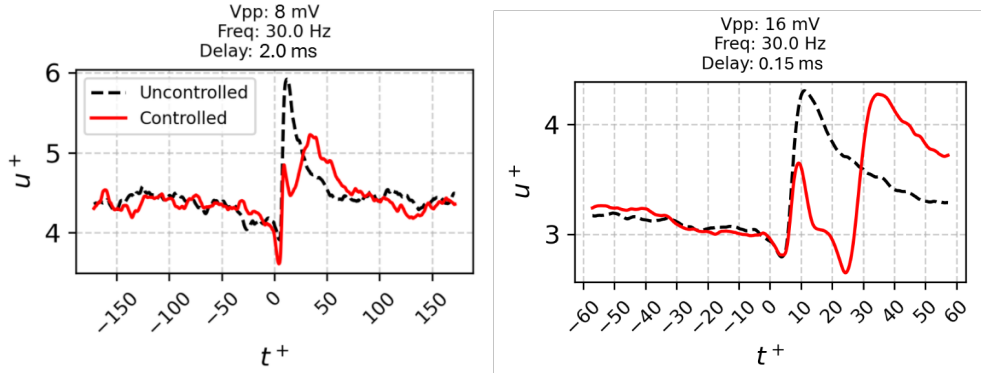


Fig. 3.46 Comparison between controlled flows obtained with a set of actuation parameters involving low amplitude $\widehat{A} = 7$ mV, $f = 30$ Hz, $\Delta t = 2$ ms (left) and with a set employing high voltage $\widehat{A} = 16$ mV, $f = 30$ Hz, $\Delta t = 0.15$ ms (right). Dashed black lines: uncontrolled flow, blue line: controlled flow by the half-sine driving function ("new-wave" first control set-up with signal generator and voltage divider circuit)

3.4.3 Control Parameter Sensitivity and Optimization Maps

To navigate the expansive parameter space and identify the optimal operational regimes for the opposition control, parametric maps were generated for both the analog signal generator and the Arduino Giga configurations. These scatter maps provide a macroscopic view of the system's efficacy, plotting the mean skin friction reduction ($\Delta\tau_{wall}$) against the primary independent variables. The value of $\Delta\tau_{wall}$ was computed as explained at the end of Section 3.4.1.

Fig. 3.47 displays the control map for the signal generator, illustrating the interplay between the time delay (Δt) and the actuation frequency (f). The color gradient represents the percentage reduction in skin friction, with the highest performance clusters (yellow/green markers) localized at specific low-delay settings (e.g., $\Delta t < 1$ ms) and distinct frequencies. The presence of discrete performance peaks separated by regions of negative effect (drag increase, denoted by dark purple mark-

ers) highlights the extreme sensitivity of the wall-bounded turbulence to the phase alignment between the coherent sweep structures and the synthetic jet actuation.

Conversely, Fig. 3.48 presents the parametric map for the Arduino Giga set-up, operating with a customized triangular waveform. Here, the sensitivity is evaluated as a function of the signal asymmetry percentage ($x\%$) and the time delay. The map demonstrates that introducing a temporal asymmetry into the blowing/suction cycle alters the control authority. Optimal configurations (red markers) are achieved at specific combinations of delay and asymmetry, suggesting that tailoring the shape of the actuation wave to the natural timescales of the turbulent sweeps can yield substantial localized drag reduction, reaching peaks comparable to the analog generator.

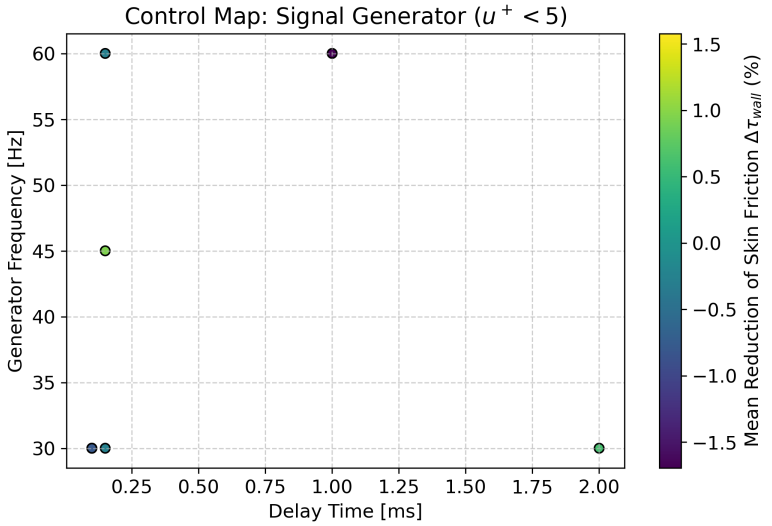


Fig. 3.47 Parametric control map for the signal generator configuration. The scatter plot correlates actuation frequency and time delay with the resulting mean skin friction reduction ($\Delta\tau_{wall}$), highlighting discrete optimal operating regions in the parameter space.

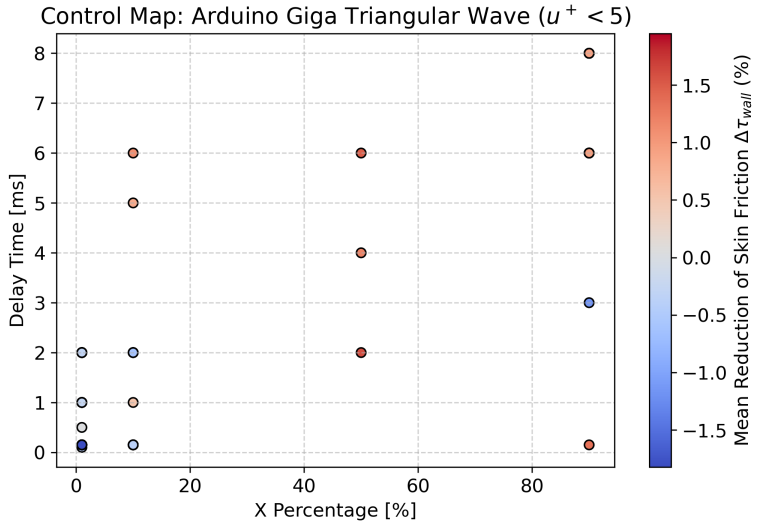


Fig. 3.48 Parametric control map for the Arduino Giga set-up utilizing a triangular waveform. The map evaluates control efficacy as a function of the signal's spatial asymmetry ($x\%$) and delay time, revealing the impact of customized wave shapes on wall-bounded turbulence manipulation.

3.4.4 Comparison of Optimal Control Configurations

Building upon the parametric mapping, a direct temporal comparison between the most effective test cases of each hardware configuration was conducted to assess the physical mechanism of friction reduction. Fig. 3.49 juxtaposes the conditionally-averaged velocity profiles of the optimal signal generator case and the optimal Arduino Giga case.

In both instances the activation of the optimal opposition control (solid red and blue traces) results in a drastic suppression of the velocity peak. By injecting momentum in precise opposition, the synthetic actuator counters the downwash of the turbulent structure, preventing high-velocity fluid from reaching the viscous sublayer. Notably, despite operating under different voltage and waveform conditions, both the analog and digital control setups achieve a comparable maximum skin friction reduction of approximately 1.58% and 1.95%, validating the adaptability of the opposition control logic across different hardware architectures.

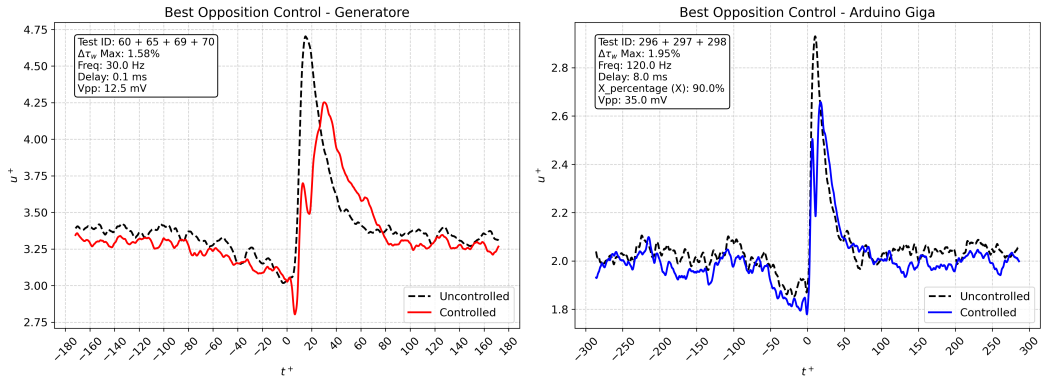


Fig. 3.49 Conditionally-averaged near-wall velocity profiles for the optimal control configurations. Left: signal generator at 30 Hz, 0.1 ms delay, and 13 mV. Right: Arduino Giga at 120 Hz, 8.0 ms delay, 90% asymmetry, and 35 mV. Both cases demonstrate a remarkable attenuation of the u^+ convective peak.

3.4.5 Statistical Distribution of Control Efficacy

To ensure that the observed maxima are not statistical outliers and to evaluate the overall robustness of the experimental campaign, the probability density of the skin friction reduction was visualized using a violin plot of two control setups results(Fig. 3.50).

As highlighted before, the analysis of the acquired data was restricted to control cases that were repeated more than one time to ensure better repeatability. Also, measurements with $u'^+ > 5$ were excluded from the analysed dataframe in order to focus on the near-wall region to better evaluate the $\Delta\tau_{wall}$. The resulting set of control parameters for both control set-ups, signal generator and Arduino Giga, are respectively listed in Tables 3.6 and 3.7

Table 3.6 Experimental parameter space bounds for the first control set-up with the signal generator , with restrictions of repeatability and near-wall measurement applied.

Parameter	**Symbol**	**Unit**	**Min**	**Max**
Voltage amplitude	V_{pp}	[mV]	7	25
Time delay	Δt	[ms]	0.1	2.0
Frequency	f	[Hz]	30	60

Table 3.7 Experimental parameter space bounds for the second control set-up Arduino Giga, with restrictions of repeatability and near-wall measurement applied.

Parameter	**Symbol**	**Unit**	**Min**	**Max**
Voltage amplitude	V_{pp}	[mV]	20	100
Time delay	Δt	[ms]	0.1	8.0
Frequency	f	[Hz]	5.0	200
x %	$x\%$	[%]	1	90

This statistical representation highlights the differing behaviors of the two hardware setups. The signal generator exhibits a broader, more stretched distribution, characterized by a higher variance. While it records substantial drag reduction peaks, it is also highly susceptible to off-design conditions, resulting in severe performance penalties (drag increases down to -3%). In contrast, the Arduino Giga dataset displays a more concentrated probability density centered marginally above zero. Although it encompasses a wider range of experimental parameters (including varying wave asymmetries and higher voltages), the digital set-up demonstrates a statistically more consistent behavior, maintaining a dense cluster of positive control outcomes, alongside the expected tails corresponding to misaligned phase parameters.

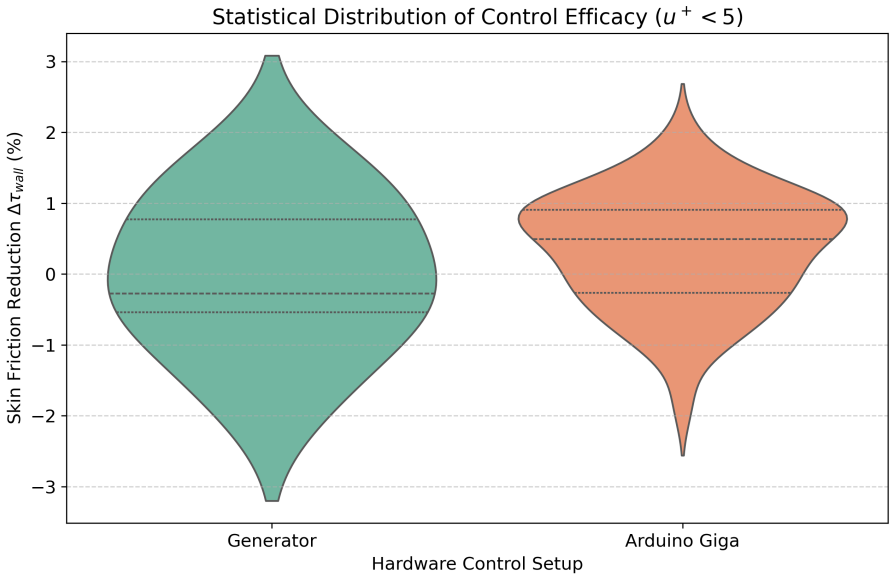


Fig. 3.50 Statistical distribution of the active control efficacy restricted to the near wall region results ($u^+ < 5$) for the signal generator and Arduino Giga configurations. The violin plots illustrate the probability density and interquartile ranges, comparing the variance and robustness of the two hardware setups.

3.4.6 Energetic Saturation and Actuation Limits

A critical aspect of active flow control is determining the energetic threshold beyond which further actuation input yields diminishing returns or actively degrades the flow state. This phenomenon, known as energetic saturation, is analyzed in Fig. 3.51, which plots the skin friction reduction against the actuation amplitude ($V_{pp} = \widehat{A}$).

Firstly, it's evident from the scatter plot that at fixed values of voltage amplitude, different skin fiction reduction values are obtained. It is vital to stress that in the scatter plot, for every voltage amplitude analysed the other parameters change (frequency and delay time for the signal generator and frequency, delay time and $x\%$ for the Arduino Giga set-up). This fact justifies the different skin friction reduction magnitudes at the same voltage amplitudes, as shown in the previous sections different sets of control parameters imply different effects on the controlled flow.

The scatter plot, augmented with linear regression trendlines and confidence intervals, clearly demonstrates a negative correlation between excessive voltage and control performance. For both the signal generator (clustered at lower voltages) and

the Arduino Giga (tested up to 100 mV), increasing the actuation amplitude beyond a specific threshold does not linearly translate into greater drag reduction. Instead, the trendline assumes a negative slope, confirming the observations of the previous sections, indicating that an overly energetic synthetic jet disrupts the delicate balance of the near-wall cycle, due to the previously observed velocity recovery or *"synthetic sweep"* caused by a harsher suction phase. In fact, rather than selectively canceling the incoming sweeps, excessive blowing introduces spurious kinetic energy into the near wall region, effectively overriding the opposition logic and resulting in a net increase in wall shear stress (negative $\Delta\tau_{wall}$). This highlights the necessity of fine-tuning the voltage fed to the actuator to match, rather than overwhelm, the natural scales of the targeted turbulent structures.

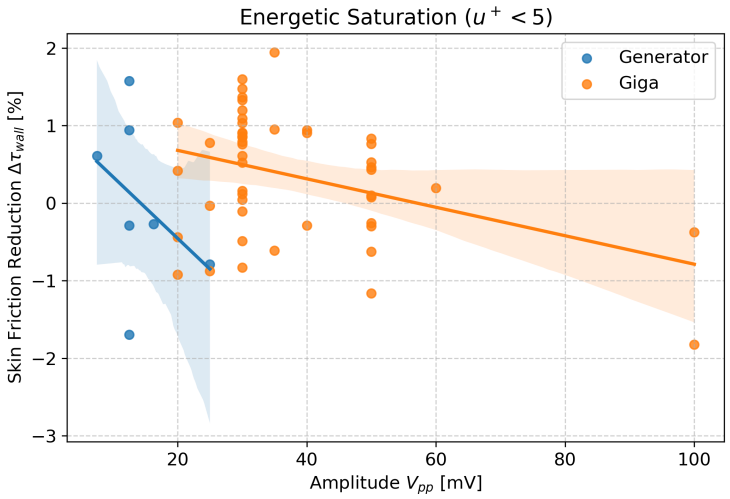


Fig. 3.51 Energetic saturation analysis correlating the actuation amplitude ($V_{pp} = \widehat{A}$) with the resulting skin friction reduction. The negative slope of the regression lines indicates that excessive actuation energy introduces spurious momentum in the wall-bouded turbulence, degrading the control performance and leading to a net increase in drag.

3.5 Concluding Remarks

The experimental campaigns and the extensive data analysis presented in this chapter provide a comprehensive evaluation of the active opposition control strategy. By systematically progressing from the characterization of the synthetic jet in still-air air to its real-time implementation within a fully developed turbulent wall-bounded flow,

the physical mechanisms governing targeted drag reduction have been rigorously quantified.

A primary takeaway from this investigation is the critical importance of waveform optimization. The baseline sinusoidal configuration ("old-wave") showed that while a rapid blowing phase can oppose the sweep event, an overly aggressive membrane retraction inevitably induces a detrimental "velocity overshoot." This secondary entrainment essentially acts as a synthetic sweep, penalizing the overall flow manipulation. By transitioning to the Arduino GIGA set-up and deploying customized, asymmetric triangular waveforms ("new-wave"), this adverse suction effect was almost completely suppressed, yielding a much cleaner aerodynamic intervention.

Furthermore, the expansive parametric survey mapped the absolute boundaries of the system's control authority. While both the analog and digital hardware configurations achieved a comparable peak skin-friction reduction ($\Delta\tau_{wall}$) of approximately 1.58% and 1.95%, the digital set-up exhibited superior statistical robustness across a broader array of off-design conditions. Crucially, the analysis unequivocally identified a strict energetic saturation limit. Pumping excessive voltage into the actuator does not equate to proportional drag reduction; rather, it triggers the previously mentioned velocity overshoot "bubble" of the streamwise velocity component, due to the strong suction phase of the speaker. Other than that, high voltage amplitudes have shown to cause velocity fluctuations in the jet v^+ profile that may be caused by the loudspeaker membrane oscillations and introduce spurious kinetic energy into the near-wall flow.

Ultimately, these results confirm that effective flow control relies less on raw actuation power and significantly more on the precise, synchronization of the jet with the natural advection scales of the coherent sweep structures. The physical insights and methodological refinements detailed in this chapter establish the necessary foundation for the final conclusions and future research perspectives, which will be outlined in the final chapter.

Chapter 4

Conclusions and Future Work

In summary, this research has shown the feasibility of active opposition control as a practical mechanism for drag reduction in wall bounded turbulent flows. By transitioning from traditional analog signal generation to the , digital control capabilities of the Arduino GIGA, this work has effectively investigated the effects of the control parameters required to suppress near-wall coherent structures without inducing the detrimental velocity overshoot observed in earlier configurations.

The rigorous identification of the energetic saturation limit stands as a crucial contribution to the field, providing a clear boundary between efficient control and counterproductive actuation. This finding highlights that the path forward lies not in increasing raw power, but in the precise, synchronization of the jet with the natural advection scales of the flow.

Ultimately, the results presented in this thesis bridge the gap between idealized laboratory experiments and the complex requirements of real-world aerodynamic implementations. The proposed evolution, which is shifting from single-point actuation to distributed arrays and integrating data-driven, adaptive control algorithms, sets a clear trajectory for future developments. As demonstrated, the synergy between robust mechanical control and advanced predictive modeling represents the most promising direction toward achieving significant, sustainable drag reduction in practical aerospace applications.

4.1 Summary of the Experimental Work

The primary objective of this thesis was to experimentally investigate, characterize, and optimize an active opposition control strategy aimed at reducing skin-friction drag within a fully developed turbulent channel flow. The fundamental principle underlying this control scheme was the targeted interception and suppression of near-wall coherent structures[1], specifically high-momentum sweep events, utilizing a zero-net-mass-flux (ZNMF) synthetic jet, following the observation and experimental studies of Rebbeck and Choi[5, 6].

The experimental campaign was conducted in an open-loop wind tunnel, the same as in Di Cicca and Saccaggi studies [62, 61, 17], employing a dual hot-wire anemometry set-up. This configuration allowed for the real-time detection of incoming sweeps via a threshold-based gradient technique, subsequently triggering the actuator and monitoring the downstream localized flow response.

An important technical development in this research consisted in the progressive refinement of the actuation hardware to improve the electro-mechanical response of the synthetic jet. By transitioning from a standard, commercially available analog signal generator to a customized, Arduino GIGA microcontroller, the limitations of symmetric harmonic actuation were overcome. This digital architecture facilitated the deployment of tailored asymmetric triangular waveforms, granting the system independent, control over the frequency, amplitude, and temporal asymmetry of the jet cycle. Consequently, it became possible to execute a highly targeted manipulation of the flow field, aimed to minimize the adverse aerodynamic side-effects typically associated with the suction phase of synthetic jets.

4.2 Key Findings and Physical Insights

The rigorous post-processing and conditional averaging of the experimental datasets yielded several critical insights into the complex dynamics of active flow control. The most significant conclusions drawn from this work are detailed below:

- **Actuator characterization and waveform optimization:** Testing the synthetic jet in still-air conditions proved to be a fundamental prerequisite (see Sections 3.1, 3.2). It was demonstrated that the baseline sinusoidal driving

function produced an excessively severe suction phase, especially at high driving voltages. In the presence of a turbulent crossflow, this rapid suction translated into a *"velocity overshoot bubble"* generating a *synthetic sweep* after the targeted natural one that defeated the purpose of the control (see Section 3.3). By employing the custom triangular waveform to enforce a rapid blowing phase followed by a prolonged, gentle suction phase, this overshoot was completely suppressed. Further analysis highlighted that excessive input voltages trigger structural ringing in the loudspeaker membrane, introducing secondary velocity peaks that disrupt the intended aerodynamic profile (see Section 3.2.1).

- **Importance of phase alignment:** While long-term, time-averaged statistics confirmed that the control input did not induce macroscopic effects within the wall-bounded turbulence (see Section 3.3.1), they were largely insufficient to capture the localized, highly intermittent nature of the control interactions. Space-time topological reconstructions of the conditionally sampled events clearly revealed that precise temporal synchronization is absolutely mandatory, as detailed in Section 3.3.3. The actuator must produce the opposing jet at the exact moment the sweep passes, shielding the physical surface from the natural high-momentum downwash.

- **Control efficacy and statistical robustness:** An extensive parametric mapping was conducted, spanning over 350 distinct operational conditions, using both the signal generator and the Arduino Giga to create the driving functions varying the voltage, frequency, delay time, and triangular wave asymmetry (to control the suction phase) for the second control set-up, as detailed in Section 3.4. This survey, by focusing on repeated viscous sublayer and results, by imposing a limit on $u^+ = y^+ < 5$, proved that the active opposition control is highly sensitive to the tuning parameters. Both the analog and digital control configurations achieved a comparable maximum localized skin-friction reduction ($\Delta\tau_{wall}$) of approximately 1.58% and 1.95%, (Section 3.4.4). However, evaluating the statistical distributions of the control efficacy revealed a stark contrast: the Arduino GIGA set-up is statistically far more robust, maintaining a dense cluster of positive drag reduction outcomes and avoiding the severe performance penalties (drag increases) frequently observed in the analog set-up under off-design conditions (see Section 3.4.5).

- **Identification of the energetic saturation limit:** The study unequivocally identified a rigid energetic saturation threshold for the synthetic jet. Increasing the actuation amplitude beyond an optimal voltage does not correlate with proportional drag reduction. Instead, excessive actuation momentum actively disrupts the delicate near-wall cycle. Rather than selectively canceling the incoming sweeps, over-blowing implies a stronger suction phase and a consequent recovery in streamwise velocity near-wall, destroying the local equilibrium, degrading the control performance, and ultimately leading to a net increase in wall shear stress (Section 3.4.6).

4.3 Outlook and Recommendations for Future Work

The findings presented in this thesis establish a robust experimental and methodological foundation for the future development of highly efficient, real-time active flow control systems. While the localized mitigation of single sweep events was demonstrated, scaling this technology to practical engineering implementations requires further conceptual leaps.

Future research at the laboratory scale should prioritize the transition from single-point actuation to distributed control arrays. Deploying a spanwise array of synthetic jets would enable the simultaneous detection and mitigation of multiple quasi-streamwise vortices across the entire turbulent domain, multiplying the net drag reduction effect.

Furthermore, the integration of data-driven methodologies and deep learning represents the most promising avenue for the evolution of this technology. Implementing advanced machine learning algorithms, such as Convolutional Neural Networks or Feed Forward Neural Networks, could allow future setups to replace intrusive hot-wire probes with non-intrusive wall-pressure or shear-stress sensor arrays. These trained models could dynamically predict the optimal actuation timing, amplitude, and waveform asymmetry in real-time, adapting instantly to varying Reynolds numbers. Coupling the robust aerodynamic insights gained from the custom asymmetric waveforms in this study with adaptive predictive control algorithms will be the critical next step toward deploying active opposition control in full-scale aerospace applications.

Appendix A

Hot-Wire Probes Calibration Procedure

The following algorithm details the automated procedure developed to manage the simultaneous calibration of both the upstream and downstream hot-wire probes. To ensure maximum accuracy during the experimental campaigns, it was crucial to calibrate the boundary layer probes immediately before each testing session, thereby minimizing errors induced by daily variations in ambient temperature and pressure.

The procedure begins by establishing a connection with the National Instruments (NI) acquisition system to record the raw voltage signals generated by the anemometer bridges and the differential pressure transducer. First, the zero-velocity voltage offsets are acquired with the wind tunnel turned off. Subsequently, the algorithm enters a loop, prompting the user to incrementally increase the wind tunnel speed (RPM). At each step, a time-averaged voltage reading is stored for the probes and the transducer.

Once the velocity sweep is complete, the script calculates the air density using the Ideal Gas Law based on the current ambient parameters. The reference flow velocity (U) for each calibration point is derived from the pressure transducer voltage, converting it to pressure with its calibration constants and then to velocity using Bernoulli's principle. Finally, the algorithm performs a non-linear least-squares optimization to fit the experimental data points and extract the A, B, and n coefficients of King's Law ($E^2 = A + B \cdot U^n$) independently for both the front and rear probes.

Algorithm 1 Automated hot-wire calibration and coefficient extraction

Require: Ambient Temperature T_{amb}, Atmospheric Pressure P_{atm}, Transducer Constant k

Ensure: King's Law coefficients (A, B, n) for both Front and Rear probes

Initialize:
Establish connection with NI data acquisition server
Define sampling frequency and acquisition time window
Calculate air density: $\rho \leftarrow \frac{P_{atm}}{R_{air} \cdot T_{amb}}$
Initialize empty arrays: $Array_U$, $Array_E_{front}$, $Array_E_{rear}$, $Array_E_{tr}$
Acquire Zero-Velocity Offsets:
Wait for wind tunnel to be perfectly still ($RPM = 0$)
Acquire raw voltage array for time window
$E_{tr,0} \leftarrow \text{mean}(E_{transducer})$
$E_{front,0} \leftarrow \text{mean}(E_{HW_front})$
$E_{rear,0} \leftarrow \text{mean}(E_{HW_rear})$
Append offsets to respective arrays
Velocity Sweep Loop:
while $Acquisition$ is $True$ **do**
    Prompt user to input target wind tunnel RPM
    if User input is *'exit'* **then**
        $Acquisition \leftarrow False$
        break
    end if
    Wait for flow to stabilize
    Acquire raw voltage array for time window
    $\overline{E_{tr}} \leftarrow \text{mean}(E_{transducer})$
    $\overline{E_{front}} \leftarrow \text{mean}(E_{HW_front})$
    $\overline{E_{rear}} \leftarrow \text{mean}(E_{HW_rear})$
    Append means to $Array_E_{tr}$, $Array_E_{front}$, $Array_E_{rear}$
end while
Data Post-Processing:
for $i = 0$ **to** length of $Array_E_{tr}$ **do**
    Calculate reference dynamic pressure: $\Delta P \leftarrow (Array_E_{tr}[i] - E_{tr,0}) \cdot k$

Calculate reference velocity: $U[i] \leftarrow \sqrt{\frac{2 \cdot \Delta P}{\rho}}$

end for

Optimization (King's Law Fit):

Define objective function: $f(U) = A + B \cdot U^n$

$(A_{front}, B_{front}, n_{front}) \leftarrow$ NonLinearLeastSquaresFit$(U, Array_E^2_{front})$

$(A_{rear}, B_{rear}, n_{rear}) \leftarrow$ NonLinearLeastSquaresFit$(U, Array_E^2_{rear})$

Output:

Save coefficients (A, B, n) to `.npz` arrays for subsequent real-time control scripts

Plot calibration curves E vs U overlaying raw scatter data with fitted King's Law curves

Appendix B

Continuous Acquisition and Data Logging Pseudocode for Jet Characterization

Before implementing the real-time active opposition control in crossflow, it was mandatory to isolate and characterize the fluid dynamic response of the synthetic jet actuator in still-air. This characterisation step maps the relationship between the electrical input parameters issued to the loudspeaker amplifier and the resulting localized velocity fields near the orifice.

The following unified algorithm outlines the acquisition routine developed for both iterations of the experimental set-up. In the initial configuration, utilizing an analog signal generator, the driving parameters (frequency f_{gen} and amplitude V_{pp}) were either adjusted manually or communicated via a serial protocol through an RS232 connection. In the upgraded digital configuration, the workstation interfaces directly with an Arduino GIGA microcontroller via serial commands. This digital upgrade requires a broader set of parameters to define the custom triangular wave: the wave period (T), the peak-to-peak voltage (V_{pp}), the temporal asymmetry factor ($x\%$), and the actuation delay (Δt).

Regardless of the active hardware, the script acts as a data logger interfacing with the remote National Instruments workstation. To ensure the statistical convergence of the turbulent fluctuations generated during the blowing phase, the acquisition time window was set to 100-120 seconds at a high sampling rate (10 kHz). The raw 1D array received from the server is reshaped, and the voltage signal from the downstream boundary layer hot-wire probe is converted into physical velocity using

the previously calibrated King's Law coefficients. Finally, the instantaneous velocity profile is scaled by the friction velocity u_τ to obtain the non-dimensional velocity u^+, which is plotted for verification and archived.

Algorithm 2 Still-Air jet characterization and data acquisition

---

Require: Hardware Set-up (*Analog* or *Arduino*), Sampling Frequency f_s, Total Time t, Friction Velocity u_τ, King's Law Coefficients

Ensure: Reshaped voltage channels, instantaneous physical velocity u, and inner-scaled velocity u^+

Initialize Environmental Parameters:
Instantiate `AmbientClass` object with current lab temperature T and pressure P
Set crossflow friction velocity: $u_\tau \leftarrow 0.161$ m/s (for normalization reference)
Configure Actuation Hardware:
if Hardware Set-up is *Analog signal generator* **then**
    Input parameters: Frequency f_{gen}, Amplitude V_{pp}
    Apply hardware voltage divider circuit: $V_{pp,eff} \leftarrow \frac{V_{pp}}{divider}$
    (Optional) Send parameters via RS232: `client_program(ip, "RS232 " +` f_{gen} `+ " " +` V_{pp}`)`
else if Hardware Set-up is *Arduino GIGA* **then**
    Input parameters: Period T, Voltage V_{pp}, Asymmetry $x\%$, Delay Δt
    Activate digital control: `client_program(ip, "actuation GIGA on")`
    Send waveform string: `client_program(ip, "arduino GIGA " +` V_{pp} `+ " " +` T `+ " " +` $x\%$ `+ " " +` Δt`)`
end if
Data Acquisition and Reshaping:
Pack configuration command: $msg \leftarrow \text{concat}(f_s, t)$
Send parameters to NI workstation and issue start command
$Array_Raw \leftarrow \text{client_program}(ipServer, \text{"start"})$ ▷ Receive raw streaming 1D array
Compute number of channels: $N_{channels} \leftarrow \text{floor}\left(\frac{\text{length}(Array_Raw)}{f_s \cdot t}\right)$
Reshape 1D array into matrix: $Matrix_Data \leftarrow \text{reshape}(Array_Raw, [N_{channels}, f_s \cdot t])$
Anemometer Signal Conversion & Normalization:
Extract rear hot-wire voltage timeseries: $E_{rear} \leftarrow Matrix_Data[1, :]$

for $j = 0$ **to** length of E_{rear} **do**
    $u[j] \leftarrow \left(\frac{E_{rear}[j]^2 - A_{rear}}{B_{rear}}\right)^{\frac{1}{n_{rear}}}$ ▷ Convert via King's Law
    $u^+[j] \leftarrow \frac{u[j]}{u_\tau}$ ▷ Convert to inner wall units
end for
Visualization and Archiving:
Generate plot: u^+ vs. Time (ms) to verify jet stability and absence of clipping
Save structural data to `.npz` file with hardware-specific operational parameters

Appendix C

Multi-Axis Traverse System and Probe Positioning Control Pseudocode

To perform velocity profile measurements and accurate conditional sampling within the wall-bounded turbulence, the precise spatial positioning of the hot-wire probes is of paramount importance. The downstream Dantec 55P15 boundary layer probe must be positioned at specific wall-normal distances (y) and aligned longitudinally (x) with respect to the synthetic jet orifice. This task is handled by a multi-axis motorized translation system operated remotely via TCP/IP commands issued to the stepper motor drivers.

The following algorithm describes the interactive control script developed to manage the positioning of the probe during the translation stages.

The control logic operates as a continuous state machine driven by user command-line inputs. The main routines include: a mechanical homing sequence (*origin*), an automated positioning routing to place the sensor exactly at the nominal measurement location (*control*), and a high-clearance retraction sequence (*safe-org*) designed to move the probe assembly away from the wall before performing a homing check, thus preventing the prongs from hitting the surface.

Algorithm 3 Interactive traverse positioning and collision avoidance routine

Require: Target destination command from user interface, Controller IP Address ip

Ensure: Multi-axis stepper motor displacement commands transmitted via TCP/IP socket

Initialize:
Open network socket communication with the motor controller server
Define nominal control point coordinates: $X_{ctrl} \leftarrow 42.5$ mm, $Y_{ctrl} \leftarrow -7.8$ mm
Define safe homing clearance coordinates: $X_{safe} \leftarrow 42.5$ mm, $Y_{safe} \leftarrow 35.0$ mm
$Keep_Going \leftarrow True$
while $Keep_Going$ is $True$ **do**
    Prompt user for operation mode input (*cmd*)
    if *cmd* = 'origin' **then**
        Execute mechanical reference homing sequence via `do_mechanical_org(ip)`
    else if *cmd* = 'control' **then**
        Prompt confirmation to move to nominal point: $[X_{ctrl}, Y_{ctrl}]$
        if User confirmation is *'yes'* **then**
            Send absolute motion command for Axis 1 (Vertical): `"move_abs 1 " +` Y_{ctrl}
            Send absolute motion command for Axis 0 (Longitudinal): `"move_abs 0 " +` X_{ctrl}
        end if
    else if *cmd* = 'safe-org' **then**
        Prompt confirmation to move to safety clearance: $[X_{safe}, Y_{safekeys}]$
        if User confirmation is *'yes'* **then**
            Retract vertical axis first to clear wall: `"move_abs 1 " +` Y_{safe}
            Align longitudinal translation stage: `"move_abs 0 " +` X_{safe}
            Prompt verification to execute physical hardware homing
            if Homing confirmation is *'yes'* **then**
                Send low-level hardware home command string: `"mv_axis_command;H:1,1,1"`
            end if
        end if
    else if *cmd* = 'move' **then**
        Call relative displacement interactive menu: `move(ip, "Relative")`
    else if *cmd* = 'move-abs' **then**
        Call absolute positioning interactive menu: `move(ip, "Absolute")`
    else if *cmd* = 'probe-out' **then** ▷ Multi-step macro trajectory to safely extract probe from test section

Step 1: Move vertical stage to zero clearance position
Step 2: Retract longitudinal stage to full reverse clearance (-100 mm)
Step 3-5: Sequence vertical axis extensions (40 mm $\rightarrow$ 80 mm $\rightarrow$ 140 mm) to clear outer frame
else if *cmd* = 'probe-in' **then** ▷ Macro trajectory to re-insert probe assembly into flow channel
Step 1: Reset vertical translation stage to zero reference position
Step 2: Advance longitudinal stage to initial test section entryway reference (0 mm)
else if *cmd* = 'stop' **then**
$Keep_Going \leftarrow False$ ▷ Terminate control loop and release network socket
else
Print warning: "Invalid operation command"
end if
end while

Appendix D

Data Post-Processing and Conditional Sampling in Still-Air Flow Pseudocode

Following the acquisition of the raw anemometry data, an automated post-processing pipeline was developed to analyze the synthetic jet's fluid dynamic signature in still-air conditions. The objective of this algorithm is to extract the conditionally-averaged velocity profile of the jet's blowing and suction cycle, allowing for a systematic comparison between the baseline sinusoidal wave (*Old Wave*) and the customized asymmetric waveform (*New Wave*) across different wall-normal distances (y^+).

The script iterates through the experimental dataset (comprising 54 distinct tests), reading the raw voltage arrays alongside their corresponding electrical metadata, such as the actuation frequency (f_{gen}), amplitude (V_{pp}), phase shift (α), and the status of the hardware voltage divider circuit. After converting the anemometer voltages to physical velocities via King's Law and normalizing them into inner wall units (u^+,t^+), the algorithm performs a peak detection routine. By evaluating the local maxima based on a prominence threshold, the exact timing of each blowing event is identified.

Subsequently, a conditional sampling technique is applied: the algorithm isolates a specific temporal window around each detected peak, extracts the instantaneous velocity fluctuations, and computes the ensemble average ($\overline{v'}^+$) for that specific test case. Finally, the aggregated statistical data is structured into a unified DataFrame, enabling automated parametric comparative analysis (e.g., evaluating the effect

of increasing frequency, amplitude, or waveform shape on the near-wall velocity overshoot).

Algorithm 4 Conditionally-averaged conditional sampling of the synthetic jet

---

Require: Dataset folders containing raw data `.npz`, Ambient Parameters (T, P), King's Law Coefficients, Hardware Divider configuration list

Ensure: Conditionally averaged velocity profiles $\overline{v'}^{+}$ grouped by y^{+}, f_{gen}, V_{pp}, and Waveform Type

Initialization and Viscous Scaling:
Load T, P and calculate air properties (ρ, ν)
Recompute reference friction velocity: $u_\tau \leftarrow 0.1611$ m/s
Compute inner scales: $l_\tau \leftarrow \frac{\nu}{u_\tau}, \quad t_\tau \leftarrow \frac{\nu}{u_\tau^2}$
Define spatial measurement grid: $y^{+}_{vect} \leftarrow [y^{+}_1, y^{+}_2, y^{+}_3]$ based on probe physical distances
Data Loading and Inner Normalization:
for each $test_folder$ **in** sorted dataset **do**
    Load $Matrix_Data$, f_{gen}, V_{pp}, and Waveform Type (*Old* or *New*)
    Extract hardware divider status and compute true $Voltage_Offset$ and Phase Shift (α)
    Extract rear probe signal: $E_{rear} \leftarrow Matrix_Data[1, :]$
    Convert to velocity: $u \leftarrow \text{KingsLaw}(E_{rear})$
    Filter *NaN* values and normalize: $u^{+} \leftarrow \frac{u}{u_\tau}$
    Store u^{+} timeseries and test parameters in $EventMatrix$
end for
Peak Detection and Conditional Sampling:
for $i = 0$ **to** length of $EventMatrix$ **do**
    $u^{+}_{curr} \leftarrow EventMatrix[i]$
    Define dynamic prominence threshold: $Th \leftarrow \max(u^{+}_{curr}) \cdot 0.15$
    Identify blowing events: $Peaks_Idx \leftarrow \text{find_peaks}(u^{+}_{curr}, \text{prominence} = Th)$
    Phase-Averaging Loop:
    Calculate period length in samples: $L_{expected} \leftarrow \frac{f_s}{f_{gen}}$
    Define sampling bounds: $\Delta_{pre} \leftarrow L_{expected} \cdot 0.3, \quad \Delta_{post} \leftarrow L_{expected} \cdot 1.2$
    Initialize empty array $Matrix_Windows$
    for each idx **in** $Peaks_Idx$ (excluding first and last) **do**

Extract local event: $Window \leftarrow u^{+}_{curr}[idx - \Delta_{pre} \ : \ idx + \Delta_{post}]$
Append $Window$ to $Matrix_Windows$
end for
Compute ensemble average: $\overline{v'}^{+} \leftarrow \text{mean}(Matrix_Windows, \text{axis} = 0)$
Generate non-dimensional time window array t^{+}
Save $\overline{v'}^{+}$ to $Mean_Event_List$
end for
Database Structuring and Comparative Analysis:
Construct tabular `DataFrame` mapping each $\overline{v'}^{+}$ profile to its y^{+}, f_{gen}, V_{pp}, and Waveform Type
Execute plotting routines to generate comparative parametric graphs:
$\rightarrow$ Plot 1: *Old Wave* vs *New Wave* at fixed y^{+}
$\rightarrow$ Plot 2: Evaluate Voltage Divider circuit attenuation effects
$\rightarrow$ Plot 3: Actuation Frequency Sweep (30Hz $\rightarrow$ 110Hz)
$\rightarrow$ Plot 4: Actuation Amplitude Sweep (Energetic Saturation Check)

Appendix E

Automated Vertical Flow Survey and Profiling Pseudocode

To thoroughly investigate the spatial influence of the active opposition control strategy within the studied wall-bounded turbulence, a wall-normal spatial discretization (y-sampling) is required. Mapping the velocity field at discrete vertical coordinates allows for the quantification of local skin-friction drag reduction and the reconstruction of the modified turbulent profile.

The following interactive algorithm outlines the control pipeline developed to manage the vertical traverse progression while coordinating data acquisition. The script initializes by importing local ambient parameters and defining the target active flow control parameters via the `ControlParameters` class (specifying actuation frequency f_{gen}, amplitude V_{pp}, phase delay Δt, and hardware voltage divider circuit configuration). To achieve high statistical convergence of the turbulent stresses and long-term wall-bounded turbulence modifications under active actuation, a substantial sampling time window of 240 seconds at 10 kHz is enforced for every single measurement point.

The core of the architecture relies on an interactive loop where the experimentalist inputs relative wall-normal displacements (Δy). The algorithm internally tracks and accumulates these values to maintain an absolute spatial coordinate system (y_{abs}) relative to the wall origin. At each vertical step, the script triggers a physical displacement of the automated traverse stage via a TCP/IP command. It then consecutively invokes two distinct high-level routines: `getUncontrolledFlow` and `getControlledFlow`. This back-to-back sampling methodology ensures that both the baseline turbulent flow and the actively controlled state are recorded under

identical structural and environmental conditions, eliminating uncertainties stemming from sensor drift or slow temperature fluctuations.

Algorithm 5 Interactive vertical traverse survey and dual-state acquisition

Require: Control parameters (`CpClass`), Acquisition parameters (`acqPar`), Calibration parameters (`kingPar`), Motor Controller IP address *ipServer*

Ensure: Hierarchical directory tree storing twin datasets (Uncontrolled vs. Controlled) across an absolute vertical coordinate vector y_{abs}

Initialize System and Boundary Conditions:
Query remote server to acquire current ambient parameters (T, P)
Instantiate `AmbientClass` and compute viscous scales
Load target control configuration: $f_{gen} \leftarrow 30$ Hz, $V_{pp} \leftarrow 0.05$ V, $\Delta t \leftarrow 0.15$ ms, divider $\leftarrow 4$
Initialize absolute coordinate accumulator: $y_{abs} \leftarrow 0.0$ mm
Directory Set-up and Metadata Serialization:
Generate next chronological root test folder: $Path_{ext} \leftarrow$ create_next_folder$(\dots)$
Serialize and write configuration files (`.txt` and `.pickle`) for reproducibility
Interactive Spatial Profiling Loop:
while *True* **do**
    Prompt experimentalist for vertical step input (*response*)
    if *response* matches *'stop'* **then**
        break ▷ Terminate vertical survey session
    end if
    if *response* is not a valid numerical digit **then**
        Output warning: "Invalid format, re-input step displacement"
        continue
    end if
    Traverse Actuation and Tracking:
    Convert input to float: $\Delta y \leftarrow$ float$(response)$
    Update absolute coordinate reference: $y_{abs} \leftarrow y_{abs} + \Delta y$
    Define localized storage subfolder: $Path_{dist} \leftarrow$ join$(Path_{ext}, \text{string}(y_{abs}))$
    Create directory path on local disk
    Transmit relative motion command to vertical stage (Axis 1):
    `client_program(ipServer, "move_rel 1 " + Δy)`

Wait for mechanical vibration settlement
Dual-State Acquisition Sequence:
Step 1: Uncontrolled Baseline Acquisition
Call `getUncontrolledFlow(ipServer,` y_{abs}`, acqPar, kingPar, saveMode,` $Path_{dist}$`)` ▷ Records natural turbulent uncontrolld flow state for 240 s
Step 2: Actively Controlled Acquisition
Call `getControlledFlow(ipServer,` y_{abs}`, acqPar, kingPar, saveMode,` $Path_{dist}$`, CpClass)` ▷ Triggers synthetic jet actuation and records modified flow field for 240 s
end while
Session Termination:
Close interactive loop, release socket resources, and log operational notes to file

Appendix F

Data Post-Processing and Statistical Analysis Pseudocode

Multi-Point Wall-Bounded Turbulence Statistics and Space-Time Topology Reconstruction

Following the spatial multi-state acquisition across the vertical traverse stations, a comprehensive data reduction pipeline was implemented to evaluate the impact of the opposition control strategy on the wall-bounded turbulence structure. This algorithm performs a dual-fold analysis: it computes the wall-normal profiles of the first four statistical moments of the turbulent velocity fluctuations and reconstructs the continuous space-time topology of targeted coherent structures via multi-dimensional interpolation.

The script initializes by applying specific calibration corrections that account for the experimental virtual origin offset (Δy_{offset}) and updates the reference friction velocity (u_τ) based on the specific campaign index (e.g., Simulation 10 or 13). This precise scaling is mandatory to correctly transform relative traverse positions into non-dimensional inner wall units (y^+). For each vertical coordinate, the raw hot-wire voltage signals are converted to physical velocity fluctuations via King's Law. The algorithm then computes individual profiles for the mean velocity (U^+), Reynolds normal stress ($\overline{u'u'}^+$), skewness ($\mathscr{S}$), and flatness/kurtosis ($\mathscr{F}$ using Pearson's definition), directly benchmarking them against a baseline DNS dataset [23] to verify the canonical state of the flow and identify localized dampening.

Subsequently, the conditional averaging routine (`analyseEvent`) is executed at every vertical station, incorporating the convective time-delay vector (Δt_{delay}) to

align the tracking windows. To visualize the global interaction between the synthetic jet and the incoming high-speed sweep event, the discrete one-dimensional time-series are aggregated. A structured, grid spanning the (t^+, y^+) plane is defined, and a two-dimensional cubic spline interpolation is applied to the scattered data points. This yields continuous spatial-temporal scalar fields of the inner-scaled turbulent fluctuations (u'^+), providing an intuitive topological mapping that clearly illustrates the structural deflection or attenuation of turbulent structures under active control.

Algorithm 6 Wall-bounded statistical profiling and 2D space-time reconstruction

---

Require: Vertical survey directory tree, simulation index (Sim_{ID}), calibration parameters (`kingPar`), reference DNS database object (`DNS_Stat`)

Ensure: Comparative profiles of U^+, $\overline{u'u'}^+$, $\mathscr{S}$, $\mathscr{F}$ versus y^+; continuous 2D space-time interpolated scalar fields $\mathscr{U}^+(t^+, y^+)$ for uncontrolled and controlled states

Virtual Origin Correction and Viscous Scaling:
Load ambient metadata and recompute local kinematic viscosity ν
if $Sim_{ID} == 10$ **then**
    Set wall-distance hardware offset: $\Delta y_{offset} \leftarrow 0.162$ mm
    Set target friction velocity: $u_\tau \leftarrow 0.1650$ m/s
else
    if $Sim_{ID} == 13$ **then**
        Set wall-distance hardware offset: $\Delta y_{offset} \leftarrow 0.284$ mm
        Set target friction velocity: $u_\tau \leftarrow 0.1525$ m/s
    end if
end if
Compute absolute physical coordinates: $y_{abs} \leftarrow y_{relative} + \Delta y_{offset}$
Map to inner wall coordinates: $y^+ \leftarrow \frac{y_{abs} \cdot 10^{-3}}{l_\tau}$
Single-Point Higher-Order Statistical Moments Loops:
for each $station_folder$ at coordinate $y^+[i]$ **do**
    Load time-resolved raw signals for *Controlled* and *Uncontrolled* states
    Convert voltage arrays to physical velocities: $u_{con} \leftarrow \text{King}(E_{con})$, $u_{unc} \leftarrow \text{King}(E_{unc})$
    Compute Statistical Observables (Moments 1 to 4):
    Mean velocity profile: $U^+_{con}[i] \leftarrow \frac{\text{mean}(u_{con})}{u_\tau}$, $U^+_{unc}[i] \leftarrow \frac{\text{mean}(u_{unc})}{u_\tau}$
    Reynolds normal stress: $\overline{u'u'}^+_{con}[i] \leftarrow \frac{\text{var}(u_{con})}{u_\tau^2}$, $\overline{u'u'}^+_{unc}[i] \leftarrow \frac{\text{var}(u_{unc})}{u_\tau^2}$

Velocity skewness: $\mathscr{S}_{con}[i] \leftarrow \text{skewness}(u_{con}), \quad \mathscr{S}_{unc}[i] \leftarrow \text{skewness}(u_{unc})$
Flatness (Pearson's Kurtosis): $\mathscr{F}_{con}[i] \leftarrow \text{kurtosis}(u_{con}, \text{fisher=False}), \quad \ldots$
Event-Locked Conditional Averaging Extraction:
Extract mean controlled fluctuation profile around trigger:
$[u'^{+}_{con,i}, t^{+}_{con,i}] \leftarrow \text{analyseEvent}(u_{con}, \text{Trigger}_{con}, \Delta t_{delay})$
Extract mean uncontrolled fluctuation profile around trigger:
$[u'^{+}_{unc,i}, t^{+}_{unc,i}] \leftarrow \text{analyseEvent}(u_{unc}, \text{Trigger}_{unc}, \Delta t = 0)$
end for
Benchmarking and 2D Topological Grid Interpolation:
Plot profiles (U^+, $\overline{u'u'}^+$, $\mathscr{S}$, $\mathscr{F}$) vs. y^+ alongside validation `DNS_Stat` curves
Flatten and stack scattered arrays into coordinate vectors:
$\mathbf{X} \leftarrow [t^{+}_{i,j}], \quad \mathbf{Y} \leftarrow [y^{+}_{i} \cdot \mathbf{1}], \quad \mathbf{Z}_{con} \leftarrow [u'^{+}_{con,i,j}], \quad \mathbf{Z}_{unc} \leftarrow [u'^{+}_{unc,i,j}]$
Construct uniform, structured mesh grid:
$[\mathscr{T}^+, \mathscr{Y}^+] \leftarrow \text{meshgrid}(\text{linspace}(t^{+}_{min}, t^{+}_{max}, 300), \text{linspace}(y^{+}_{min}, y^{+}_{max}, 300))$
Map scattered topology to structured domain via 2D cubic spline interpolation:
$\mathscr{U}^{+}_{con}(\mathscr{T}^+, \mathscr{Y}^+) \leftarrow \text{griddata}((\mathbf{X}, \mathbf{Y}), \mathbf{Z}_{con}, (\mathscr{T}^+, \mathscr{Y}^+), \text{method='cubic'})$
$\mathscr{U}^{+}_{unc}(\mathscr{T}^+, \mathscr{Y}^+) \leftarrow \text{griddata}((\mathbf{X}, \mathbf{Y}), \mathbf{Z}_{unc}, (\mathscr{T}^+, \mathscr{Y}^+), \text{method='cubic'})$
Visualization:
Generate synchronized color-mesh fields (`pcolormesh`) using bounded colorbars to map the raw spatial-temporal footprint of the coherent structures

Appendix G

Acquisition Algorithms: Repeatability Study of Active Opposition Control

This appendix details the unified experimental pipeline implemented to assess the efficacy of the active flow control strategies. To evaluate the interaction with sweep events and the resulting skin friction drag reduction in turbulent channel flows, the experimental set-up utilized two distinct actuation controllers: an analog signal generator for baseline sinusoidal actuation, and an Arduino GIGA microcontroller for complex, customizable wave configurations (e.g., incorporating the triangular modulation parameter $x\%$).

Despite the inherent differences in hardware communication protocols—utilizing RS232 serial commands for the generator and custom TCP/IP string instructions for the Arduino board—the data acquisition and post-processing methodologies were strictly unified. This architectural choice ensures that the conditional sampling of the turbulent structures via trigger thresholds, and the subsequent evaluation of the wall shear stress variations ($\Delta\tau_w$), remain invariant and consistent across all test cases.

Algorithm 7 Unified data acquisition and conditional processing pipeline

---

Require: Hardware Set-up $S \in \{\text{Generator}, \text{Arduino GIGA}\}$, Control Params θ, King's Law `kingPar`

Ensure: Statistical dataset `AllData.npz` and $\Delta\tau_w$ performance metrics

Phase 1: Environmental Initialization & Calibration

1: Initialize `AmbientClass` (T, P, rpm) and compute u_τ for inner-wall scaling

Set sampling frequency $f_s \leftarrow 10000$ Hz and acquisition window T_s

Phase 2: Baseline (Uncontrolled) Acquisition

if $S ==$ Generator **then**

    Wait for User: `DISCONNECT` actuator cable

else if $S ==$ Arduino GIGA **then**

    `client_program("actuation GIGA off")`

end if

Configure acquisition: `client_program("set acquisition params...")`

$\mathbf{Data}_{unc} \leftarrow$ `client_program("start")`

$\mathbf{u}_{unc} \leftarrow$ `kingPar.convertToVel`$(\mathbf{Data}_{unc})$

$[\text{MeanVel}_{unc}, \dots] \leftarrow$ `analyse`$(\mathbf{u}_{unc}, \text{trigger}_{unc}, \Delta t = 0)$

Phase 3: Actuator Configuration (Hardware Branch)

if $S ==$ Arduino GIGA **then**

    `client_program("arduino GIGA " +` $V_{pp}, \text{period}, x\%, \Delta t_{delay}$ `)`

    `client_program("actuation GIGA on")`

else if $S ==$ Generator **then**

    Wait for User: `CONNECT` actuator cable

    `client_program("RS232 " +` $f_{gen}, V_{pp}, \Delta t_{delay}$ `)`

end if

Phase 4: Controlled Acquisition

Configure acquisition and `start` recording $\mathbf{Data}_{con}$

$\mathbf{u}_{con} \leftarrow$ `kingPar.convertToVel`$(\mathbf{Data}_{con})$

Evaluate convective time delay overlap for target structure

$[\text{MeanVel}_{con}, \dots] \leftarrow$ `analyse`$(\mathbf{u}_{con}, \text{trigger}_{con}, \Delta t_{delay})$

Phase 5: Performance Evaluation & Serialization

$\tau_{w,unc} \leftarrow \mu \cdot \left(\frac{\text{MeanVel}_{unc}}{4 \cdot \nu / u_\tau} \right)$ and $\tau_{w,con} \leftarrow \mu \cdot \left(\frac{\text{MeanVel}_{con}}{4 \cdot \nu / u_\tau} \right)$

$\Delta\tau_w \leftarrow \frac{\int \tau_{w,unc}\, dt - \int \tau_{w,con}\, dt}{\int \tau_{w,unc}\, dt}$ ▷ Relative drag reduction in target window

`np.savez`$(\text{"AllData.npz"}, \mathbf{u}_{con}, \mathbf{u}_{unc}, \Delta\tau_w, \text{setup_metadata})$

Appendix H

Near Wall Controlled Flow Data Post-Processing Pseudocode

To systematically evaluate the efficacy of the active opposition control across the entire experimental parametric space, a comprehensive automated post-processing script was developed. This algorithm parses the extensive dataset comprising over 350 individual test cases, bridging the results from both the analog signal generator and the digital Arduino GIGA setups.

The primary objective of this routine is to quantify the global performance of the control strategy by computing the percentage reduction in mean skin friction ($\Delta\tau_{wall}$) for every valid configuration. A critical spatial constraint is enforced early in the pipeline: any test where the downstream hot-wire probe drifted beyond the viscous sublayer ($u^+ \geq 5$) is automatically discarded to prevent the misinterpretation of outer-layer turbulent structures.

For valid datasets, the script executes a dual-phase analysis. In the first phase, it categorizes the data based on hardware configuration and groups tests featuring identical control parameters ($V_{pp}, f, \Delta t, x\%$). An ensemble-averaging routine is then applied across these identical runs to ensure statistical repeatability, generating aggregated mean velocity profiles. In the second phase, the script extracts the absolute best-performing cases for each set-up and generates the macroscopic visualizations discussed in Chapter 3: parametric scatter maps to identify optimal operational regions, linear regression plots to highlight the energetic saturation limits of the synthetic jet, and probability density functions (violin plots) to benchmark the statistical robustness of the two hardware configurations.

Algorithm 8 Parametric aggregation and global performance mapping

Require: Root directory containing 350+ experimental datasets, ambient fluid properties (μ, ν), friction velocity u_τ

Ensure: Aggregated velocity profiles, Parametric scatter maps, Saturation regressions, Performance distributions, Best-case comparison

Initialize Global Variables:
Define dynamic time-scaling factor: $t_\tau \leftarrow \frac{2\nu}{u_\tau^2}$ ▷ Corrects temporal alignment in aggregated means
Initialize empty DataFrames: DF_{gen}, DF_{giga}
Initialize structural trackers: $Best_{gen} \leftarrow [max = -\infty]$, $Best_{giga} \leftarrow [max = -\infty]$
Phase 1: Dataset Parsing and Spatial Filtering
for each $file$ **in** $Root_Directory$ **do**
    Extract control parameters: $\Delta t, V_{pp}, f_{gen}$ and (if GIGA) $x\%$
    Load u^+ temporal arrays for Controlled and Uncontrolled states
    Evaluate spatial constraint: $\overline{u^+}_{rear} \leftarrow \text{mean}(u_{unc})/u_\tau$
    if $\overline{u^+}_{rear} \geq 5.0$ **then**
        continue ▷ Discard data point: Probe out of viscous sublayer
    end if
    Skin Friction Reduction Calculation:
    Compute $\tau_{wall,unc} \leftarrow \frac{\mu \cdot \overline{u_{unc}}}{4\nu/u_\tau}$ and $\tau_{wall,con} \leftarrow \frac{\mu \cdot \overline{u_{con}}}{4\nu/u_\tau}$
    Calculate percentage reduction: $\Delta\tau_{wall}\% \leftarrow \text{mean}\left(\frac{\tau_{wall,unc} - \tau_{wall,con}}{\tau_{wall,unc}}\right) \cdot 100$
    Append metadata, temporal arrays, and $\Delta\tau_{wall}$ to respective DF_{gen} or DF_{giga}
    Update $Best_{gen}$ or $Best_{giga}$ if current $\Delta\tau_{wall}$ is the absolute maximum
end for
Phase 2: Repeatability and Conditionally-Averaged Aggregation
for each $Setup_DF$ **in** $[DF_{gen}, DF_{giga}]$ **do**
    Group data rows by identical control parameters $(V_{pp}, f_{gen}, \Delta t, x\%)$
    for each $Group$ **do**
        if Number of tests in $Group \leq 1$ **then**
            continue ▷ Skip non-repeated runs to enforce statistical significance
        end if
        Interpolate multiple time-series onto a common non-dimensional time vector t^+

Compute ensemble-averaged response: $\overline{U^+}_{unc}$ and $\overline{U^+}_{con}$

Generate subplots validating test-to-test repeatability and save aggregated profiles

end for

end for

Phase 3: Macroscopic Data Visualization

Control Maps: Generate 2D scatter plots of f_{gen} vs Δt (for Generator) and $x\%$ vs Δt (for GIGA), with colormap driven by $\Delta\tau_{wall}$

Energetic Saturation: Execute linear regression ($\Delta\tau_{wall}$ vs V_{pp}) to identify actuation limits

Statistical Distribution: Construct Violin and Swarm plots combining both setups to evaluate median performance and variance

Best Cases: Extract peak profiles from $Best_{gen}$ and $Best_{giga}$, format with t^+ and u^+ tracking, and plot side-by-side comparison

References

[1] S. K. Robinson. Coherent motions in the turbulent boundary layer. *Annual Review of Fluid Mechanics*, 23(Volume 23, 1991):601–639, 1991.

[2] A. G. Kravchenko, H. Choi, and P. Moin. On the relation of near-wall streamwise vortices to wall skin friction in turbulent boundary layers. *Physics of Fluids A: Fluid Dynamics*, 5(12):3307–3309, 12 1993.

[3] H. Choi, P. Moin, and J. Kim. Active turbulence control for drag reduction in wall-bounded flows. *Journal of Fluid Mechanics*, 262:75–110, 1994.

[4] E. P. Hammond, T. R. Bewley, and P. Moin. Observed mechanisms for turbulence attenuation and enhancement in opposition-controlled wall-bounded flows. *Physics of Fluids*, 10(9):2421–2423, 09 1998.

[5] H. Rebbeck and K. Choi. Opposition control of near-wall turbulence with a piston type actuator. *Physics of Fluids - PHYS FLUIDS*, 13:2142–2145, 08 2001.

[6] H. Rebbeck and K. Choi. A wind-tunnel experiment on real-time opposition control of turbulence. *Physics of Fluids - PHYS FLUIDS*, 18, 03 2006.

[7] T. Theodorsen. Mechanism of turbulence. In *Proceedings of the Second Midwestern Conference on Fluid Mechanics*, pages 1–18, Columbus, Ohio, 1952. Ohio State University.

[8] U. Aleks. Vortex generators: Preventing stalls at high and low speeds. https://www.boldmethod.com/learn-to-fly/aerodynamics/vortex-generators/, 09 2015.

[9] Friendship Systems. Turbine blade cooling. https://www.caeses.com/blog/2019/turbine-blade-cooling, March 2019. Accessed: 2026-05-04.

[10] R. D. Whalley and K. Choi. The starting vortex in quiescent air induced by dielectric-barrier-discharge plasma. *Journal of Fluid Mechanics*, 703:192–203, 2012.

[11] Lufthansa Technik. Aeroshark: The only certified and proven sharkskin technology. https://www.lufthansa-technik.com/en/aeroshark, 2024. Accessed: 2024-12-20.

[12] D. W. Bechert, M. Bruse, W. Hage, J. G. T. van der Hoeven, and G. Hoppe. Experiments on drag-reducing surfaces and their optimization with adjustable geometry. *Journal of Fluid Mechanics*, 338:59–87, 1997.

[13] R. García-Mayoral and J. Jiménez. Hydrodynamic stability and breakdown of the viscous regime over riblets. *Journal of Fluid Mechanics*, 678:317–347, 2011.

[14] R. García-Mayoral and J. Jiménez. Drag reduction by riblets. *Philosophical transactions. Series A, Mathematical, physical, and engineering sciences*, 369:1412–27, 04 2011.

[15] T. Kouser, H. Zulfiqar, M. Misbah, and L. M. Alhems. Passive drag reduction technologies. *ChemBioEng Reviews*, 10(6):1110–1122, 2023.

[16] R. M. Kelso, T. T. Lim, and A. E. Perry. An experimental study of round jets in cross-flow. *Journal of Fluid Mechanics*, 306:111–144, 1996.

[17] E. Saccaggi and G. M. Di Cicca. Application of a neural network for predicting the control effect on sweep events in a fully turbulent channel flow. In *AIAA AVIATION FORUM AND ASCEND*, Las Vegas, Nevada, USA, 2025. AIAA American Institute of Aeronautics and Astronautics.

[18] Dantec Dynamics. *Miniature wire probe, straight - 55P11*. Dantec Dynamics A/S, Skovlunde, Denmark. Technical specifications for boundary layer hot-wire probes.

[19] Dantec Dynamics. *Miniature wire probe, boundary layer - 55P15*. Dantec Dynamics A/S, Skovlunde, Denmark. Technical specifications for boundary layer hot-wire probes with offset prongs.

[20] Arduino. Arduino uno rev3 with long pins. https://docs.arduino.cc/retired/boards/arduino-uno-rev3-with-long-pins, 2024. Last revised 14 March 2024; accessed 18 June 2026.

[21] Research & Innovation, King Fahd University of Petroleum and Minerals. Agilent 33120a function/arbitrary waveform generator. https://ri.kfupm.edu.sa/css/research/facilities/agilent-33120a-function-arbitrary-waveform-generator, 2026. Accessed 18 June 2026.

[22] J. Hylén. Arduino giga r1 user manual. https://docs.arduino.cc/tutorials/giga-r1-wifi/cheat-sheet, 2026. Last revised 01 January 2026; accessed 18 June 2026.

[23] R. D. Moser, J. Kim, and N. N. Mansour. Direct numerical simulation of turbulent channel flow up to re$_\tau$=590. *Physics of Fluids*, 11(4):943–945, 04 1999.

[24] C. Lee, J. Kim, D. Babcock, and R. Goodman. Application of neural networks to turbulence control for drag reduction. *Physics of Fluids - PHYS FLUIDS*, 9:1740–1747, 06 1997.

[25] K. Mahesh. The interaction of jets with crossflow. *Annual Review of Fluid Mechanics*, 45(Volume 45, 2013):379–407, 2013.

[26] R. Rathnasingham. *System identification and active control of a turbulent boundary layer*. Doctoral thesis, Massachusetts Institute of Technology, Department of Aeronautics and Astronautics, 1997.

[27] R. F. Blackwelder and R. E. Kaplan. On the wall structure of the turbulent boundary layer. *Journal of Fluid Mechanics*, 76(1):89–112, 1976.

[28] Z. Li, X. Dang, P. Lv, and H. Duan. Blowing-only opposition control: Characteristics of turbulent drag reduction and implementation by deep learning. *AIP Advances*, 11(3):035016, 03 2021.

[29] S. L. Brunton, B. R. Noack, and P. Koumoutsakos. Machine learning for fluid mechanics. *Annual Review of Fluid Mechanics*, 52(Volume 52, 2020):477–508, 2020.

[30] S. J. Kline and S. K. Robinson. Quasi-coherent structures in the turbulent boundary layer. i - status report on a community-wide summary of the data. In *Near Wall Turbulence. Proceedings of the Zaric Memorial*, jan 1990. NASA Technical Reports Server, Document ID 19910049113; Accession Number 91A33736.

[31] S. J. Kline and S. K. Robinson. Turbulent boundary layer structure: Progress, status, and challenges. In *Structure of Turbulence and Drag Reduction. Proceedings of the IUTAM Symposium, Zurich, Switzerland, July 25–28, 1989*, pages 3–22. Springer-Verlag, Berlin and New York, 1990. Bibcode: 1990stdr.proc....3K.

[32] P. G. Runstadler, S. J. Kline, and W. C. Reynolds. An experimental investigation of flow structure of the turbulent boundary layer. Technical Report MD-8, Department of Mechanical Engineering, Stanford University, Stanford, California, 1963.

[33] S. J. Kline, W. C. Reynolds, F. A. Schraub, and P. W. Runstadler. The structure of turbulent boundary layers. *Journal of Fluid Mechanics*, 30(4):741–773, 1967.

[34] Y. G. Guezennec, U. Piomelli, and J. Kim. On the three-dimensional structure of wall-bounded turbulent flows. *Physics of Fluids A: Fluid Dynamics*, 1(4):764–771, 1989.

[35] S. K. Robinson. The kinematics of turbulent boundary layer structure. Technical report, NASA Technical Memorandum 103859, 1990.

[36] P. Moin. Analysis of turbulence data generated by numerical simulations. AIAA Paper AIAA Paper 87-0194, American Institute of Aeronautics and Astronautics, Reno, NV, 1987.

[37] S. K. Robinson, S. J. Kline, and P. R. Spalart. A review of quasi-coherent structures in a numerically simulated turbulent boundary layer. Technical Report TM-102191, NASA, 1989.

[38] G. Dacome, R. Mörsch, M. Kotsonis, and W. J. Baars. Opposition flow control for reducing skin-friction drag of a turbulent boundary layer. *Phys. Rev. Fluids*, 9:064602, Jun 2024.

[39] W. W. Willmarth and B. J. Tu. Structure of turbulence in the boundary layer near the wall. *The Physics of Fluids*, 10(9):S134–S137, 1967.

[40] W. W. Willmarth and S. S. Lu. Structure of the Reynolds stress near the wall. *Journal of Fluid Mechanics*, 55(1):65–92, 1972.

[41] T. J. Black. An analytical model for turbulent boundary layer momentum transfer. *ASME Paper No. 68-FE-42*, 1968.

[42] G. R. Offen and S. J. Kline. A proposed model of the bursting process in turbulent boundary layers. *Journal of Fluid Mechanics*, 70(2):209–228, 1975.

[43] M. R. Head and P. Bandyopadhyay. New aspects of turbulent boundary layer structure. *Journal of Fluid Mechanics*, 107:297–338, 1981.

[44] A. K. Praturi and R. S. Brodkey. A stereoscopic visual study of coherent structures in turbulent shear flow. *Journal of Fluid Mechanics*, 89(2):251–272, 1978.

[45] R. F. Blackwelder and J. H. Haritonidis. Scaling of the bursting frequency in turbulent boundary layers. *Journal of Fluid Mechanics*, 132:87–103, 1983.

[46] J. L. Lumley. The structure of inhomogeneous turbulent flows. In A. M. Yaglom and V. I. Tatarsky, editors, *Atmospheric turbulence and radio wave propagation*, pages 166–178. Nauka, Moscow, 1967.

[47] A. N. Kolmogorov. The local structure of turbulence in incompressible viscous fluid for very large Reynolds numbers. *Proceedings of the Royal Society of London. Series A: Mathematical and Physical Sciences*, 434(1890):9–13, 1991. Originally published in Dokl. Akad. Nauk SSSR (1941) 30: 301-305.

[48] S. B. Pope. *Turbulent Flows*. Cambridge University Press, Cambridge, 2000.

[49] S. Ghaemi. Passive and active control of turbulent flows. *Physics of Fluids*, 32(8):080401, 2020.

[50] Y. Kametani and K. Fukagata. Direct numerical simulation of spatially developing turbulent boundary layers with uniform blowing or suction. *Journal of Fluid Mechanics*, 681:154–172, 2011.

[51] J. J. Wang, K. Choi, L. H. Feng, T. N. Jukes, and R. D. Whalley. Recent developments in dbd plasma flow control. *Progress in Aerospace Sciences*, 62:52–78, 2013.

[52] D. Greenblatt and I. J. Wygnanski. The control of flow separation by periodic excitation. *Progress in Aerospace Sciences*, 36(7):487–545, 2000.

[53] A. Glezer and M. Amitay. Synthetic jets. *Annual Review of Fluid Mechanics*, 34(Volume 34, 2002):503–529, 2002.

[54] D. Tanish, P. Swagata, K. Upamanyu, and M. Saptarshi. Review of active and passive devices for drag reduction. *Acceleron Aerospace Journal*, 4(4):1056–1081, 2025. Review Paper.

[55] Y. S. Wang, W. X. Huang, and C. X. Xu. Active control for drag reduction in turbulent channel flow: the opposition control schemes revisited. *Fluid Dynamics Research*, 48(5):055501, 2016.

[56] BASF Coatings. Sharkskin technology for airplanes. https://www.basf-coatings.com/global/en/products-and-solutions/sharkskin-technology, 2024. Accessed: 2024-12-20.

[57] A. G. Kravchenko, H. Choi, and P. Moin. On the relation of near-wall streamwise vortices to wall skin friction in turbulent boundary layers. *Physics of Fluids A: Fluid Dynamics*, 5(12):3307–3309, 1993.

[58] E. Laurien and L. Kleiser. Numerical simulation of boundary-layer transition and transition control. *Journal of Fluid Mechanics*, 199:403–440, 1989.

[59] J. Park and H. Choi. Machine-learning-based feedback control for drag reduction in a turbulent channel flow. *Journal of Fluid Mechanics*, 904:A24, 2020.

[60] Z. Li, X. Dang, P. Lv, and H. Duan. Blowing-only opposition control: Characteristics of turbulent drag reduction and implementation by deep learning. *AIP Advances*, 11(3):035016, 2021.

[61] E. Saccaggi and G. M. Di Cicca. Bayesian optimisation of an opposition control strategy in a fully turbulent channel flow. *Journal of Fluid Mechanics*, 1028:A39, 2026.

[62] G. M. Di Cicca. Proportional opposition control of turbulence. In *27th International Congress of the Aeronautical Sciences (ICAS)*, Nice, France, 2010. ICAS.

[63] Pandas development team. Pandas: Python data analysis library. https://pandas.pydata.org, 2026. Latest version: 3.0.4, released Jun 28, 2026.